Observatório Nacional

MINISTÉRIO DA CIÊNCIA, TECNOLOGIA, INOVAÇÕES E COMUNICAÇÕES

ON THE COSMIC ACCELERATION AND MATTER CLUSTERING IN MODIFIED $f(R)$ GRAVITY MODELS

Bruno Wesley Nogueira Ribeiro

Tese de Doutorado apresentada ao Programa de Pós-graduação em Astronomia do Observatório Nacional/MCTIC, como parte dos requisitos necessários à obtenção do Título de Doutor em Astronomia.

Orientador: Armando Bartolome Bernui Leo

Co-orientadora: Marcela Campista Borges de Carvalho

Rio de Janeiro
Novembro de 2024

ON THE COSMIC ACCELERATION AND MATTER CLUSTERING IN MODIFIED $f(R)$ GRAVITY MODELS

Bruno Wesley Nogueira Ribeiro

TESE SUBMETIDA AO PROGRAMA DE PÓS-GRADUAÇÃO EM ASTRONOMIA DO OBSERVATÓRIO NACIONAL/MCTIC COMO PARTE DOS REQUISITOS NECESSÁRIOS PARA A OBTENÇÃO DO TÍTULO DE DOUTOR EM ASTRONOMIA.

Examinada por:

Prof. Nome do Primeiro Examinador Sobrenome, D.Sc.

Prof. Nome da Segunda Examinadora Sobrenome, Ph.D.

Dr. Nome da Terceira Examinadora Sobrenome, D.Sc.

Prof. Nome do Quarto Examinador Sobrenome, Ph.D.

Prof. Nome do Quinto Examinador Sobrenome, Ph.D.

RIO DE JANEIRO, RJ – BRASIL
NOVEMBRO DE 2024

Ribeiro, Bruno Wesley Nogueira

On the cosmic acceleration and matter clustering in modified $f(R)$ gravity models/Bruno Wesley Nogueira Ribeiro. – Rio de Janeiro: ON/MCTIC, 2024.

XXVII, 183 p.: il.; 29, 7cm.

Orientador: Armando Bartolome Bernui Leo

Co-orientadora: Marcela Campista Borges de Carvalho

Tese (doutorado) – ON/MCTIC/Programa de Pós-graduação em Astronomia, 2024.

Bibliography: p. 132 – 157.

1. $f(R)$ gravity. 2. Modified gravity. 3. Appleby-Battye model. I. Campista Borges de Carvalho, Marcela. II. Observatório Nacional/MCTIC, Programa de Pós-graduação em Astronomia. III. Título.

Dedico esta tese de doutorado à memória de meus queridos avós, Lizete e Diomédio, que, embora não estejam mais fisicamente presentes, permanecem vivos em minhas lembranças e em cada passo desta prazerosa jornada.

Agradecimentos

A realização deste trabalho representa o ápice de uma longa jornada de aprendizado, esforço e dedicação, e não seria possível sem o apoio e a colaboração de tantas pessoas especiais que marcaram minha trajetória.

Inicio agradecendo aos meus queridos avós Lizete e Diomédio, cuja memória sempre esteve presente como fonte de inspiração e força. A eles, dedico este trabalho com todo o amor e gratidão, por terem plantado as sementes que germinaram em mim valores e sonhos.

Agradeço aos meus pais e ao meu padrasto, que me deram suporte incondicional em todos os momentos, e a toda minha família, por serem meu alicerce e por celebrarem cada conquista ao meu lado.

Expresso minha profunda gratidão ao meu orientador, Armando Bernui, e à minha coorientadora, Marcela Campista, pela paciência, orientação e confiança. Suas contribuições foram essenciais para o desenvolvimento deste trabalho e para o meu amadurecimento acadêmico.

Aos amigos da pós-graduação em Astronomia do Observatório Nacional – RJ, meus mais sinceros agradecimentos. Sousa, Ayslana, Rayff, Camila, Fernanda, Gabriel, Danilo, Xiaoyun – e todos da família Casa Branca –, gostaria de dizer que cada momento compartilhado dentro e fora dos prédios do ON foi único e inesquecível. Nossas conversas, risadas e desafios superados juntos foram fundamentais para tornar esta caminhada mais leve e prazerosa.

Agradeço imensamente ao grupo de Cosmologia Computacional e Observacional do Observatório Nacional (CCOON) pelo privilégio de fazer parte, debater e desenvolver pesquisa científica de qualidade com vocês.

Agradeço também a todos os professores, servidores e funcionários do Observatório Nacional, por serem parte de uma instituição que promove a excelência científica e acolhe seus estudantes com tanto zelo. Ao Observatório Nacional, minha eterna gratidão por ter sido minha casa acadêmica durante essa jornada.

Por fim, agradeço à CAPES pelo apoio financeiro que viabilizou esta pesquisa, permitindo que eu me dedicasse integralmente ao desenvolvimento deste trabalho.

Muito obrigado!

"O conhecimento torna a alma jovem e diminui a amargura da velhice. Colhe, pois, a sabedoria. Armazena suavidade para o amanhã."

Leonardo da Vinci

Resumo da Tese apresentada ao Programa de Pós-graduação em Astronomia do Observatório Nacional/MCTIC como parte dos requisitos necessários para a obtenção do título de Doutor em Astronomia (D.Sc.)

ON THE COSMIC ACCELERATION AND MATTER CLUSTERING IN MODIFIED $f(R)$ GRAVITY MODELS

Bruno Wesley Nogueira Ribeiro

Novembro/2024

Orientador: Armando Bartolome Bernui Leo

Co-orientadora: Marcela Campista Borges de Carvalho

Programa: Astronomia

Entender a origem da atual expansão acelerada do universo é um dos maiores desafios da cosmologia moderna e da física de partículas. No contexto do modelo padrão da cosmologia, o modelo ΛCDM, essa aceleração é atribuída à constante cosmológica Λ, ou, equivalentemente, à densidade de energia do vácuo quântico, que é reconhecida como a forma mais simples de energia escura. Acontece que, seja por meio de uma constante cosmológica ou de formas mais gerais de energia escura, essa explicação para a origem da aceleração cósmica recente apresenta algumas inconsistências internas. Por um lado, dentro da visão padrão da cosmologia, dois problemas envolvendo a constante cosmológica preocupam tanto os físicos de partículas quanto os cosmólogos: (i) a densidade de energia do vácuo medida através de observações cosmológicas é surpreendentemente menor do que a estimada pela teoria quântica de campos (até 120 ordens de magnitude, dependendo da teoria utilizada); e (ii) as densidades normalizadas de energia do vácuo e da matéria possuem valores curiosamente próximos hoje, o que parece ser uma coincidência cósmica. Por outro lado, deveria ser possível observar a energia escura diretamente, uma vez que ela corresponde a aproximadamente 70% da densidade total de energia do universo, de acordo com observações atuais. No entanto, nenhuma energia escura foi observada diretamente a nível fundamental (na física de partículas) até o momento. Todas as evidências de uma componente energética que exerce pressão negativa sobre o universo vêm de observações cosmológicas indiretas.

A fim de evitar os problemas inerentes à constante cosmológica, ou a formas mais gerais de energia escura, alguns cenários alternativos baseados em uma modificação adequada da Relatividade Geral, a teoria atual da gravidade, foram propostos. Este é o caso das teorias de gravidade $f(R)$, que generalizam a gravitação substituindo o termo $R-2\Lambda$ na Lagrangiana de Einstein-Hilbert por uma função geral do escalar de Ricci, R. Sabe-se que essas teorias explicam adequadamente a aceleração cósmica como um efeito da geometria do espaço-tempo, em vez de uma forma exótica de energia escura. Elas também são conformemente equivalentes à teoria de Einstein com a adição de um grau de liberdade extra no setor gravitacional, o *scalaron*, um campo escalar canônico cujo potencial é unicamente determinado pela curvatura escalar de Ricci, R.

Nesta tese, estudamos a viabilidade cosmológica de três modelos $f(R)$, a saber, os modelos de Appleby-Battye, Hu-Sawicki e Starobinsky. Inicialmente, derivamos as equações de movimento para cada modelo e as resolvemos numericamente para parâmetros importantes do *background* cosmológico: a taxa de Hubble $H(z)$ e a equação de estado $w_{\rm DE}(z)$. Como o background cosmológico é altamente degenerado, seguimos para o nível perturbativo resolvendo numericamente as equações diferenciais relacionadas ao contraste de densidade da matéria $\delta_{\rm m}(z)$ e à taxa de crescimento normalizada na escala física correspondente à $8\,{\rm Mpc}/h$, $[f\sigma_8](z)$, para cada modelo. Em seguida, realizamos análises estatísticas MCMC e restringimos os parâmetros livres dos modelos de Appleby-Battye e de Hu-Sawicki, considerando três conjuntos de dados cosmológicos: medições de $H(z)$ pelo método dos cronômetros cósmicos, $[f\sigma_8](z)$ a partir das observações do *redshift-space distortion*, e medições de $m_{\rm B}(z)$ de supernovas do tipo Ia das colaborações Pantheon+ e SH0ES. Nossos resultados são consistentes com os reportados na literatura para os parâmetros cosmológicos, como a constante de Hubble (H_0), a densidade normalizada da matéria ($\Omega_{\rm m,0}$), a variância das flutuações da matéria na escala de $8\,{\rm Mpc}/h$ ($\sigma_{8,0}$) e a magnitude absoluta ($M_{\rm B}$), em ambos os casos. Além disso, nossos *best-fits* dos parâmetros dos modelos foram: $b = 2.28^{+6.52}_{-0.55}$ (apenas dados de SNe Ia) e $b = 2.18^{+5.41}_{-0.55}$ (combinação de dados SNe+CC+RSD), abrangendo a Relatividade Geral ($b \gg 1$) no nível de confiança de 2σ, para o modelo de Appleby-Battye; e $\mu = 77.0^{+18.0}_{-56.0}$ (apenas dados de SNe Ia) e $\mu = 93.0^{+41.0}_{-55.0}$ (combinação de dados SNe+CC+RSD), o que exclui a Relatividade Geral ($\mu = 0$) no nível de confiança de 2σ, para o modelo de Hu-Sawicki. Por fim, o critério de informação Akaike penalizou tanto o modelo de Appleby-Battye quanto o de Hu-Sawicki devido ao fato de cada um ter um parâmetro independente adicional em comparação com o modelo de referência ΛCDM plano: $\Delta AIC = 0.716$ e $\Delta AIC = 132.969$, respectivamente. No entanto, nossos resultados mostram que o modelo de Appleby-Battye exibe um valor de AIC muito próximo ao do modelo ΛCDM plano ($\Delta{\rm AIC} \sim 0.7$), tornando-o uma alternativa competitiva ao

modelo padrão na descrição da expansão acelerada e do crescimento das estruturas no universo, porém sem exigir qualquer energia escura exótica.

Palavras-Chave: Gravidade $f(R)$; Gravidade modificada; Modelo de Appleby-Battye; Modelo de Hu-Sawicki; Modelo de Starobinsky

Abstract of Thesis presented to Observatório Nacional/MCTIC as a partial fulfillment of the requirements for the degree of Doctor of Astronomy (D.Sc.)

ON THE COSMIC ACCELERATION AND MATTER CLUSTERING IN MODIFIED $f(R)$ GRAVITY MODELS

Bruno Wesley Nogueira Ribeiro

November/2024

Advisor: Armando Bartolome Bernui Leo

Co-advisor: Marcela Campista Borges de Carvalho

Department: Astronomy

Understanding the origin of the current accelerated expansion of the universe is one of the greatest challenges in modern cosmology and particle physics. In the context of the standard cosmological model, the ΛCDM model, this acceleration is attributed to the cosmological constant Λ, or, equivalently, to the energy density of the quantum vacuum, which is recognized as the simplest form of dark energy. It turns out that, whether through a cosmological constant or more general forms of dark energy, this explanation for the origin of recent cosmic acceleration has some internal shortcomings. On the one hand, within the standard view of cosmology, two issues involving the cosmological constant concern both particle physicists and cosmologists: (i) the vacuum energy density measured via cosmological observations is astoundingly smaller than that estimated by quantum field theory (up to 120 orders of magnitude, depending on the theory used); and (ii) the normalized vacuum and matter energy densities have curiously close values today, which appears to be a cosmic coincidence. On the other hand, it should be possible to observe dark energy directly, since it corresponds to approximately 70% of the total energy density of the universe according to current observations. However, no dark energy has been observed directly at a fundamental level (in particle physics) to date. All evidence of an energetic component exerting negative pressure on the universe comes from indirect cosmological observations.

In order to avoid the issues inherent to a cosmological constant, or to more general forms of dark energy, some alternative scenarios based on a suitable modification of General Relativity, the current theory of gravity, have been proposed. This is the

case with the $f(R)$ theories of gravity, which generalize gravitation by replacing the term $R - 2\Lambda$ in the Einstein-Hilbert Lagrangian by a general function of the Ricci scalar, R. Theses theories are known to properly explain cosmic acceleration as an effect of the spacetime geometry, instead of an exotic form of dark energy. They are also conformally equivalent to Einstein's theory with the addition of an extra degree of freedom in the gravitational sector, the *scalaron*, a canonical scalar field whose potential is uniquely determined by the Ricci scalar curvature, R.

In this thesis, we study the cosmological viability of three $f(R)$ models, namely, the Appleby-Battye, Hu-Sawicki, and Starobinsky models. We first derive the equations of motion for each model and numerically solve them for important parameters of the cosmological background: the Hubble rate $H(z)$ and the equation of state $w_{\rm DE}(z)$. Since the cosmological background is highly degenerate, we proceed to the perturbative level by numerically solving the differential equations related to the matter density contrast $\delta_{\rm m}(z)$ and the normalized growth rate at the physical scale of $8\,{\rm Mpc}/h$, $[f\sigma_8](z)$, for each model. Next, we perform MCMC statistical analyses and constrain the free parameters of the Appleby-Battye and Hu-Sawicki models by considering three cosmological datasets: $H(z)$ measurements from the cosmic chronometer method, $[f\sigma_8](z)$ from redshift-space distortion observations, and type Ia supernovae $m_{\rm B}(z)$ measurements from Pantheon+ and SH0ES collaborations. Our results are consistent with those reported in the literature for the cosmological parameters, such as the Hubble constant (H_0), the normalized matter density ($\Omega_{\rm m,0}$), the variance of matter fluctuations at the scale of $8\,{\rm Mpc}/h$ ($\sigma_{8,0}$), and the absolute magnitude ($M_{\rm B}$), in both cases. Additionally, our best-fit model parameters were: $b = 2.28^{+6.52}_{-0.55}$ (SNe Ia data alone) and $b = 2.18^{+5.41}_{-0.55}$ (SNe+CC+RSD data combination), encompassing General Relativity ($b \gg 1$) at 2σ CL, for the Appleby-Battye model, and $\mu = 77.0^{+18.0}_{-56.0}$ (SNe Ia data alone) and $\mu = 93.0^{+41.0}_{-55.0}$ (SNe+CC+RSD data combination), which excludes General Relativity ($\mu = 0$) at 2σ CL, for the Hu-Sawicki model. Finally, the Akaike information criterion penalized both the Appleby-Battye and Hu-Sawicki models due to each having an additional independent parameter compared to the flat-ΛCDM reference model: $\Delta AIC = 0.716$ and $\Delta AIC = 132.969$, respectively. However, our results show that the Appleby-Battye model exhibits an AIC value very close to that of the flat-ΛCDM model (ΔAIC ~ 0.7), making it a competitive alternative to the standard model in describing the accelerated expansion and growth of structures in the universe, but without requiring any exotic dark energy.

Keywords: $f(R)$ gravity; Modified gravity; Appleby-Battye model; Hu-Sawicki model; Starobinsky model

List of Figures

3.1 Map of the universe as seen by the SDSS. 23
3.2 Expanding universe. 24
3.3 Nearby Hubble diagram. 25
3.4 Evolution of H_0 estimations from CMB and distance-ladder data. . . 26
3.5 Current H_0 measurements 27
3.6 BBN (a) nuclear reactions and (b) light elements abundances. 29
3.7 Dependence of light element abundances on $\eta_{b\gamma}$. 30
3.8 Blackbody spectrum of the CMB. 32
3.9 CMB fluctuations map from the WMAP and Planck probes. 33
3.10 Planck 2018 temperature power spectrum. 35
3.11 Geometry of the universe. 43
3.12 Evolution of energy densities in the universe. 47
3.13 Evolution of the scale factor $a(t)$. 48
3.14 Planck 2018 observational constraints on the $\Omega_{\rm m} - \sigma_8$ plane. 64
3.15 Planck 2018 curvature constraints in the ΛCDM+$\Omega_{\rm K}$ extension. . . . 64
3.16 DESI 2024 DE constraints on the $w_0 - w_a$ plane (BAO+CMB/SNe). 66
3.17 DESI 2024 DE constraints on the $w_0 - w_a$ plane (BAO+CMB+SNe). 67

5.1 Curves for the R^2-AB model: (a) H and (b) $w_{\rm DE}$. 112
5.2 Curves for the R^2-AB model with varying b: (a) H and (b) $w_{\rm DE}$ . . . 112
5.3 Curves for the R^2-AB model: (a) $\delta_{\rm m}$ and (b) $f\sigma_8$. 112
5.4 Curves for the R^2-AB model with varying b: (a) $\delta_{\rm m}$ and (b) $f\sigma_8$. . . . 113
5.5 Curves of $H(z)$ for the R^2-AB, HS, and Starobinsky models. 115
5.6 Curves of (a) $w_{\rm DE}$ and (b) $f\sigma_8$ for the three $f(R)$ models. 115
5.7 MCMC results for the R^2-AB model using PN$^+$ SNe Ia data alone. . 120
5.8 MCMC results for the R^2-AB model using PN$^+$ + CC + RSD data. . 121
5.9 MCMC results for the HS model using PN$^+$ SNe Ia data alone. . . . 123
5.10 MCMC results for the HS model using PN$^+$ + CC + RSD data. . . . 124

List of Tables

3.1 Summary of solutions for a single-component universe. 47
3.2 Planck's six primary cosmological parameters. 63

5.1 Minimum allowed values for the Starobinsky model parameter. 107
5.2 31 $H(z)$ measurements obtained using the CC method. 116
5.3 20 $f\sigma_8(z)$ measurements derived from RSD observations. 117
5.4 Best-fit values obtained from our MCMC likelihood analyses. 124
5.5 χ^2 statistics for model comparison: ΛCDM *vs.* AB *vs.* HS model. . . 125

A.1 Evolution of H_0 estimates from CMB and distance-ladder data. . . . 159
A.2 50 recent H_0 measurements from current observations. 160

List of Symbols

t	cosmic time
τ	proper time
η	conformal time
z	cosmological redshift
a	scale factor
$g_{\mu\nu}$	metric tensor
$\eta_{\mu\nu}$	Minkowski metric
$\delta_{\mu\nu}$	Kronecker tensor
R	Ricci scalar
$R_{\mu\nu}$	Ricci tensor
$R^{\lambda}_{\mu\nu\rho}$	Riemann tensor
$G_{\mu\nu}$	Einstein tensor
$T_{\mu\nu}$	stress-energy tensor
T	trace of the stress-energy tensor
$\Gamma^{\lambda}_{\mu\nu}$	Levi-Civita connection
$\mathcal{T}^{\lambda}_{\mu\nu}$	torsion tensor
ds	infinitesimal interval
c	speed of light
Λ	cosmological constant
ρ	energy density

P	pressure
v	scalar three-velocity
v^i	three-velocity
v^μ	coordinate velocity
u^μ	four-velocity
γ_{L}	Lorentz factor
S_{EH}	Einstein-Hilbert action
$\mathcal{L}_{\mathrm{EH}}$	Einstein-Hilbert Lagrangian
$\mathcal{L}_{\mathrm{M}}$	matter-energy Lagrangian
g	determinant of the metric tensor
ϕ_{M}	matter-energy fields
κ^2	Einstein's constant
m_{Pl}	reduced Planck mass
G	Newtonian universal constant
r_{sw}	Schwarzschild radius
v_{scp}	scape velocity
r	comoving distance
d	physical distance
H	Hubble-Lemaître parameter
$\mathcal{H}$	conformal Hubble-Lemaître parameter
t_0	present time
H_0	Hubble-Lemaître constant
h	normalized Hubble-Lemaître constant
$\eta_{\mathrm{b}\gamma}$	baryon-to-photon ratio
$\mathcal{N}$	numerical density

T	temperature
$\hbar$	reduced Planck's constant
k_{B}	Boltzmann's constant
ν	frequency
k	wavenumber
T_0	current temperature
$\Theta(\hat{n})$	temperature fluctuations
$\Theta(k)$	amplitude of the spectrum of fluctuations
Θ_{lm}	multipole moments
Y_{lm}	spherical harmonics
δ_{ij}	Kronecker delta
C_l	angular power spectrum
$\mathcal{D}_l$	Planck angular power spectrum
θ_{MC}	acoustic angular scale at decoupling
τ_{re}	optical depth to reionization
A_{s}	spectral amplitude of the primordial fluctuations
n_{s}	scalar spectral index
ρ_{cr}	critical density
Ω_{b}	normalized baryon density
Ω_{r}	normalized radiation energy density
Ω_{m}	normalized matter density
Ω_Λ	normalized vacuum energy density
Ω_{DE}	normalized dark energy density
Ω	normalized total energy density
Ω_0	current normalized total energy density

Ω_{K}	normalized curvature density
w	equation of state
$\mathcal{R}$	physical scale
σ_8	spectral amplitude of matter fluctuations at physical scale of $8\,\mathrm{Mpc}/h$
q	deceleration parameter
r_{H}	Hubble sphere
r_{p}	particle horizon
r_{s}	sound horizon
$\mathcal{X}$	conformal distance
d_{L}	luminosity distance
d_{A}	angular diameter distance
m_{B}	apparent magnitude
M_{B}	absolute magnitude
K	curvature of the spatial three-section
$\Omega_{\mathrm{m},0}$	current normalized matter density
$\Omega_{\mathrm{r},0}$	current normalized radiation density
$\sigma_{8,0}$	current spectral amplitude of matter fluctuations at $8\,\mathrm{Mpc}/h$
$\delta g_{\mu\nu}$	metric perturbations
δR	Ricci scalar perturbations
$\delta R_{\mu\nu}$	Ricci tensor perturbations
$\delta G_{\mu\nu}$	Einstein tensor perturbations
$\delta T_{\mu\nu}$	matter-energy perturbations
Φ	lapse function (scalar metric perturbation)
Ψ	scalar curvature perturbation (scalar metric perturbation)
$\delta\rho$	energy density perturbations

δq	momentum density perturbations
δP	pressure perturbations
Π_{ij}	anisotropic stress
δ	density contrast
$\Phi_{\rm B}$	1st Bardeen potential
$\Psi_{\rm B}$	2nd Bardeen potential
ζ	curvature perturbation
$\mathcal{S}$	comoving curvature perturbation
$f_{\rm g}$	growth function
γ	growth index
$f\sigma_8$	normalized growth rate
S_φ	canonical inflationary action
φ	inflaton scalar field
$V(\varphi)$	inflaton potential
ϵ_V	1st slow-roll parameter
η_V	2nd slow-roll parameter
N	number of e-folds
$\delta\varphi$	inflaton perturbations
ξ	primordial gauge-invariant perturbation
$\mathcal{P}_\xi$	primordial scalar power spectrum
A_ξ	amplitude of the primordial power spectrum
n_ξ	primordial spectral index
$\mathcal{P}_{\rm T}$	primordial tensor power spectrum
$\mathcal{P}_{\rm s}$	scalar power spectrum
$r_{\rm inf}$	tensor-to-scalar ratio

$\mathcal{G}$	Gauss-Bonnet invariant
Q	non-metricity scalar
ψ	Bans-Dicke scalar field
$\omega_{\rm BD}$	Brans-Dicke parameter
$\omega(\psi)$	generalized Brans-Dicke parameter
$\mathscr{G}_{\rm AB}$	five-dimensional metric tensor
$\mathscr{R}_{\rm AB}$	five-dimensional Ricci tensor
$\mathscr{R}$	five-dimensional Ricci scalar
$\mathfrak{z}$	extra compactified dimension
A_μ	eletromagnetic four-potential
$F_{\mu\nu}$	Faraday tensor
$f(R)$	arbitrary function of the Ricci scalar
$\tilde{G}_{\mu\nu}$	modified Einstein tensor
R_0	current scalar curvature
$\hat{R}$	Palatini Ricci scalar
$\hat{R}_{\mu\nu}$	Palatini Ricci tensor
$\hat{\Gamma}^{\lambda}_{\mu\nu}$	Palatini non-metric connection
$\mathcal{A}$	conformal coupling function
β	conformal coupling parameter
$V_{\rm eff}$	effective potential
$m_{\rm eff}$	effective mass
$\rho_{\rm eff}$	effective density
$P_{\rm eff}$	effective pressure
$w_{\rm eff}$	effective equation of state
δf	$f(R)$ perturbations

$M_{\rm s}$	scalaron rest-mass
$\Phi_{\rm eff}$	effective gravitational potential
$G_{\rm eff}$	effective gravitational constant
$R_{\rm vac}$	scalar curvature of vacuum
$\epsilon_{\rm AB}$	Appleby-Battye model parameter
b	Appleby-Battye independent parameter
m_0^2	current curvature scale from the Hu-Sawicki model
c_1	Hu-Sawicki model parameter
c_2	Hu-Sawicki idependent parameter
μ	redefined Hu-Sawicki idependent parameter
$R_{\rm S}$	current curvature scale from the Starobinsky model
$\lambda_{\rm S}$	Starobinsky independent parameter
n	fixed parameter of the Hu-Sawicki and Starobinsky models
$\Xi(R)$	correction terms to the General Relativity
Δ	scalaron mass scale
$\mathcal{M}$	scalaron mass
$M_{\rm Pl}$	Planck mass
$\delta_{\rm bias}$	bias factor
$v_{\rm sp}$	velocity scale parameter
$\sigma_8^{\rm tr}$	matter fluctuation amplitude of the cosmological tracer
$\tilde{\mu}_{\rm obs}$	observed distance modulus
$\tilde{\mu}_{\rm theo}$	theoretical distance modulus
X_1	light curve correction
X_2	brightness correction
$\tilde{\nu}_1$	stretch of the light curve correction

$\tilde{\nu}_2$ color at maximum brightness correction

$\delta_{\tilde{\mu}-\text{bias}}$ bias factor

$\mathscr{P}$ probability distribution functions

$\mathcal{L}(\vartheta)$ Gaussian likelihood

C_{ij} covariance matrix

σ_i error at datum i

χ^2 chi-square function

$\mathscr{N}$ number of data points

ϖ number of independently adjusted parameters

$\bar{\chi}^2$ reduced chi-square

List of Abbreviations

DM dark matter

CDM cold dark matter

CMB cosmic microwave background

DE dark energy

ΛCDM Lambda cold dark matter

EoS equation of state

SNe Ia Type Ia supernovae

GR General Relativity

QFT quantum field theory

CPL Chevallier-Polarski-Linder

MTGs modified theories of gravity

ETGs extended theories of gravity

AB Appleby-Battye

R^2-AB R^2-corrected Appleby-Battye

HS Hu-Sawicki

FLRW Friedmann-Lemaître-Robertson-Walker

BAO baryonic acoustic oscillations

LSS large-scale structure

MCMC markov-chain monte carlo

CC cosmic chronometers

RSD redshift-space distortion

AIC Akaike information criterion

SR Special Relativity

PR principle of relativity

EP equivalence principle

PGC principle of general covariance

PC principle of causality

CTC closed timelike curve

NEC Null Energy Condition

WEC Weak Energy Condition

SEC Strong Energy Condition

DEC Dominant Energy Condition

CP cosmological principle

BBN big bang nucleosynthesis

RW Robertson-Walker

HBB Hot Big Bang

SDSS Sloan Digital Sky Survey

SH0ES supernovae H_0 for the equation of state

SBF surface brightness fluctuation

QSO quasi-stellar object or quasar

GW gravitational wave

GL gravitational lensing

FRB fast radio burst

HST-KP Hubble space telescope key project

CHP Carnegie Hubble program

WMAP Wilkinson Microwave Anisotropy Probe

ACT Atacama Cosmology Telescope

SNe II Type II supernovae

LS last scattering

RD radiation-dominated

MD matter-dominated

Λ**D** vacuum-dominated

GUT Grand Unified Theory

PGWs primordial gravitational waves

SMC standard model of cosmology

PPN parametrized post-Newtonian

ψ**MDE** ψ-matter dominated epoch

SPS stellar population synthesis

EGS extra-galactic sources

LRG luminous red galaxies

ELG emission-line galaxies

PN$^+$ Pantheon+

PN Pantheon

PDF probability distribution function

Contents

List of Figures xii

List of Tables xiii

List of Symbols xxi

List of Abbreviations xxii

1 Introduction 1

2 Fundamentals of General Relativity 6

2.1 Physical principles and assumptions . . . 6
2.2 Mathematical tool . . . 9
2.2.1 Metric tensor . . . 9
2.2.2 Geodesic connection . . . 11
2.2.3 Curvature and related tensors . . . 12
2.3 Stress-energy tensor . . . 14
2.3.1 General features . . . 14
2.3.2 Energy conditions . . . 15
2.3.3 Perfect fluid . . . 16
2.4 Field equations . . . 17
2.4.1 Variational approach . . . 18
2.4.2 Vaccum energy . . . 18
2.4.3 Newtonian limit . . . 20

3 Standard Cosmological Model 22

3.1 Expanding universe . . . 23
3.2 Primordial nucleosynthesis . . . 28
3.3 Cosmic Microwave Background . . . 31
3.4 Background dynamics . . . 36
3.4.1 Cosmological redshift . . . 36
3.4.2 Cosmological distances . . . 38

3.4.3 Robertson-Walker metric . . . 41
3.4.4 Friedmann equations . . . 44
3.4.5 Cosmic acceleration . . . 46
3.5 Cosmological perturbations . . . 48
3.5.1 Metric perturbations . . . 49
3.5.2 Fluid perturbations . . . 50
3.5.3 Newtonian gauge . . . 50
3.5.4 Perturbed equations . . . 51
3.6 Structure formation . . . 52
3.6.1 Super-horizon (non-)evolution . . . 53
3.6.2 Adiabatic perturbations . . . 53
3.6.3 Contrast equation and growth rate . . . 54
3.7 Primordial inflation . . . 56
3.7.1 HBB issues . . . 57
3.7.2 Inflationary dynamics . . . 58
3.7.3 Slow-roll approximation . . . 59
3.7.4 Primordial power spectrum . . . 60
3.7.5 HBB issues revisited . . . 61
3.8 Flat-ΛCDM model and observations . . . 63

4 Modified Gravity and Cosmology 68
4.1 Why modifying gravity? . . . 68
4.1.1 Quantum gravity motivation . . . 69
4.1.2 Astrophysical and cosmological motivation . . . 70
4.1.3 Mathematical motivation . . . 71
4.2 What a good MTG should do? . . . 72
4.3 Theories of modified gravity . . . 73
4.3.1 The prototype: Brans–Dicke theory . . . 74
4.3.2 General scalar-tensor theories . . . 75
4.3.3 Higher dimensional theories . . . 76
4.3.4 Higher order theories . . . 78
4.4 $f(R)$ theories of gravity . . . 80
4.4.1 Generalized Einstein-Hilbert action . . . 81
4.4.2 Field equations: the metric formalism . . . 81
4.4.3 Newtonian weak-field approximation . . . 82
4.4.4 Palatini formalism . . . 83
4.4.5 Equivalence between theories . . . 85
4.4.6 Einstein and Jordan frames . . . 86
4.4.7 Chameleon mechanism . . . 87

4.4.8 Theoretical and observational bounds . . . 89
4.5 $f(R)$ cosmology . . . 90
4.5.1 Background dynamics . . . 90
4.5.2 Autonomous equations . . . 91
4.5.3 Critical points . . . 93
4.5.4 $f(R)$ classification and viable models . . . 96
4.5.5 $f(R)$ cosmological perturbations . . . 98
4.5.6 Modified contrast equation and growth rate . . . 99

5 $f(R)$ models: Numerical Solutions & Observational Constraints 102
5.1 Three viable $f(R)$ models . . . 102
5.1.1 Appleby-Battye model . . . 103
5.1.2 Hu-Sawicki model . . . 105
5.1.3 Starobinsky model . . . 106
5.2 High curvature regime . . . 107
5.3 Weak curvature singularity . . . 107
5.4 Cosmological evolution . . . 109
5.5 Initial conditions and numerical results . . . 110
5.6 Cosmological datasets . . . 114
5.6.1 Cosmic Chronometers . . . 114
5.6.2 Normalized growth rate . . . 116
5.6.3 Pantheon+ and SH0ES . . . 117
5.7 Analyses and Results . . . 118
5.8 Summary . . . 126

6 Conclusions 128

Bibliography 132

A Appendix A 158

B Appendix B 161

Chapter 1

Introduction

Over a little more than two millennia, great questions have challenged the human intellect, but none of them still seem as alive as *what the cosmos is made of*. This issue has gained even more prominence over the last two decades, as the discovery of the universe's accelerated expansion has strengthened the idea that the universe may not only consist of visible matter, i.e., dust and radiation, to which we were accustomed, and cold dark matter (cold DM or CDM), necessary to explain the anomaly in galaxy rotation curves and the acoustic peaks in the power spectrum of the cosmic microwave background (CMB), but also an exotic form of energy, generically called dark energy (DE), whose primary attribute is having negative pressure. In the context of the standard ΛCDM model, such a negative pressure that accelerates the expansion of the universe is attributed to a positive cosmological constant, Λ, with equation of state (EoS) given by $w_\Lambda = P_\Lambda/\rho_\Lambda = -1$.

In 1998, two distinct groups of astrophysicists investigating the remnant light of stellar explosions known as Type Ia supernovae (SNe Ia) – one led by S. Perlmutter and the other by B. Schmidt and A. G. Riess – simultaneously concluded that the universe is currently expanding at an accelerated rate, rather than decelerating as previously expected. By combining the luminosity distance with the redshift of 58 SNe Ia known at the time, both groups found that the data was consistent with accelerated expansion at more than 99.9 % ($3.9\,\sigma$) CL [1, 2].

In the context of General Relativity (GR), a spatially flat universe, strongly favored by observations, cannot undergo accelerated expansion in a scenario that includes only non-relativistic matter and radiation. For such acceleration to occur, an unknown form of energy, called dark energy, must exist and predominantly fill space. The defining feature of dark energy is its negative pressure [3, 4].

It has been known since the works of A. Einstein [5] and W. de Sitter [6] that the cosmological constant, Λ, with an EoS parameter given by $w_\Lambda = -1$, possesses this property, making it the simplest form of DE. In this context, Λ reappears in the field equations of GR (this time on the right-hand side), and from the perspective of

quantum field theory (QFT), it is reinterpreted as the contribution of the quantum vacuum to the matter fields present in the universe [7].

The discovery of recent cosmic acceleration in 1998 inaugurated a novel era of research in both cosmology and modern particle physics fields. Notably, the quantum-mechanical interpretation of the cosmological constant, derived from the quantum vacuum energy density, has led to what is considered one of the most disastrous predictions in the history of physics. Estimates of Λ from cosmology and QFT can differ by up to 120 orders of magnitude – a discrepancy known as the cosmological constant problem or the vacuum catastrophe [8, 9]. Additionally, the question arises as to why the energy density of the vacuum is so close to the matter density today, a puzzle referred to as the cosmic coincidence problem [10, 11].

Although such issues concerning the cosmological constant gained proportion only after the discovery of the cosmic acceleration, they were first formulated as early as the late 1960s by Y. Zeldovich [7], and have been thoroughly investigated since the 1980s through the use of scalar fields [12–14]. Unfortunately, none of these attempts were successful. More critically, S. Weinberg demonstrated through a *no-go theorem*[1] that replacing Λ with a dynamic scalar field to explain the current energy density of the quantum vacuum is not physically viable [8]. Consequently, other DE models were proposed as alternatives to the cosmological constant, such as the decaying vacuum [15], running vacuum [16], quintessence [17, 18], k-essence [19], and Chaplygin gas [20].

The simplest and most direct way in order to investigate the nature of DE is by parameterizing its equation of state $w_{\rm DE}$ as a function of time t, or, equivalently, of redshift z. In principle, there are no restrictions on modeling $w_{\rm DE}(z)$, and therefore any parameterization can be considered. Nonetheless, it is expected that a good parameterization will be well-motivated, either through the QFT or even by the unsolved quantum gravity. Additionally, since observations strongly agree with the standard ΛCDM model, it is preferable that such a parameterization arises from an expansion around $w_{\rm DE} = -1$, which corresponds to the cosmological constant Λ, with higher-order terms being negligible. As a result, numerous parameterizations of DE have been proposed in the literature, with the most well-known thus far including the linear [21], Chevallier-Polarski-Linder (CPL) [22, 23], logarithmic [24], Wetterich [25], Hannestad-Mörtsell [26], Gong-Zhang [27], Jassal-Bagla-Padmanabhan [28], Lee [29], and Barboza-Alcaniz [30].

Although most of these models fit the observational data well, no DE particle has been detected to date. Moreover, accepting a DE fluid that fills space necessarily implies a modification of the standard model of particle physics, which is one of

[1] In theoretical physics, a *no-go theorem* is a mathematical statement showing that a particular situation is not physically possible, based on the principles of quantum mechanics.

the most thoroughly tested theories to date. Consequently, some alternatives to DE, such as inhomogeneous cosmologies [31, 32] and the recent void-dominated cosmology [33], have been proposed.

Another way to address the issues related to DE and properly explain the current phase of cosmic acceleration is through the so-called $f(R)$ theories, a particular case of modified theories of gravity (MTGs) or extended theories of gravity (ETGs). These theories are considered modifications of GR, obtained by replacing the term $R - 2\Lambda$ in the Einstein-Hilbert Lagrangian with an arbitrary function of the Ricci scalar, R. This class of theories is conformally equivalent to Einstein's theory with the addition of an extra degree of freedom in the gravitational sector, the *scalaron*, a canonical scalar field whose potential is uniquely determined by the scalar curvature R [34, 35].

Modifying gravity is actually an old task that dates back to the very conception of GR theory. The first attempts took into account theories aligned with Mach's principle, such as the prototype Brans-Dicke theory [36] and general scalar-tensor theories [37], theories compatible with Maxwell's electromagnetism, such as the Kaluza-Klein higher-dimensional theories [38–40], and theories subject to renormalization, like the general higher-order theories [41, 42]. Recently, some modified theories of gravity have been proposed to explain the cosmic acceleration of the universe; this is the case of the $f(R)$ theories [43].

The $f(R)$ models offer alternative scenarios in which the recent cosmic acceleration is an effect of the spacetime geometry, rather than an unknown and exotic form of energy, such as DE. However, on theoretical grounds, the majority of these models are rejected, with only those that reduce to GR in some limit, and for this called *viable* models [44–46]. In fact, a critical feature is that, in general, they cannot be naturally incorporated into any high-energy theory; they require proper fine-tuning related to the unbounded growth of the scalaron mass [45]. Various approaches have been proposed to mitigate this problem, such as introducing additional terms in the $f(R)$ action, like an R^2 term, with a sufficiently small coefficient to ensure the existence of primordial inflation [35, 47]. These additional terms are intended to stabilize the scalaron mass and alleviate the fine-tuning requirements, making the models consistent with observations.

The first successful $f(R)$ model was proposed by Starobinsky in order to explain early inflation, with the generic form $R + \epsilon R^2$, where $\epsilon > 0$ [48]. Since then, many $f(R)$ models have been proposed, considering from simple polynomial forms to more complex functions of R (e.g., Amendola et al. [44], Tsujikawa [45], Hu-Sawicki [46], Starobinsky [47], Appleby-Battye [49–51], Li-Barrow [52], Amendola-Tsujikawa [53], Cognola et al. [54], Linder [55], Elizalde et al. [56], Xu-Chen [57], Nautiyal et al. [58], Gogoi-Goswami [59], and Oikonomou [60, 61]).

Notice, however, that within the class of viable models, there is a degeneracy because various $f(R)$ models describe the accelerated cosmic expansion as accurately as the flat-ΛCDM. In such cases, the best model for replicating matter clustering in the observed universe [62–66] must be determined at the perturbative level [67].

It turns out that alternative cosmological models undergo a statistically less efficient process of fitting observational data, mainly because they have more parameters than the flat-ΛCDM model, which has only six free parameters. However, this is not always the case when Bayesian statistical analysis is applied, as the results can vary significantly depending on the choice of priors.

In this thesis, we will primarily investigate the R^2-corrected Appleby-Battye (AB) model, proposed in Ref. [51], which, for simplicity, will be referred to throughout the text as the R^2-AB model. This model is an improvement of the original AB model [49, 50], where a term proportional to R^2, with a sufficiently small coefficient to ensure primordial inflation, was added to resolve the *weak curvature singularity* problem [35, 51], generically present in $f(R)$ models. There are several reasons for analyzing this model. First, it has passed many important tests (e.g., classical and semi-classical stability, Solar System constraints, correct primordial nucleosynthesis of light elements, and includes radiation, matter, and dark energy epochs), making it a viable alternative for explaining the current accelerated epoch. Additionally, no studies have yet analyzed this model using cosmological data to investigate its parameters. Notably, if this model shows good agreement with observational data, it could provide a geometrical explanation for the current accelerated expansion, eliminating the need for assuming a (non-physical) dark energy component in the universe. Finally, we compare this model with the flat-ΛCDM concordance model and with other two $f(R)$'s widely used for fitting different observational dataset, the Hu-Sawicki (HS) [46] and Starobinsky [47] models.

For this purpose, we have structured the thesis into four major chapters, in addition to this Introduction and the final Conclusions, as well as two appendices, A and B. In Chapter 2, we introduce the current theory of gravity, Einstein's General Relativity, which serves as the foundation for modern cosmological theory. From this theory, the necessary modifications are made in the geometric sector to address phenomena on both small scales, such as renormalization and quantization, and cosmological scales, such as the recent cosmic acceleration. In Chapter 3, we present modern cosmology, focusing on the standard Friedmann-Lemaître-Robertson-Walker (FLRW) model and the flat-ΛCDM concordance model. We also discuss the current status of relevant cosmological observations, such as the CMB, BAO, and LSS data. Chapter 4 outlines the framework of modified gravity theories, covering their key motivations, concepts, tools, viability criteria, main theories, and alignment with observations. The first half of the chapter focuses on pioneering work in Brans-Dicke

theories, general scalar-tensor theories, and higher-order theories of gravity, while the second half is dedicated to $f(R)$ theories and their developments in cosmology. In Chapter 5, we delve into the study of the R^2-corrected Appleby-Battye, Hu-Sawicki, and Starobinsky $f(R)$ models. We numerically solve these models and perform MCMC simulations, considering: *i*. SNe Ia data exclusively, and *ii*. joint analysis of SNe+CC+RSD data, for the R^2-AB and HS models. The results are compared to the flat-ΛCDM reference model using the Akaike information criterion (AIC). Finally, in Appendix A, we provide tables detailing the history of H_0 measurements that led to the current Hubble tension. Appendix B contains the main Python codes used in our analyses.

Chapter 2

Fundamentals of General Relativity

General Relativity theory is the natural generalization of Special Relativity (SR) when considering gravitational fields, or non-inertial observers. Since the Newtonian description of gravity cannot be properly incorporated into a relativistic framework, GR also offers an extended and improved approach to this phenomenon. The basic idea is that, while most fundamental forces of nature are described by fields defined on spacetime – such as the electromagnetic field and the fields characterizing the weak and strong nuclear interactions – gravity is inherent in the very structure of spacetime. Ultimately, gravity is a manifestation of the curvature of spacetime.

In this chapter, we will discuss the key aspects of GR, such as physical principles, mathematical tools, field equations, and the Newtonian limit. This foundation will help us understand how the geometric and matter-energy quantities arise, correlate, and what their respective roles are in the field equations. In other words, we will explore how gravity can be explained through the geometric properties of spacetime and how it affects and responds to the matter-energy content.

2.1 Physical principles and assumptions

The theoretical framework of the natural sciences, particularly physics, is built upon a strong foundation of physical principles. Unlike physical laws, which are statements about the behavior of nature that can be derived from experimental observations, physical principles are accepted as true from the outset; they do not emerge directly from experience but are supported by it. For example, the principle of energy conservation is widely regarded as true, as a plethora of phenomena can only be explained in light of this principle, and no experiment to date has demonstrated its violation.

In this context, GR theory relies on three basic principles [68–72]:

1. the principle of relativity (PR) asserts that all observers are equally valid in describing physical laws,

2. the equivalence principle (EP) states that the effects of gravity and acceleration are locally indistinguishable, i.e., there are no local experiments that can discern between the two effects, and

3. the principle of general covariance (PGC) complements the equivalence principle (EP) by requiring that all physical laws be expressed in the same mathematical form for any coordinate system.

Some notes about both the EP and PGC deserve to be highlighted. First, the EP is often divided into two forms in textbooks:

2*a*. the weak EP, stating that inertial mass is equal to gravitational mass, and

2*b*. the strong EP, which states that even in a strong gravitational field it is possible to locally define an observer for which the laws of SR (the flat Minkowski spacetime) are valid.

A direct consequence of the EP is the *gravitational redshift* [73], i.e., the change in the energy of photons as they propagate in the gravitational field, while the PGC requires for a theoretical description based on tensor quantities.

In addition, GR theory makes the following assumptions about the spacetime, gravity and matter:

i. spacetime is a four-dimensional curved *manifold* endowed with a metric[1],

ii. gravity is, actually, a manifestation of the curvature of the spacetime,

iii. spacetime curves onto itself and its curvature is locally determined by the distribution of the matter-energy sources, and

iv. free particles, including photons, follow a geodesic in the curved spacetime.

Therefore, two notable differences between Einstein's and Newton's theories of gravity are as follows: First, in Newton's view, gravity is formulated as a fundamental force, while in Einstein's view, it is an effect of the curvature of spacetime. Second, according to Einstein's theory, radiation is able to produce a gravitational field and is also affected by it.

[1]metric is a mathematical object capturing all the geometric and causal structure of the spacetime, defining the notions of time, distance, volume, curvature, angle, and causality [68–72].

GR is also based on the principle of causality (PC), which states that each point in spacetime, considered as an event, must have a notion of past, present, and future that is the same for all observers. Briefly, the PC establishes a unidirectional relationship between cause and effect, where the cause always precedes the effect. This understanding of causality arises from SR but needs to be generalized in GR:

- the effect must belong to the future light cone of its cause for all curved spacetime; and
- since the curvature of spacetime can *tilt* light cones from one place to another, causality must be considered a local notion, i.e., an object is influenced directly only by its immediate surroundings.

The first statement is known as the strong PC, whereas the second is referred to as the weak PC.

In principle, it is possible for light cones to be distorted enough that an observer can move toward the future along a timelike path and yet intersect itself at a point in its past – this phenomenon is known as a closed timelike curve (CTC). Although CTCs do not violate causality, they are known to give rise to paradoxes (e.g., the grandfather paradox). To ensure the absence of CTCs and their paradoxical consequences, restrictions are imposed on the matter-energy distribution, referred to as energy conditions.

Another principle that GR has attempted to incorporate is Mach's principle. This principle argues against the Newtonian view of absolute space and time, which violates the PR, and supports the universal relativity of motion. Mach's conjecture states that every motion, even non-uniform ones, should be understood in relation to the global matter distribution in the universe. Thus, inertia arises from the interaction between all bodies in the universe. However, GR does not fully incorporate Mach's principle, as some remnants of Newtonian absolute space are still present in the Einstein field equations.

Finally, GR must reduce to the other two theories in the following situations:

1. in the limit of zero gravity, it must recover flat Minkowski spacetime, and
2. in the limit of weak gravitational field and slow motions, it must reduce to Newtonian gravity.

The first point is straightforward, as GR is a natural generalization of SR in the presence of gravitational fields, or, equivalently, when non-inertial observers are considered. The second point, although incomplete, shows that Newtonian gravity has achieved countless successes and continues to be verified in observations involving the formation and dynamics of small celestial bodies, planetary systems, stars, galaxies, and galaxy clusters.

2.2 Mathematical tool

The first mathematical notion infused in GR theory, arising from the PGC, is that of tensors living on a four-dimensional curved manifold – one temporal and three spatial – known as relativistic spacetime. While the 3+1 dimensional relativistic spacetime defines the environment where physics process occur, tensors describe the physical quantities involved in theses processes. The main tensors addressed in GR theory are:

- the metric tensor, $g_{\mu\nu}$;
- the Riemann tensor, $R^{\lambda}_{\mu\nu\rho}$;
- the Ricci tensor, $R_{\mu\nu}$;
- the Einstein tensor, $G_{\mu\nu}$; and
- the stress-energy tensor, $T_{\mu\nu}$.

Another important quantity in this theory is the Levi-Civita connection, also known as the Christoffel symbols, denoted by $\Gamma^{\lambda}_{\mu\nu}$. These symbols, whose components transform according to a specific law, are sometimes referred to as pseudo-tensors.

2.2.1 Metric tensor

The metric tensor, or simply the metric, defines the entire geometric and causal structure of relativistic spacetime, deriving the notions of space, time and causality. To begin, let us consider the case of SR, where the interval between events occurring in spacetime is described by the Minkowsky line element,

$$ds^2 = \eta_{\alpha\beta} d\xi^{\alpha} d\xi^{\beta} \,, \tag{2.1}$$

where $\eta_{\alpha\beta}$ is the Minkowski metric $\eta_{\alpha\beta} = \mathrm{diag}(-1, 1, 1, 1)$ and ξ^{α} represents a freely falling (inertial) coordinate system. From this point onward, we will use Einstein's summation convention, where a pair of repeated indices – one covariant and the other contravariant – implies summation, as follows.

- Greek alphabet is used for time and space components, where the indices take on values $\alpha, \beta, \mu, \nu, ... = (0, 1, 2, 3)$.
- Latin alphabet is used for spatial components only, where the indices take on values $i, j, k, l... = (1, 2, 3)$.

A sum index, such as α in Eq. (2.1), is a dummy index, since any symbol can replace it without changing the meaning of the expression (as long as it does not coincide with another index already used in the same term).

In the curved spacetime of GR, it is convenient to use a generic coordinate system x^μ, such that $\xi^\alpha = \xi^\alpha(x^\mu)$, and the infinitesimal variation $d\xi^\alpha$ is given by

$$d\xi^\alpha = \frac{\partial \xi^\alpha}{\partial x^\mu} dx^\mu \,. \tag{2.2}$$

By replacing equation above in Eq. (2.1), we obtain the general line element

$$ds^2 = g_{\mu\nu} dx^\mu dx^\nu \,, \tag{2.3}$$

where the metric tensor $g_{\mu\nu}$ was defined as [68]

$$g_{\mu\nu} \equiv \frac{\partial \xi^\alpha}{\partial x^\mu} \frac{\partial \xi^\beta}{\partial x^\nu} \eta_{\alpha\beta} \,. \tag{2.4}$$

The metric tensor is also referred to as the fundamental tensor and has the following properties: (i) it is symmetric in the sense of

$$g_{\mu\nu} = g_{\nu\mu} \,, \tag{2.5}$$

and (ii) the inverse metric, denoted by $g^{\mu\nu}$, is defined so that

$$g_{\mu\lambda} g^{\lambda\nu} = \delta^\nu_\mu \equiv \begin{cases} 1 \,, & \text{if } \mu = \nu \\ 0 \,, & \text{if } \mu \neq \nu \end{cases} \,, \tag{2.6}$$

where δ^ν_μ is the Kronecker tensor. The metric tensor also has a signature, often defined either as a pair of integers specifying the number of negative and positive components in spacetime, or as an explicit list of signs along the leading diagonal. In our convention, we adopt the metric signature $(-,+,+,+)$, in which the time coordinate is negative, and the spatial components are positive. Therefore, a vector U^μ is classified as

$$\begin{cases} \textit{timelike} \\ \textit{null} \\ \textit{spacelike} \end{cases} \,, \quad \text{if} \quad g_{\mu\nu} U^\mu U^\nu \begin{cases} < 0 \\ = 0 \\ > 0 \end{cases} \,. \tag{2.7}$$

As we will see below, these relations are crucial in describing what kind of paths the particles (massive and non-massive) follow in the general relativistic spacetime. In effect, if the tangent vectors to a curve are timelike, null or spacelike, we describe the curve as timelike, null or spacelike, respectively.

The last noteworthy property of general relativistic spacetime is the so-called metric compatibility, which is established by the condition

$$\nabla_\alpha g_{\mu\nu} = 0\,. \tag{2.8}$$

This proposition allows us, first of all, to commute the metric tensor $g_{\mu\nu}$ with the covariant derivative ∇_α, such that

$$g_{\mu\nu}\nabla_\alpha V^\nu = \nabla_\alpha\left(g_{\mu\nu}V^\nu\right) = \nabla_\alpha V_\mu\,, \tag{2.9}$$

$$g_{\mu\nu}\nabla_\alpha W^{\nu\rho} = \nabla_\alpha\left(g_{\mu\nu}W^{\nu\rho}\right) = \nabla_\alpha W^\rho_\mu\,, \tag{2.10}$$

whatever the fields V^ν and $W^{\nu\rho}$ defined in the curved spacetime. The vanishing of the covariant derivative of the metric, or metric compatibility, is the condition for choosing a specific connection. If the geometry of spacetime is also assumed to be torsion-free, this connection is the Levi-Civita connection [69–72].

2.2.2 Geodesic connection

In counterpart, the connection determines the trajectory of free particles, i.e., the geodesic structure, in general relativistic spacetime. Let us consider a particle moving freely under the exclusive influence of gravity. According to the EP, there exists a locally inertial coordinate system ξ^α in which the particle's equation of motion follows a straight line in spacetime, i.e. [68]

$$\frac{d^2\xi^\alpha}{d\tau^2} = 0\,, \tag{2.11}$$

where τ is the proper time defined as

$$-c^2 d\tau^2 \equiv ds^2\,. \tag{2.12}$$

In terms of an arbitrary coordinate system x^λ, Eq. (2.11) becomes

$$\frac{d^2x^\lambda}{d\tau^2} + \Gamma^\lambda_{\mu\nu}\frac{dx^\mu}{d\tau}\frac{dx^\nu}{d\tau} = 0\,. \tag{2.13}$$

where $\Gamma^\lambda_{\mu\nu}$ is called an *affine connection*, defined as [68]

$$\Gamma^\lambda_{\mu\nu} \equiv \frac{\partial x^\lambda}{\partial\xi^\alpha}\frac{\partial^2\xi^\alpha}{\partial x^\mu\partial x^\nu}\,, \tag{2.14}$$

Notice that, in principle, we can set another connection simply by permuting the lower indices μ and ν in Eq. (2.14). Then one can define the torsion tensor as

$$\mathcal{T}^{\lambda}_{\mu\nu} \equiv \Gamma^{\lambda}_{\mu\nu} - \Gamma^{\lambda}_{\nu\mu} \,. \tag{2.15}$$

Consequently, a torsion-free connection is achieved when the connection coefficients are symmetric, and vice versa, i.e.,

$$\mathcal{T}^{\lambda}_{\mu\nu} = 0 \quad \Leftrightarrow \quad \Gamma^{\lambda}_{\mu\nu} = \Gamma^{\lambda}_{\nu\mu} \,. \tag{2.16}$$

In this case, the connection is called the Levi-Civita connection, and its components with respect to a system of local coordinates are known as the Christoffel symbols. Thus, these coefficients are alternatively called either the Levi-Civita connection or the Christoffel symbols.

In GR, we assume both properties of metric compatibility, as expressed in Eq. (2.8), and torsion-free, as stated in Eq. (2.16), such that the Christoffel symbols are computed by

$$\Gamma^{\lambda}_{\mu\nu} = \frac{1}{2} g^{\lambda\rho} \left(\partial_{\mu} g_{\rho\nu} + \partial_{\nu} g_{\mu\rho} - \partial_{\rho} g_{\mu\nu} \right) \,. \tag{2.17}$$

Christoffel symbols can be of two kinds: the above form corresponds to the second kind, whereas the first is defined as $\Gamma_{\lambda\mu\nu} = g_{\lambda\rho}\Gamma^{\rho}_{\mu\nu}$. Moreover, it is direct to derive that they are unique [69–72].

In the context of GR, we need to work with two additional hypotheses: metric compatibility, characterized by Eq. (2.8), and a torsion-free connection, achieved by Eq. (2.16). In this framework, the connection is the Levi-Civita connection, whose coefficients are the Christoffel symbols, determined by Eq. (2.17). Consequently, all relativistic geometric quantities are defined entirely in terms of the metric $g_{\mu\nu}$.

2.2.3 Curvature and related tensors

In a two-dimensional manifold, the curvature at a given point is characterized by a scalar, known as the Gaussian curvature. In contrast, for a three-dimensional manifold, a second-order tensor, called the Ricci tensor, is required to describe the curvature. However, for an $\mathbf{N}$-dimensional Riemannian manifold, with $\mathbf{N} > 3$, the curvature at a given point is characterized by a fourth-order tensor, known as the Riemann tensor. Consequently, both the Ricci and Riemann tensors are often referred to as curvature tensors.

Let $\mathcal{U}^{\lambda}$ be a vector defined in the GR $3+1$ dimensional spacetime. The Riemann tensor $R^{\lambda}_{\mu\nu\rho}$ measures the non-commutativity of the covariant derivatives ∇_{ν} and ∇_{ρ}, expressed as

$$\left(\nabla_{\nu}\nabla_{\rho} - \nabla_{\rho}\nabla_{\nu} \right) \mathcal{U}^{\lambda} = R^{\lambda}_{\mu\nu\rho} \mathcal{U}^{\mu} \,. \tag{2.18}$$

In terms of the Christoffel symbols, we shall have

$$R^{\lambda}_{\mu\nu\rho} \equiv \partial_\nu \Gamma^{\lambda}_{\mu\rho} - \partial_\rho \Gamma^{\lambda}_{\mu\nu} + \Gamma^{\sigma}_{\mu\rho}\Gamma^{\lambda}_{\sigma\nu} - \Gamma^{\sigma}_{\mu\nu}\Gamma^{\lambda}_{\sigma\rho}\,. \tag{2.19}$$

In a flat geometry and Cartesian coordinates, the derivatives commute, and $\Gamma^{\lambda}_{\mu\nu} = 0$, which implies that $R^{\lambda}_{\mu\nu\rho} = 0$. The converse is also true. In general, Riemann tensor has $\mathbf{N}^4$ components. However, it possesses the following symmetries,

$$R_{\lambda\mu\nu\rho} = -R_{\lambda\mu\rho\nu}\,, \tag{2.20}$$

$$R_{\lambda\mu\nu\rho} = -R_{\mu\lambda\rho\nu}\,, \tag{2.21}$$

$$R_{\lambda\mu\nu\rho} = R_{\nu\rho\lambda\mu}\,, \tag{2.22}$$

where $R_{\lambda\mu\nu\rho} \equiv g_{\lambda\sigma}R^{\sigma}_{\mu\nu\rho}$, which allows reducing this number to just $\mathbf{N}^2(\mathbf{N}^2-1)/12$ independent components; this means 20 for $\mathbf{N} = 4$, 6 for $\mathbf{N} = 3$, and only one for $\mathbf{N} = 2$. Such symmetries follow from the Bianchi's identities,

$$R^{\lambda}_{\mu\nu\rho} + R^{\lambda}_{\nu\rho\mu} + R^{\lambda}_{\rho\mu\nu} = 0\,, \tag{2.23}$$

$$\nabla_\sigma R^{\lambda}_{\mu\nu\rho} + \nabla_\nu R^{\lambda}_{\mu\rho\sigma} + \nabla_\rho R^{\lambda}_{\mu\sigma\nu} = 0\,. \tag{2.24}$$

The Riemann tensor defined above has two successive contractions resulting in further curvature quantities of great importance in GR. First, the Ricci tensor

$$R_{\mu\nu} \equiv R^{\lambda}_{\mu\nu\lambda} = \partial_\nu \Gamma^{\lambda}_{\mu\lambda} - \partial_\lambda \Gamma^{\lambda}_{\mu\nu} + \Gamma^{\rho}_{\mu\lambda}\Gamma^{\lambda}_{\rho\nu} - \Gamma^{\rho}_{\mu\nu}\Gamma^{\lambda}_{\rho\lambda}\,, \tag{2.25}$$

and second, the Ricci scalar

$$R \equiv g^{\mu\nu}R_{\mu\nu} = R^{\mu}_{\mu}\,. \tag{2.26}$$

There are, in principle, two other possible contractions of the Riemann tensor. The first contraction vanishes, $R^{\lambda}_{\lambda\nu\rho} = 0$, because of Eq. (2.20), and the second is the negative of the Ricci tensor, $R^{\lambda}_{\mu\lambda\nu} = -R^{\lambda}_{\mu\nu\lambda} = -R_{\mu\nu}$, due to Eq. (2.21). As a result, the Ricci tensor and Ricci scalar defined in Eqs. (2.25) and (2.26) are the two only successive traces of the Riemann tensor.

The Ricci tensor is symmetric, i.e.,

$$R_{\mu\nu} = R_{\nu\mu}\,. \tag{2.27}$$

Thus, it has a total of 10 independent components. Of course, this number coincides with the number of independents components of both the Einstein and stress-energy tensors, main tensors appearing in the field equations of GR.

Finally, the Einstein tensor $G_{\mu\nu}$ is defined as

$$G_{\mu\nu} \equiv R_{\mu\nu} - \frac{1}{2} R g_{\mu\nu} \,. \tag{2.28}$$

Using Bianchi's identities it is possible to verify that

$$\nabla_\mu G^{\mu\nu} = 0 \,, \tag{2.29}$$

where $G^{\mu\nu} = g^{\mu\lambda} g^{\nu\rho} G_{\lambda\rho}$. As the covariant derivatives of both the constant Λ and metric tensor $g_{\mu\nu}$ vanish, we can introduce the term $\Lambda g_{\mu\nu}$ in Eq. (2.28) such that

$$\nabla_\mu \left(G^{\mu\nu} + \Lambda g^{\mu\nu} \right) = 0 \,. \tag{2.30}$$

The term Λ is the cosmological constant, and the expression inside the parentheses forms the left-hand side of the GR field equations. Since the right-hand side of these equations is given by a constant multiplied by the stress-energy tensor $T_{\mu\nu}$, which has a vanishing divergence, the left-hand side must also be divergenceless.

2.3 Stress-energy tensor

The stress-energy tensor, often referred to as the stress-momentum-energy tensor or momentum-energy tensor and denoted by $T_{\mu\nu}$, is a second-order tensor that characterizes matter fields (i.e., continuum matter distribution) in relativistic spacetime. It provides a unified description of all sources of the gravitational field (curvature), encapsulating the contributions from stress, momentum, and energy. Since mass and energy are indistinguishable according to SR, radiation fields also work as sources of gravitational fields, as well as being affected by them.

2.3.1 General features

Every component of the stress-energy tensor encodes a physical property of the continuum matter distribution. In a given frame, we have to:

- T_{00} corresponds to the energy density,
- T_{0i} denotes the energy flux in the i-direction,
- T_{i0} is the i^{th} component of the momentum density, and finally
- T_{ij} is the flux of the i^{th} component of the momentum in the j-direction.

Because this tensor is symmetric, i.e.,

$$T_{\mu\nu} = T_{\nu\mu} \,, \tag{2.31}$$

the flux energy in the i-direction corresponds to the i^{th} component of the momentum density. T_{ij} components, in turn, are divided in two pieces: first, $i = j$ components correspond to the isotropic pressure along of the matter distribution, and second, $i \neq j$ describe the shear stresses obeying $T_{ij} = T_{ji}$.

In addition to being symmetric, the stress-energy tensor must also be divergence-free, i.e.,

$$\nabla_\mu T^{\mu\nu} = 0\,, \tag{2.32}$$

where $T^{\mu\nu} \equiv g^{\mu\lambda} g^{\nu\rho} T_{\lambda\rho}$ is the full covariant form of the stress-energy tensor $T_{\mu\nu}$. Eq. (2.32) represents the energy-momentum conservation, which emerges as a direct consequence of the symmetries present in general relativistic spacetime, particularly in relation to the principle of general covariance discussed in Section 2.1.

2.3.2 Energy conditions

In GR and allied theories, the stress-energy tensor $T_{\mu\nu}$ capture the distribution of stress, energy, and momentum associated with matter-energy fields. However, the field equations *per se* does not specify what kinds of states of matter-energy fields are physically admissible. Instead, such criteria are derived from specific guidelines known as energy conditions.

There are several different ways to formulate the standard energy conditions in classical GR. Here, we will describe the four most commonly encountered conditions using their physical forms.

1. Null Energy Condition (NEC): This condition stipulates that for every future-pointing null vector field $\mathscr{V}^\mu$, we must have

$$T_{\mu\nu}\, \mathscr{V}^\mu \mathscr{V}^\nu \geq 0\,. \tag{2.33}$$

   The NEC implies that the energy density measured along any null geodesic is non-negative, which is essential for the consistency of causal structures in spacetime.

2. Weak Energy Condition (WEC): For every future-pointing timelike vector field $\mathscr{W}^\mu$, the WEC requires that

$$T_{\mu\nu}\, \mathscr{W}^\mu \mathscr{W}^\nu \geq 0\,. \tag{2.34}$$

   This condition ensures that the energy density as measured by any observer is non-negative.

3. Strong Energy Condition (SEC): The SEC imposes the requirement that for

any future-pointing timelike vector field $\mathscr{W}^\mu$,

$$\left(T_{\mu\nu} - \frac{1}{2}\mathrm{T}g_{\mu\nu}\right)\mathscr{W}^\mu\mathscr{W}^\nu \geq 0\,, \tag{2.35}$$

where T is the trace of the stress-energy tensor, defined as $\mathrm{T} \equiv g^{\mu\nu}T_{\mu\nu} \equiv T^\mu_\mu$. The SEC essentially asserts that the energy density and pressures combined should result in an attractive gravitational effect.

4. Dominant Energy Condition (DEC): The DEC states that for every future-pointing timelike vector field $\mathscr{W}^\mu$,

$$T_{\mu\nu}\mathscr{U}^\mu \geq 0\,, \tag{2.36}$$

and the vector T_μ derived from the stress-energy tensor must be causal. This means that the flow of energy-momentum must be such that it can be associated with physical particles, ensuring that they move slower than the speed of light.

While such energy conditions have physical relevance, especially in ensuring causality, they cannot be considered absolute. In fact, some observed quantum phenomena are known to violate certain conditions. For example, in the Casimir effect [74, 75], the energy density existing between two conducting plates held parallel at a very small separation is negative. Thus, the Casimir effect apparently violates the NEC [76].

2.3.3 Perfect fluid

In many interesting situations covering both astrophysics and cosmology, the source of the gravitational field can be taken to be a perfect fluid as a first approximation. Fundamentally, a fluid is a special kind of continuum of matter, consisting of a very large number of particles, such that its behavior is described solely in terms of average or bulk quantities. In a perfect fluid, effects like viscosity and heat conduction vanish. Ultimately, we can think of the universe on sufficiently large scales, as observations have pointed to a minimum scale of statistical homogeneity and isotropy of about 200 Mpc, as a perfect fluid.

A perfect fluid can be characterized by two scalar fields, its energy density $\rho(t)$ and its pressure $P(t)$, as well as a vector field, its four-velocity $u^\mu(t)$, which depend only on time. The stress-energy tensor for this fluid is given by [69–71]

$$T^{\mu\nu} = \left(\rho + \frac{P}{c^2}\right)u^\mu u^\nu + Pg^{\mu\nu}\,. \tag{2.37}$$

The four-velocity is defined in a general frame as

$$u^\mu \equiv \frac{dx^\mu}{d\tau} = \gamma_{\rm L} v^\mu = \gamma_{\rm L}(c, v^i)\,, \tag{2.38}$$

where $\gamma_{\rm L} \equiv dt/d\tau = 1/\sqrt{1 - v^2/c^2}$ is known as the Lorentz factor. In the fluid rest frame, the four-velocity u^μ is given by [71]

$$u^\mu = (c, 0, 0, 0)\,. \tag{2.39}$$

Notice that only in its rest frame does the fluid not exhibit heat conduction, i.e., $T^{0i} = T^{i0} = 0$. We also emphasize that $v^\mu \equiv dx^\mu/dt$ is the coordinate velocity, $v^i = dx^i/dt$ is the spatial three-velocity, and $v \equiv |\vec{v}| = \sqrt{v^i v_i}$ is the magnitude of the three-velocity $\vec{v}$. Since we have set $c^2 d\tau^2 = -g_{\mu\nu} dx^\mu dx^\nu$, the four-velocity obeys

$$g_{\mu\nu} u^\mu u^\nu \equiv u_\mu u^\mu = -c^2\,. \tag{2.40}$$

The four-velocity u^μ does not represent the velocity of the particles through space, which can vary in magnitude. Rather, it describes their velocity through spacetime, at which they always travel at a constant rate.

After some calculations, the covariant energy-momentum conservation for the perfect fluid results in

$$\nabla_\mu (\rho u^\mu) + \frac{P}{c^2} \nabla_\mu u^\mu = 0\,, \tag{2.41}$$

and

$$\left(\rho + \frac{P}{c^2}\right) u^\mu \nabla_\mu u^\nu + \left(g^{\mu\nu} + \frac{1}{c^2} u^\mu u^\nu\right) \nabla_\mu P = 0\,. \tag{2.42}$$

These equations correspond to the continuity and acceleration equations, respectively. Our assertion regarding the divergenceless nature of the stress-energy tensor is now clear. As we will demonstrate later, Eqs. (2.41) and (2.42) must reduce to the classical continuity and Euler equations for slowly moving particles ($v \ll c$) and small pressures ($P/c^2 \ll \rho$).

2.4 Field equations

Just as Maxwell's equations describe the electromagnetic fields produced by charges and currents, Einstein's field equations govern how the metric $g_{\mu\nu}$ responds to energy and momentum of matter fields $T_{\mu\nu}$ and vice versa.

After some unsuccessful attempts to couple the metric of relativistic spacetime to the stress-energy tensor, Einstein formulated the following field equations:

$$G_{\mu\nu} + \Lambda g_{\mu\nu} = \kappa^2 T_{\mu\nu}\,, \tag{2.43}$$

where κ^2 is the Einstein's constant, which shall be determined by requiring that the field equations (2.43) reduce to the Poisson equation for the Newtonian potential in the weak-field, time-independent, slowly-moving-particles limit.

The field equations (2.43) are formulated in such a way that, according to Bianchi's identities, metric compatibility of the connection, and energy-momentum conservation, both sides of the equality are divergence-free. They constitute a set of 10 generally covariant, non-linear second-order PDEs[2] in the metric tensor $g_{\mu\nu}$.

2.4.1 Variational approach

As with most field theories, the Einstein's field equations (2.43) can be derived from a variational principle known as the *principle of least action*. The functional giving rises to the GR field equations is the Einstein-Hilbert (EH) action,

$$S_{\mathrm{EH}} = \int d^4x\sqrt{-g}\left[\frac{1}{2\kappa^2}(R-2\Lambda)+\mathcal{L}_{\mathrm{M}}(g_{\mu\nu},\phi_{\mathrm{M}})\right], \tag{2.44}$$

where g is the determinant of the metric and $\mathcal{L}_{\mathrm{M}}$ is the Lagrangian density of the matter fields ϕ_{M}. The gravity Lagrangian density has been taken to be

$$\mathcal{L}_{\mathrm{EH}} \equiv \frac{1}{2\kappa^2}\sqrt{-g}(R-2\Lambda)\,. \tag{2.45}$$

Since the Ricci scalar R is a function of the metric only, expressed ast $R = R(g_{\mu\nu})$, the variation of Eq. (2.44) with respect to the metric tensor gives the field equations (2.43), where

$$T_{\mu\nu} \equiv -\frac{2}{\sqrt{-g}}\frac{\delta\left(\sqrt{-g}\mathcal{L}_{\mathrm{M}}\right)}{\delta g^{\mu\nu}}\,. \tag{2.46}$$

The factor $\sqrt{-g}$ is included in order to ensure that $\sqrt{-g}\mathcal{L}$ transform as a scalar under coordinate transformation $x^\mu \to \tilde{x}^\mu\left(x^\mu\right)$. This property ensures that S_{EH} is invariant under general coordinate transformations and that the resulting tensor field equations are divergence-free, meaning that Bianchi's identities and energy-momentum conservation are automatically satisfied.

2.4.2 Vaccum energy

A notable feature of GR is that the sources of the gravitational field are represented by the entire stress-energy tensor, such that in the absence of such sources, we have $T_{\mu\nu} = 0$. In this case, the Einstein's field equations are given by

$$G_{\mu\nu} = -\Lambda g_{\mu\nu}\,. \tag{2.47}$$

[2]The acronym PDEs corresponds to partial differential equations.

The strategy here of moving the cosmological constant term to the right-hand side and considering it as part of the stress-energy tensor is advantageous, as we can now interpret Λ as the energy density of the vacuum, such that

$$T_{\mu\nu}^{\text{vac}} \equiv T_{\mu\nu}^{\Lambda} = -\Lambda g_{\mu\nu} \,. \tag{2.48}$$

Notice that the energy-momentum conservation is automatically satisfied, i.e., $\nabla^{\mu} T_{\mu\nu}^{\text{vac}} \equiv g^{\mu\rho}\nabla_{\rho} T_{\mu\nu}^{\text{vac}} = 0$. Although the vacuum is not a traditional source of the gravitational field, this interpretation is important, as QFT predicts that it should possess some form of energy and momentum [77]. In this way, we can write Einstein's field equations as

$$G_{\mu\nu} = \kappa^2 T_{\mu\nu} \,, \tag{2.49}$$

where

$$T_{\mu\nu} \equiv T_{\mu\nu}^{\text{M}} + T_{\mu\nu}^{\text{vac}} \,. \tag{2.50}$$

Here, the letter M stands for matter and radiation fields. Meanwhile, the terms cosmological constant and vacuum energy are essentially interchangeable.

In general, the vacuum state must be Lorentz invariant, such that the associated stress-energy tensor $T_{\mu\nu}^{\text{vac}}$ needs to be proportional to the diagonal Minkowski metric $\eta_{\mu\nu}$ in any locally inertial frame, i.e.,

$$T_{\mu\nu}^{\text{vac}} = -\rho_{\text{vac}}\, \eta_{\mu\nu} \,, \tag{2.51}$$

where ρ_{vac} is the vacuum energy density. This can be straightforwardly generalized from inertial frames to arbitrary coordinates as

$$T_{\mu\nu}^{\text{vac}} = -\rho_{\text{vac}}\, g_{\mu\nu} \,. \tag{2.52}$$

As we have seen previously, a perfect fluid is described by a diagonal stress-energy tensor. It follows from this that the vacuum must behave like a perfect fluid with equation of state given by

$$w_{\text{vac}} \equiv \frac{P_{\text{vac}}}{\rho_{\text{vac}}} = -1 \,. \tag{2.53}$$

The vacuum energy density must be constant throughout spacetime since its gradient would not be Lorentz invariant.

By comparing Eqs. (2.52) and (2.49), we obtain

$$P_{\text{vac}} = -\rho_{\text{vac}} = -\frac{\Lambda}{\kappa^2} \,. \tag{2.54}$$

In quantum mechanics, a harmonic oscillator with frequency ν has a ground state energy given by $E_0 = \frac{1}{2}\hbar\nu$. A quantized field can be thought of as a collection of

an infinite number of these oscillators, with each mode contributing to the ground state energy. Adding all of these contributions together yields an infinite result. However, we can rule out the very high-momentum modes introducing a certain ultraviolet momentum cutoff. The final vacuum energy, which is the sum of the energies of the ground state oscillations of all the fields in the theory, scales as $\rho_{\text{vac}} \sim m_{\text{Pl}}^4 \sim (10^{18}\,\text{GeV})^4$.

2.4.3 Newtonian limit

Given the previous success of universal gravitation in explaining the inhomogeneities at small scales (e.g., galaxies, galaxy clusters, superclusters, and filaments) and compact objects (e.g., comets, moons, planets, and stars), it is necessary for GR to recover Newtonian theory in the limit of weak, static, and slow-motion gravitational fields. This is referred to as the Newtonian limit or weak-field approximation.

In order to realize the Newtonian limit of the GR field equations, let us start by considering the Einstein field equations in the alternative form

$$R_{\mu\nu} = \kappa^2 \left(T_{\mu\nu} - \frac{1}{2} \mathrm{T} g_{\mu\nu} \right) , \tag{2.55}$$

where $\mathrm{T} \equiv g^{\mu\nu} T_{\mu\nu} = T^{\mu}_{\mu}$ is the trace of the stress-energy tensor. The important equation here is the one corresponding to the time-time, or 0-0, component, as it reduces to the usual Poisson equation for the gravitational potential Φ.

Next, we consider that our weak field arises from a perfect fluid whose particles have small velocities v compared to the speed of light c. Such a fluid has a stress-energy tensor given by

$$T^{\mu\nu} = \rho\, u^{\mu} u^{\nu} . \tag{2.56}$$

The above equation corresponds to the limits $v \ll c$ and $P/c^2 \ll \rho$ in Eq. (2.37), as the majority of classical distributions obey. In the rest frame of the fluid itself, the four-velocity can be described as the diagonal matrix $u^{\mu} = (c, 0, 0, 0)$. It follows from this that

$$\mathrm{T} = -T_{00} = -\rho c^2 . \tag{2.57}$$

As we are looking for a weak field corresponding to small deviations from the SR flat spacetime, the geometric aspect of the problem consists of expanding the metric $g_{\mu\nu}$ around the Minkowski metric $\eta_{\mu\nu}$, such that

$$g_{\mu\nu} = \eta_{\mu\nu} + h_{\mu\nu} , \tag{2.58}$$

in which $|h_{\mu\nu}| \ll 1$ configures a small perturbation in the locally flat spacetime due to slow-velocity-particles distribution in Eq. (2.56). After some straightforward

calculations, the first-order approximation yields the following result:

$$R_{00} = -\frac{1}{2}\nabla^2 h_{00}\,, \tag{2.59}$$

where $\nabla^2 \equiv \delta^{ij}\partial_i\partial_j$ is the Laplacian operator. Then, by replacing Eqs. (2.57) and (2.59) into Eq. (2.55), we obtain

$$-\frac{1}{2}\nabla^2 h_{00} = \frac{1}{2}\kappa^2\rho c^2\,. \tag{2.60}$$

The perturbations $h_{\mu\nu}$ carried by the metric can be defined in multiple ways, as there is a gauge freedom when choosing the perturbative variables. By fixing what is called the Newtonian gauge, where $h_{00} = -2\Phi/c^2$, we obtain

$$\nabla^2\Phi = \frac{1}{2}\kappa^2\rho\,, \quad \kappa^2 \equiv \frac{8\pi G}{c^4}\,, \tag{2.61}$$

which is the classical Poisson equation for the Newtonian potential Φ. Notice that we also find the Einstein's constant in terms of the Newtonian constant G. By replacing the default values of the constants above, we obtain $\kappa^2 \simeq 2.077 \times 10^{-43}\ \mathrm{N}^{-1}$.

To complete our task of recovering the full Newtonian limit from GR theory, we should now examine Eqs. (2.41) and (2.42), which automatically reduce to

$$\nabla_\mu\left(\rho v^\mu\right) = 0\,, \tag{2.62}$$

$$\rho v^\mu \nabla_\mu v^\nu + \left(\eta^{\mu\nu} + \frac{1}{c^2}v^\mu v^\nu\right)\nabla_\mu P = 0\,, \tag{2.63}$$

respectively. In three-vector notation, they can be rewritten as

$$\frac{\partial\rho}{\partial t} + \nabla\cdot(\rho\vec{v}) = 0\,, \tag{2.64}$$

$$\rho\left(\frac{\partial}{\partial t} + \vec{v}\cdot\nabla\right)\vec{v} = -\nabla P\,. \tag{2.65}$$

As is known, Eqs. (2.64) and (2.65) are the classical continuity and Euler equations, respectively, for a perfect fluid.

To summarize, we have seen that General Relativity theory suitably recovers the classical Newtonian description of gravity and fluid dynamics in the limit of weak fields and slow motions. In carrying out this limit, we found both a way to represent Einstein's constant κ in terms of Newton's constant G and an alternative justification for energy-momentum conservation: $T^{\mu\nu}$ is divergence-free, ensuring that both the continuity and Euler equations are recovered in the context of a weak gravitational field and a non-relativistic perfect fluid.

Chapter 3

Standard Cosmological Model

Paraphrasing R. Rosenfeld in his paper *A Cosmologia* [78], published in 2005, one hundred years after Einstein's miraculous year and also decreed the world year of physics, "Cosmology is the *science* that studies the *structure*, *evolution*, and *composition* of the universe: *science* is the method for developing and testing models, *structure* concerns all of issues involved in the form and organization of matter in the universe, *evolution* argues about the different phases that the universe has gone through, and *composition* is what the universe is made of".

Modern cosmology is based on GR plus the cosmological principle (CP) and is supported by three observational pillars: (*i*) Hubble's law describing the expanding universe; (*ii*) big bang nucleosynthesis (BBN) explaining the present abundances of light elements; and (*iii*) the cosmic microwave background (CMB), thermal radiation left over from the first few hundred thousand years, . In this picture, the spacetime geometry is described by the Robertson-Walker (RW) metric and the dynamics of the universe is governed by the Friedmann equations. These elements, along with particle theory and inflation, result in the Friedmann-Lemaître-Roberton-Walker (FLRW) cosmology, also referred to as the Hot Big Bang (HBB) model.

The CP states that *at large enough scales the universe is nearly homogeneous and isotropic*. *Homogeneous* means that it is symmetric under spatial translations (i.e., there are no privileged points), whereas *isotropic* means that it is symmetric under rotations (i.e., there are no privileged directions) [79–83]. The transition to homogeneity is observed at scales $\mathcal{R}_H \gtrsim 100$ Mpc [84–86] or $\theta_H \gtrsim 15^\circ$ [62, 87]. This is often verified through LSS observations. Figure 3.1, which corresponds to the galaxy map of the universe constructed by the Sloan Digital Sky Survey (SDSS), provides important datasets to confirm the validity of the CP.

In this chapter, we shall discuss the most relevant aspects of standard HBB cosmology, including its three observational pillars, the background and pertubative dynamics, structure formation, the initial conditions as set up by inflation, and the current status of observations.

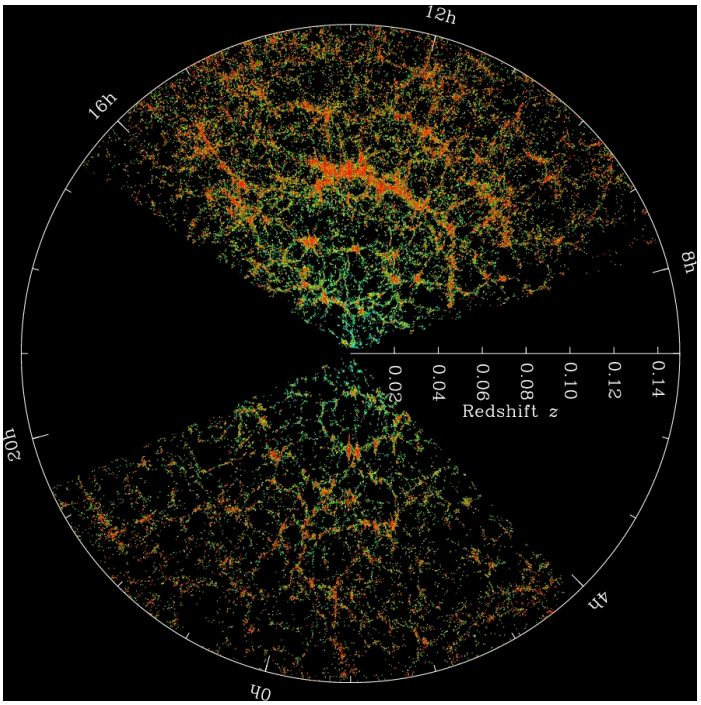

Figure 3.1: Map of the universe as seen by the SDSS. Each point represents a galaxy, with color indicating the $g - r$ color of that galaxy. Credit: M. Blanton and SDSS. Image available at https://www.sdss4.org/science/orangepie/.

3.1 Expanding universe

The expansion of the universe is a purely cosmological effect, characterized by the increase in physical distance between gravitationally unbound parts of the observed universe over time, while the objects involved remain approximately fixed in their comoving positions. It is worth noting that this expansion of space is not observed in system such as the Solar System, inside the galaxies, or even throughout the galaxy clusters. It turns out that, on these scales, gravity acts in an attractive way, keeping such systems bound and stable for a very long time until they collapse.

We can picture space as a two-dimensional grid, as in Figure 3.2, which expands uniformly as time evolves. It is also convenient to describe the expansion effect by introducing the scale factor $a(t)$, such that $0 \leq a(t) \leq 1$; at the beginning of the universe, $a(t) \to 0$, whereas today, $a_0 \equiv a(t_0) \equiv 1$. Here and throughout, the subscript "0" denotes the value of a quantity today. As the grid expands, points on it maintain their comoving coordinates, so the difference between any two comoving coordinates remains constant. Nevertheless, the physical distance $\vec{d}$ is proportional to the scale factor,

$$\vec{d}(t) = a(t) \times \vec{r}. \tag{3.1}$$

Since $\vec{r}$ does not changes over time, it is called *comoving distance*. This relation can also be written in terms of modulus: $d(t) = a(t)r$, where $d \equiv |\vec{d}|$ and $r \equiv |\vec{r}|$.

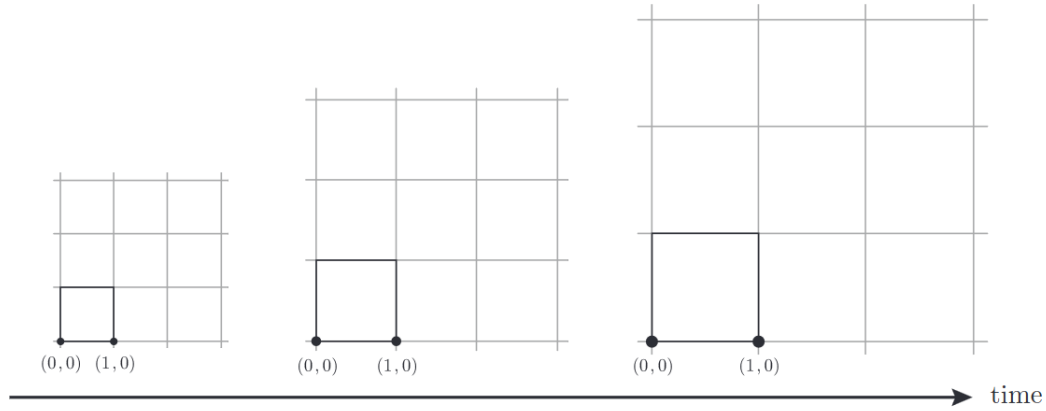

Figure 3.2: Expanding universe. The comoving distance associated with the coordinate position $\vec{r}$ remains approximately constant as the grid expands, whereas the physical distance $\vec{d}$ increases over time [79].

By differentiating Eq. (3.1) with respect to time, we obtain the following expression for the recessional velocities,

$$v = Hd\,, \tag{3.2}$$

where $v \equiv \dot{d}(t)$ and $H = H(t)$ is defined as

$$H(t) \equiv \frac{\dot{a}(t)}{a(t)}\,. \tag{3.3}$$

Here, the *dots* denote time derivative. Eq. (3.1) is known as the Hubble-Lemaître law, though it is sometimes referred to as the Hubble-Humason law or even the Hubble-Humason-Lemaître law. $v(t)$ are the recessional velocities and $H(t)$ is the Hubble parameter. As we will see later, $H(t)$ is related to both the energy density and the spatial curvature of the universe through the Friedmann equations.

For relatively nearby galaxies, Hubble's law can be approximated by

$$v \simeq H_0 d\,, \tag{3.4}$$

where $H_0 \equiv H(t_0)$ is the Hubble constant, which measures the current expansion rate of the universe. Present measurements of H_0 are parameterized by h via

$$H_0 = 100\,h\,\mathrm{km\,s^{-1}\,Mpc^{-1}}\,. \tag{3.5}$$

The inverse of the Hubble constant gives the current time scale of the universe, $t_0 \sim H_0^{-1}$. Based on the standard flat-ΛCDM cosmological model, the best estimate of the universe age is known to be approximately 13.8 Gyr [88].

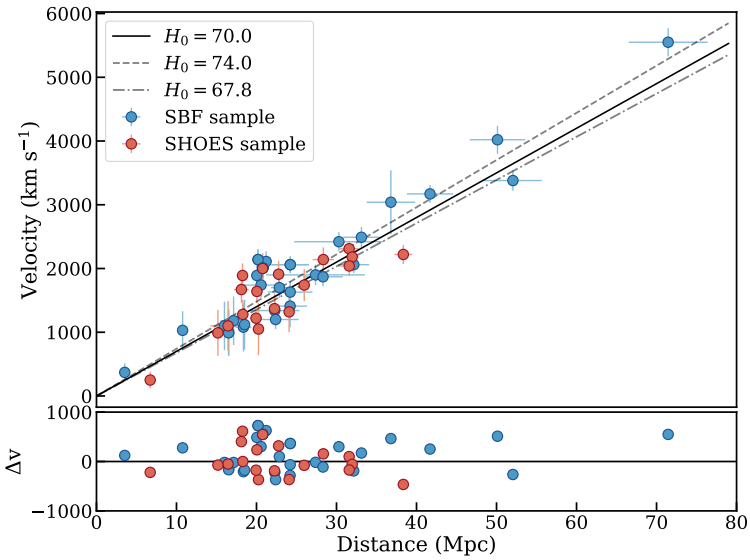

Figure 3.3: Nearby Hubble diagram for galaxies with SBF (blue) and Cepheid (red) distance measurements, for values of $H_0 = 67.8\,\mathrm{km\,s^{-1}\,Mpc^{-1}}$ (dot-dashed line), $H_0 = 70.0\,\mathrm{km\,s^{-1}\,Mpc^{-1}}$ (solid line), and $H_0 = 74.0\,\mathrm{km\,s^{-1}\,Mpc^{-1}}$ (dashed line). The bottom panel displays the residuals for both the SBF and SH0ES samples, calculated assuming $H_0 = 74.0\,\mathrm{km\,s^{-1}\,Mpc^{-1}}$ [89].

The most direct evidence we have pointing to a dynamic expanding universe is the Hubble diagram. E. Hubble [90] was the first to observe that distant nebulae move away from us with recessional velocities proportional to their respective distances, and elaborated the first $v \times d$ diagram. Such diagram has been refined since Hubble's time due to new, increasingly deep, and accurate observations. In Figure 3.3, we show a current version of the Hubble diagram, constructed for galaxies with surface brightness fluctuation (SBF) and Cepheid distance measurements (see Ref. [89] for more details). As we can see, the recessional velocities are approximately a linear function of the physical distance, allowing Eq. (3.4) to be used quite safely for nearby galaxies.

The late-time local universe is not the only way in order to measure the Hubble constant. Current measurements of H_0 arise from both late-time and early-time observations, which can be classified as model-dependent or model-independent. Model-dependent measurements assume a standard flat-ΛCDM cosmology and cover both late-time (BAO) and early-time (CMB and lensing) observations. In contrast, model-independent measurements are essentially late-universe observations (e.g., SNe, QSOs, GWs, GL, masers, FRBs, among others). However, there is a known statistical tension between these two methods of determining the universe's current expansion rate, H_0, which can reach up to $\sim 4\sigma - 6\sigma$, depending on the data sets utilized for comparison [91]. This tension is known as the Hubble (or H_0) tension and is recognized through the two main measurements:

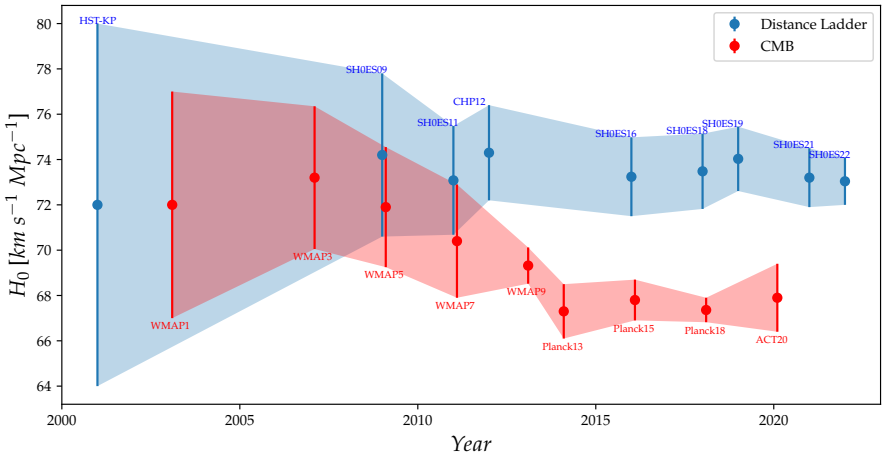

Figure 3.4: Evolution of Hubble constant measurements from 2001 to 2022 using the local distance ladder (blue) and CMB (red) observations. The local distance ladder is primarily calibrated using Cepheids, as in HST-KP [92], CHP [93], and SH0ES [94–100]. In contrast, WMAP [101–105], Planck [88, 106, 107], and ACT [108] perform indirect measurements based on the ΛCDM model using CMB data. Table A.1 provides more details about each measurement in this plot.

- $H_0^{\text{SH0ES}} = 73.04 \pm 1.04$ km s^{-1} Mpc^{-1}, from Riess et al. (2022) [100]; and
- $H_0^{\text{Planck}} = 67.36 \pm 0.54$ km s^{-1} Mpc^{-1}, from Planck Collaboration (2020) [88].

SH0ES measurement is based on local Cepheid–SN Ia *distance ladder*, whereas Planck measurements consider CMB data and assumes the ΛCDM cosmological model. These measurements represent a 5σ statistical tension.

A comprehensive list of H_0 measurements is available in Ref. [109], along with several pertinent details. The authors of this compilation have considered 216 measurements taken between 2012, when a tension tendency can be noticed (see Figure 3.4), to 2022. Of these, 107 measurements are based on the ΛCDM model, while 109 are model-independent.

In Figure 3.4, we show the history evolution of the Hubble tension in light of the distance ladder (Cepheid-SN Ia) and CMB estimators since 2001. As we can see, these measurements agreed up until 2011/2012. However, between 2007 and 2014, we verify a substantial decrease in the H_0 value as measured through the CMB observations, while it remains approximately constant for the local distance ladder Cepheid-SNe Ia observations. Due to the significant progress made by the collaborations, H_0 measurements have gotten more precise and accurate, with corresponding uncertainties getting fewer and lower. As a result, the Hubble tension was confirmed in 2020 mainly through the SH0ES and Planck results. The H_0 values used in this plot are summarized and referred to in Table A.1.

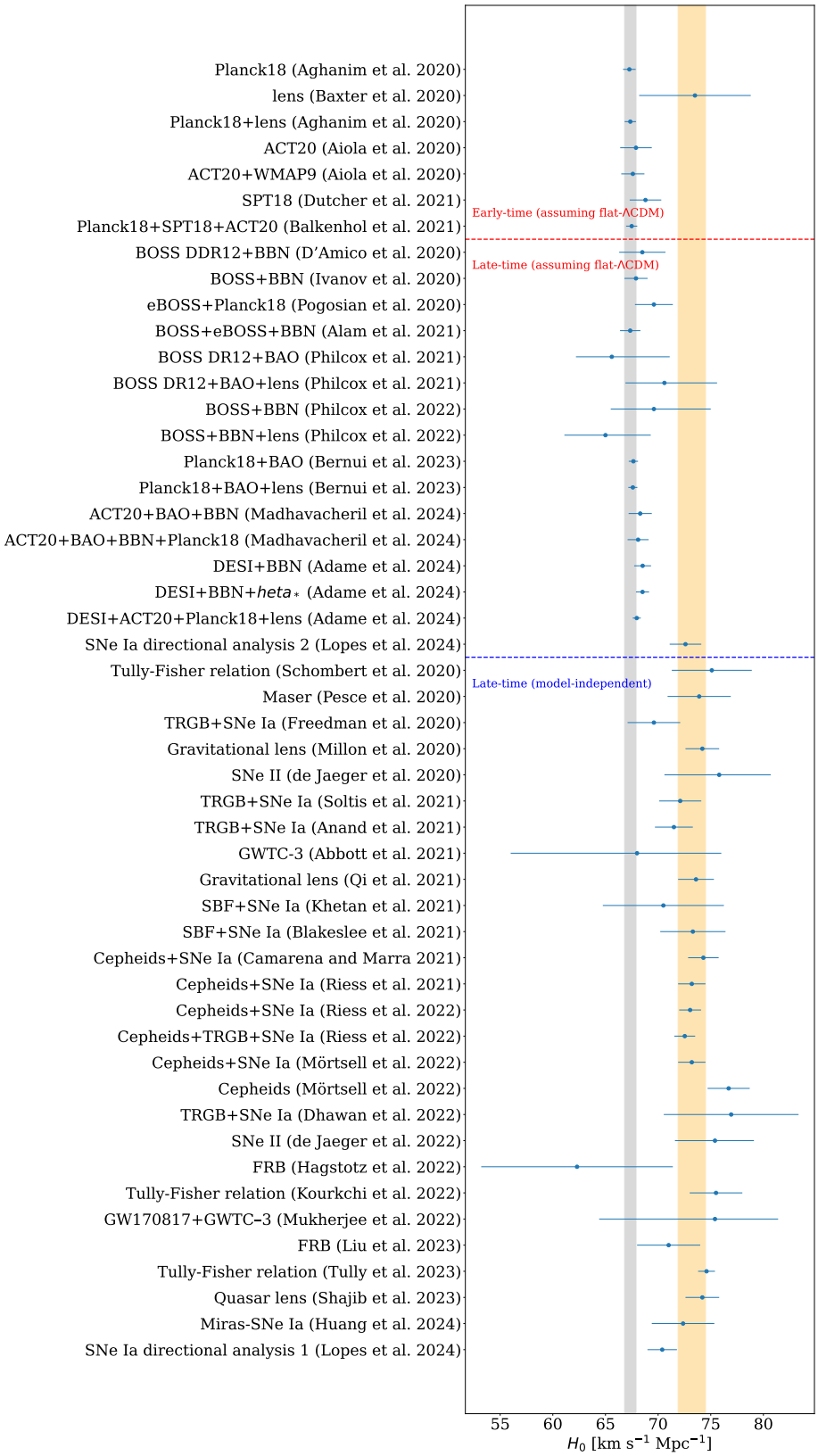

Figure 3.5: Current H_0 measurements from early-time, late-time, and combined early-late-time probes, assuming or not cosmological model.

Figure 3.5 summarizes 50 recent H_0 measurements taken from 2020 onwards, spanning several cosmological probes that cover both the early and late universe. Table A.2 contains details on these measurements, including year, value, method, author, and reference. We then have divided the measurements between those that assume a flat-ΛCDM cosmology and those that are model-independent. we include early-time observations (CMB, lensing, and BBN), late-time observations (BAO), and combined observations. In contrast, model-independent measurements consist only late-time observations (SNe Ia, SNe II, GWs, GL, FRBs, masers, and QSO lensing). Notably, there is a significant statistical disagreement between the ΛCDM-based data and model-independent observations, which reach up to $\sim 4\sigma - 6\sigma$.

The Hubble tension should not be so surprising, given the number of systematic errors that still persist in the measurements. As a matter of fact, there have always been unresolved tensions between various measurements of the current Hubble rate H_0 [110, 111]. Either way, the Hubble tension may indicate either that our present distance calibrations need to be reevaluated or that a novel physics that may explain the early universe that is not included in the ΛCDM model is emerging. As a result, various scenarios beyond standard model have been explored to solve, or at least attenuate, this tension (see Refs. [112–115] for a review of solutions).

3.2 Primordial nucleosynthesis

Primordial nucleosynthesis, also known as big bang nucleosynthesis (BBN), refers to the synthesis of light elements that took place seconds after the origin of the universe, when its temperature cooled to 1 MeV, and lasted for approximately a dozen minutes. At that time, the components of the cosmic plasma included:

- relativistic particles in equilibrium: photons (γ), electrons (e^-);
- decoupled relativistic particles: neutrinos (ν); and
- non-relativistic particles: baryons (b).

According to the HBB model, the early stages of the universe likely resembled a highly compressed neutron plasma, which degraded into these particles as cosmic expansion reduced their temperature and pressure. The remaining neutrons were then captured by the freshly generated protons to form deuterium nuclei, and subsequent neutron capture produced increasingly heavier nuclei, leading to the present abundances of light elements. This essentially summarizes the standard BBN scenario. See Ref. [116] for reviewing this topic.

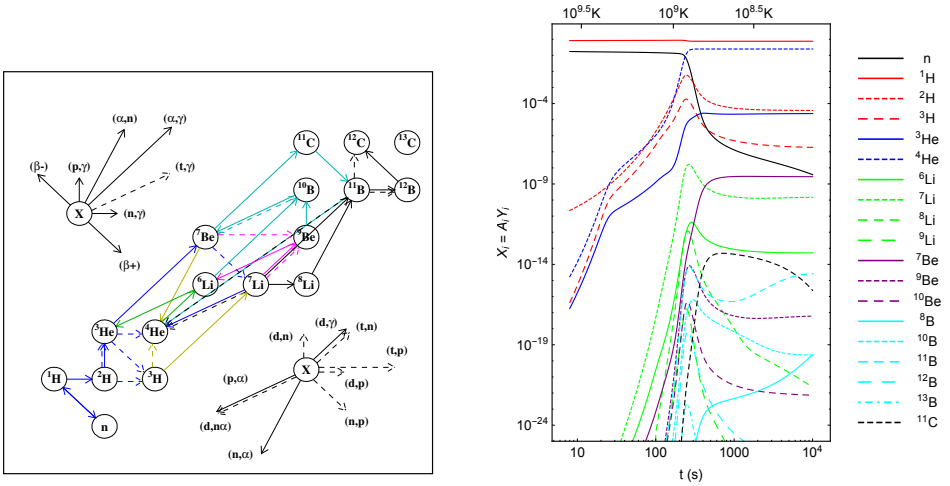

(a) (b)

Figure 3.6: (a) Nuclear network of the most important chain reactions in BBN. The network up to ^{7}Be, corresponding to reactions (3.7) to (3.13), is shown in blue color; (b) Evolution of light element abundances over time [117].

In the standard BBN, the abundances of light nuclei are usually parameterized by the baryon-to-photon ratio, defined as

$$\eta_{\mathrm{b}\gamma} \equiv \frac{\mathcal{N}_{\mathrm{b}}}{\mathcal{N}_\gamma} = 6.0 \times 10^{-10} \left(\frac{\Omega_{\mathrm{b}} h^2}{0.022} \right) . \tag{3.6}$$

Current observations determine $\Omega_{\mathrm{b}} h^2 \approx 0.0224$, which corresponds to the universe being composed of approximately 4% of baryons and $\eta_{\mathrm{b}\gamma} \approx 6.0 \times 10^{-9}$ [88]. Thus, we conclude that there must have been far fewer baryons than relativistic particles during the first moments of the universe.

At temperatures $T \gtrsim 0.1\,\mathrm{MeV}$, no light nuclei are formed, so only free protons and neutrons existed at this time. Below this temperature, light nuclei are formed primarily via the following nuclear chain reactions:

$$n \leftrightarrow {}^1\mathrm{H} + e^- + \bar{\nu} \tag{3.7}$$

$${}^1\mathrm{H} + n \leftrightarrow \mathrm{D} + \gamma \tag{3.8}$$

$$\mathrm{D} + {}^1\mathrm{H} \leftrightarrow {}^3\mathrm{H} + \gamma \tag{3.9}$$

$$\mathrm{D} + \mathrm{D} \leftrightarrow {}^3\mathrm{He} + n \tag{3.10}$$

$$\mathrm{D} + {}^3\mathrm{H} \leftrightarrow {}^4\mathrm{He} + \gamma \tag{3.11}$$

$${}^3\mathrm{H} + {}^4\mathrm{He} \leftrightarrow {}^7\mathrm{Li} + \gamma \tag{3.12}$$

$${}^3\mathrm{He} + {}^4\mathrm{He} \leftrightarrow {}^7\mathrm{Be} + \gamma \tag{3.13}$$

As can we see, stable nuclei of hydrogen-1 (^{1}H), deuterium (D), helium-3 (^{3}He),

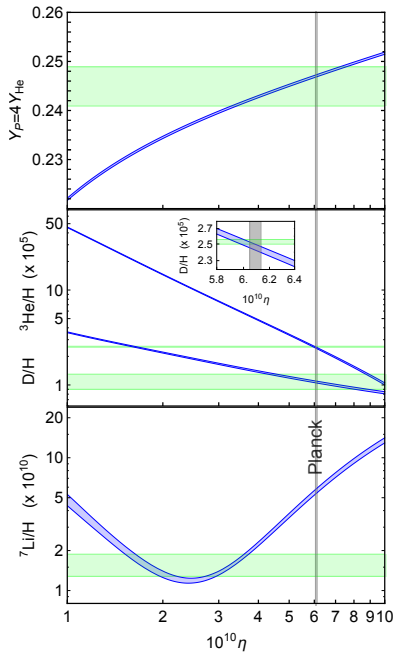

Figure 3.7: Dependence of ^{4}He (top), ^{4}He (middle-top), D (middle-bottom), and ^{7}Li (bottom) on $\eta_{b\gamma}$, along with Planck constraints (gray narrow rectangle) [117].

helium-4 (^{4}He), lithium-7 (^{7}Li), and the unstable isotopes tritium (^{3}H) and beryllium-7 (^{7}Be), were created during this process.

As expected, many other nuclear reactions that take place during primordial nucleosynthesis can also produce light nuclei. Out of these hundreds of reactions, the most important ones are shown in Figure 3.6(a). Furthermore, the equations governing this process are very difficult to address analytically. Of course, there are some procedures that involve good approximations. However, the most accurate way to do this and compare results to observations is numerical, using computational codes. As examples, we have the public codes NUC123 [118], PArthENoPE [119, 120], PRIMAT [117], and alterBBN [121, 122]. The last one even allows us to estimate light element abundances in alternative cosmological models. Figure 3.6(b) details the prediction for light abundances in base-ΛCDM using the PRIMAT code.

Figure 3.7 compares the key abundances with observations from Planck satellite. Except for the primordial lithium-7, all other abundances are in agreement with observations:

- $Y_{\rm P} \equiv 4\mathcal{N}_{\rm He}/\mathcal{N}_{\rm b} = 0.246 \pm 0.035$ [88],
- $[{\rm D/H}] \times 10^5 = 2.527 \pm 0.030$ [123],
- $[^3{\rm He/H}] \times 10^5 = 1.1 \pm 0.2$ [124], and
- $[^7{\rm Li/H}] \times 10^{10} = 1.58^{+0.35}_{-0.28}$ [125].

The predicted value for the ^{7}Li abundance, $[^7\mathrm{Li/H}] \times 10^{10} = 5.623 \pm 0.247$ [117], is around three times the measured value, $[^7\mathrm{Li/H}] \times 10^{10} = 1.58^{+0.35}_{-0.28}$ [125]. This disagreement is known as the *lithium problem* and can be addressed in three ways: (*i*) astrophysical, i.e., stars destroy lithium after BBN; (*ii*) nuclear, i.e., reactions destroy lithium during BBN; or (*iii*) cosmological, i.e., a new physics beyond the standard model is responsible for destroying ^{7}Li. For a thorough analysis on this subject, consult Refs. [126, 127].

3.3 Cosmic Microwave Background

The cosmic microwave background is a blackbody radiation that originated from the interactions between photons and free electrons in the primordial universe, which reached very low rates when the universe was approximately 380,000 years old. According to the standard model, at temperatures $T \gtrsim 1\,\mathrm{eV}$, photons were tightly coupled to the electrons via Compton scattering, which in turn strongly interacted with protons via Coulomb scattering. When the temperature dropped below 0.3 eV, nuclei and electrons combined to form the first neutral atoms (as the BBN previously discussed) and the density of free electrons sharply decreased. As a consequence, the photon mean free path increased rapidly, eventually reaching a length at which interactions with baryonic matter became nearly nonexistent around $T = 0.25\,\mathrm{eV}$. This marks the final effective photon-electron interaction, known as the surface of last scattering (LS). From that point on, photons have been traveling freely through space being observed today as the CMB radiation. Thus, the CMB offers a unique window for exploring the primordial features of the universe [128–134].

At sufficiently early times, the rapid collisions between photons and free electrons kept radiation in thermal equilibrium with the hot, dense matter. Thus, the CMB photons at frequency between ν and $\nu + d\nu$, at temperature T, should present a blackbody spectrum whose number density $\mathcal{N}_T$ is given by

$$\mathcal{N}_T(\nu)\, d\nu = \frac{8\pi\nu^2/c^3}{\exp\left(2\pi\hbar\nu/k_\mathrm{B}T\right) - 1}\, d\nu\,. \tag{3.14}$$

Here, $\hbar$ is the reduced Planck's constant and k_B is the Boltzmann's constant. Let us now supposes that the last scattering occurred at time t_LS, and that no interactions between photons and free electrons occurred thereafter. Because the space expands, its volume increases proportionally to $a^3(t)$ and the photon frequencies are redshifted as $\nu \to \nu\,[a(t)/a(t_\mathrm{LS})]$. Consequently, at any time t, we should have

$$\mathcal{N}(\nu, t)\, d\nu = \frac{8\pi\nu^2/c^3}{\exp\left[2\pi\hbar\nu/k_\mathrm{B}T(t)\right] - 1}\, d\nu = \mathcal{N}_{T(t)}(\nu)\, d\nu\,, \tag{3.15}$$

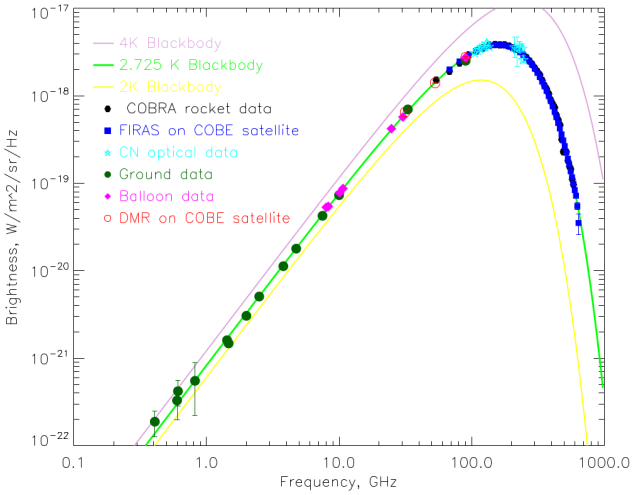

Figure 3.8: CMB flux measurements *vs.* frequency, along with expected blackbody curves for three distinct temperature values: $T_0 = 2\,\mathrm{K}$ (yelow), $T_0 = 2.725\,\mathrm{K}$ (green), and $T_0 = 4\,\mathrm{K}$ (pink). As shown, the data indicate an almost perfect blackbody at the current temperature $T_0 \simeq 2.725\,\mathrm{K}$ [135].

where

$$T(t) = \left[\frac{a(t_{\mathrm{LS}})}{a(t)}\right] T(t_{\mathrm{LS}})\,. \tag{3.16}$$

In other words, the blackbody shape of the CMB spectrum was preserved even after the last scattering, though with a redshifted temperature, as given by Eq. (3.16).

The CMB blackbody spectrum at the current temperature $T_0 = 2.725 \pm 0.001\,\mathrm{K}$ was confirmed in the 1990s by the FIRAS and DMR instruments on board the COBE telescope [136], at 95% CL [137]. However, COBE/FIRAS and COBE/DMR were not the end of the history, since they only made measurements in a small range of wavelengths around the Planckian peak. In order to cover the remaining low and very high frequencies, more ground-based, balloon-borne, and rocket-borne experiments were supplied. Figure 3.8 shows the fit of COBE/FIRAS, COBE/DMR, balloons, ground, cyanogen (CN), and COBRA rocket measurements to a Planckian curve confirming a precisely blackbody radiation at $T_0 \simeq 2.725\,\mathrm{K}$ [135]. A number of measurements of the CMB frequency spectrum derived from various observations are listed in Ref. [138].

The COBE satellite not only measured the blackbody spectrum of the CMB but also discovered small fluctuations in its temperature spatial distribution of around 10^{-5} [139], essential for LSS formation. These fluctuations were further investigated by COBE's successor, the WMAP satellite, and are currently being studied by the Planck satellite. WMAP produced CMB maps with better resolution than COBE and provided measurements with better accuracy and precision, confirming, along with BOOMERANG [140] and MAXIMA [141] experiments, a flat-ΛCDM universe and a primordial phase of approximately slow-roll single-field inflation [142]. The

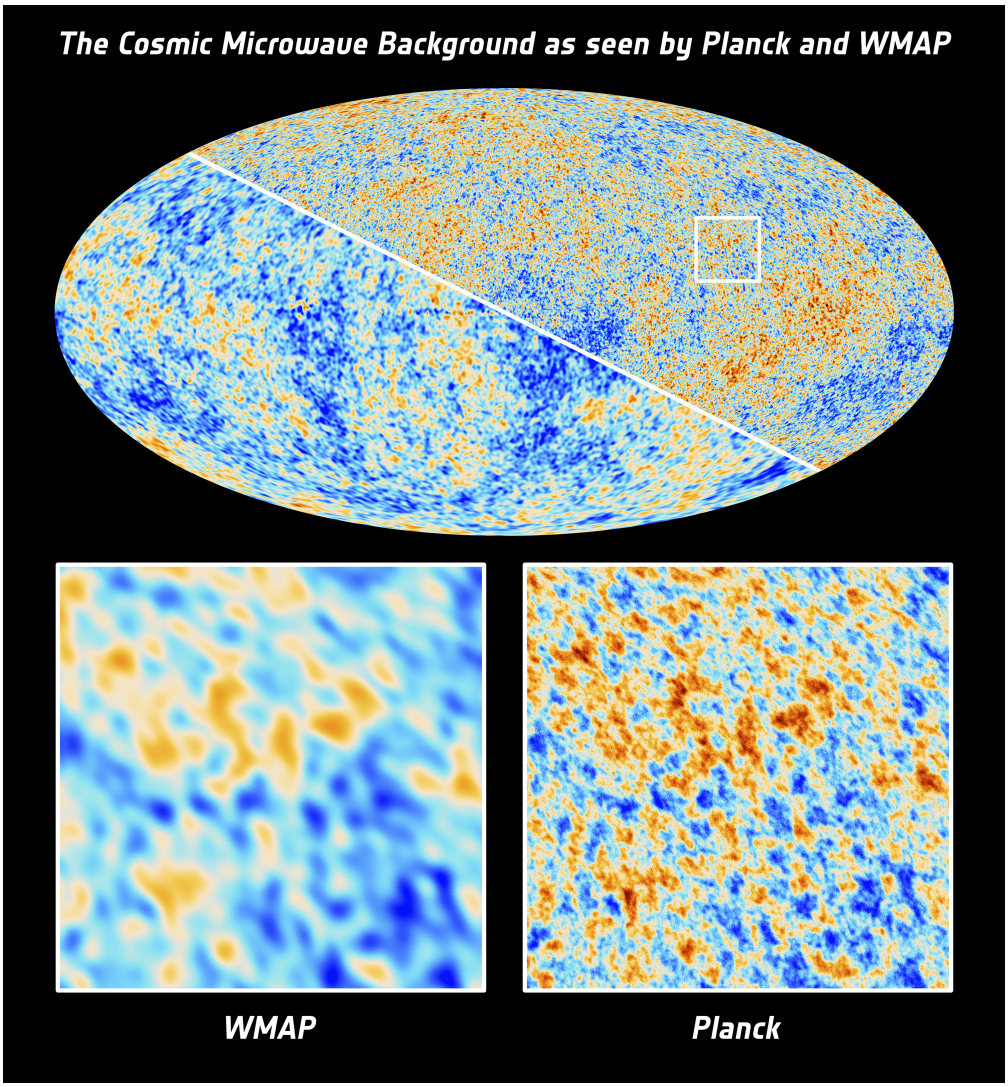

Figure 3.9: CMB temperature fluctuations map as seen by NASA's WMAP (lower left half) and by its successor ESA's Planck satellite (upper right half). WMAP represented a major advance in observational cosmology revealing in great detail the inhomogeneities of the oldest radiation background in the universe, but the Planck satellite offers even greater resolution and sensitivity, thus, providing the most accurate image to date of the CMB. Credit: NASA/WMAP Science Team; ESA and Planck Collaboration.

Planck telescope, in turn, has produced CMB maps even better than WMAP, with an impressively higher resolution than its predecessor, carried out very improved measurements with exceedingly small error bars, and placed even tighter constraints on cosmological parameters. Figure 3.9 shows the CMB temperature fluctuations map as seen by NASA's WMAP and ESA's Planck satellite.

According to the standard model, the CMB fluctuations were generated from the initial conditions set up after the primordial inflationary epoch, when $T \sim 10^{14}\,\mathrm{GeV}$. Approximately 10^{-33} s after the Big Bang, the energy density was briefly dominated by a slowly-rolling scalar field known as the *inflaton*. Because the inflaton has negative pressure, the scale factor – i.e., the length scales of the universe – was inflated by a factor of $\sim 10^{40}$, as in a quasi-de Sitter expansion. Quantum fluctuations in the inflaton were stretched beyond the Hubble horizon during such superluminal expansion and frozen. In a very simplified view, upon returning within the horizon, such fluctuations were converted into the CMB temperature fluctuations observed today. Under the assumption that there were no interactions of the inflaton with any other scalar fields in the standard inflationary scenario, the CMB fluctuations are expected to be described by an approximately Gaussian field [143–146].

Let $T(\hat{n}) \equiv T_0 [1 + \Theta(\hat{n})]$ be the measured CMB temperature in a direction $\hat{n}$ in the sky, where T_0 is the average CMB temperature today and $\Theta(\hat{n}) \equiv \Delta T(\hat{n})/T_0$ is the fractional temperature fluctuation. The comparison between temperatures at two distinct points, $\hat{n}$ and $\hat{n}'$, is made using the two-point correlation function [79],

$$C(\theta) = \langle \Theta(\hat{n})\, \Theta(\hat{n}') \rangle \ , \tag{3.17}$$

where $\theta \equiv \hat{n} \cdot \hat{n}'$ and the angle brackets denote an average over an ensemble of universes. As we observe fluctuations on the spherical surface of last scattering, it is convenient to expand the temperature field in spherical harmonics

$$\Theta(\hat{n}) = \sum_{lm} \Theta_{lm} Y_{lm}(\hat{n}) \ , \tag{3.18}$$

where Θ_{lm} is called the multipole moments and Y_{lm} are the spherical harmonics, also depending only on the direction $\hat{n}$.

For a statistically isotropic fluctuation field, the *ensemble average* is determined by the angular power spectrum C_l through the relation

$$\langle \Theta_{lm} \Theta^*_{l'm'} \rangle = \delta_{ll'} \delta_{mm'} C_l \, . \tag{3.19}$$

The angular power spectrum is the Fourier transform of the two-point correlation

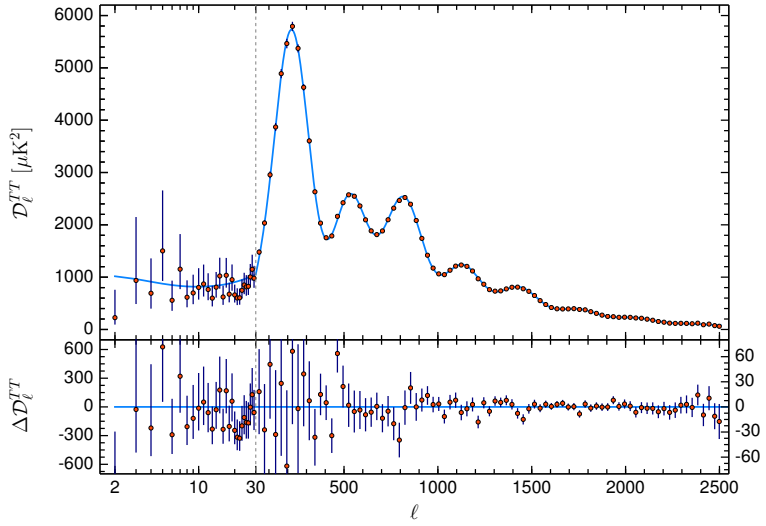

Figure 3.10: Planck 2018 temperature power spectrum. The red dots represent CMB data from observed temperature fluctuations, while the solid blue curve shows the best-fitting spectrum based on the ΛCDM model. The lower panel displays the residuals with respect to this model [88].

function. Indeed, replacing Eq. (3.18) into Eq. (3.17), we obtain

$$C(\theta) = \sum_l \frac{2l+1}{4\pi} C_l P_l(\cos\theta)\,, \tag{3.20}$$

where $P_l(\cos\theta)$ are the Legendre polynomials. Using the orthogonality of $P_l(\cos\theta)$, we can write

$$C_l = 2\pi \int_{-1}^{1} d\cos\theta\, C(\theta) P_l(\cos\theta)\,. \tag{3.21}$$

Therefore, the information provided in the $C_l's$ is exactly the same as in $C(\theta)$. The variance of the temperature anisotropy field is

$$C(0) = \sum_l \frac{2l+1}{4\pi} C_l \approx \int d\ln l \frac{l(l+1)C_l}{2\pi} \tag{3.22}$$

The argument in the above integral is related to the CMB power spectrum $\Delta_{\rm T}^2$ by

$$\Delta_{\rm T}^2 \equiv \frac{l(l+1)}{2\pi} C_l T_0^2\,, \tag{3.23}$$

which will be independent of l if the fluctuations are scale-invariant. Notice that $\Delta_{\rm T}^2$ is the same as $\mathcal{D}_l$ in the Planck papers. Figure 3.10 exhibits the theoretical prediction according to a fiducial flat-ΛCDM model against the Planck 2018 data for the power spectrum $\mathcal{D}_l^{TT}$, where the superscript TT indicates data derived from temperature-temperature correlations in the two-point correlation function.

A very important (possibly the most relevant) feature behind Figure 3.10 is that it simultaneously incorporates all six major cosmological parameters that define the standard flat-ΛCDM cosmology, namely: (*i*) the physical baryon density $\Omega_{\rm b}h^2$, (*ii*) the physical cold dark matter density $\Omega_{\rm c}h^2$, (*iii*) the acoustic angular scale at decoupling $\theta_{\rm MC}$, (*iv*) the optical depth to reionization $\tau_{\rm re}$, (*v*) the spectral amplitude of the primordial fluctuations $A_{\rm s}$, and (*vi*) the scalar spectral index $n_{\rm s}$. Any other parameter of cosmological interest, so-called secondary parameter (e.g., the current Hubble rate H_0, total matter density $\Omega_{\rm m}$, cosmological constant density Ω_Λ, current age of the universe t_0, matter fluctuation amplitude σ_8, among others), is derived using auxiliary data.

3.4 Background dynamics

Up to this point, our discussions have focused only on the physical foundations and the observational pillars of the standard HBB cosmology. We will continue our explanation with the dynamic description of the universe according to the usual Friedmann-Lemaître-Robertson-Walker (FLRW) approach.

3.4.1 Cosmological redshift

Prior to the detection of gravitational waves in 2015, all of our knowledge about the cosmos was primarily derived from the light coming from distant objects. As we know, light can be understood classically as electromagnetic waves propagating, or, quantum mechanically, as freely propagating photons. In the expanding universe, the wavelength of light emitted by a distant source gets stretched, or, equivalently, the photons lose energy. This phenomenon is known as cosmological redshift, which can be interpreted as a Doppler effect due to the relative motion between source and the observer, arising from the expansion of the universe.

Let us consider the situation in which a galaxy A at time t_1 emits a light signal with wavelength λ_1, and an observer in another galaxy B at t_0 receives it but measures a wavelength equal to λ_0. Since physical lengths are proportional to the scale factor, we should have

$$\frac{\lambda_0}{\lambda_1} = \frac{a(t_0)}{a(t_1)}\,. \tag{3.24}$$

An expanding universe, where $a(t_0) > a(t_1)$, implies an increase in wavelength, such that $\lambda_0 > \lambda_1$. In contrast, a contracting space, with $a(t_0) < a(t_1)$, implies an decrease in wavelength, i.e., $\lambda_0 < \lambda_1$.

To quantify the displacement of the spectral lines of a source due to the expansion

of the universe, let us define the redshift z as

$$z \equiv \frac{\lambda_0 - \lambda_1}{\lambda_1} = \frac{v}{c}\,. \tag{3.25}$$

By replacing Eq. (3.24) into Eq. (3.25), we find for a light-emitting source at t_1 and an observer at t_0,

$$1 + z = \frac{a(t_0)}{a(t_1)} = \frac{1}{a(t_1)}\,. \tag{3.26}$$

The second equality is achieved when setting $a(t_0) \equiv 1$. Analyzing Eq. (3.25), it is possible to verify only two situations:

(a) when $z > 0$, or $\lambda_0 > \lambda_1$, we have a redshift;

(b) when $z < 0$, or $\lambda_0 < \lambda_1$, we have a blueshift.

From Eq. (3.26), we conclude that the observed spectral lines of a distant source are redshifted throughout the cosmic expansion. It was the observation of this effect in the spectra of the galaxies studied by E. Hubble and other researchers that allowed the astronomer to measure the recessional velocities and thus discover the expansion of the universe.

Let us now see how this relates to the Hubble law. It turns out we can expand the scale factor $a(t_1)$ in the following power series:

$$a(t_1) = a(t_0)\left[1 + (t_1 - t_0)H_0 - \frac{q_0}{2}(t_1 - t_0)^2 H_0^2 + \ \ldots\right]\,. \tag{3.27}$$

For nearby sources for which $|(t_1 - t_0)H_0| \ll 1$, we can truncate the series in linear order, obtaining $z \simeq H_0(t_0 - t_1)$. Since $(t_0 - t_1)$ multiplied by the speed of light c is simply the physical distance d, we find that

$$cz \simeq H_0 d\,, \tag{3.28}$$

which is the nearby Hubble law expressed in terms of the observable redshift z. By comparing Eq. (3.28) to Eq. (3.25), we have now another way to define nearby sources comprising the local universe. That is $cz \ll v$, or, equivalently, $z \ll v/c$. Hence, considering physical distances as $d \lesssim 400\,\mathrm{Mpc}$ and $H_0 \sim 70\,\mathrm{km\,s^{-1}\,Mpc^{-1}}$, the local universe corresponds to $z \lesssim 0.1$. The definition of the local universe is not a consensus in the literature, since some authors report it as being given by $z < 0.05$ [147], $z < 0.1$ [148, 149], or even $z < 0.2$ [150–152].

As we have seen, the observable redshift is a monotonic function of time in the Hubble expanding universe, with with $z = 0$ corresponding to the present age and $z \to \infty$ to the initial Big Bang singularity. This allows us to organize events in the universe's timeline by assigning a specific redshift value to each of them.

For example, primordial inflation occurred at $z \sim 10^{26}$, BBN at $z \sim 10^{8}$, radiation-matter equality at $z \simeq 3400$, recombination at $z \simeq 1400$, last scattering and photons decoupling at $z \simeq 1100$, reionization between $20 \gtrsim z \gtrsim 6$, and matter-DE equality at $z \sim 0.326$ [79–81].

3.4.2 Cosmological distances

Measuring distances in cosmology is a truly challenging task, since many issues can be involved, such as environmental pollution, incomplete astrophysical models, dependence on the cosmological model for very distant sources, limitations of current instruments, uncontrolled effects, among others. Fortunately, there are some ways in which we can do this appropriately.

Initially, two forms of cosmological distances have already been mentioned when we talk about the Hubble expansion: the comoving distance r and the physical distance $d(t)$. While the first one is related to the coordinate position of an object, remained constant throughout the expansion, the second one depends on cosmic time t as the physical space between the bodies is being stretched. Such distances are connected through the scale factor $a(t)$ via Eq. (3.1).

Other three important distances are the Hubble sphere $r_{\rm H}(t)$, the particle horizon $r_{\rm p}(t)$, and the sound horizon $r_{\rm s}(t)$. As we have written explicitly, these are measures that evolve over time. Ultimately, the Hubble sphere is the radius where objects receding from the origin according to Hubble's law are instantaneously receding at the speed of light, the particle horizon establishes the causal limit of the structures in the universe, and the sound horizon corresponds to the preferred distance for the structure formation in the universe [153].

Nevertheless, none of these distance measurements assist astrophysicists and astronomers in determining the distance to objects in the sky using their telescopes. For this purpose, two additional distance estimators were developed. The first we are talking about is the luminosity distance $d_{\rm L}(z)$, determined from the measured flux $F_{\rm L}(z)$, or luminosity L, due to a bright source at redshift z. The second involves the measured angular size $\delta\theta_{\rm A}$ and physical size $s_{\rm A}$ of an object at redshift z, which can be used to determine its angular diameter distance, $d_{\rm A}(z)$. It is worth mentioning that although these estimators assume relatively simple forms, they carry with them all the astrophysical difficulties involved in obtaining, for example, the correct luminosity of distant sources. In addition, any physical distance to light sources outside the local universe is significantly affected by the nonlinear terms in Eq. (3.27), specifically the acceleration term $q(t)$ and beyond, and by the curvature of the spatial section, leading to a dependence on the cosmological model.

Hubble sphere

As the Hubble law states that distant sources are moving away with a recessional velocity proportional to the distance, there must be a distance in which the bodies have $v = c$. This distance is the Hubble sphere, defined by

$$r_{\rm H}(t) \equiv \frac{c}{H(t)}. \tag{3.29}$$

In the literature on the inflationary universe, it is common to refer to $r_{\rm H}$ as the *horizon*. It is also often stated to be the boundary beyond which causal influences cannot propagate, due to the special relativity constraint that no cause can propagate faster than the speed of light [153]. However, both claims are misleading. First, in the context of inflation, the Hubble sphere is not a true horizon because structures that have crossed it can reenter after inflation ends; the horizon they reenter is called the *revised horizon*, determined by the distance that light can travel in a non-inflationary FLRW universe. Second, although photons are in the superluminal region (and thus recede from us beyond an appropriate distance), the Hubble sphere also recedes. As long as the Hubble sphere recedes faster than the photons immediately outside it, those photons eventually enter a subluminal region and approach us. See Ref. [154] for a detailed discussion of these misconceptions.

Particle horizon

Because the speed of light and the age of universe have finite values, there exists a particle horizon $r_{\rm p}(t)$ determining the maximum distance from which we can retrieve information from the past. A photon emitted at the Big Bang would have traveled the greatest possible distance to reach observer at time t, given by

$$\Delta\tau \equiv \tau - \tau_i = \int_{t_i}^{t} \frac{c\,dt}{a(t)}\,, \tag{3.30}$$

where the subscript i corresponds to the initial Big Bang time, and $\Delta\tau$ is called the comoving particle horizon, which defines a causality limit for structures in the universe. The physical particle horizon is therefore given by

$$r_{\rm p}(t) = a(t)\Delta\tau\,. \tag{3.31}$$

Although $r_{\rm H}(t)$ and $r_{\rm p}(t)$ are the same for most of the history of the universe, the Hubble sphere and particle horizon are conceptually distinct. For example, during primordial inflation, these distances differ significantly: in inflation, $r_{\rm H} \approx$ *constant*. while $r_{\rm p} \propto \exp(Ht)$.

Sound horizon

The early universe was susceptible to baryonic acoustic oscillations due to the dark matter pits affecting the frequency of photons, and then the high interaction rates in the photon-electron-baryon (or simply photon-baryon) fluid. These oscillations propagated throughout the universe at the speed of sound $c_{\rm s}$, defined by

$$c_{\rm s} \equiv \left[3\left(1+\frac{3\rho_b}{4\rho_\gamma}\right)\right]^{-1/2} . \tag{3.32}$$

Here, the subscripts b and γ stand for baryons and photons, respectively. Thus, the maximum distance covered by baryonic acoustic oscillations before photon-baryon decoupling is the sound horizon, which is given by

$$r_{\rm s}(t) = a(t)\int_{t_{\rm B}}^{t_*}\frac{c_{\rm s}\,dt}{a(t)}\,, \tag{3.33}$$

where $t_{\rm B}$ denotes the onset of baryonic acoustic oscillations, and t_* represents the time of decoupling. After decoupling, the baryonic acoustic oscillations are frozen, allowing structures to grow and cluster more likely along spherical surfaces with a radius equal to the sound horizon.

Luminosity distance

So far, observing the emitted light by celestial bodies is the most effective method in order to explore the universe, in particular, for measuring distances. In the Hubble expanding universe, spherically symmetric and isotropic light source with known luminosity L (i.e., a *standard candle*) at redshift z has an observed (at $z=0$) luminosity flux $F_{\rm L}(z)$ given by

$$F_{\rm L}(z) = \frac{L}{4\pi d_{\rm L}^2(z)}\,, \tag{3.34}$$

where $d_{\rm L}(z)$ is the luminosity distance, defined as

$$d_L(z) \equiv \mathcal{X}(r)(1+z)\,. \tag{3.35}$$

Here, $\mathcal{X}(r) \equiv \int_0^r d\tilde{r}/\sqrt{1-K\tilde{r}^2/R_0^2}$ [1] is the conformal distance in a universe with constant curvature given by K, and current physical curvature scale denoted by R_0. Notice that assuming a spatially flat three-section for which $K/R_0^2 = 0$, the quantity $\mathcal{X}(r)$ is simply the radial comoving distance r.

[1] This integral is obtained assuming a null geodesic in the Robertson-Walker metric, which are the paths followed by photons in a statistically homogeneous and isotropic universe [65, 83, 155, 156]. In the part that follows, we will talk about the Robert-Walker metric.

For galaxies in the local universe [157, 158], the Hubble's law can be written as $cz = H_0 d_{\rm L}$. This formula has the advantage of having only observational quantities. Finally, $d_{\rm L}(z)$ can be given in terms of apparent magnitude $m_{\rm B}$(z) by

$$d_{\rm L}(z) = 10^{\frac{m_{\rm B}(z) - M_{\rm B}}{5} + 1}\,, \tag{3.36}$$

where $M_{\rm B}$ is the absolute magnitude, defined as the apparent magnitude that the object would have if it were viewed from a distance of exactly 10 parsecs (without extinction or dimming). In this case, $d_{\rm L}$ is given in parsec.

Angular diameter distance

A classic way to determine distances in astronomy is measuring the angle $\delta\theta_{\rm A}$ subtended by an object of known physical size $s_{\rm A}$ (i.e., a *standard ruler*). For distant objects so that $\delta\theta_{\rm A} \ll 1$, we can write

$$d_{\rm A} = \frac{s_{\rm A}}{\delta\theta_{\rm A}}\,. \tag{3.37}$$

Relating this to the expansion of the universe, the angular diameter distance, defined as $d_{\rm A}(t) \equiv a(t)\mathcal{X}(r)$, gives

$$d_{\rm A}(z) = \frac{\mathcal{X}(r)}{1+z}\,. \tag{3.38}$$

Combining now this relation with Eq. (3.35), we get the Etherington's reciprocity theorem, also known as the distance duality relation [159],

$$d_{\rm A}(z) = \frac{d_{\rm L}(z)}{(1+z)^2}\,. \tag{3.39}$$

This relation is completely general, valid for any cosmological scenario based on a Riemannian (and pseudo-Riemannian) geometry. The only requirements for its validity are that the source and observer are connected via null geodesics, and that the number of photons is conserved.

3.4.3 Robertson-Walker metric

The statistical homogeneity and isotropy postulated by the cosmological principle reduce the form of the metric tensor to a restricted family of spacetimes known as the Robertson-Walker (RW) metric, in a universe filled with various forms of matter, energy and curvature. Spatial homogeneity implies that every point in the spacetime web is equivalent, while spatial isotropy asserts that there are no privileged directions around any point. Mathematically, homogeneity represents symmetry under translations, while isotropy stands for symmetry under rotations.

Since the universe is not static, we are looking for a metric that is homogeneous and isotropic in space, but not in time. In GR, this translates into the statement that the universe can be foliated into *spacelike* slices such that each slice is homogeneous and isotropic. Therefore, we search for a metric as

$$ds^2 = -c^2 dt^2 + \mathcal{F}_{ij} dx^i dx^j \,, \tag{3.40}$$

where $\mathcal{F}_{ij} = \mathcal{F}_{ij}(t, x^i)$. Considering now two arbitrary slices $t = t_1$ and $t = t_2 > t_1$, the CP states that a triangle formed by three particles in t_1 has its shape maintained when it reaches t_2. Hence,

$$\mathcal{F}_{ij} = a^2(t)\gamma_{ij}(x^i) \,, \tag{3.41}$$

where the purely spatial metric tensor, γ_{ij}, obeys

$$R_{ijkl} = \frac{K}{R_0^2} \left(\gamma_{ik}\gamma_{jl} - \gamma_{il}\gamma_{jk}\right) \,, \tag{3.42}$$

and thus

$$R_{ij} = \gamma^{kl} R_{kijl} = \frac{2K\gamma_{ij}}{R_0^2} \,. \tag{3.43}$$

Here, K/R_0^2 represents the Gaussian curvature of the spatial three-section; the CP requires that K be a constant. Metrics that satisfy Eq. (3.42), and hence Eq. (3.43), are referred to as maximally symmetric metrics.

Since the spatial three-section is spherically symmetric, the purely spatial metric takes the form

$$\gamma_{ij} dx^i dx^j = e^{\mathcal{Q}} dr^2 + r^2 \left(d\theta^2 + \sin^2\theta d\phi^2\right) \,, \tag{3.44}$$

where $\mathcal{Q} = \mathcal{Q}(r)$. By solving Eqs. (3.43), it is straightforward to show that

$$\mathcal{Q}(r) = -\ln\left(1 - \frac{Kr^2}{R_0^2}\right) . \tag{3.45}$$

Therefore, the metric satisfying the requirements set out by the spatial homogeneity and isotropy follows from the line element

$$ds^2 = -c^2 dt^2 + a^2(t) \left[\frac{dr^2}{1 - \frac{Kr^2}{R_0^2}} + r^2 \left(d\theta^2 + \sin^2\theta \, d\phi^2\right)\right] \,, \tag{3.46}$$

known as the Robertson-Walker line element or Robertson-Walker metric. Notice that the substitutions

$$a \to \frac{a}{\sqrt{|K|}} \,, \quad r \to \sqrt{|K|}\, r \,, \quad K \to \frac{K}{|K|} \,, \tag{3.47}$$

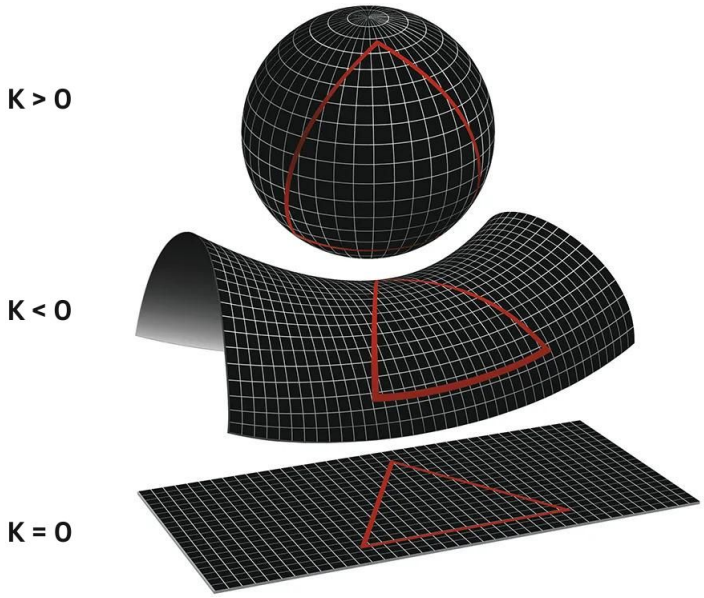

Figure 3.11: Geometry of the universe. The first case shows a spherical curvature ($K > 0$), indicating a closed universe. The second case displays a hyperbolic curvature ($K < 0$), indicating an open universe. The third case is the flat, Euclidean universe with $K = 0$. The geometry of the universe is related to the total energy density, Ω_0, and determines whether the universe will expand forever or eventually collapse. Credit: NASA/WMAP Science Team.

for $K \neq 0$, leave Eq. (3.46) invariant. Therefore, the actually relevant curvature parameter is $K \to K/|K|$, giving rise to the three cases of interest $|K| = 0$ or 1.

- $K = +1$ corresponds to a spherical geometry,
- $K = -1$ corresponds to a hyperbolic geometry,
- $K = 0$ corresponds to a flat (or Euclidean) geometry.

Figure 3.11 illustrates a 2D representation for each of the geometries described here. It is possible to notice that whereas a triangle drawn on a flat surface has the sum of its internal angles equal to 180°, on spherical surface it is greater than 180° and in hyperbolic surface it is less than 180°.

The propagation of signals at the speed of light c can be understood within the context of a homogeneous and isotropic universe. As massless particles like photons follow null geodesics ($ds^2 = 0$), Eq. (3.46) yields $c\,dt/a(t) = \pm\, dr/\sqrt{1 - Kr^2/R_0^2}$, where the "+" and "−" signs correspond to the emission and observation of a photon, respectively. Thus, for a photon emitted at any time t at a distance r and observed at time t_0 at the origin $r = 0$, we shall have

$$\int_t^{t_0} \frac{c\,dt}{a(t)} = -\int_r^0 \frac{d\tilde{r}}{\sqrt{1 - K\tilde{r}^2/R_0^2}} \equiv \mathcal{X}(r)\,. \tag{3.48}$$

The solution of this equation corresponds to the following three cases:

$$\mathcal{X}(r) = \begin{cases} \frac{R_0}{\sqrt{|K|}} \sin^{-1}\left(\sqrt{\frac{|K|r^2}{R_0^2}}\right) & \text{if} \quad K > 0 \\ \frac{R_0}{\sqrt{|K|}} \sinh^{-1}\left(\sqrt{\frac{|K|r^2}{R_0^2}}\right) & \text{if} \quad K < 0 \\ r & \text{if} \quad K = 0 \end{cases} . \tag{3.49}$$

In a flat universe, the conformal distance to an object $\mathcal{X}(r)$ is just its coordinate distance r. On the other hand, because $\sin^{-1}(y) > y$ and $\sinh^{-1}(y) < y$ in a closed universe, the conformal distance to an object is greater than its coordinate distance, whereas in an open universe it is less than its coordinate distance. Current combined analysis of data come from CMB, lensing, BAO, and SNe Ia observations point out to a essentially flat universe [88, 160], as predicted by cosmic inflation.

3.4.4 Friedmann equations

Thus far, we have separately discussed the main ingredients for constructing the HBB standard cosmology, namely: (*i*) the GR theory describing the gravitational field, and (*ii*) the cosmological principle, which leads to the perfect fluid description for the material distribution in the universe and the RW metric. We will now combine these ingredients into a cosmological recipe in order to derive the motion equations that describe the evolution of the universe.

By replacing both the perfect fluid energy-moment tensor in Eq. (2.37), setting vacuum energy to vanish ($T_{\mu\nu}^{\text{vac}} = 0$), and RW metric in Eq. (3.46) into Einstein's equations (2.49), we obtain the Friedmann equations (in units as $c = 1$),

$$H^2 = \kappa^2 \left(\rho_{\text{r}} + \rho_{\text{m}} + \rho_{\text{K}}\right) \tag{3.50}$$

and

$$2\dot{H} + 3H^2 = -\kappa^2 \left(P_{\text{r}} + P_{\text{m}} + P_{\text{K}}\right) , \tag{3.51}$$

where (recall) $\kappa^2 \equiv 8\pi G$ is the Einstein constant. We have defined the curvature density[2] as $\rho_{\text{K}} \equiv -3K/\kappa^2 a^2$. For the time being, we have disregard any contribution from a cosmological constant. Since all radiation (r), matter (m), and curvature (K) fields behave as simple barotropic fluids, the pressures $P_i \equiv P_i(\rho_i)$ can be described through the equation of state

$$P_i = w_i \rho_i \, , \quad w_i = \begin{cases} 1/3, & \text{for radiation} \\ 0, & \text{for matter} \\ -1/3, & \text{for curvature} \end{cases} . \tag{3.52}$$

[2]Beware! Although it is possible to describe curvature as a perfect fluid with $w_{\text{K}} = -1/3$, this is misleading. In fact, curvature belongs on the left-hand side of the field equations.

The conservation of the energy-momentum states that each of the material or curvature components must satisfy the fluid equation

$$\dot{\rho}_i + 3H(\rho_i + P_i) = 0\,. \tag{3.53}$$

Since each of the components are conserved separately, the sum also vanish, i.e., $\sum_i [\dot{\rho}_i + 3H(\rho_i + P_i)] = 0$, where $i = (\mathrm{r}, \mathrm{m}, \mathrm{K})$. Using Eq. (3.52) to solve Eq. (3.53), we obtain

$$\rho_i(a) = \rho_{i,0}\, a^{-3} \exp\left[-3\int_{a_0}^{a} \frac{w_i(\tilde{a})d\tilde{a}}{\tilde{a}}\right], \tag{3.54}$$

where $\rho_{i,0} \equiv \rho_i(t_0)$ is the energy density of the i^{th} material component at the present time $t = t_0$. If the EoS parameter w_i is constant, then

$$\rho_i(a) = \rho_{i,0}\, a^{-3(1+w_i)}\,. \tag{3.55}$$

As a result, we shall have three distinct cases: (i) radiation, for which $w_\mathrm{r} = 1/3$, thus evolving as $\rho_\mathrm{r} = \rho_{\mathrm{r},0}\, a^{-4}$; (ii) non-relativistic matter, for which $w_\mathrm{m} = 0$, thus evolving as $\rho_\mathrm{m} = \rho_{\mathrm{m},0}\, a^{-3}$; and (iii) curvature, for which $w_\mathrm{K} = -1/3$, thus evolving as $\rho_\mathrm{K} = \rho_{\mathrm{K},0}\, a^{-2}$. These solutions correspond to single-component universes, so a more realistic picture of nature involves a mixture of radiation, matter, curvature, and even exotic dark energy, which we will discuss later.

The Friedmann equation (3.50) can be rewritten in a more convenient form if we set the critical value of the total density such that the universe is spatially flat today. Such a critical density is thus defined as

$$\rho_\mathrm{cr} \equiv \frac{H_0^2}{\kappa^2} = \frac{3H_0^2}{8\pi G}\,. \tag{3.56}$$

In terms of the normalized Hubble constant, h, the critical density can be expressed as $\rho_\mathrm{cr} = 1.9 \times 10^{-29}\, h^2\, \mathrm{g/cm^3}$. It is used in order to define the physical density, or density parameter,

$$\Omega_i(a) \equiv \frac{\rho_i(a)}{\rho_\mathrm{cr}}\,. \tag{3.57}$$

In terms of this parameter, the Friedmann equation is then given as

$$H^2(a) = H_0^2 \left(\frac{\Omega_{\mathrm{r},0}}{a^4} + \frac{\Omega_{\mathrm{m},0}}{a^3} + \frac{\Omega_{\mathrm{K},0}}{a^2}\right), \tag{3.58}$$

where we have set $\Omega_{i,0} \equiv \Omega_i(a_0)$. This form of expressing the Friedmann equation is particularly appropriate, since $\Omega_{i,0}$ is often observed directly and takes values in the range $0 \leq \Omega_{i,0} \leq 1$.

Finally, Eqs. (3.50), (3.51), and (3.53) can be combined to yield the acceleration

equation, also known as the Raychaudhuri equation,

$$\frac{\ddot{a}}{a} = -\frac{\kappa^2}{6} \sum_{\mathrm{M=r,m}} \left(\rho_{\mathrm{M}} + 3P_{\mathrm{M}}\right), \tag{3.59}$$

where the subscript M stands only for radiation and matter. As there is no presence of curvature term in this equation, we shall always have $\ddot{a} < 0$, meaning that the universe's expanding velocity is decreasing over time. This makes sense if we consider that all of conventional forms of matter gravitate towards collapsing.

However, by the end of the 1990s, two different teams of astrophysicists – one led by S. Perlmutter and the other by B. Schmidt – discovered that the universe is currently expanding at an accelerated rate, $q(t_0) < 0$ [1, 2]. In the context of GR, we have seen that this acceleration cannot be explained solely through known conventional energy forms, such non-relativistic matter or radiation. Examining Eq. (3.59), we conclude that to achieve $\ddot{a} > 0$, it is required that $\rho + 3P < 0$, or, equivalently, $w < -1/3$. In other words, the material content driving the acceleration of the universe must have negative pressure.

3.4.5 Cosmic acceleration

We have seen that in order to explain the current cosmic acceleration in light of the standard cosmology, based only on GR theory and the CP, it is necessary to postulate a new form of energy in such a way that $\rho + 3P < 0$, which require at least $w < 0$. Such a exotic component is generically called the dark energy (DE), having EoS given by

$$w_{\mathrm{DE}} = \frac{P_{\mathrm{DE}}}{\rho_{\mathrm{DE}}}\,. \tag{3.60}$$

Because the physical nature of DE is unknown, various parameterizations of w_{DE} have been proposed in the literature (see Refs. [161–163] for reviewing dark energy models).

The simplest theoretical explanation for the current acceleration is that it originates from the energy density of the quantum vacuum. We have seen that a positive cosmological constant, when inserted into the right-hand side of the Einstein equations, can be interpreted as the contribution of the quantum vacuum from the matter fields existing in the universe. In this case, we can add the energy density due to cosmological constant to the total energy density, allowing the Friedmann equation to be expressed as

$$H^2 = H_0^2 \left(\frac{\Omega_{\mathrm{r},0}}{a^4} + \frac{\Omega_{\mathrm{m},0}}{a^3} + \frac{\Omega_{\mathrm{K},0}}{a^2} + \Omega_\Lambda\right), \tag{3.61}$$

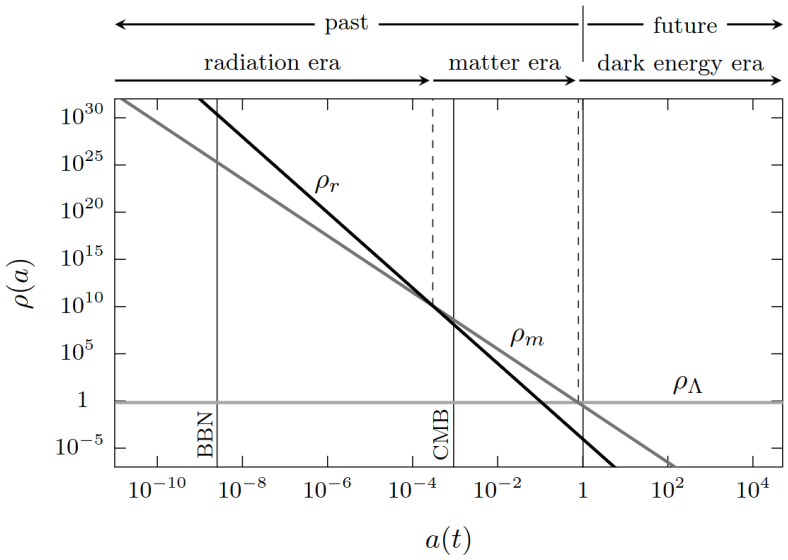

Figure 3.12: Evolution of energy densities in the universe. Radiation dominated the energy density, ρ, until close to the time of CMB formation. As $\rho_{\rm r}$ decreases faster than $\rho_{\rm m}$, matter became the dominant component afterward. At sufficiently late times ($z \sim 0.5$), the cosmological constant becomes more significant than any other component [79].

$\rho(a)$	$a(t)$	$H(t)$	Era
$\propto a^{-4}$	$\propto t^{1/2}$	$= 1/2t$	RD
$\propto a^{-3}$	$\propto t^{2/3}$	$= 2/3t$	RD
$\propto a^{0}$	$\propto e^{H_0\sqrt{\Omega_\Lambda}\,t}$	$= H_0\sqrt{\Omega_\Lambda}$	ΛD

Table 3.1: Summary of solutions for a single-component universe.

where

$$\Omega_\Lambda \equiv \frac{\rho_\Lambda}{\rho_{\rm cr}} = \frac{\Lambda}{3H_0^2}\,. \tag{3.62}$$

Since $w_\Lambda = -1$, Eq. (3.55) gives us $\rho_\Lambda = \rho_{\Lambda,0}$. Hence, the acceleration condition translates to $\rho + 3P = 2\rho_{\rm r} + \rho_{\rm m} - 2\rho_\Lambda < 0$, implying $\rho_\Lambda > (2\rho_{\rm r} + \rho_{\rm m})/2$, where the matter-energy content now also includes the cosmological constant. This means that the observed acceleration is achieved as the universe is currently dominated by the quantum vacuum energy ρ_Λ. Consequently, the universe must have undergone three different evolution phases: (i) the radiation-dominated (RD) era, where $\rho \propto a^{-4}$ and $a \propto t^{1/2}$; (ii) the matter-dominated (MD) era, where $\rho \propto a^{-4}$ and $a \propto t^{2/3}$; and (iii) the current vacuum-dominated (ΛD) era, where $\rho \propto a^0$ and $a \propto \exp\left(H_0\sqrt{\Omega_\Lambda}\,t\right)$. Figure 3.12 illustrates the evolution of each material contents and the different phases the universe undergoes. Table 3.1, in turn, summarizes the solutions for single-component universe.

Since $H_0 \equiv H(t_0)$, the parentheses in Eq. (3.61) must equal unity, leading to $\Omega_0 \equiv \Omega_{\rm M,0} + \Omega_\Lambda = 1 - \Omega_{\rm K,0}$, where Ω_0 represents the current total density. This

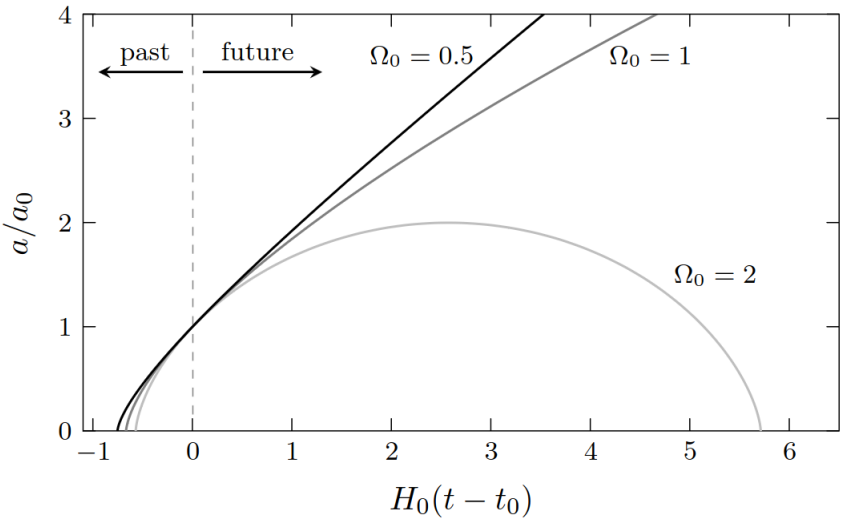

Figure 3.13: Evolution of the scale factor $a(t)$ for a universe containing only a mixture of non-relativistic matter and spatial curvature. The fate of the universe depends on the total amount of matter. If the universe is closed ($\Omega_0 > 1$), then it re-collapses in a *Big Crunch*, while if it is open ($\Omega_0 < 1$), it will expands forever. The flat case ($\Omega_0 = 1$) lies in the intermediate region and also leads to an eternally expanding universe, although more slowly than in the open case [79].

results in three situations:

- $\Omega_0 > 1$, indicating a spherical closed universe;
- $\Omega_0 < 1$, indicating a hyperbolic open universe; and
- $\Omega_0 = 1$, indicating a Euclidean open universe.

Therefore, the current total amount of matter-energy Ω_0 dictates both the spatial geometry and fate of the universe: *closed* indicates that the current amount of matter is sufficient to reverse the expansion and cause the universe to collapse, while *open* signifies that Ω_0 is not large enough to stop the expansion, resulting in an eternal expansion of the universe (see Figure 3.13).

3.5 Cosmological perturbations

Thus far, we have treated the universe as a perfectly homogeneous fluid, such that physical properties like density and pressure depend only on time. However, it was previously discussed the existence of small fluctuations about 10^{-5} in the CMB temperature distribution. These fluctuations are associated with perturbations in the global distribution of material and play a crucial role in the growth of LSS. As long as these perturbations remain relatively small, we can analyze them using linear perturbation theory.

To describe such an inhomogenous universe, we expand the Einstein equations order by order in perturbations to both the metric and the stress-energy tensor,

$$\begin{cases} g_{\mu\nu}(\eta, x^i) &= \bar{g}_{\mu\nu}(\eta) + \delta g_{\mu\nu}(\eta, x^i) \\ T_{\mu\nu}(\eta, x^i) &= \bar{T}_{\mu\nu}(\eta) + \delta T_{\mu\nu}(\eta, x^i) \end{cases} , \quad \eta \equiv \int \frac{dt}{a(t)} , \tag{3.63}$$

where η is the conformal time. As it is well known, a generic perturbation can be decomposed into scalar, vector, and tensor modes. Scalars modes are connected to matter fluctuations, vector modes are responsible for generating primordial magnetic fields, and tensor modes give rise to gravitational waves. Since these perturbations are very small, i.e., $|\delta g_{\mu\nu}|, |\delta T_{\mu\nu}| \ll \bar{g}_{\mu\nu}, \bar{T}_{\mu\nu}$, we will discuss only linear perturbations. Furthermore, we will focus only on the scalar modes, as we are primarily interested in matter fluctuations, essential for understanding the growth of structures.

3.5.1 Metric perturbations

The basic idea is to consider small perturbations around the flat RW metric [79],

$$ds^2 = a^2(\eta) \left[-(1 + 2\Phi)\, d\eta^2 + 2\mathcal{B}_i d\eta dx^i + (\delta_{ij} + 2\mathcal{E}_{ij})\, dx^i dx^j \right] , \tag{3.64}$$

where we use conformal time η instead of cosmic time t. The functions $\Phi = \Phi(\eta, x^i)$, $\mathcal{B}_i = \mathcal{B}_i(\eta, x^i)$, and $\mathcal{E}_{ij} = \mathcal{E}_{ij}(\eta, x^i)$ represent scalar, vector, and tensor perturbations, respectively.

Since the perturbations are decoupled at linear order, the scalar-vector-tensor decomposition allows us to express

$$\mathcal{B}_i = \partial_i B + B_i , \tag{3.65}$$

$$\mathcal{E}_{ij} = \Psi \delta_{ij} + \left(\partial_i \partial_j - \frac{1}{3} \delta_{ij} \nabla^2 \right) E + \frac{1}{2} (\partial_i E_j + \partial_j E_i) + E_{ij} . \tag{3.66}$$

In order to eliminate redundant information in the metric perturbations, we impose the conditions $\partial^i B_i = \partial^i E_i = \partial^i E_{ij} = E^i_i = 0$. This leaves 10 metric degrees of freedom [164, 165]:

- Scalar perturbations: $\{\Phi, B, \Psi, E\}$;
- Vector perturbations: $\{B_i, E_i\}$;
- Tensor perturbations: $\{E_{ij}\}$.

Therefore, by applying the scalar-vector-tensor decomposition and imposing the necessary constraints, we reduce the number of independent metric perturbations to 10 degrees of freedom. This simplification enables us to isolate the relevant physical modes for cosmological analysis.

3.5.2 Fluid perturbations

The most general way to establish perturbations in a perfect fluid, considering a flat expanding space, is to set [79]

$$\begin{array}{rcl} T_0^0 & \equiv & -\left(\bar{\rho}+\delta\rho\right) \\ T_j^0 & \equiv & \left(\bar{\rho}+\bar{P}\right)\left(v_j+B_j\right) \\ T_0^i & \equiv & -\left(\bar{\rho}+\bar{P}\right)v^i \\ T_j^i & \equiv & \left(\bar{P}+\delta P\right)\delta_j^i+\Pi_j^i \end{array} , \tag{3.67}$$

where $\delta\rho=\delta\rho(\eta,x^i)$ represents the matter density fluctuations, $\delta P=\delta P(\eta,x^i)$ is the pressure perturbations, $v^i=v^i(\eta,x^i)$ are the peculiar velocities, and $\Pi_j^i=\Pi_j^i(\eta,x^i)$ is the anisotropic stress.

Similarly to metric perturbations, the scalar-vector-tensor decomposition can be applied to the matter perturbations, yielding

$$v_i=\partial_i v+\mathcal{V}_i\,, \tag{3.68}$$

$$\Pi_{ij}=\left(\partial_i\partial_j-\frac{1}{3}\delta_{ij}\nabla^2\right)\Pi+\frac{1}{2}\left(\partial_i\Pi_j+\partial_j\Pi_i\right)+\pi_{ij}\,. \tag{3.69}$$

As with metric perturbations, we impose the conditions $\partial^i v_i=\partial^i\Pi_{ij}=\Pi_i^i=0$. Given the wide variety of species in the universe – such as photons (γ), baryons (b), electrons (e), neutrinos (ν), dark matter (c), etc. – the total stress-energy tensor is given by the sum $T_{\mu\nu}=\sum_a T^a_{\mu\nu}$. This implies that $\delta\rho=\sum_a\delta\rho^a$, $\delta P=\sum_a\delta P^a$, $\left(\bar{\rho}+\bar{P}\right)v_i=\sum_a\left(\bar{\rho}_a+\bar{P}_a\right)v_i^a$, and $\Pi_{ij}=\sum_a\Pi^a_{ij}$.

Finally, it is convenient to describe the matter-energy density perturbations in terms of the dimensionless density contrast, $\delta_a(\eta,x^i)\equiv\delta\rho_a(\eta,x^i)/\bar{\rho}_a(\eta)$. Ultimately, perturbation theory is valid as long as $\delta_a\ll 1$.

3.5.3 Newtonian gauge

When describing perturbations in GR theory, we are implicitly choosing a specific *time slicing* of spacetime and defining particular spatial coordinates on these time slices. A different choice of coordinates can change the values of the perturbation variables or even introduce fictitious perturbations. Consequently, the metric and matter perturbations in Eqs. (3.64) and (3.67) are not uniquely defined, but depend on the choice of coordinates, the so-called *gauge choice*.

In order to address this issue, the gauge-invariant formalism was introduced in Refs. [166, 167] and later refined in Refs. [164, 168, 169]. It follows then that one way to avoid the gauge problem is to define specific combinations of the perturbations that remain unchanged under a change of coordinates. In the case of metric

perturbations, there are the Bardeen variables

$$\begin{cases} \Phi_{\rm B} & \equiv & \Phi + \mathcal{H}\,(B - E') + (B - E')' \\ \Psi_{\rm B} & \equiv & -\Psi + \frac{1}{3}\nabla^2 E - \mathcal{H}(B - E') \end{cases} , \tag{3.70}$$

whereas for the matter perturbations we have

$$\begin{cases} \delta\rho_a^{(gi)} & \equiv & \delta\rho_a + \bar{\rho}_a'\,(B - E') \\ \delta P_a^{(gi)} & \equiv & \delta P_a + \bar{P}_a'\,(B - E') \end{cases} . \tag{3.71}$$

Here, the *primes* indicate differentiation with respect to conformal time η. Notice that these are only scalar perturbations, as they are the ones we are interested. Otherwise, we would also need to find vector-invariant perturbations.

We could proceed by deriving equations for the invariant perturbations defined in the previous equations. However, we can significantly reduce the manual work involved by fixing the gauge. The preferred gauge for studying structure formation is the Newtonian gauge, for which $B = E = 0$. In this gauge, we then have $\Phi_{\rm B} \equiv \Phi$, $\Psi_{\rm B} \equiv \Psi$, $\delta\rho_a^{(gi)} \equiv \delta\rho_a$, and $\delta P_a^{(gi)} \equiv \delta P_a$. Consequently, the perturbed RW metric in Eq. (3.64) takes the form

$$ds^2 = a^2\left[-(1 + 2\Phi)d\eta^2 + (1 + 2\Psi)\,\delta_{ij}dx^i dx^j\right] , \tag{3.72}$$

which is the same as that obtained from the Newtonian limit, where Φ represents the Newtonian gravitational potential.

3.5.4 Perturbed equations

Once the fluctuations have been characterized, we can derive the fluid equations in the Newtonian gauge. The energy-momentum conservation, $\nabla^\mu \delta T^a_{\mu\nu} = 0$, leads to:

1. The linearized continuity equation ($\nu = 0$):

$$\delta' = -\left(1 + \frac{\bar{P}}{\bar{\rho}}\right)\left(\partial^i v_i - 3\Phi'\right) - 3\mathcal{H}\left(\frac{\delta P}{\delta\rho} - \frac{\bar{P}}{\bar{\rho}}\right)\delta\,, \tag{3.73}$$

2. The linearized Euler equation ($\nu = i$):

$$v_i' = -\left(\mathcal{H} + \frac{\bar{P}'}{\bar{\rho} + \bar{P}}\right) v_i - \frac{(\partial_i \delta P - \partial^j \Pi_{ij})}{\bar{\rho} + \bar{P}} - \partial_i \Psi\,. \tag{3.74}$$

These equations, which describe the evolution of a specific species a (the subscript has been omitted here to avoid overloading the notation), must be solved together under appropriate initial conditions.

Next, the mathematical relations between the perturbations are derived from the linearized Einstein equations $\delta G_\mu^\nu = 8\pi G \delta T_\mu^\nu$, yielding

$$\begin{aligned}
\nabla^2\Psi - 3\mathcal{H}\left(\Psi' + \mathcal{H}\Phi\right) &= 4\pi G a^2 \bar{\rho}\delta\,, & (3.75)\\
-\left(\Psi' + \mathcal{H}\Phi\right) &= 4\pi G a \delta q\,, & (3.76)\\
\Psi - \Phi &= 8\pi G a^2 \Pi\,, & (3.77)\\
\Psi'' + \mathcal{H}\Phi' + 2\mathcal{H}\Psi' - \frac{1}{3}\nabla^2\left(\Psi - \Phi\right) + \left(2\mathcal{H}' + \mathcal{H}^2\right)\Phi &= 4\pi G a^2 \delta P\,, & (3.78)
\end{aligned}$$

where $\delta q \equiv \left(\bar{\rho} + \bar{P}\right) v$ represents the momentum density perturbations. Eqs. (3.75) and (3.76) can be combined to derive the Poisson equation $\nabla^2\Psi = 4\pi G a^2 \bar{\rho}\delta_{\rm com}$, with $\bar{\rho}\delta_{\rm com} \equiv \bar{\rho}\delta - 3\mathcal{H}\delta q$, where $\delta_{\rm com}$ is the comoving density contrast. On the other hand, if no anisotropic stress is observed ($\Pi = 0$), Eq. (3.77) implies that $\Psi = \Phi$, and Eq. (3.78) simplifies to

$$\Phi'' + 3\mathcal{H}\Phi + \left(2\mathcal{H}' + \mathcal{H}^2\right)\Phi = 4\pi G a^2 \delta P\,. \tag{3.79}$$

These linearized Einstein equations must be supplemented by the continuity and Euler equations, leading to a system of coupled differential equations.

3.6 Structure formation

Every structure in the universe essentially grew from the gravitational instability. Following the initial conditions set by cosmic inflation, cosmological perturbations were established in the primordial universe and evolved over time according to the dominant content: first during the RD era, then the MD era, and finally the ΛD era. These fluctuations consist of overdensity and underdensity regions, initially on the order of $\delta \sim 10^{-4}$. The overdensity regions eventually accumulated enough matter and evolved into galaxies, clusters, superclusters, and so on, whereas the underdensity regions lost material to the overdensity regions, forming vast voids. Two counteracting effects were crucial in triggering this matter clustering process: (*i*) the background expansion, which tends to drag particles of all species apart, and (*ii*) the internal pressure due to highly interacting photons and baryons, causing the gas to move toward lower pressure regions. Since at very early times the high energy of the photons prevented baryons from grouping together, a single type of CDM, which does not interact with light, managed to cluster, forming a cosmic web. Once photon-baryon interactions dropped enough for gravity to overcome pressure, the baryons began to accumulate in the DM nodes. This process was further enhanced when baryons were released from photons influence after decoupling, particularly taking off during the MD era.

In order to understand the process of structure formation over time, we need to distinguish between two separated regimes: super-horizon ($k/\mathcal{H} \ll 1$) and sub-horizon ($k/\mathcal{H} \gg 1$) scales. It is important to note that the horizon referred to here, specifically the Hubble horizon, is not a horizon in the traditional sense [154]. In the standard HBB scenario, adiabatic fluctuations were initially frozen outside the horizon, where no significant dynamics occurred. As the horizon evolved, each perturbation mode k crossed the horizon when $k = \mathcal{H}$; some did so during the RD era (small scales) and others during the MD er (large scales), resulting in the formation of small and large structures, respectively. Ultimately, the structure formation process is suppressed in the current ΛD epoch.

3.6.1 Super-horizon (non-)evolution

Following the initial conditions, all perturbations remain frozen outside the Hubble horizon. This behavior is evident through the analysis of the curvature and comoving curvature perturbations,

$$\zeta \equiv -\Psi - \frac{\mathcal{H}}{\bar{\rho}'}\delta\rho \tag{3.80}$$

and

$$\mathcal{S} \equiv \Psi - \frac{\mathcal{H}}{\bar{\rho} + \bar{P}}\delta q\,, \tag{3.81}$$

respectively. Both curvature perturbations are gauge-invariant. Therefore, the energy conservation in Eq. (3.73) can be rewritten in terms of ζ as

$$\zeta' = -\mathcal{H}\frac{\delta P_{\rm nad}}{\bar{\rho} + \bar{P}} - \mathcal{Z}\,, \tag{3.82}$$

where

$$\frac{\mathcal{Z}}{\mathcal{H}} = -\frac{k^2}{3\mathcal{H}^2}\left[\zeta + \Psi - \frac{k^2}{\mathcal{H}^2}\frac{2\bar{\rho}}{9\left(\bar{\rho} + \bar{P}\right)}\right]\,. \tag{3.83}$$

For purely adiabatic perturbations ($\delta P_{\rm nad} = 0$) on super-Hubble scales, we find that $\zeta' \approx 0$, meaning $\zeta \approx$ *constant*. Since $\mathcal{S} = -\zeta$ for $k/\mathcal{H} \ll 1$, we conclude that $\mathcal{S}$ is also nearly constant on super-Hubble scales. As we will see, the initial conditions established by an inflationary phase are predominantly adiabatic.

3.6.2 Adiabatic perturbations

Simple inflation models predict that primordial fluctuations are adiabatic. This implies that the local state of matter at a given spacetime event (η, x^i) in the perturbed universe corresponds to the background state at a slightly different time, $\eta + \delta\eta\,(x^i)$. For a given species a, the adiabatic density and pressure perturbations are defined

as:

$$\delta\rho_a\left(\eta, x^i\right) \equiv \bar{\rho}_a\left(\eta+\delta\eta\right) - \bar{\rho}_a = \bar{\rho}_a'\delta\eta\,, \tag{3.84}$$

$$\delta P_a\left(\eta, x^i\right) \equiv \bar{P}_a\left(\eta+\delta\eta\right) - \bar{P}_a = \bar{P}_a'\delta\eta\,. \tag{3.85}$$

Since $\delta\eta$ is the same for all species, it follows that

$$\delta\eta = \frac{\delta\rho_a}{\bar{\rho}_a'} = \frac{\delta\rho_b}{\bar{\rho}_b'}\,, \quad \frac{\delta P_a}{\bar{P}_a} = \frac{\delta\rho_a}{\bar{\rho}_a}\,. \tag{3.86}$$

Using $\bar{\rho}_a' = -3\mathcal{H}\left(1+w_a\right)\bar{\rho}_a$, $\delta_a \equiv \delta\rho_a/\bar{\rho}_a$, and $c_{\mathrm{s},a}^2 \equiv \bar{P}_a/\bar{\rho}_a$, we can express the relations in Eq. (3.86) as

$$\frac{\delta_a}{1+w_a} = \frac{\delta_b}{1+w_b}\,, \quad \delta P_a = c_{\mathrm{s},a}^2\delta\rho_a\,, \tag{3.87}$$

where w_a and $c_{\mathrm{s},a}^2$ are the EoS parameter and sound speed for species a, respectively. Thus, for adiabatic perturbations in a mixture of non-relativistic matter ($w_{\mathrm{m}} = 0$) and radiation ($w_{\mathrm{r}} = 1/3$), we shall have

$$\delta_{\mathrm{m}} = \frac{3}{4}\delta_{\mathrm{r}}\,. \tag{3.88}$$

During the RD era, $c_{\mathrm{s},a}$ is the speed of light, while in the MD era, it is the speed of sound. Since all δ_a's are comparable, the species with the dominant energy density, $\bar{\rho}_a$, dictates the total density perturbation, $\delta\rho \equiv \sum_a \bar{\rho}_a\delta_a$.

3.6.3 Contrast equation and growth rate

In the process of structure formation, the evolution of initial adiabatic perturbations is governed by the balance between gravitational collapse, cosmic expansion, and gas scattering effects. However, only perturbations in DM are significant for structure growth [79, 80, 82]. In this way, we need to derive a differential equation for the matter density contrast δ_{m} incorporating each one of these elements.

On sub-horizon scales, the Newtonian approximation can be used to derive such a differential equation. However, the Newtonian description breaks down on scales comparable to or larger than the Hubble radius, as well as for relativistic fluids like photons and neutrinos. In these cases, a fully general-relativistic approach, as outlined in Section 3.5, is required for accurate modeling.

By combining the relativistic Poisson, continuity, and Euler equations obtained in Section 3.5, we derive the following differential equation for the matter contrast:

$$\ddot{\delta}_{\mathrm{m}} + 2H\dot{\delta}_{\mathrm{m}} - c_{\mathrm{s}}^2\left(\frac{1}{a^2}\nabla^2 + \frac{4\pi G\bar{\rho}_{\mathrm{m}}}{c_{\mathrm{s}}^2}\right)\delta_{\mathrm{m}} = 0\,, \tag{3.89}$$

describing how the matter fluctuations evolve over time in an expanding spacetime. This equation is a wave equation, characterized by second-order derivatives in both time, $\ddot{\delta}_{\rm m}$, and space $(c_{\rm s}/a)^2\,\nabla^2\delta_{\rm m}$. It also includes a friction-like term, $2H\dot{\delta}_{\rm m}$, due to expansion and a gravity term $(4\pi G\bar{\rho}_m/c_{\rm s}^2)\delta_{\rm m}$. In the MD epoch, the pressure term can be neglected as $c_{\rm s}\to 0$, simplifying the contrast equation to

$$\ddot{\delta}_{\rm m} + 2H\dot{\delta}_{\rm m} - 4\pi G\bar{\rho}_{\rm m}\delta_{\rm m} \simeq 0\,. \tag{3.90}$$

This is the key equation describing how the inhomogeneities evolved from the MD era to the present, according to FLRW cosmology. Its solution can be split into two modes: an increasing mode, δ_+, and a decreasing mode, δ_-. The first one determines how matter clumps together, while the second one vanishes with time.

To quantify how rapidly structures grow, we define the growth function

$$f_{\rm g}(a) \equiv \frac{d\ln\delta_{\rm m}(a)}{d\ln a}\,. \tag{3.91}$$

A widely used parameterization of this function is given by [170]

$$f_{\rm g}(a) \simeq \Omega_{\rm m}^{\gamma}\,, \tag{3.92}$$

where γ is known as the growth index. The growth index γ is typically constant in many cosmological models based on GR. In the ΛCDM model, for example, $\gamma\simeq 0.55$. In contrast, γ can vary over time in modified theories such as $f(R)$ gravity [171].

The growth function, or growth rate, $f_g(a)$, consist in a very important quantity to discriminate between different cosmological models. It can be inferred directly via RSD observations. As we will see, $f_{\rm g}$ also depends on the scale of perturbations, k, in many alternative theories, particularly in $f(R)$ gravity.

Another observational quantity related to matter fluctuations, both in the early (CMB) and late (LSS) universe, is the *root mean square* of matter fluctuations at physical scale $\mathcal{R}$, denoted by $\sigma_{\mathcal{R}}(a)$. It is defined as [80]

$$\sigma_{\mathcal{R}}(a) \equiv \frac{1}{2\pi^2}\int_0^\infty dk\,k^2\mathcal{P}_{\rm m}(k,a)\mathcal{W}^2(k\mathcal{R})\,, \tag{3.93}$$

where $\mathcal{P}_{\rm m}$ is the matter power spectrum and $\mathcal{W}$ is a *window function* for $\sigma_{\mathcal{R}}$. Since cosmological observations are often performed at the physical scale corresponding to $\mathcal{R}=8\,{\rm Mpc}/h$, the value $\sigma_{8,0}\equiv\sigma_8(a_0)$ is commonly used to denote the root mean square of matter fluctuations today.

Current constraints on the strength of matter clustering are performed using the parameter $S_8\equiv\sigma_{8,0}\sqrt{\frac{\Omega_{\rm m,0}}{0.3}}$, rather than $\sigma_{8,0}$ alone. Anyway, recent observations from early and late universe show a tension in the S_8 measurements at $2-3\sigma$ CL [114].

Let us consider the following measurements on the flat-ΛCDM basis:

- $S_8^{\rm LSS} = 0.776 \pm 0.017$ at 68% CL [172] and
- $S_8^{\rm Planck} = 0.832 \pm 0.013$ at 68% CL [88],

performed by the DES and Planck collaborations, respectively. See Refs. [173–175] for additional S_8 measurements.

Given the growth rate, $f_{\rm g}(a)$, and the amplitude of matter fluctuations, denoted by $\sigma_8(a)$, the product of these quantities yields the normalized growth rate

$$[f\sigma_8](a) = \frac{\sigma_{8,0}}{\delta_{\rm m,0}} \left[\frac{d\,\delta_{\rm m}(a)}{d\ln a} \right] , \tag{3.94}$$

where $\delta_{\rm m,0} \equiv \delta_{\rm m}(a_0)$. This combination is more commonly used than $f_{\rm g}(a)$ to derive constraints for model parameters, primarily due to the availability of data.

3.7 Primordial inflation

Primordial inflation, also known as cosmic inflation or even the initial conditions, refers to a postulated early stage of supraluminal expansion, where the scale factor grew exponentially, assumed to occur when the universe was around 10^{-34} s years old, immediately after the milestone of the Big Bang. The observed features of the late universe, such as flat three-space (the flatness problem), homogeneity in the spatial CMB temperature distribution (the horizon problem), and the absence of magnetic monopoles (the cosmic relics problem), unavoidably lead to a fine-tuning of the initial conditions following a FLRW cosmology. Furthermore, the HBB cosmology itself does not explains the physical mechanism responsible for generating cosmological perturbations (the structure formation problem) in the early universe, which later evolved into the various structures observed today. Thus, cosmic inflation is added to address the puzzles posed by HBB cosmology [176].

It must be emphasized that both the flatness and horizon problems are not strict inconsistencies in the HBB model. If we assume that the total density $\Omega(t)$ was initially exceedingly close to unity and that the universe began homogeneously over super-Hubble scales (while having just the right amount of inhomogeneity to account for structure formation), it will continue to evolve as flat and uniform. However, these assumptions imply a highly unlikely scenario for the late universe, realizable only under very specific initial conditions [177]. To allow the current universe to emerge from arbitrary initial conditions and to provide a fundamental physics explanation for primordial fluctuations, cosmic inflation was proposed around the 1980s [48, 178, 179].

3.7.1 HBB issues

Let us now briefly introduce each of the questions posed by HBB aforementioned, namely: (*i*) the flatness problem, (*ii*) the horizon problem, (*iii*) the cosmic relics problem, and (*iv*) the primordial fluctuations problem.

Flatness problem

First, we observe that setting $\Omega_0 = 1$ in the Friedmann equation, rewritten as

$$\Omega(t) - 1 = \Omega_{\rm K}(t)\,, \tag{3.95}$$

is an unstable situation, as $\Omega_{\rm K}(t) \equiv -K/\mathcal{H}^2(t)$ and the comoving Hubble radius $\mathcal{H}^{-1}(t) = [a(t)H(t)]^{-1}$ is a monotonically increasing function over time. Strictly speaking, we should have

$$|\Omega(t_{\rm BBN}) - 1| \lesssim 10^{-16}\,, \tag{3.96}$$

$$|\Omega(t_{\rm GUT}) - 1| \lesssim 10^{-55}\,, \tag{3.97}$$

$$|\Omega(t_{\rm Pl}) - 1| \lesssim 10^{-61}\,, \tag{3.98}$$

where $t_{\rm BBN} \approx 3\,{\rm min}$ corresponds to the time of BBN, $t_{\rm GUT} \sim 10^{-33}\,{\rm s}$ to the Grand Unified Theory (GUT) era, and $t_{\rm Pl} \sim 10^{-43}\,{\rm s}$ to the Planck time. Eq. (3.95) implies that any deviation from these values during their respective epochs would result in $\Omega_{\rm K}$ being significantly different from zero today.

Horizon problem

Secondly, calculations of the particle horizon angular radius using a flat-FLRW cosmology,

$$\theta_{\rm p} = \frac{\sqrt{\Omega_{\rm m,0}\,a + \Omega_{\rm r,0}} - \sqrt{\Omega_{\rm r,0}}}{\sqrt{\Omega_{\rm m,0} + \Omega_{\rm r,0}} - \sqrt{\Omega_{\rm m,0} + \Omega_{\rm r,0}}}\,, \tag{3.99}$$

where $\theta_{\rm p} \equiv d_{\rm p}/d_\alpha$, give $\theta_{\rm p}\,(t_{\rm rec}) \approx 0.017$, corresponding to an angular separation of approximately 1° in the CMB at recombination. This implies a total of around 10^4 causally disconnected regions in the CMB sky at recombination. As a result, there would be no physical reasons for the uniformity in the temperature distribution of the CMB on angular scales larger than 1°.

Cosmic relics problem

The successive spontaneous symmetry breaks that occurred in the early universe would have generated several topological defects via the *Kibble mechanism* [180]. Most of these vacuum configurations are highly stable and fall into three categories: magnetic monopoles (point-like), cosmic strings (one-dimensional), and domain

walls (two-dimensional). Hybrid defects from two or three categories, as well as non-topological configurations, are also possible. Given that the energy scale associated with the GUT era is around $10^{16}\,\mathrm{GeV}$, while the rest energy of most massive particles (e.g., neutrons and protons) is around $1\,\mathrm{GeV}$, a large number of these massive topological defects should have formed, making them potentially observable today. However, none of these relic particles have been observed to date.

Structure formation problem

CMB and LSS observations confirm the existence of small inhomogeneities in the early universe, which are expected to evolve into present cosmic structures. However, the standard HBB cosmology does not provide a physical mechanism for generating the primordial curvature perturbations $\mathcal{S}$, or ζ, which are later converted into both metric (Φ) and matter (δq) fluctuations.

3.7.2 Inflationary dynamics

It is well known that an accelerated expansion phase can be driven by a scalar field that dominates the energy density of the universe. Scalar fields are fundamental ingredients of the particle physics, representing spin-zero particles, and are often associated with symmetry breaking, such as those in GUT, supersymmetry, and others. The most famous example is the Higgs field, which breaks the electroweak symmetry. Its existence was first theorized in 1964 by P. Higgs and five other physicists [181–183], and confirmed in 2013 at the LHC at CERN [184]. P. Higgs and F. Englert were awarded the 2013 Nobel Prize in Physics for predicting the existence of both the Higgs field and Higgs boson.

The simplest model of inflation involves a homogeneous single scalar field $\varphi(t)$, called the *inflaton*, minimally coupled with gravity and characterized by its potential $V(\varphi)$. Such a theory is described by the action [81]

$$S_\varphi = \int d^4x\sqrt{-g}\left[\frac{1}{2\kappa^2}R + \frac{1}{2}g^{\mu\nu}\partial_\mu\varphi\partial_\nu\varphi - V(\varphi)\right], \tag{3.100}$$

Notice that the first term on the right-hand side corresponds to the usual Einstein-Hilbert Lagrangian, $\mathcal{L}_{\mathrm{EH}}$ (by setting $\Lambda = 0$), while the remaining two terms are associated with the inflaton field φ.

Assuming a spatially flat space and a perfect fluid, the energy-momentum tensor corresponding to the extra scalar field, φ, is described by

$$T^{(\varphi)}_{\mu\nu} = -\frac{2}{\sqrt{-g}}\frac{\delta S_\varphi}{\delta g^{\mu\nu}} = \partial_\mu\varphi\partial_\nu\varphi - g_{\mu\nu}\left[\frac{1}{2}\partial_\rho\varphi\partial^\rho\varphi + V(\varphi)\right]. \tag{3.101}$$

For an homogeneous field configuration ($\nabla^2\varphi = 0$), this leads to

$$\rho_\varphi = \frac{1}{2a^2}\left(\varphi'\right)^2 + V(\varphi)\,, \tag{3.102}$$

$$P_\varphi = \frac{1}{2a^2}\left(\varphi'\right)^2 - V(\varphi)\,. \tag{3.103}$$

Hence, the EoS for the inflaton is

$$w_\varphi = \frac{P_\varphi}{\rho_\varphi} = \frac{\left(\varphi'/\sqrt{2}a\right)^2 - V(\varphi)}{\left(\varphi'/\sqrt{2}a\right)^2 + V(\varphi)}\,. \tag{3.104}$$

By replacing both the energy density and pressure given in Eq. (3.102) and (3.103), respectively, into Eq. (3.50), we obtain the Friedmann equation in conformal time,

$$\mathcal{H}^2 = \frac{\kappa^2}{3}\left[\frac{1}{2}\left(\varphi'\right)^2 + a^2V(\varphi)\right]\,. \tag{3.105}$$

Next, the energy-momentum conservation, expressed as $\nabla^\mu T^{(\varphi)}_{\mu\nu} = 0$, leads to the Klein-Gordon equation,

$$\varphi'' + 2\mathcal{H}\varphi' + a^2V_{,\varphi}(\varphi) = 0\,, \tag{3.106}$$

where we have defined $V_{,\varphi} \equiv dV/d\varphi$. Eq. (3.105) describes the expanding universe as being dominated by a homogeneous scalar field, $\varphi(t)$, whose dynamics is determined by Eq. (3.106). Additionally, we can see from the acceleration equation (3.59) that the condition for inflation, $\ddot{a} = \mathcal{H}'/a > 0$, requires $\left(\varphi'/a\right)^2 < V(\varphi)$.

3.7.3 Slow-roll approximation

A dynamical homogeneous scalar field φ can trigger an era of accelerated expansion without spoiling the HBB successes only if its potential $V(\varphi)$ is sufficiently flat, i.e., $\left(\varphi'/a\right)^2 \ll V$ and $|\varphi''| \ll 2\mathcal{H}\varphi'$. These conditions are known as the *slow-roll* conditions [176, 177], which give us the approximation

$$2\mathcal{H}\varphi' \simeq -a^2V_{,\varphi}\,, \tag{3.107}$$

$$\mathcal{H}^2 \simeq \frac{\kappa^2}{3}a^2V\,, \tag{3.108}$$

In this case, the dynamics of inflation can be expressed in terms of the first two slow-roll parameters, defined ass [176]

$$\epsilon_V \equiv \frac{1}{2\kappa^2}\left(\frac{V_{,\varphi}}{V}\right)^2\,, \quad \eta_V \equiv \frac{1}{\kappa^2}\left(\frac{V_{,\varphi\varphi}}{V}\right)\,. \tag{3.109}$$

To effectively reach the slow-roll approximation, we must have $\epsilon_V \ll 1$ and $|\eta_V| \ll 1$, i.e., $V_{,\varphi}, V_{,\varphi\varphi} \ll V$, for a significant period of time. The inflationary phase ends when ϵ_V and η_V grow to order unity, thereby violating the slow-roll conditions.

Often, the scale factor at any instant between the beginning and end of inflation is computed in terms of the number of e-folds remaining before the end of the inflation, defined as

$$N \equiv \ln\left(\frac{a_{\rm end}}{a}\right) = \int_{\varphi_{\rm end}}^{\varphi} \frac{d\varphi}{\sqrt{2\epsilon_V}}\,, \tag{3.110}$$

where $\varphi_{\rm end}$ is the value of the scalar field at the end of the inflation. This quantity measures the amount of physical expansion during inflation. The Planck collaboration assumes an uncertainty of $50 < N_* < 60$ for a pivot scale $k_* = 0.002\,{\rm Mpc}^{-1}$, which has proven sufficient to solve the main HBB puzzles [185].

3.7.4 Primordial power spectrum

The inflaton field is assumed to have quantum fluctuations on the order of the Planck length, such that

$$\varphi(\eta, x^i) = \bar{\varphi}(\eta) + \delta\varphi(\eta, x^i)\,, \tag{3.111}$$

where $\bar{\varphi}$ corresponds to the homogeneous background value, which depends only on time, and $\delta\varphi$ describes small fluctuations around $\bar{\varphi}$ that may also depend on the spatial coordinates x^i. Once more, we will exclusively examine linear perturbations.

In this way, the perturbed energy density, pressure, and momentum density for the inflaton are given by

$$\delta\rho_\varphi = a^{-2}\left[\bar{\varphi}'\left(\delta\varphi' - \bar{\varphi}'\Phi\right) + a^2 V_{,\varphi}\delta\varphi\right]\,, \tag{3.112}$$

$$\delta P_\varphi = a^{-2}\left[\bar{\varphi}'\left(\delta\varphi' - \bar{\varphi}'\Phi\right) - a^2 V_{,\varphi}\delta\varphi\right]\,, \tag{3.113}$$

$$\delta q_\varphi = -a^{-2}\bar{\varphi}'\delta\varphi\,. \tag{3.114}$$

The relevant gauge-invariant quantity here is defined as

$$\xi \equiv \delta\varphi + \frac{\bar{\varphi}'}{\mathcal{H}}\Psi\,. \tag{3.115}$$

Therefore, the energy-moment conservation leads to the perturbed Klein-Gordon equation [176],

$$\xi'' + 2\mathcal{H}\xi' + k^2\xi + a^2\left[V_{,\varphi\varphi} - \frac{\kappa^2}{a^2}\left(\frac{a^2\bar{\varphi}'^2}{\mathcal{H}}\right)'\right]\xi = 0\,, \tag{3.116}$$

where k^2 corresponds to the eigenvalues of the Laplacian operator via $\nabla^2\xi = -k^2\xi$.

Eq. (3.116) can be solved using the Mukhanov-Sasaki method [165, 186], which

allows us to find $\xi(k)$. Such a solution is useful for obtaining the primordial power spectrum [176],

$$\mathcal{P}_\xi(k) \equiv \frac{4\pi k^3}{(2\pi)^3}|\xi(k)|^2 \simeq \begin{cases} (k/2\pi a)^2 \,, & \text{for } k \gg \mathcal{H} \\ (\mathcal{H}/2\pi)^2 \,, & \text{for } k \ll \mathcal{H} \end{cases} . \tag{3.117}$$

Quantum fluctuations generated during a slow-roll inflationary stage are expected to be nearly Gaussian. Therefore, the primordial power spectrum above contains all of information about the distribution of fluctuations.

Single-field slow-roll inflation is expected to generate a nearly scale-invariant spectrum of scalar fluctuations, given by

$$\mathcal{P}_\xi = A_\xi \left(\frac{k}{k_*}\right)^{n_\xi - 1} \approx A_\xi \,. \tag{3.118}$$

A scale-invariant spectrum ($n_\xi = 1$), meaning constant variation across all length scales, is known as the Harrison-Zel'dovich spectrum. Inflation should also have produced primordial gravitational waves (PGWs), which affect the B-modes of CMB polarization. These tensor fluctuations are related to scalar modes through the tensor-to-scalar ratio, $r_{\rm inf} = (\bar{\varphi}'/\mathcal{H})^2 \, (\mathcal{P}_{\rm T}/\mathcal{P}_\xi)$, where $\mathcal{P}_{\rm T}$ is the primordial tensor power spectrum [176].

3.7.5 HBB issues revisited

We are now ready to demonstrate how an early inflationary period resolves each of the previously raised HBB problems. First, we recall that the slow-roll conditions require the inflaton potential $V(\varphi)$ to be sufficiently flat to maintain the successes of the HBB model, starting from BBN. This implies that $V(\varphi)$ must remain nearly constant throughout much of the inflation. As a result, the Hubble rate,

$$H = \frac{\mathcal{H}}{a} \simeq \left(\frac{\kappa^2 V}{3}\right)^{1/2} , \tag{3.119}$$

is also approximately constant. By integrating this equation, we obtain the solution

$$a(t) \approx a_{\rm end} \, e^{H(t - t_{\rm end})} \,, \tag{3.120}$$

telling that the scale factor a evolves exponentially, while H remains quasi-constant, resembling a de Sitter universe. Such a similarity is evident because $(\varphi'/a)^2 \ll V$ results in an EoS parameter $w_\varphi \approx -1$, which is similar to that of the cosmological constant.

Flatness problem

Assuming $|\Omega_K| \sim 1$ at the beginning of inflation and using solution in Eq. (3.120), Eq. (3.95) becomes

$$|\Omega - 1| \approx \frac{1}{(a_{\rm end}H)^2}\, e^{-2H(t-t_{\rm end})}\,. \tag{3.121}$$

Notice that this expression tends to zero as $t \to \infty$, indicating that any curvature present in the early universe was eliminated by the exponential expansion during inflation.

Horizon problem

By substituting the solution in Eq. (3.120) into Eq. (3.31), we obtain the following expression for the particle horizon, in units where $c = 1$,

$$d_{\rm p}(t) = \frac{1}{H}\left[e^{H(t-t_{\rm end})} - 1\right]\,. \tag{3.122}$$

This means that, during inflation, the particle horizon grows exponentially, while the Hubble horizon $r_{\rm H} \approx H^{-1}$ remains approximately constant. Hence, regions that are not in causal contact today could have been causally connected before inflation.

Cosmic relics problem

Since the energy density of massive particles decreases more rapidly as $\rho \propto a^{-3}$, the sudden expansion of the scale factor suppresses the energy density as $\rho \propto \exp\left[-3H\left(t - t_{\rm end}\right)\right]$ for any relic particle produced at least 20 e-folds before the end of inflation. As a result, an inflationary period caused magnetic monopoles, predicted by certain spontaneously broken gauge theories, to effectively disappear from the universe.

Structure formation problem

Primordial fluctuations are necessary for gravitational instability to lead to structure formation. Let us recall the gauge-invariant definition of the inflationary field perturbation, ξ. By combining Eqs. (3.81), (3.102), (3.103), (3.114), and (3.115), we obtain

$$\mathcal{S} = \frac{\mathcal{H}}{\bar{\varphi}'}\xi\,. \tag{3.123}$$

The connection between the power spectra of ξ and $\mathcal{S}$ is given by

$$\mathcal{P}_{\rm s} = \left(\frac{\mathcal{H}}{\bar{\varphi}'}\right)^2 \mathcal{P}_\xi\,, \tag{3.124}$$

Symbol	Parameter	Type	Planck18 Constraints
$\Omega_{\rm b}$	baryon density	background	$\Omega_{\rm b}h^2 = 0.0224 \pm 0.0001$
$\Omega_{\rm c}$	DM density	background	$\Omega_{\rm c}h^2 = 0.120 \pm 0.001$
$\theta_{\rm MC}$	acoustic angular scale	background	$100\theta_{\rm MC} = 1.0419 \pm 0.0003$
$\tau_{\rm re}$	optical depth	background	$\tau = 0.054 \pm 0.007$
$A_{\rm s}$	spectral amplitude	inflation	$\ln(10^{10}A_{\rm s}) = 3.044 \pm 0.014$
$n_{\rm s}$	spectral index	inflation	$n_{\rm s} = 0.965 \pm 0.004$

Table 3.2: The six primary parameters of the flat-ΛCDM concordance model, as determined by the Planck collaboration [88, 185].

where the corresponding spectral index is

$$\mathcal{P}_{\rm s} = A_{\rm s}\left(\frac{k}{k_*}\right)^{n_{\rm s}-1} . \tag{3.125}$$

In this way, the comoving curvature perturbation $\mathcal{S}$, or the potential Φ, emerges from inflaton quantum fluctuations ξ. Ultimately, the perturbations ξ was stretched by inflation and converted into $\mathcal{S}$ on super-Hubble scales, where they remained frozen and eventually seeded the structure formation. After inflation, the universe underwent a brief period of reheating, during which the inflaton particles are converted into radiation, allowing the universe's dynamics to follow the FLRW cosmology.

3.8 Flat-ΛCDM model and observations

The models we have discussed so far, based on GR, the cosmological principle, and the RW metric, are known as FLRW, or HBB, cosmologies. In order to align with a wide range of astronomical observations, FLRW models need to assume the existence of non-baryonic dark matter, late-time dark energy, and initial conditions established by primordial inflation. Depending on the specific models for dark matter and dark energy, inflationary scenario, and spatial curvature assumed, cosmological models may involve seven or more free parameters.

The flat-ΛCDM model represents a particular case of FLRW cosmologies, defined by three key assumptions: (*i*) dark energy corresponds to a cosmological constant, (*ii*) dark matter is cold, and (*iii*) the spatial geometry is flat. If we also consider a single-field slow-roll inflation to set the initial conditions, we arrive at the standard model of cosmology (SMC). This model consists of six independent parameters, known as primary parameters (see Table 3.2), used by fitting the CMB primordial power spectrum (see Figure 3.10). Other cosmological parameter, such as H_0, $\Omega_{\rm m,0}$, and Ω_Λ, referred to as secondary parameters, can be derived from the six primaries combined with other observational data. Since the flat-ΛCDM model provides the best fit to a wide range of observations, it is often called the concordance model.

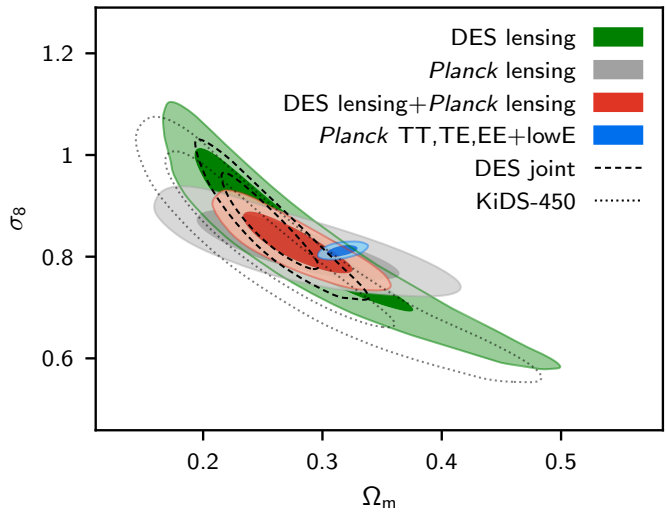

Figure 3.14: 68% and 95% constraints on the $\Omega_m - \sigma_8$ plane from DES lensing [187] (green), Planck CMB lensing (grey), joint lensing (red), Planck CMB anisotropies (blue) DES cosmic shear plus galaxy clustering [188] (dashed), and KiDS-450 [189] (dotted) in the base-ΛCDM [88].

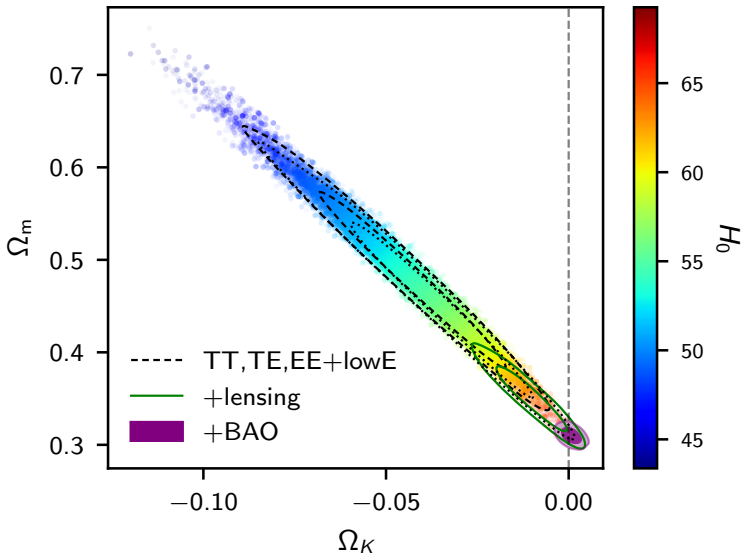

Figure 3.15: Curvature constraints in the ΛCDM+Ω_K extension from Planck CMB anisotropies (dashed lines), lensing (green lines), and BAO (purple filled contour) datasets. Note that a flat spatial three-section can only be confirmed after adding the BAO data [88].

In the last column of Table 3.2, we present the most recent measurements from the Planck collaboration for each of the primary parameters in the base-ΛCDM. These values are widely regarded in the literature as the most stringent cosmological constraints to date. Additionally, Planck provides remarkable restrictions on secondary parameters, including the most relevant ones:

- the total mater density $\Omega_{\mathrm{m},0} = 0.315 \pm 0.007$,
- the vacuum density $\Omega_{\Lambda} = 0.685 \pm 0.007$,
- the matter fluctuation amplitude $\sigma_{8,0} = 0.811 \pm 0.006$, and
- the age of the universe $t_0\,[\mathrm{Gyr}] = 13.797 \pm 0.023$,

all at 68% CL [88]. Figure 3.14 shows the superior precision of Planck's constraints compared to those from DES [187, 188] and KiDS [189] collaborations.

Let us now examine the simpler extension of the flat-ΛCDM model containing just one extra free parameter: the curvature density today, $\Omega_{\mathrm{K},0}$. This extension is referred to as ΛCDM+Ω_{K}. In this case, Planck 2018 TT,TE,EE+lowE+lensing data yields $\Omega_{\mathrm{K},0} = -0.0106 \pm 0.0065$ at 68% CL. However, when incorporating BAO observations, this value changes significantly to $\Omega_{\mathrm{K},0} = 0.0007 \pm 0.0019$, confirming an effectively Euclidean universe at 68% CL [88] (see Figure 3.15).

The second simpler extension of the flat-ΛCDM model considers DE as an additional degree of freedom, with $w_{\mathrm{DE}} \equiv w$ as a free parameter, referred to as wCDM. In this case, Planck 2018 data combined with SNe and BAO yield $w = -1.03 \pm 0.03$, consistent with $w_{\Lambda} = -1$ from ΛCDM [88].

A two-parameter dynamic DE model characterized by $w_{\mathrm{DE}}(a) = w_0 + w_a(1-a)$, where w_0 and w_a are assumed to be constants, is often tested. This relation is known as the CPL parameterization [22, 23], leading to the w_0w_aCDM extensions. For this model, Planck 2018, SNe, and BAO data provide $w_0 = -0.957 \pm 0.080$ and $w_a = -0.29^{+0.32}_{-0.26}$, also consistent with the flat-ΛCDM model [88].

Regarding primordial inflation, Planck also investigated the scale dependence of the primordial spectral index and the relative amplitude of PGWs. They obtained $dn_{\mathrm{s}}/d\ln k = -0.0045 \pm 0.0067$ at 68% CL from TT,TE,EE+lowE+lensing data, and $r_{0.002} < 0.10$ at 68% CL from TT,lowE, and lensing data. These results are consistent with a slow-roll inflationary period driven by a single scalar field, as described by the standard inflaton scenario [185].

Other astrophysical observations also constrained the cosmology as the Planck does. Utilizing data from galaxies, quasars, and Ly-α forest, the completed SDSS-IV eBOSS obtained $H_0 = (67.35 \pm 0.97)\,\mathrm{km\,s^{-1}\,Mpc^{-1}}$ and $r_{\mathrm{d}} = (149.3 \pm 2.8)\,\mathrm{Mpc}$ (from BBN+BAO data) [190], in good agreement with CMB data, both in the base-ΛCDM. In the perturbative level, the combined analysis from Planck 2018, SNe,

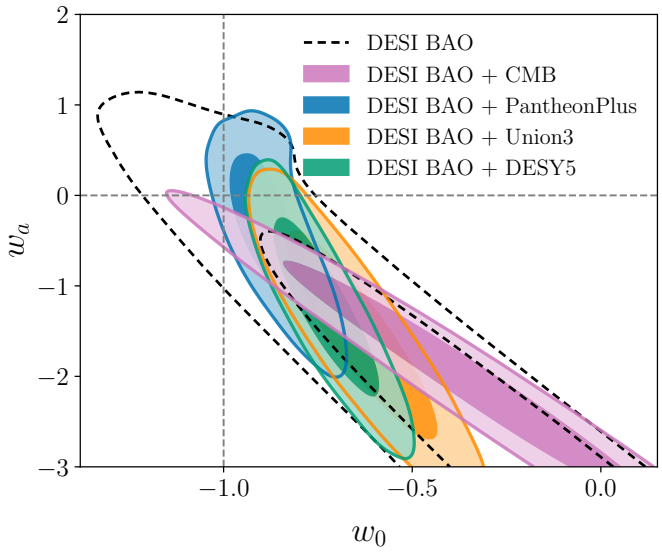

Figure 3.16: 68% and 95% marginalized posterior constraints in the $w_0 - w_a$ plane, considering the $w_0 w_a$CDM extension, from DESI BAO alone (black dashed), DESI+CMB (pink), DESI+Pantheon$^+$ [192] (blue), DESI+Union3 [193] (orange), and DESI+DESY5 [194] (green). The discrepancies with ΛCDM here are estimated to be $\gtrsim 2\sigma$ [195].

SDSS, BAO, RSD, and DES 3×2pt yielded $\sigma_{8,0} = 0.8073 \pm 0.0056$ [190]. This value is clearly in tension with the BOSS DR12 dataset combined with BBN prior, which provides $\sigma_{8,0} = 0.692^{+0.035}_{-0.041}$ [191].

The latest constraints on cosmology are due to BAO observations from the DESI DR1 BAO [196, 197]. In general, DESI DR1 BAO results conform to the flat-ΛCDM model, either alone:

$$\begin{cases} \Omega_{\mathrm{m},0} &= 0.295 \pm 0.015 \\ r_{\mathrm{d}} h &= (101.8 \pm 1.3)\,\mathrm{Mpc} \end{cases} \quad \text{at } 68\%\ \text{C.L.}\,, \tag{3.126}$$

or combined with a few other observables, for example:

$$\text{DESI+BBN+}\theta_* \begin{cases} \Omega_{\mathrm{m},0} &= 0.295 \pm 0.007 \\ H_0 &= (68.52 \pm 0.62)\,\frac{\mathrm{km}}{\mathrm{s\,Mpc}} \end{cases} \quad \text{at } 68\%\ \text{CL}\,, \tag{3.127}$$

and

$$\text{DESI+CMB} \begin{cases} \Omega_{\mathrm{m},0} &= 0.307 \pm 0.005 \\ H_0 &= (67.97 \pm 0.38)\,\frac{\mathrm{km}}{\mathrm{s\,Mpc}} \end{cases} \quad \text{at } 68\%\ \text{CL}\,. \tag{3.128}$$

For the two simpler extensions, ΛCDM+Ω_{K} and wCDM, the best constraints from the DESI collaboration indicate $\Omega_{\mathrm{K},0} = 0.0003^{+0.0048}_{-0.0054}$ for DESI BAO+BBN+θ_* and $w = -0.997 \pm 0.025$ for DESI+CMB+Pantheon$^+$, respectively. It confirms a flat

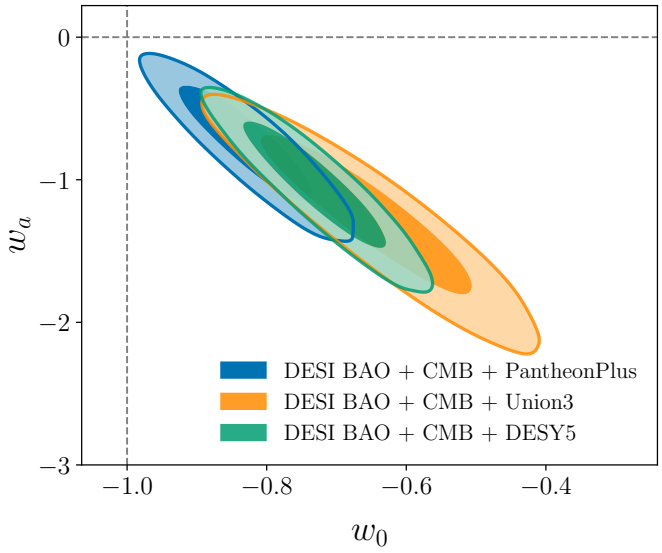

Figure 3.17: 68% and 95% marginalized posterior constraints in the $w_0 - w_a$ plane, considering the $w_0 w_a$CDM extension, from DESI+CMB+Pantheon$^+$ (blue), DESI+CMB+Union3 (orange), and DESI+CMB+DESY5 (green). The significance of the tension with ΛCDM is estimed to be 2.5σ, 3.5σ, and 3.9σ for these three cases, respectively [195].

geometry and a Λ-like DE at 68% CL. However, when the EoS is allowed to vary over time, as in the $w_0 w_a$CDM extension, DESI BAO data favor solutions with $w_0 > -1$ and $w_a < 0$, conflicting $(w_0, w_a) = (-1, 0)$ from ΛCDM. For DESI+CMB, they find $w_0 = -0.45^{+0.34}_{-0.21}$ and $w_a = -1.79^{+0.48}_{-1.00}$, indicating a tension of approximately 2.2σ. When incorporating SNe Ia information, the tension with ΛCDM: (*i*) remains at about 2.5σ for Pantheon$^+$ [192], (*ii*) increase to 3.5σ for Union3 [193], and (*iii*) reaches a maximum of 3.9σ for DESY5 [194, 197] (see figures 3.16 and 3.17).

Although the flat-ΛCDM model explains a wide range of observations effectively, many important observational inconsistencies need to be addressed: the Hubble (H_0) tension, the growth (S_8) tension, the lithium problem, CMB anisotropy anomalies, cosmic dipoles, low baryon temperature, the age of the universe, and other open questions (see Ref. [198] for a review). Currently, the most explored issues are the H_0 and S_8 tensions, along with those related to the dark sector. By far, the most serious problem with the SMC is the so-called vacuum catastrophe, in which the observed vacuum density ρ_Λ is on the order of $10^{60} - 10^{120}$ times smaller than what is expected from QFT. Part of the community considers these problems indicative of novel physics underlying the early stages of the universe, while a few attribute them to systematic effects or incomplete (astro)physical models. A minority believes that observational data may be biased by the assumption of a fiducial cosmology. Anyway, "*problems are opportunities*", and new scenarios beyond standard model deserve investigation, as there are compelling motivations for doing so.

Chapter 4

Modified Gravity and Cosmology

In this chapter, we discuss the formal foundations on which modified (or extended) theories of gravity rest, and we examine their role within the modern cosmological framework. We begin by presenting the primary motivations for modifying GR and outlining the criteria that an MTG must satisfy to be considered successful. Following this, we explore four widely discussed MTGs: the Brans-Dicke prototype theory and its extension to general scalar-tensor theories, higher-dimensional theories, and higher-order gravity. However, our main focus is on the so-called $f(R)$ theories, or $f(R)$ gravity, as this particular class of higher-order theories offers a possible explanation for the late-time acceleration of the universe without the need to invoke dark energy. Consequently, the majority of this chapter is dedicated to developing $f(R)$ gravity, its equivalence with scalar-tensor theories, its feasibility criteria, cosmological implications, and observational signatures.

4.1 Why modifying gravity?

GR theory provides an impressive description of gravity and matter, accurately describing regimes ranging from microscopic to intermediate astrophysical scales (e.g., Solar System and compact objects). Unlike the Newtonian formulation, GR offers a geometric view of gravity, unifying space, time, and matter-energy. In GR, space and time are part of a more fundamental entity called spacetime, which curves in response to matter-energy, thereby guiding the paths that particles necessarily follow. From a field theory perspective, GR describes gravitational interaction as mediated by a massless spin-2 boson, known as the *graviton*, which interacts non-minimally with other particles (e.g., scalar fields).

While GR is in full agreement with several astrophysical and cosmological observations, it is expected to break down at the Planck scale ($l_{\rm Pl} \sim 1.6 \times 10^{-35}\,\mathrm{m}$), where a quantum theory of gravity is required in order to describe phenomena occurring at such small length scales. Additionally, phenomena like the accelerated expansion

of the universe, the large-scale structure of the cosmos, galaxy cluster dynamics, and the rotation curves of spiral galaxies suggest that GR might be an incomplete theory of gravity [199].

Another compelling reason for extending Einstein's theory is to fully incorporate Mach's Principle into gravitation. According to this principle, the local inertial frame is determined by the average motion of distant objects, implying that the gravitational coupling at any spacetime point is determined by surrounding matter. This means gravity could vary with spacetime location, necessitating a reformulation of inertia and the equivalence principle. The first alternative to Einstein's GR, and the prototype for alternative theories of gravity, was the Brans-Dicke theory [36]. In this theory, Mach's idea are implemented via a *variable gravitational constant*, corresponding to a scalar field coupled non-minimally to the 3+1 geometry.

Thus far, we have presented good reasons for going beyond GR, which can be divided into three categories: quantum gravity, astrophysical and cosmological, and mathematical motivations. In the following sections, we will discuss each of these in more detail. However, in this thesis, we would like to emphasize that in this thesis, we will focus only on the cosmological motivations.

4.1.1 Quantum gravity motivation

One of the main challenges in modern theoretical physics is to build a unified theory, known as the Grand Unified Theory (GUT), which can simultaneously describe all four fundamental interactions of nature: electromagnetic, weak, strong, and gravitational forces. These theories are often referred to as *theories of everything*, with the main candidates being string and superstring theories [200, 201], and M-theory [202], which unifies the five different string theories through supersymmetry [203] and supergravity [204]. However, this long-standing dream, pursued since Einstein's time, has been frustrated primarily because of gravitation.

In principle, all fundamental fields, including gravity, should be described using quantum mechanics. Yet, gravity presents unique challenges, as it describes both the gravitational degrees of freedom and the background spacetime in which these degrees of freedom reside, it is not possible to renormalize and quantize GR in the usual way. This dual role makes it impossible to renormalize and quantize General Relativity (GR) in the standard way. As a result, Einstein's theory remains valid only within the low-energy and large-scale domains, while it breaks down at high energy and very small scales.

There are two main approaches in order to quantizing a classical field theory: the canonical and covariant methods. The covariant method allows for the construction of a renormalizable theory of gravity at one-loop in the perturbative series, pro-

viding corrections to the Einstein-Hilbert action by adding non-minimally coupled terms between scalar fields and geometry, such as ψR, or terms-like R^2, $R^{\mu\nu}R_{\mu\nu}$, $R^{\mu\nu\lambda\rho}R_{\mu\nu\lambda\rho}$, $R\Box R$, and $R\Box^k R$ [205]. In fact, such terms appear in the low-energy limit of string theories [206, 207] or Kaluza-Klein theories [38–40] when extra spatial dimensions are compactified. Additionally, modifying GR to include quadratic terms in the Ricci scalar leads to interesting inflationary scenarios, which are expected to complement the SMC [48].

Finally, theoretical advances in emergent gravity, which posits that gravity emerges from the thermodynamic properties of spacetime, have shown that Einstein field equations can be derived from local considerations of equilibrium thermodynamics [208]. This leads to the conclusion that GR is simply one possible state of gravity corresponding to thermodynamic equilibrium, and that when this equilibrium is perturbed at higher energies, near-equilibrium configurations corresponding to ETGs should emerge [205].

4.1.2 Astrophysical and cosmological motivation

In Chapter 3, we discussed the main aspects of HBB cosmology and how the flat-ΛCDM model best fits a wide range of cosmological observations. However, it was shown that the SMC suffers from certain observational problems, leading to the inflationary hypothesis [48, 178, 179] Furthermore, the SMC requires the inclusion of DM and DE, about which we have no information from particle physics, nor have they been directly observed to date. These deficiencies may stem from an incomplete and insufficient description of gravity, such as that provided by GR [205].

In this context, cosmic inflation provides a dual motivation for extending GR: quantum and cosmological. First, it occurs at very high energy scales, close to the Planck scale, where quantum gravity is expected to provide a complete description. Second, it is well known that adding a term proportional to R^2, with a coefficient small enough to preserve the successes of HBB, to the Einstein-Hilbert Lagrangian leads to cosmic acceleration. In fact, in 1980, A. Starobinsky demonstrated that R^2-type corrections to the Einstein-Hilbert Lagrangian can modify the Friedmann equations to describe an inflationary universe [48]. The Starobinsky model gave rise to a class of modified theories of gravity known as $f(R)$ gravity.

The DM hypothesis also play a dual role here. First, astrophysical observations suggest the presence of non-baryonic matter primarily filling the galactic halo and LSS gaps. Furthermore, the physics underlying BAO observations considers the existence of decoupled DM in the early universe, forming potential wells around which the photon-baryon fluid oscillated. This mechanism leaves an imprint in the CMB angular power spectrum, best matched by adjusting the cosmological model

to include approximately 26% of DM. Second, admitting the existence of a new component in the matter sector necessitates a explanation of its origin through particle physics; this is the same as asking what particle(s) the DM is made of. Another way to address the challenges associated with DM is to modify the geometric sector of Einstein's equations, i.e., in the Einstein-Hilbert Lagrangian, to account for these effects.

DE, in turn, is currently the most pressing problem for the SMC. Both LSS (mainly SNe Ia) and CMB observations indicate that the universe is undergoing an accelerated expansion phase driven by DE, known only for its property of exerting negative pressure. The simplest explanation for DE is that it has a constant EoS equal to -1, i.e., it is a cosmological constant. Since Λ is interpreted *a priori* as the quantum vacuum energy density, its contribution to the total energy density can be estimated from QFT. While QFT predicts a maximum value of $\rho_{\text{vac}} \sim 10^{74}\,\text{GeV}^4$, cosmological observations constraint it to $\rho_\Lambda \sim 10^{-47}\,\text{GeV}^4$. This discrepancy, spanning approximately 120 orders of magnitude between theoretical and observed values, is regarded as the most disastrous prediction in physics of all time, known as the cosmological constant problem, or vacuum catastrophe [8, 9]. Furthermore, the cosmological constant (or DE in general), has a normalized energy density that is comparable to the matter energy density today, a phenomenon referred to as the coincidence problem [10, 11].

In this context, modifications to the Einstein-Hilbert Lagrangian are made in order to produce an accelerated universe at late times. This can be considered as being equivalent to an inflationary universe but slowed by matter, whose density remains significant today. According to observations, matter (baryons plus DM) comprises around 31%, while DE makes up about 69% of the total energy density in the universe (recall Section 3.8 of Chapter 3). Given the similarity between the current acceleration phase and the primordial inflationary one, $f(R)$ gravity becomes a viable alternative to the undetected DE.

4.1.3 Mathematical motivation

A third motivation for extending GR arises from mathematical considerations. Notably, no quantum theory of gravity or GUT candidate yields exactly GR as its classical low-energy limit. In fact, theories such as strings and superstrings theory, M-theory, supergravity, and loop quantum gravity [209] emerge from effective actions that inherently include non-minimal couplings to geometry or higher-order terms in curvature invariants. These interactions between quantum scalar fields and background geometry introduce corrections to the Einstein-Hilbert Lagrangian, explained via corrections in one-loop (or higher) in high-curvature regime [205].

Furthermore, it is well known that higher-order theories (formulated in the Jordan conformal frame) can be recast as GR with scalar field(s) coupled to gravity (formulated in the Einstein conformal frame) via a Legendre transformation on the metric. This has led to debates over whether the mathematical equivalence between different conformal representations of the theory implies physical equivalence as well. If the answer is *no*, this argument does not justify extending gravity. However, if the answer is *yes*, it means that GR does not account for all degrees of freedom inherent in the gravitational field.

Finally, a last mathematical motivation for extending GR is rooted in the Palatini method of variation, also known as the Palatini formalism or Palatini approach. The key idea behind this formalism is to treat the connection $\Gamma^{\lambda}_{\mu\nu}$ as independent of the spacetime metric $g_{\mu\nu}$. Physically, this decouples the geodesic and metric structures of spacetime, enabling an extension of GR. By considering $\Gamma^{\lambda}_{\mu\nu}$ independent of $g_{\mu\nu}$, one can even drop the symmetry condition on $\Gamma^{\lambda}_{\mu\nu}$. Historically, this approach was employed by Einstein, in 1925, during his attempt to unify GR with Maxwell's electromagnetism [210].

4.2 What a good MTG should do?

A good MTG must meet certain minimum requirements from a phenomenological standpoint, just as GR does. These requirements can be divided into four regimes: Newtonian, post-Newtonian, extragalactic, and cosmological. As is well known, Newtonian gravity was highly successful in explaining gravity phenomena on Earth and astronomical observations mapping the orbits of planets, compact objects, and the potential wells of self-gravitating structures. In the post-Newtonian regime, the parametrized post-Newtonian (PPN) expansion of GR has provided the most precise estimates for laboratory and Solar System experiments. At the extragalactic scale, GR predicted phenomena such as black holes, relativistic stars, GL, and GWs. At cosmological scales, the ΛCDM model – where GR plays a central whole – provides a powerful framework for explaining early-universe observations, such as BBN and the CMB, as well as the growth of cosmic structures.

For a MTG to be considered successful, it must satisfy the following criteria:

i. Reproduce Newtonian dynamics in the weak-field, slow-motion limit;

ii. Pass the highly precise classical Solar System tests;

iii Explain extragalactic phenomena, such as black hole dynamics, GL, GWs, and the matter power spectrum;

iv. Address the formation of large-scale structures, including galaxies, galaxy clusters, superclusters, voids, and filaments; and

v. Reproduce viable cosmological dynamics consistent with the current range of astronomical observations (BBN, CMB, BAO, SNe, etc.).

In particular, an outstanding MTG must reproduce the current phase of DE-driven cosmic acceleration.

Of course, any MTG must ultimately be integrated into a broader framework of quantum gravity. However, we will not address that aspect in this thesis, as our primary goal here is to explain the current acceleration phase of the universe using the Hubble and luminosity distance functions without assuming any exotic components in the stress-energy tensor, such as DE. Given the highly degenerate nature of the background, we also explore the perturbative level through the normalized growth function.

4.3 Theories of modified gravity

Modifying GR is an arduous task mainly for two reasons: (*i*) its excellent agreement with current observations, as discussed previously, and (*ii*) its internal structure is tightly constrained by consistency requirements, which arise from the nature of the graviton – described as a massless spin-2 particle. This implies that only a limited number of modifications to GR can be performed without violating these key points. In light of this, we recognize (at least) three viable approaches to extending GR:

1. Introducing non-minimal coupling terms between matter fields (particularly scalar fields) and geometry in the effective gravitational Lagrangian;

2. Incorporating higher-order invariants of the curvature tensor, $R^{\lambda}_{\mu\nu\rho}$, into the Einstein-Hilbert Lagrangian; or

3. Extending the general spacetime to include extra dimensions.

First, GR constrains gravitational effects to be mediated solely by a single rank-2 tensor, the metric tensor $g_{\mu\nu}$, or equivalently, a massless spin-2 particle, the graviton, in the QFT framework. The first approach to extending gravity allows the gravitational field to interact with extra (specially scalar) fields. The most extensively studied theory in this context is scalar-tensor gravity, which introduces a coupling of the form ψR, where ψ is a scalar field. Moreover, there is the possibility that the additional field(s) could be vector, as in the Einstein-Æther model [211], or even both, as in tensor-vector-scalar gravity [212].

In GR, we are required to work with a Lagrangian that is a simple linear function of the Ricci scalar R. The second way to modify gravity thus involves extending the effective gravitational Lagrangian to include higher-order invariants of the curvature tensor, such as R^2, $R^{\mu\nu}R_{\mu\nu}$, $R^{\mu\nu\lambda\rho}R_{\mu\nu\lambda\rho}$, $R\,\Box R$, and $R\,\Box^k R$. The most widely studied class of such theories is $f(R)$ gravity, which generalizes GR by considering arbitrary functions of the Ricci scalar in the gravitational Lagrangian. Moreover, higher-order theories also extend beyond $f(R)$ gravity by incorporating other curvature invariants. Some examples of these theories include Gauss-Bonnet gravity [213], based on the Gauss-Bonnet term $\mathcal{G}$[1], non-local gravity [215], which relies on the non-locality term $\Box^{-1}R$, and teleparallel gravity along with its generalizations [216], which involve either the torsion scalar $\mathcal{T}$ or the non-metricity scalar Q[2].

The third approach in order to extending GR is even more radical, as it involves introducing extra dimensions to the theory. Theories like Kaluza-Klein, superstring theory, supergravity, and bosonic string theory postulate extra spatial dimensions. There are also more unconventional models, such as those proposing multiple time dimensions, with two [218] or three [219] time dimensions, although these theories are less explored due to their speculative nature and the lack of empirical support. Anyway, extra dimensions are typically expected to be compactified at extremely small scales, on the order of the Planck length, making experimental verification challenging in the near future. So far, the experience has shown us no evidence supporting the existence of extra dimensions at either laboratory or astronomical scales.

4.3.1 The prototype: Brans–Dicke theory

The Brans-Dicke theory [36, 220], sometimes called the Jordan-Brans-Dicke theory, was one of the first modifications to GR designed to introduce two key elements: the possibility of a dynamical coupling to gravity and the incorporation of Mach's principle. This theory builds upon the following action,

$$S_{\rm BD} = \frac{1}{2\kappa^2}\int d^4x\sqrt{-g}\left[\psi R - \frac{\omega_{\rm BD}}{\psi}g^{\mu\nu}\nabla_\mu\psi\nabla_\nu\psi\right] + S_{\rm M}\left[g_{\mu\nu},\phi_{\rm M}\right], \qquad (4.1)$$

where $\omega_{\rm BD}$ is the Brans-Dicke parameter, and ψ is an additional scalar field, often called the Brans-Dicke field.

[1]The topological Gauss-Bonnet invariant is a particular combination of curvature invariants, defined as $\mathcal{G} \equiv R^{\mu\nu\lambda\rho}R_{\mu\nu\lambda\rho} - 4R^{\mu\nu}R_{\mu\nu} + R^2$. This term naturally arises in the regularization and renormalization of QFTs in curved spacetime [214].

[2]The metricity assumption in Eq. (2.8) can be relaxed in order to produce a non-metricity tensor, defined as $Q_{\rho\mu\nu} \equiv \nabla_\rho g_{\mu\nu}$. In this way, it can be verified that the non-metricity scalar is defined as $Q \equiv -\frac{1}{4}Q_{\mu\nu\rho}Q^{\mu\nu\rho} + \frac{1}{2}Q_{\mu\nu\rho}Q^{\rho\nu\mu} + \frac{1}{4}Q_\mu Q^\mu - \frac{1}{2}Q_\mu\tilde{Q}^\mu$, where $Q_\mu \equiv Q^\nu_{\mu\nu}$ and $\tilde{Q}^\mu \equiv Q^{\nu\mu}_\nu$ are acquired from contractions of the non-metricity tensor [217].

One of the key features of this theory is that matter is not coupled directly to the scalar field ψ (this is known as minimal coupling), as indicated by the matter action S_{M} not depending on ψ. However, ψ couples directly to the Ricci scalar R (a non-minimum coupling), so the gravitational field is described by both the metric $g_{\mu\nu}$ and scalar field ψ.

By varying the Brans-Dicke action with respect to $g_{\mu\nu}$ and ψ, we derive two sets of equations. First, the field equations, analogous to Einstein's equations:

$$G_{\mu\nu} - \frac{\omega_{\mathrm{BD}}}{\psi^2}\left[\nabla_\mu\psi\nabla_\nu\psi - \frac{1}{2}g_{\mu\nu}\left(\nabla\psi\right)^2\right] - \frac{1}{\psi}\left(\nabla_\mu\nabla_\nu\psi - g_{\mu\nu}\Box\psi\right) = \frac{\kappa^2}{\psi}T_{\mu\nu}\,. \tag{4.2}$$

Second, a wave equation governing the behavior of the scalar field ψ:

$$\frac{2\omega_{\mathrm{BD}}\Box\psi}{\psi} - \frac{\omega_{\mathrm{BD}}}{\psi^2}g^{\mu\nu}\nabla_\mu\psi\nabla_\nu\psi + R = 0\,. \tag{4.3}$$

By contracting the first equation with $g_{\mu\nu}$ and substituting the second one into the result, we obtain the equation

$$\Box\psi = \frac{\kappa^2\mathrm{T}}{2\omega_{\mathrm{BD}}+3}\,, \tag{4.4}$$

which demonstrates that the matter distribution acts as a source for ψ, thereby satisfying the requirements of Mach's principle. Consequently, ψ can be viewed as an auxiliary geometrical contribution to the usual Einstein field equations.

Originally, Brans and Dicke's idea was to define an *effective gravitational constant* as (in our units)

$$G_{\mathrm{eff}}(\psi) \equiv \frac{G}{\psi}\,, \tag{4.5}$$

thereby introducing a variable gravitational coupling, inspired by Dirac's ideas. It is often said that as $\omega_{\mathrm{BD}} \to \infty$, the Brans-Dicke theory reduces to Einstein's GR. This is based on the assumption that in this limit, $\psi \propto \omega_{\mathrm{BD}}^{-1}$. However, this assumption is not valid in all cases. Some solutions show that $\psi \propto \omega_{\mathrm{BD}}^{-1/2}$, which cannot be continuously deformed into corresponding GR solutions [221]. For instance, the solution discussed in Section 4 of Ref. [222] exhibits the expected asymptotic behavior but does not possess a true GR limit.

4.3.2 General scalar-tensor theories

Scalar-tensor theories are natural extensions of the Brans-Dicke theory, incorporating two key generalizations to its action:

1. The Brans-Dicke parameter, ω_{BD}, becomes a general function of the scalar field ψ, denoted as $\omega(\psi)$, and

2. A potential term, $V(\psi)$, is introduced for the scalar field in the Lagrangian.

Thus, the action describing these theories is expressed as

$$S_{\rm st} = \frac{1}{2\kappa^2}\int d^4x\sqrt{-g}\left[\psi R - \frac{\omega(\psi)}{\psi}g^{\mu\nu}\nabla_\mu\psi\nabla_\nu\psi - V(\psi)\right] + S_M\left[g_{\mu\nu},\phi_{\rm M}\right]\,. \tag{4.6}$$

where $S_{\rm M}$ is the matter action, and $\phi_{\rm M}$ represents the matter fields. The field equations that arise from this action, after appropriate manipulations, are

$$G_{\mu\nu} - \frac{\omega(\psi)}{\psi^2}\left[\nabla_\mu\psi\nabla_\nu\psi - \frac{1}{2}g_{\mu\nu}\left(\nabla\psi\right)^2\right] - \frac{1}{\psi}\left(\nabla_\mu\nabla_\nu\psi - g_{\mu\nu}\Box\psi\right) + \frac{V(\psi)g_{\mu\nu}}{2\psi} = \frac{\kappa^2}{\psi}T_{\mu\nu}\,, \tag{4.7}$$

while the equation governing the scalar field ψ is

$$\left[2\omega(\psi)+3\right]\Box\psi + \omega_{,\psi}(\psi)g^{\mu\nu}\nabla_\mu\psi\nabla_\nu\psi - \psi V_{,\psi}(\psi) + 2V(\psi) = \kappa^2{\rm T} \tag{4.8}$$

where $\omega_{,\psi} \equiv d\omega/d\psi$ and $V_{,\psi} \equiv dV/d\psi$. The Brans-Dicke theory can be recovered by taking $\omega \to \omega_{\rm BD}$ and $V \to 0$.

Scalar-tensor theories, in particular, Brans-Dicke theory, have been extensively studied in the literature. Although many old and new findings in this regard are very interesting, exploring them is not part of the aim of this thesis. See Refs. [37, 221] for a comprehensive review.

4.3.3 Higher dimensional theories

GR is formulated on a (pseudo-)Riemaniann 3+1 dimensional manifold. However, Riemannian geometry is not restricted to 3+1 dimensions, allowing us to consider spacetime with more general dimensions. In fact, the possibility of extra dimensions was proposed as early as the initial development of GR, beginning with the work of G. Nordström [223], T. Kaluza [38], and O. Klein [39]. In principle, the idea of extra dimensions arose from the attempt to reconcile the principles of quantum mechanics and GR.

Given the wide variety of theories that attempt to explain gravity from the perspective of a spacetime with dimensions beyond the known 3+1 of GR, and the fact that, in principle, these theories lack a mathematical framework to unify them into a single general description (as was the case with scalar-tensor theories), we shall limit our discussion to the notions proposed by Kaluza and Klein.

The Kaluza-Klein theory emerges as an attempt in order to unify gravity and electrodynamics by considering GR on a 4+1 dimensional manifold, where one of the spatial dimensions is small and compact. Let $\mathbb{D} \equiv \mathscr{D}+1$ be the total dimensions of the theory, where $\mathscr{D}$ corresponds to the number of spatial dimensions and 1

represents the time. The Kaluza-Klein theory is formulated in $\mathbb{D} = 5$, or $\mathscr{D} = 4$. The generalized Einstein-Hilbert action for a 4+1 dimensional spacetime is given by

$$S_{\mathbb{D}} = \frac{1}{2\kappa_{\mathbb{D}}^2} \int d^{\mathbb{D}}\mathrm{X}\sqrt{-\mathscr{G}}\mathscr{R} + S_{\mathrm{M}}\left[\mathscr{G}_{\mathrm{AB}}, \phi_{\mathrm{M}}\right] , \tag{4.9}$$

where $\kappa_{\mathbb{D}}^2$ is Einstein's constant in $\mathbb{D}$ dimensions, $\mathscr{G}$ is the determinant of the $\mathbb{D}$-dimensional metric $\mathscr{G}_{\mathrm{AB}}$, and $\mathscr{R}$ is the trace of the $\mathbb{D}$-dimensional Ricci tensor $\mathscr{R}_{\mathrm{AB}}$, with indices A, B running from 0 to 4 (4 being the Kaluza-Klein extra dimension).

The issue with considering extra dimensions is that gravity has not been observed as an interaction in $\mathbb{D} > 4$ dimensions, either in laboratory experiments or astronomical observations. For example, the Newtonian potential due to a point source in a $\mathbb{D}$-dimensional universe scale as $\Phi \propto r^{-(\mathbb{D}-3)}$, meaning that planetary orbits remain stable only for $\mathbb{D} = 4$. This implies that any extra dimensions, if they exist, must be relevant only at very small scales, on the order of the Planck length, or on cosmological scales far beyond the Solar System.

The solution is to consider that the extra dimensions are compactified on a circle of radius $L/2\pi$. To formalize this, let us define the coordinates $\mathrm{X}^A = (x^\mu, \mathfrak{z})$, where the coordinate $\mathfrak{z}$ lies along the compact direction, such that $0 \leq \mathfrak{z} \leq L$. In this framework, we can expand the metric along the extra dimension $\mathfrak{z}$ as a Fourier series,

$$\mathscr{G}_{\mathrm{AB}}(x, \mathfrak{z}) = \sum_n \mathscr{G}_{\mathrm{AB}}^{(n)}(x)\, e^{in\mathfrak{z}/L} . \tag{4.10}$$

This implies the existence of an infinite number of extra fields in $\mathscr{D}$ dimensions. Modes with $n \neq 0$ correspond to massive fields with mass $|n|/L$, whereas the $n = 0$ mode corresponds to a massless field. Since $L \sim l_{\mathrm{Pl}}$, the Fourier modes converge, allowing us to consider only the first mode, i.e., the $n = 0$ mode.

Focusing now on the zero modes $\mathscr{G}_{\mathrm{AB}}^{(0)}(x)$, we decompose the metric components to define the following new fields:

$$\mathscr{G}_{\mu\nu}^{(0)} \equiv g_{\mu\nu}\, e^{2\mathscr{A}\psi} + A_\mu A_\nu\, e^{2\mathscr{B}\psi} , \tag{4.11}$$

$$\mathscr{G}_{\mu\mathfrak{z}}^{(0)} \equiv A_\mu\, e^{2\mathscr{B}\psi} , \tag{4.12}$$

$$\mathscr{G}_{\mathfrak{z}\mathfrak{z}}^{(0)} \equiv e^{2\mathscr{B}\psi} , \tag{4.13}$$

where $\mathscr{A} \equiv 1/\sqrt{2(\mathscr{D}-1)(\mathscr{D}-2)}$ and $\mathscr{B} \equiv -(\mathscr{D}-2)\mathscr{A}$. It is important to note that the physical size of the compact dimension $\mathfrak{z}$ is not necessarily given by L, but by $Le^{\mathscr{B}\psi(x)}$. In the language of field theory, $g_{\mu\nu}(x)$, $A_\mu(x)$, and $\psi(x)$ represent the metric, the gauge field, and the dilaton field, respectively. Ultimately, the gauge field $A_\mu(x)$ corresponds to the eletromagnetic four-potential described in Maxwell's covariant equations.

In these terms, the $\mathscr{D}$-dimensional effective action is given by

$$S_{\text{eff}} = \frac{L}{2\kappa_{\mathbb{D}}^2} \int d^{\mathscr{D}}x\sqrt{-g}\left[R - \frac{1}{2}(\nabla\psi)^2 - \frac{1}{4}e^{-2\mathscr{A}(\mathscr{D}-1)\psi}F^2\right], \tag{4.14}$$

where $F^2 = F_{\mu\nu}F^{\mu\nu}$, and $F_{\mu\nu}$ is the Faraday tensor representing the electromagnetic field strength. This action leads to the following field equations:

$$G_{\mu\nu} = \frac{1}{2}\left[\nabla_\mu\psi\nabla_\nu\psi - \frac{1}{2}(\nabla\psi)^2 g_{\mu\nu} + \left(F_{\mu\sigma}F^\sigma_\nu - \frac{1}{4}F^2 g_{\mu\nu}\right)e^{-2\mathscr{A}(\mathscr{D}-1)\psi}\right], \tag{4.15}$$

$$\nabla^\mu\left[e^{-2\mathscr{A}(\mathscr{D}-1)\psi}F_{\mu\nu}\right] = 0\,, \tag{4.16}$$

$$\Box\psi = -\frac{1}{2}(\mathscr{D}-1)\mathscr{A}e^{-2\mathscr{A}(\mathscr{D}-1)\psi}F^2\,. \tag{4.17}$$

The first equation shows how four-dimensional matter (electromagnetic radiation) arises purely from the geometry of the fifth-dimensional empty space, while the second one is clearly a form of Maxwell's equations. The third equation can be interpreted as a source equation for the dilaton field ψ.

Kaluza-Klein theory was originally designed for $\mathscr{D} = 4$ (or $\mathbb{D} = 5$). However, its developers were frustrated by the presence of the dilaton in the resulting four-dimensional effective theory, which introduced an extra degree of freedom. This occurs because one cannot simply set $\psi = 0$ while retaining a non-trivial Maxwell field $\tilde{F}_{\mu\nu}$, as doing so would conflict with the field equations (4.15), (4.16), and (4.17) [43]. As a result, Kaluza-Klein theory has three dynamical variables – namely $g_{\mu\nu}$, A_μ, and ψ – whereas GR involves only $g_{\mu\nu}$.

Unfortunately, Kaluza-Klein theory faces some technical challenges. First, to ensure that L accurately reflects the compactification scale, ψ must be stabilized near zero. This requires a potential $V(\psi)$ that admits a stable solution, a challenge known as the moduli stabilization problem [224–227]. Additionally, from a cosmological perspective, physicists wonder how the universe evolved into a state where only three spatial dimensions grew to macroscopic scales. More specifically, what mechanism in the early universe prevented the extra spatial dimensions from expanding as much as the usual three? Or, did these dimensions initially expand and then contract to their current state? [43].

4.3.4 Higher order theories

The third class of extended theories of gravity is known as higher-order theories. The term higher-order refers to the fact that these theories incorporate, by construction, higher-order terms in curvature invariants, leading to field equations that involve derivatives of the metric tensor higher than second-order.

The central idea behind higher-order theories is to generalize the gravitational Lagrangian $\mathcal{L}_{\rm EH} \equiv (R - 2\Lambda)/2\kappa^2$ to be a more general function of the Ricci scalar, or even for depending on other curvature invariants. Examples of such invariants include R^2, $R^{\mu\nu}R_{\mu\nu}$, $R^{\mu\nu\lambda\rho}R_{\mu\nu\lambda\rho}$, $R\,\Box R$, and $R\,\Box^k R$. The first case gives rise to the classical $f(R)$ theories of gravity, which are extensively explored in the literature and are the primary focus of this thesis. The second case leads to theories of fourth, sixth, eighth, or higher-order, depending on the curvature invariants chosen.

To start, consider a theory that includes the three linear and quadratic contractions of the Riemann tensor: R, $R^{\mu\nu}R_{\mu\nu}$, and $R_{\mu\nu\rho\sigma}R^{\mu\nu\rho\sigma}$. The most general action that can be constructed in this case is

$$S_{\rm HO} = \frac{1}{2\kappa^2}\int d^4x\sqrt{-g}\, f(R, R^{\mu\nu}R_{\mu\nu}, R^{\mu\nu\rho\sigma}R_{\mu\nu\rho\sigma}) + S_{\rm M}\left(g_{\mu\nu}, \phi_{\rm M}\right) \tag{4.18}$$

where f is an arbitrary function of its arguments. Varying this action with respect to the metric tensor yields the following field equations:

$$\mathscr{I}^{(1)}_{\mu\nu} + \mathscr{I}^{(2)}_{\mu\nu} + \mathscr{I}^{(3)}_{\mu\nu} = \kappa^2 T_{\mu\nu}\,, \tag{4.19}$$

where

$$\left\{\begin{array}{rcl} \mathscr{I}^{(1)}_{\mu\nu} & \equiv & -\frac{1}{2}f g_{\mu\nu} + f_{,R}R_{\mu\nu} + 2f_{,C}R^{\rho}{}_{(\nu}R_{\mu)\rho} + 2f_{,I}R^{\epsilon\sigma\rho}{}_{(\nu}R_{\mu)\rho\sigma\epsilon}\,, \\ \mathscr{I}^{(2)}_{\mu\nu} & \equiv & \nabla^\rho\nabla^\sigma f_{,R}\left(g_{\rho\sigma}g_{\mu\nu} - g_{\mu\rho}g_{\nu\sigma}\right) + \Box\left(f_{,C}R_{\mu\nu}\right) + g_{\mu\nu}\nabla^\rho\nabla^\sigma\left(f_{,C}R_{\rho\sigma}\right)\,, \\ \mathscr{I}^{(3)}_{\mu\nu} & \equiv & -2\nabla^\rho(f_{,C}R_{\rho(\mu)\nu)} - 4\nabla^\rho\nabla^\sigma(f_{,I}R_{\sigma(\mu\nu)\rho})\,, \end{array}\right. \tag{4.20}$$

with $C \equiv R^{\mu\nu}R_{\mu\nu}$, $I \equiv R^{\mu\nu\rho\sigma}R_{\mu\nu\rho\sigma}$, and $f_{,\Upsilon} \equiv df/d\Upsilon$ where $\Upsilon = (R, C, I, ...)$. Clearly, these equations are of fourth-order. However, if we consider f to be linear in the second derivatives of the metric tensor, i.e., $f\left(..., \Box R\right)$, the field equations will be of sixth-order. By induction, $f\left(..., \Box^2 R\right)$ will yield equations of eight-order.

It turns out that the above description is too general and could hardly be considered itself as a viable immediate alternative to GR. Instead, theorists tend to pursue simpler paths by examining specific cases of the function f that involve only one or, at most, two curvature invariants simultaneously. This is the case with $f(R)$ theories, Gauss-Bonnet gravity $f(\mathcal{G})$, teleparallel gravities $f(\mathcal{T})$ and $f(Q)$, non-local theories $f(\Box^{-1}R)$ and $f(R, \Box^{-1}R)$, $f(R, \mathcal{G})$ theories, and $f(R, \mathcal{T})$ gravity. Among all higher-order theories, $f(R)$ gravity is the simplest and most extensively explored, and it will receive significant emphasis throughout this thesis.

4.4 $f(R)$ theories of gravity

Among the higher-order theories of gravity, the most widely studied is $f(R)$ gravity, which is also the primary focus of this thesis. This section delves deeper into $f(R)$ gravity compared to previous discussions on scalar-tensor and higher-dimensional theories. Comprehensive reviews on $f(R)$ gravity can be found in the literature; see, e.g., Refs. [35, 43, 45]).

The program to developing a renormalizable and potentially quantizable theory of gravitation gravitation has its roots in the early days of GR. However, the study of such theories gained renewed interest at least three times post-1960. First, in the 1960s, it was discovered that adding counter terms to Einstein's equations could resolve certain singularities in the stress-energy tensor that arose from the quantization of matter fields interacting with a classical gravitational field. In particular, a $\ln \infty$ singularity could be mitigated with a counter term derived from a Lagrangian quadratic in the Riemann tensor [228]. Then, around the 1980s, it was shown that $f(R)$ theories enhance renormalization properties [41] and can naturally lead to an inflationary phase in the early universe [48]. More recently, $f(R)$ theories have emerged as viable alternative to DE for explaining the current accelerated expansion of the universe, with this acceleration viewed as a geometric effect.

This latter point – the ability of $f(R)$ theories to explain the late accelerated expansion without invoking DE – is the motivation for investigating them here. While promising, these theories face numerous challenges. Key issues in $f(R)$ gravity include the following [35]:

- Different approaches (metric, Palatini or hybrid) result in distinct field equations;
- The Cauchy problem is not well-formulated in the Palatini formalism;
- $f(R)$ models are susceptible to various instabilities, such as the unbounded growth of the scalaron mass in high-curvature regimes, as well as Dolgov-Kawasaki, ghost, and matter instabilities [51];
- Some $f(R)$ models fail to pass local Solar System tests or do not yield viable cosmological evolution, consistent with observations.

Finally, $f(R)$ theories are often considered purely phenomenological, allowing for various functional forms of f. In principle, an $f(R)$ model needs only to satisfy local gravity tests and align well with cosmological observations – particularly adhering to the constraints outlined by Amendola et al. [44].

4.4.1 Generalized Einstein-Hilbert action

In general, the extended class of $f(R)$ theories is built upon the generalized Einstein-Hilbert action

$$S_{\rm f} = \frac{1}{2\kappa^2}\int d^4x\sqrt{-g}\, f(R) + S_{\rm M}[g_{\mu\nu},\phi_{\rm M}]\,, \tag{4.21}$$

where $f(R)$ is, *a priori*, an arbitrary function of the Ricci scalar R. The first term in this action represents modifications to the geometric sector, while the second one corresponds to the usual matter action $S_{\rm M}$, including both visible and potentially DM). Notice that GR with a cosmological constant Λ corresponds to the particular case $f(R) = R - 2\Lambda$.

4.4.2 Field equations: the metric formalism

By varying the action with respect to the metric $g_{\mu\nu}$, we obtain the field equations

$$f_{,R}(R)R_{\mu\nu} - \frac{1}{2}g_{\mu\nu}f(R) - (\nabla_\mu\nabla_\nu - g_{\mu\nu}\,\Box)\, f_{,R}(R) = \kappa^2 T_{\mu\nu}\,, \tag{4.22}$$

and the trace equation,

$$Rf_{,R}(R) - 2f(R) + 3\,\Box f_{,R}(R) = \kappa^2 {\rm T}\,, \tag{4.23}$$

where we have set $f_{,R}(R) \equiv df(R)/dR$. Since $\nabla^\mu T_{\mu\nu} = 0$ holds, the physical consistence of Eqs. (4.22) requires that the left-hand side has no divergence. In fact, if we define a modified Einstein tensor as

$$\tilde{G}_{\mu\nu} \equiv f_{,R}(R)R_{\mu\nu} - \frac{1}{2}g_{\mu\nu}f(R) - (\nabla_\mu\nabla_\nu - g_{\mu\nu}\,\Box)\, f_{,R}(R)\,, \tag{4.24}$$

we find that $\nabla^\mu\tilde{G}_{\mu\nu} = 0\ \forall\nu$. Finally, note that because these equations involve second-order derivatives of the Ricci scalar, which itself has second-order derivatives of the metric tensor, these modified Einstein field equations form a set of fourth-order equations on $g_{\mu\nu}$.

In the absence of matter, Eqs. (4.22) simplifies to

$$Rf_{,R}(R) - 2f(R) = 0\,, \tag{4.25}$$

where the positive real roots of this equation yield the de Sitter vacuum solutions, which are foundational for describing both the early and late-time cosmic acceleration phases. There will then be acceptable de Sitter solutions under the following condition [51],

$$\left.\frac{f_{,R}(R)}{f_{,RR}(R)}\right|_{R=R_*} > R_*\,, \tag{4.26}$$

where $f_{,RR}(R) \equiv d^2 f(R)/dR^2$ and R_* is a positive real root of Eq. (4.25).

As we will later explore, metric $f(R)$ gravity is a special class of scalar-tensor theories, where the Brans-Dicke parameter vanishes. Ultimately, when $f_{,RR}(R) \neq 0$, this introduces a new scalar degree of freedom, the scalaron, making $f(R)$ gravity a non-perturbative extension of Einstein's gravity. In this framework, we view $f(R)$ gravity as a phenomenological semi-classical theory derived from an underlying quantum theory, with degrees of freedom that remain inactive at lower curvature scales ($R \sim R_0$).

4.4.3 Newtonian weak-field approximation

Given the success of Newtonian gravity in describing the observed inhomogeneities at small scales and compact objects, $f(R)$ gravity must recover Newton's theory in the weak-field limit, specially for $R \gg R_0$.

We start from a maximally symmetric vacuum solution that satisfies

$$R_{\lambda\mu\nu\rho} = \frac{R_0}{12}\left(g_{\lambda\nu}g_{\mu\rho} - g_{\lambda\rho}g_{\mu\nu}\right) , \tag{4.27}$$

$$R_{\mu\nu} = \frac{R_0}{4} g_{\mu\nu} , \tag{4.28}$$

where the constant scalar curvature R_0 satisfies Eq. (4.25). To proceed, we derive the Newtonian limit by performing a weak-field expansion around the symmetric de Sitter vacuum. Expanding the field equations (4.22) to first-order around this background yields

$$\begin{aligned} f_{,R}(R_0)\delta R_{\mu\nu} - \frac{1}{4} f_{,RR}(R_0) R_0 g_{\mu\nu}\delta R - \frac{1}{2} f(R_0)\left(\delta g_{\mu\nu} - \frac{1}{2} g_{\mu\nu}\delta g\right) \\ - f_{,RR}(R_0)\left(\nabla_\mu\nabla_\nu\delta R + \frac{1}{2} g_{\mu\nu}\Box\delta R\right) = \kappa^2\left(T_{\mu\nu} - \frac{1}{2} g_{\mu\nu}\mathrm{T}\right) , \end{aligned} \tag{4.29}$$

where

$$\delta R_{\mu\nu} = \frac{1}{2}\left(\nabla_\mu\nabla^\rho\delta g_{\rho\nu} + \nabla_\nu\nabla^\rho\delta g_{\rho\mu}\right) + \frac{R_0}{3}\left(\delta g_{\mu\nu} - \frac{1}{4} g_{\mu\nu}\delta g\right) - \frac{1}{2}\left(\nabla_\mu\nabla_\nu\delta g + \Box\delta g_{\mu\nu}\right) , \tag{4.30}$$

and

$$\delta R = \delta g^{\mu\nu} R_{\mu\nu} + g^{\mu\nu}\delta R_{\mu\nu} . \tag{4.31}$$

For consistency with Newtonian gravity, it is necessary that

$$f(R_0) \sim R_0 \approx 0 , \tag{4.32}$$

at least at mass scales where Newton's law has been verified, corresponding to a

small mass scale. To obtain non-oscillatory attractive solutions, we further impose $R_0 \geq 0$, $f(R_0) \geq 0$, $f_{,R}(R_0) \geq 0$, and $f_{,RR}(R_0) \geq 0$, which allow us to discard the second and third terms of the equation as negligible in comparison to the others. Thus, in the weak-field limit, we arrive at

$$f_{,R}(R_0)\delta R_{\mu\nu} \approx \kappa^2 \left(T_{\mu\nu} - \frac{1}{2} g_{\mu\nu} \mathrm{T} \right), \tag{4.33}$$

by requiring

$$f_{,R}(R_0) \sim 1\,, \quad f_{,RR}(R_0) \ll f_{,R_0}(R_0)\,. \tag{4.34}$$

It has long been recognized that retaining fourth-order derivative terms in Eq. (4.33) can induce strong curvature effects on all length scales [49]. This emphasizes the importance of properly setting the function $f(R)$ and its derivatives to recover the Newtonian limit effectively.

4.4.4 Palatini formalism

The metric formalism we have used so far in order to derive field equations of a particular theory is not the only method; other approaches, like the Palatini formalism, also exist.

The Palatini approach was first introduced by Einstein in 1925 [229] but became known as such due to a historical misunderstanding [230]. The fundamental idea behind this procedure is to treat the connection $\Gamma^{\lambda}_{\mu\nu}$, which appears in the Ricci scalar, as an independent variable from the metric $g_{\mu\nu}$. Physically, this means the spacetime's metric and geodesic structures are decoupled, and the connection is distinct from the Levi-Civita connection.

In GR, the Palatini and metric formalisms yield equivalent field equations since the field equations for $\Gamma^{\lambda}_{\mu\nu}$ return the Levi-Civita connection of $g_{\mu\nu}$. However, for ETGs like $f(R)$ gravity or scalar-tensor theories, these two approaches produce distinct field equations and physical implications.

To apply the Palatini formalism to $f(R)$ gravity, we introduce a modified Ricci scalar, $\hat{R} \equiv g^{\mu\nu}\hat{R}_{\mu\nu}$, where $\hat{R}_{\mu\nu}$ is built using a non-metric connection, given as $\hat{\Gamma}^{\lambda}_{\mu\nu}$. Replacing R with $\hat{R}$ in the action (4.21) and varying with respect to $g_{\mu\nu}$ and $\hat{\Gamma}^{\lambda}_{\mu\nu}$ gives [34]

$$f_{,\hat{R}}(\hat{R})\hat{R}_{\mu\nu} - \frac{1}{2} g_{\mu\nu} f(\hat{R}) = \kappa^2 T_{\mu\nu} \tag{4.35}$$

and

$$\hat{\nabla}_{\rho} \left[\sqrt{-g} f_{,\hat{R}}(\hat{R}) g^{\mu\nu} \right] = 0\,, \tag{4.36}$$

where $f_{,\hat{R}}(\hat{R}) \equiv df(\hat{R})/d\hat{R}$, and $\hat{\nabla}_{\mu}$ represents the covariant derivative based on $\hat{\Gamma}^{\lambda}_{\mu\nu}$.

Solving the latter equation leads to the non-metric connection

$$\hat{\Gamma}^{\lambda}_{\mu\nu} = \Gamma^{\lambda}_{\mu\nu} + \frac{1}{2f_{,\hat{R}}}\left(\delta^{\lambda}_{\nu}\partial_{\mu}f_{,\hat{R}} + \delta^{\lambda}_{\mu}\partial_{\nu}f_{,\hat{R}} - g^{\lambda\rho}g_{\mu\nu}\partial_{\rho}f_{,\hat{R}}\right) . \tag{4.37}$$

Therefore, the generalized Ricci tensor and scalar respectively give

$$\hat{R}_{\mu\nu} = R_{\mu\nu} + \frac{3}{2}\frac{\nabla_{\mu}f_{,\hat{R}}\nabla_{\nu}f_{,\hat{R}}}{f^{2}_{,\hat{R}}} - \frac{1}{f_{,\hat{R}}}\left(\nabla_{\mu}\nabla_{\nu}f_{,\hat{R}} - g_{\mu\nu}\Box f_{,\hat{R}}\right) \tag{4.38}$$

and

$$\hat{R} = R + \frac{3}{2}\frac{\nabla_{\mu}f_{,\hat{R}}\nabla^{\mu}f_{,\hat{R}}}{f_{,\hat{R}}} - 3\frac{\Box f_{,\hat{R}}}{f_{,\hat{R}}} . \tag{4.39}$$

In the GR limit, where $f_{,\hat{R}} = 1$, we recover the Levi-Civita connection, $\hat{\Gamma}^{\lambda}_{\mu\nu} = \Gamma^{\lambda}_{\mu\nu}$, along with $\hat{R}_{\mu\nu} = R_{\mu\nu}$ and $\hat{R} = R$. This confirms that the metric and Palatini approaches yield the same field equations for GR.

In the Palatini formalism, spacetime's dual (metric and geodesic) structure is naturally translated into a bimetric structure of the theory, where the second metric is defined from Eq. (4.36) as $\hat{g}_{\mu\nu} \equiv f_{,\hat{R}}(\hat{R})g_{\mu\nu}$. It is straightforward to check that $\hat{\Gamma}^{\lambda}_{\mu\nu} = (1/2)\hat{g}^{\lambda\rho}\left(\partial_{\mu}\hat{g}_{\rho\nu} + \partial_{\nu}\hat{g}_{\mu\rho} - \partial_{\rho}\hat{g}_{\mu\nu}\right)$ [34, 205].

Though the Palatini formalism is a tool for studying ETGs (see Refs. [231–234] for some investigations), we will proceed with the metric approach in this thesis for several reasons. Physically, the metric formalism aligns better with foundational principles:

1. The torsion-free condition in the metric approach allows setting $\Gamma^{\lambda}_{\mu\nu} = 0$ locally, which is compatible with EP; and

2. Affine and metric geodesics coincide, preserving covariance naturally.

Mathematically, the Levi-Civita connection uniquely satisfies metric compatibility and naturally arises as the minimal-action solution in GR. Additionally, the Palatini $f(R)$ gravity faces significant issues:

1. Curvature singularities at star surfaces [235];

2. Conflicts with the standard model of particle physics [236, 237];

3. An ill-posed Cauchy problem, and [238]; and

4. The scalaron lacks dynamism, preventing chameleon mechanisms [239].

These challenges make the metric formalism more suitable for this thesis, as it is more compatible with physical principles and observed phenomena.

4.4.5 Equivalence between theories

In both the metric and Palatini formulations of $f(R)$ theories, we find equivalence to scalar-tensor theories, where derivatives of $f(R)$ serve as the Brans-Dicke parameter. Additionally, $f(R)$ gravity can be translated into the GR framework minimally coupled to a scalar field. This leads us to the Jordan and Einstein frames, linked via Legendre and conformal transformations.

Starting from action (4.21) in the metric formalism, we introduce a new field, ς, and rewrite the action equivalently as

$$S_{\rm met} = \frac{1}{2\kappa^2}\int d^4x\sqrt{-g}\left[f\left(\varsigma\right) + f_{,\varsigma}\left(\varsigma\right)\left(R-\varsigma\right)\right] + S_{\rm M}\left[g_{\mu\nu},\phi_{\rm M}\right] , \tag{4.40}$$

where $f_{,\varsigma}(\varsigma) \equiv df(\varsigma)/d\varsigma$. Varying this action with respect to ς gives $f_{,\varsigma\varsigma}(\varsigma)(R-\varsigma) = 0$, so for $f_{,\varsigma\varsigma}(\varsigma) \neq 0$, we find $\varsigma = R$. Defining $\psi \equiv f_{,\varsigma}(\varsigma)$, we obtain

$$S_{\rm met} = \frac{1}{2\kappa^2}\int d^4x\sqrt{-g}\left[\psi R - V\left(\psi\right)\right] + S_{\rm M}\left[g_{\mu\nu},\phi_{\rm M}\right] , \tag{4.41}$$

where $V(\psi) \equiv \varsigma(\psi)\psi - f\left(\varsigma(\psi)\right)$. Notice that this action is equivalent to that in Eq. (4.6) for scalar-tensor theories with Brans-Dicke parameter $\omega = 0$.

In the Palatini formalism, the procedure is similar, substituting the metric Ricci scalar R with the non-metric $\hat{R}$ in action (4.40), so $\varsigma = \hat{R}$ when $f_{,\varsigma\varsigma}(\varsigma) \neq 0$. Using Eq. (4.39), we obtain

$$S_{\rm Pal} = \frac{1}{2\kappa^2}\int d^4x\sqrt{-g}\left[\psi R + \frac{3}{2\psi}g^{\mu\nu}\nabla_\mu\psi\nabla_\nu\psi - V(\psi)\right] + S_{\rm M}\left[g_{\mu\nu},\phi_{\rm M}\right] , \tag{4.42}$$

matching the action (4.6) for scalar-tensor theories with $\omega = -3/2$.

The equivalence between different formulations of ETGs not only enriches the theoretical understanding but also offers practical empirical benefits. Ultimately, constraints derived from one framework can be translated into another. A prominent example is the PPN expansion, which links the first PPN parameter, $\gamma_{\rm PPN}$, to the Brans-Dicke parameter, ω. The relationship,

$$\gamma_{\rm PPN} = \frac{\omega+1}{\omega+2} \tag{4.43}$$

yields $\gamma_{\rm PPN} = 1/2$ for metric $f(R)$ gravity and $\gamma_{\rm PPN} = -1$ for Palatini $f(R)$ gravity. However, these theoretical values significantly differ from the Cassini constraint, $\gamma_{\rm PPN} = 1 + (2.1 \pm 2.3) \times 10^{-5} \approx 1$, corresponding to $\omega > 40000$ [240]. Such a discrepancy could cast doubt on $f(R)$ theories. However, in metric approach, the chameleon-like screening mechanism provides a potential resolution, allowing the theory to evade these constraints. We will delve further into this mechanism below.

4.4.6 Einstein and Jordan frames

In $f(R)$ theories, two key conformal representations are the Jordan and Einstein frames. Eqs. (4.22) and (4.23) in the metric formalism, or equivalently Eqs. (4.35) and (4.36) in the Palatini formalism, define the Jordan frame. Next, we derive the Einstein frame for $f(R)$ theories specifically in the metric formalism, leaving the Palatini approach for a later section.

To proceed, we define a new set of variables $y = f_{,R}(R)$ and $g^{\rm E}_{\mu\nu} = y g_{\mu\nu}$, alongside a scalar field redefinition $y = \exp\left(-\sqrt{2\kappa^2/3}\,\mathscr{C}\right)$. This leads to an action that describes Einstein gravity minimally coupled to a scalar field $\mathscr{C}$,

$$S^{\rm E}_{\rm met} = \int d^4x\sqrt{-g^{\rm E}}\left[\frac{R^{\rm E}}{2\kappa^2} - \frac{1}{2}\left(\nabla\mathscr{C}\right)^2 - V(\mathscr{C})\right] + S_{\rm M}\left[g^{\rm E}_{\mu\nu}y^{-1}, \phi_{\rm M}\right]\,, \tag{4.44}$$

where $R^{\rm E}$ is the scalar Ricci for the metric $g^{\rm E}_{\mu\nu}$, and the modified Einstein tensor takes the form

$$\tilde{G}_{\mu\nu} = \nabla_\mu\mathscr{C}\nabla_\nu\mathscr{C} - \frac{1}{2}g^{\rm E}_{\mu\nu}\nabla_\sigma\mathscr{C}\nabla^\sigma\mathscr{C} - g^{\rm E}_{\mu\nu}V(\mathscr{C})\,, \tag{4.45}$$

where the bare potential is defined as

$$V(\mathscr{C}) = \left.\frac{Rf_{,R}(R) - f(R)}{2\kappa^2 f^2_{,R}(R)}\right|_{R=R(\mathscr{C})}\,. \tag{4.46}$$

In this setup, the Jordan frame corresponds to the variable set $\{g_{\mu\nu}\}$, whereas the Einstein frame corresponds to $\{y, g^{\rm E}_{\mu\nu}\}$. The function $R(\mathscr{C}) = R\left[y\left(\mathscr{C}\right)\right]$ is obtained by inverting the relation $y = f_{,R}(R)$, which is always possible if $f_{,RR}(R) \neq 0$ [205]. Eqs. (4.44) and (4.45) are expressed in what is called the Einstein frame.

The conformal coupling function is given by

$$\mathcal{A}(\mathscr{C}) = \frac{1}{\sqrt{f_{,R}(R)}} = \exp\left(\kappa\beta\mathscr{C}\right)\,, \tag{4.47}$$

with the conformal coupling parameter $\beta = 1/\sqrt{6}$. Varying the action (4.44) with respect to $g^{\rm E}_{\mu\nu}$ and $\mathscr{C}$ gives, respectively,

$$R^{\rm E}_{\mu\nu} = \kappa^2\left[\mathscr{T}^{\rm E}_{\mu\nu} + \nabla_\mu\mathscr{C}\nabla_\nu\mathscr{C} + V(\mathscr{C})g^{\rm E}_{\mu\nu}\right]\,, \tag{4.48}$$

and

$$\Box^{\rm E}\mathscr{C} = V_{,\mathscr{C}} - \frac{{\rm T}^{\rm E}\mathcal{A}_{,\mathscr{C}}}{\mathcal{A}}\,, \tag{4.49}$$

where $\mathscr{T}^{\rm E}_{\mu\nu} \equiv T^{\rm E}_{\mu\nu} - \frac{1}{2}{\rm T}^{\rm E}g^{\rm E}_{\mu\nu}$, $V_{,\mathscr{C}} \equiv dV/d\mathscr{C}$, and $\mathcal{A}_{,\mathscr{C}} \equiv d\mathcal{A}/d\mathscr{C}$. All quantities with the superscript E represent values in the Einstein frame.

Finally, we can rewrite the scalar field Eq. (4.49) in terms of an effective potential $V_{\rm eff}(\mathscr{C})$ as

$$\Box^{\rm E}\mathscr{C} = \frac{dV_{\rm eff}(\mathscr{C})}{d\mathscr{C}}\,, \tag{4.50}$$

where

$$V_{\rm eff}(\mathscr{C}) = V(\mathscr{C}) + \rho^{\rm E}\left[\mathcal{A}(\mathscr{C}) - 1\right]\,. \tag{4.51}$$

Here, $\rho^{\rm E} \equiv -{\rm T}^{\rm E}/\mathcal{A}$ is the conserved energy density in the Einstein frame, which is independent of $\mathscr{C}$, and matter is assumed to be non-relativistic.

4.4.7 Chameleon mechanism

In $f(R)$ theories, the conformal coupling function $\mathcal{A}(\mathscr{C})$ in Eq. (4.47) introduces an additional, non-gravitational interaction mediated by the scalar field $\mathscr{C}$, often referred to as a fifth force. This force, due to the conformal coupling parameter $\beta \sim 1$, significantly affects particle motion, as matter is no longer purely subject to gravitational interactions in the Einstein frame. The effective potential $V_{\rm eff}(\mathscr{C})$ imparts a variable effective mass to the scalar field, which strongly depends on the ambient material density.

This density-dependent mass property is central to what is known as a chameleon theory. In high-density environments, such as in the Solar System, the scalar field becomes effectively heavy, thereby suppressing the fifth force and allowing the theory to remain compatible with local gravitational constraints. Conversely, in low-density environments, such as on cosmological scales, the field acquires a low effective mass, enabling the fifth force to play a significant role, potentially driving cosmic acceleration. This adaptability of the scalar field's mass across different densities allows the theory to meet both local experimental constraints and large-scale cosmological observations.

The behavior of the effective potential $V_{\rm eff}(\mathscr{C})$ is determined by the choice of the function $f(R)$. With an appropriate form for $f(R)$, the potential may indeed exhibit a minimum, given by

$$\left.\frac{dV_{\rm eff}}{d\mathscr{C}}\right|_{\mathscr{C}=\mathscr{C}_{\rm min}} = 0\,, \tag{4.52}$$

where $\mathscr{C}_{\rm min}$ denotes the scalar field value at this minimum. Around this minimum, the effective mass $m^2_{\rm eff}$ of the field is given by

$$m^2_{\rm eff} = \left.\frac{d^2V_{\rm eff}}{d\mathscr{C}^2}\right|_{\mathscr{C}=\mathscr{C}_{\rm min}} = \left[V_{,\mathscr{C}\mathscr{C}} + \kappa^2\beta^2\rho^{\rm E}\exp\left(\kappa\beta\mathscr{C}\right)\right]_{\mathscr{C}=\mathscr{C}_{\rm min}}\,, \tag{4.53}$$

where $V_{,\mathscr{C}\mathscr{C}} \equiv d^2V/d\mathscr{C}^2$. This equation shows that the effective mass $m_{\rm eff}$ is environment-dependent, varying with the local matter density $\rho^{\rm E}$. For regions with

high matter density, such as the Solar System, $m_{\rm eff}$ becomes large so that the fifth force range is so small that it cannot be detected ($m_{\rm eff} > 10^{-3}\,{\rm eV}$ for $\lambda < 0.2\,{\rm mm}$). In contrast, in low-density cosmological environments, $m_{\rm eff}$ is small, allowing $\mathscr{C}$ to drive the observed cosmic acceleration [241].

For an $f(R)$ theory to exhibit a chameleon mechanism, three specific conditions must be satisfied simultaneously:

i. $V_{,\mathscr{C}} < 0$, meaning that the effective potential $V_{\rm eff}$ has a minimum;

ii. $V_{,\mathscr{C}\mathscr{C}} > 0$, implying that the effective mass squared $m^2_{\rm eff}$ is positive; and

iii. $V_{,\mathscr{C}\mathscr{C}\mathscr{C}} < 0$, so that $m^2_{\rm eff}$ increases with the environmental matter density $\rho^{\rm E}$.

Using the definition $f_{,R} \equiv \exp\left(-\sqrt{2\kappa^2/3}\,\mathscr{C}\right)$, we can derive

$$V_{,\mathscr{C}}(\mathscr{C}) = \frac{\beta}{\kappa}\frac{R, f_R - 2f}{f^2_{,R}}, \tag{4.54}$$

$$V_{,\mathscr{C}\mathscr{C}}(\mathscr{C}) = \frac{1}{3}\left(\frac{R}{f_{,R}} + \frac{1}{f_{,RR}} - \frac{4f}{f^2_{,R}}\right), \tag{4.55}$$

$$V_{,\mathscr{C}\mathscr{C}\mathscr{C}}(\mathscr{C}) = \frac{2\kappa\beta}{3}\left(\frac{3}{f_{,RR}} + \frac{f_{,R}f_{,RRR}}{f^3_{,RR}} + \frac{R}{f_{,R}} - \frac{8f}{f^2_{,R}}\right). \tag{4.56}$$

Merely hiding the scalar field in high-density regions is not enough to circumvent the stringent constraints set by local gravity tests. The chameleon mechanism must also effectively influence the test masses used in laboratory experiments, ensuring that the scalar field remains concealed even under highly controlled conditions. As a consequence, the form of $f(R)$ is greatly constrained. Fortunately, $f(R)$ theories in the metric formalism naturally accommodate a chameleon mechanism.

In the Palatini formalism, the situation is problematic, particularly concerning the chameleon mechanism. By making similar variable redefinitions as in the metric formalism, where $\hat{y} = f_{,\hat{R}}(\hat{R})$, $\hat{g}^{\rm E}_{\mu\nu} = \hat{y}\hat{g}_{\mu\nu}$, and $\hat{y} = \exp\left(-\sqrt{2\kappa^2/3}\,\mathscr{L}\right)$, the Palatini $f(R)$ gravity in the Einstein frame takes the form

$$S^{\rm E}_{\rm Pal} = \int d^4x\sqrt{-\hat{g}^{\rm E}}\left[\frac{\hat{R}^{\rm E}}{2\kappa^2} - V(\mathscr{L})\right] + S_{\rm M}\left[\hat{g}^{\rm E}_{\mu\nu}\hat{y}^{-1}, \phi_{\rm M}\right]. \tag{4.57}$$

From this action, the scalar field equation is derived as

$$2\,\mathscr{L}V_{\mathscr{L}} + {\rm T}^{\rm E} = 0\,, \tag{4.58}$$

where $V_{\mathscr{L}} \equiv dV_{\mathscr{L}}/d\mathscr{L}$. This equation shows that the scalar field $\mathscr{L}$ is algebraically linked to the trace of the energy-momentum tensor, ${\rm T}^{\rm E}$. Consequently, the scalar

field does not satisfy a wave-like equation (i.e., $\Box^{\mathrm{E}}\mathscr{L} = 0$), and thus there is no well-defined effective potential or mass for $\mathscr{L}$. This lack of dynamism in the scalar field makes it impossible for the Palatini formalism to support a chameleon mechanism. Without a dynamic scalar field that can acquire a large effective mass in high-density regions, Palatini $f(R)$ gravity fails to implement the screening effects necessary to meet local gravity test constraints [239]. This incompatibility with a chameleon-like screening mechanism fundamentally limits the Palatini approach's viability in describing gravity at both cosmological and local scales.

4.4.8 Theoretical and observational bounds

From the analysis in previous subsections, it becomes evident that the mathematical form of $f(R)$ in modified gravity cannot be arbitrary. For these theories to be both theoretically sound and phenomenologically viable, they must satisfy several critical requirements [51]:

1. Stability in the interval of R relevant to cosmological interest, i.e.,

$$f_{,R}(R) > 0 \quad \text{and} \quad f_{,RR}(R) > 0; \tag{4.59}$$

2. A correct Newtonian limit, i.e.,

$$|f(R) - R| \ll R, \quad |f_{,R}(R) - 1| \ll 1, \quad R f_{,RR}(R) \ll 1, \tag{4.60}$$

   for $R \gg R_0$, where R_0 is the present-day curvature scalar;

3. Indistinguishability from GR at the current level of accuracy in laboratory experiments and Solar System tests of gravity;

4. Recovery of GR in the high-curvature regime, i.e.,

$$\lim_{R\to\infty} f(R) = R - 2\Lambda, \tag{4.61}$$

   which also requires $f_{,R}(\infty) = 1$, implying $0 < f_{,R}(R) < 1$ for all R; and

5. A stable (or metastable) asymptotic de Sitter future.

In the first condition, $f_{,R}(R) > 0$ ensures that gravity be attractive (i.e., gravitons are not ghosts) while $f_{,RR}(R) > 0$ prevents the scalaron from becoming a tachyon in the high-curvature regime.The second and third conditions represent the need for MTGs to reduce to Newton's theory in the weak-field and slow-motion limit, where gravity is well-constrained by the PPN expansion. The fourth condition accounts for the fact that several primordial probes, such as the CMB, strongly agree with

the robust predictions of the flat-ΛCDM model, such as the BBN, an early RD age, and another middle MD age. Finally, the fifth condition ensures a stable de Sitter future, which is essential for explaining the observed current accelerated expansion of the universe.

4.5 $f(R)$ cosmology

Before deriving cosmological dynamics within the framework of $f(R)$ gravity, we emphasize that all previously stated assumptions regarding the distribution of matter and the curvature of spatial three-section are preserved here. This approach allows us to focus solely on modifications to the gravitational sector of the field equations and to analyze their implications for cosmology. Essentially, we continue to adhere to the CP, the flat RW metric, and energy-momentum conservation. Additionally, we shall adopt the metric formalism from this point onward, meaning that all results derived henceforth will apply solely within the context of the Levi-Civita metric compatible connection $\Gamma^{\lambda}_{\mu\nu}$.

4.5.1 Background dynamics

By substituting the RW metric from Eq. (3.46) into Eqs. (4.22), we obtain the Friedmann equations

$$3H^2 = \kappa^2 \left(\rho_{\rm M} + \rho_{\rm DE}\right) , \tag{4.62}$$

$$2\dot{H} + 3H^2 = -\kappa^2 \left(P_{\rm M} + P_{\rm DE}\right) , \tag{4.63}$$

where we have defined

$$\kappa^2 \rho_{\rm DE} \equiv \frac{1}{2}\left[R f_{,R}(R) - f(R)\right] - 3H\dot{f}_{,R}(R) + 3H^2\left[1 - f_{,R}(R)\right] , \tag{4.64}$$

$$\kappa^2 P_{\rm DE} \equiv -\frac{1}{2}\left[R f_{,R}(R) - f(R)\right] + 2H\dot{f}_{,R}(R) - (2\dot{H} + 3H^2)\left[1 - f_{,R}(R)\right] + \ddot{f}_{,R}(R) . \tag{4.65}$$

Here, the Ricci scalar is given by

$$R = 6\left(\dot{H} + 2H^2\right) , \tag{4.66}$$

as in the GR case. Essentially, $\rho_{\rm DE}$ and $P_{\rm DE}$ correspond to the energy density and pressure contributions, respectively, arising from the modification in the gravitational sector, $R \to f(R)$. Naturally, these terms depend on the specific form of the $f(R)$ function.

By dividing Eq. (4.65) by Eq. (4.64), we obtain $w_{\rm DE} = P_{\rm DE}/\rho_{\rm DE}$, where $w_{\rm DE}$ functions as an equation of state for a barotropic fluid (though it is not, in fact, a

physical fluid). It can then be verified that this geometric component satisfies the continuity equation,

$$\dot{\rho}_{\rm DE} + 3H\left(\rho_{\rm DE} + P_{\rm DE}\right) = 0\,. \tag{4.67}$$

In particular, for the GR case, where $f(R) \equiv R - 2\Lambda$, Eqs. (4.64) and (4.65) reduce to those of a cosmological constant with $P_{\rm DE} = -\rho_{\rm DE}$, implying $w_{\rm DE} \equiv w_\Lambda = -1$.

By combining the first two equations, we arrive at the acceleration equation,

$$\frac{\ddot{a}}{a} = -\frac{\kappa^2}{6}\left(\rho_{\rm eff} + 3P_{\rm eff}\right) = -\frac{\kappa^2\rho_{\rm eff}}{6}\left(1 + 3w_{\rm eff}\right)\,, \tag{4.68}$$

where $\rho_{\rm eff} \equiv \rho_{\rm M} + \rho_{\rm DE}$, $P_{\rm eff} \equiv P_{\rm M} + P_{\rm DE}$, and $w_{\rm eff} \equiv P_{\rm eff}/\rho_{\rm eff}$. Then, by combining Eqs. (4.68) and (4.62), we obtain

$$w_{\rm eff} = -1 - \frac{2\dot{H}}{3H^2}\,. \tag{4.69}$$

Notice that the current accelerated expansion can be achieved if $P_{\rm eff} < -\rho_{\rm eff}/3$, or, equivalently, $w_{\rm eff} < -1/3$.

Finally, the deceleration parameter is given by

$$q\left(t\right) \equiv -\frac{\ddot{a}}{aH^2} = -1 - \frac{\dot{H}}{H^2}\,, \tag{4.70}$$

where H, $\dot{H}$, and $\ddot{a}$ are solutions of Eqs. (4.62), (4.63), and (4.68), respectively. Notice that R includes the first time derivative of H, implying it also involves the second derivative with respect to the scale factor $a(t)$. Since the Friedmann equations contain the second time derivative of f, they are effectively fourth-order in time with respect to the scale factor. To solve them, we thus require four initial conditions: $a(t_i)$, $\dot{a}(t_i)$, $\ddot{a}(t_i)$, and $\dddot{a}(t_i)$.

4.5.2 Autonomous equations

The minimal cosmological model is known to have a series of well-established eras, meaning that a generic model should start with a very short inflationary period, followed by a RD epoch, then a MD epoch, and, finally, the current acceleration phase. In this context, $f(R)$ models that fit this cosmic history are referred to as cosmologically viable (or simply viable). Consequently, the universe's timeline, as consistent with observations, constrains the possible forms of the $f(R)$ function. We will now examine the conditions under which an $f(R)$ model is viable for reproducing this cosmic chronology.

For general $f(R)$ models, it is convenient to use the dimensionless variables [44]:

$$x_1 = -\frac{\dot{f}_{,R}}{H f_{,R}}\,, \tag{4.71}$$

$$x_2 = -\frac{f}{6H^2 f_{,R}}\,, \tag{4.72}$$

$$x_3 = \frac{R}{6H^2} = \frac{\dot{H}}{H^2} + 2\,, \tag{4.73}$$

$$x_4 = \frac{\kappa^2 \rho_r}{3H^2 f_{,R}}\,. \tag{4.74}$$

From Eq. (4.62), we obtain the following algebraic identity,

$$\tilde{\Omega}_{\rm m} \equiv \frac{\kappa^2 \rho_{\rm m}}{3H^2 f_{,R}} = 1 - x_1 - x_2 - x_3 - x_4\,. \tag{4.75}$$

The equations of motion then follow straightforwardly:

$$\frac{dx_1}{dN} = -1 - x_3 - 3x_2 + x_1^2 - x_1 x_3 + x4\,, \tag{4.76}$$

$$\frac{dx_2}{dN} = \frac{x_1 x_3}{p} - x_2\left(2x_3 - 4 - x_1\right)\,, \tag{4.77}$$

$$\frac{dx_3}{dN} = -\frac{x_1 x_3}{p} - 2x_3\left(x_3 - 2\right)\,, \tag{4.78}$$

$$\frac{dx_4}{dN} = -2x_3 x_4 + x_1 x_4\,, \tag{4.79}$$

where $N \equiv \ln a$ and

$$p \equiv \frac{d\log f_{,R}}{d\log R} = \frac{R f_{,RR}}{f_{,R}}\,, \tag{4.80}$$

$$s \equiv -\frac{d\log f}{d\log R} = -\frac{R f_{,R}}{f} = \frac{x_3}{x_2}\,. \tag{4.81}$$

Since Eq. (4.80) allows us to write R in terms of x_3/x_2, and Eq. (4.81) can also be rewritten in terms of this ratio, we find that $p = p(s)$.

Finally, it is convenient to express w_{DE} and $w_{\rm eff}$ as

$$w_{\rm DE} = \frac{1}{3}\frac{1 - x_4 f_{,R} - 2x_3}{1 - f_{,R}\left(1 - x_1 - x_2 - x_3\right)}\,, \tag{4.82}$$

$$w_{\rm eff} = -\frac{1}{3}\left(2x_3 - 1\right)\,, \tag{4.83}$$

Notice that in Ref. [44], the term $f_{,R}$ in the first of the above equations is always divided by a term referred to as F_0. In our approach here, $F_0 = 1$.

4.5.3 Critical points

The cosmological dynamics can then be analyzed through the analytical properties of the phase space associated with the system of equations (4.76) to (4.79). For a more pedagogical approach, we divide the analysis into two parts (following Ref. [44]). First, we disregard radiation component ($x_4 = 0$) and then reconsider it.

In the absence of radiation, the critical points of the system for any $p(s)$ are:

$$P_1 : (x_1, x_2, x_3) = (0, -1, 2), \quad \tilde{\Omega}_{\rm m} = 0, \quad w_{\rm eff} = -1\,, \tag{4.84}$$

$$P_2 : (x_1, x_2, x_3) = (-1, 0, 0), \quad \tilde{\Omega}_{\rm m} = 2, \quad w_{\rm eff} = 1/3\,, \tag{4.85}$$

$$P_3 : (x_1, x_2, x_3) = (1, 0, 0), \quad \tilde{\Omega}_{\rm m} = 0, \quad w_{\rm eff} = 1/3\,, \tag{4.86}$$

$$P_4 : (x_1, x_2, x_3) = (-4, 5, 0), \quad \tilde{\Omega}_{\rm m} = 0, \quad w_{\rm eff} = 1/3\,, \tag{4.87}$$

$$P_5 : (x_1, x_2, x_3) = \left(\frac{3p}{x_p}, -\frac{y_p}{2x_p^2}, \frac{y_p}{2x_p}\right), \quad \tilde{\Omega}_{\rm m} = \frac{\bar{z}_p}{2x_p^2}, \quad w_{\rm eff} = -\frac{p}{x_p}\,, \tag{4.88}$$

$$P_6 : (x_1, x_2, x_3) = \left(\frac{2\bar{x}_p}{z_p}, \frac{\bar{y}_p}{pz_p}, -\frac{x_p\bar{y}_p}{pz_p}\right), \quad \tilde{\Omega}_{\rm m} = 0, \quad w_{\rm eff} = -\frac{j_p}{3pz_p}\,, \tag{4.89}$$

where $x_p \equiv 1+p$, $y_p \equiv 1+4p$, $z_p \equiv 1+2p$, $\bar{x}_p \equiv 1-p$, $\bar{y}_p \equiv 1-4p$, $\bar{z}_p \equiv 2-3p-8p^2$, and $j_p \equiv 2-5p-6p^2$. Broadly speaking, we examine the fixed points in light of the behavior of the effective EoS parameter, $w_{\rm eff}$. We select solutions that produce both a standard MD epoch (i.e., $w_{\rm eff} = 0 \to a \propto t^{2/3}$, or $x_3 = 1/2$) and a late acceleration phase. Starting with the MD era, the only possible solution is $p = 0$ (P_5); the other possibility, $m = -(5 \pm \sqrt{73})/12$ (P_6), is ruled out because it has $\tilde{\Omega}_{\rm m} = 0$, which does not yield a standard MD epoch when a non-relativistic fluid is in charge [242, 243]. On the other hand, only P_1, P_5, and P_6 can produce accelerated solutions. Thus, an $f(R)$ theory compatible with observations would have trajectories passing near P_5 with p close to zero and resting on an accelerated attractor [44].

In what follows, we describe the stability of fixed points by classifying them as attractors, saddles, or repulsors in phase space, using linearization techniques.

- P_1: With $w_{\rm eff} = -1$, this point corresponds to de Sitter solutions ($\dot{H} = 0$), and has eigenvalues

$$-3\,, \ \frac{-3}{2} \pm \frac{\sqrt{25 - 16/p_1}}{2}\,, \tag{4.90}$$

  where $p_1 = p(s = -2)$. Consequently, P_1 is stable for $0 < p_1 \leq 1$ and a saddle point otherwise.

- P_2: This point is characterized by a ψ-matter dominated epoch (ψMDE) in which a field ψ and matter coexist with constant energy fractions. Its eigenvalues are given by

$$-2\,, \ \frac{1}{2}\left(\mathscr{E}_2 \pm \sqrt{\mathscr{E}_2^2 - 4\mathscr{F}_2}\right)\,, \tag{4.91}$$

where

$$\mathscr{E}_2 \equiv 7 + \frac{1}{p_2} - \frac{s(1+s)}{p_2^2}\frac{dp_2}{ds}\,, \quad \mathscr{F}_2 \equiv 12 + \frac{3}{p_2} - \frac{s(3+4s)}{p_2^2}\frac{dp_2}{ds}\,. \tag{4.92}$$

If p is constant, the eigenvalues reduce to $-2, 3, 4 + 1/p_2$ and P_2 is a saddle point. However, it is a stable node on the subspace $x_3 = sx_2$ for $-1/4 < p < 0$. The necessary and sufficient condition for P_2 to exist is

$$\lim_{x_{2,3}\to 0} \frac{x_3}{p_2} = 0\,, \tag{4.93}$$

corresponding to $\frac{f_{,R}}{H^2 f_{,RR}} \to 0$ for $\frac{R}{H^2} \to 0$ and $\frac{f}{H^2 f_{,R}} \to 0$. Thus, the incorrect MD era is generally intrinsic to $f(R)$ models.

- P_3: Similar to P_2, this point is characterized by a kinetic epoch but with a vanished matter energy fraction. The eigenvalues are

$$2\,,\ \frac{1}{2}\left(\mathscr{E}_3 \pm \sqrt{\mathscr{E}_3^2 - 4\mathscr{F}_3}\right)\,, \tag{4.94}$$

where

$$\mathscr{E}_3 \equiv 9 - \frac{1}{p_3} + \frac{s(1+s)}{p_3^2}\frac{dp_3}{ds}\,, \quad \mathscr{F}_3 \equiv 20 - \frac{5}{p_3} + \frac{s(5+4s)}{p_3^2}\frac{dp_3}{ds}\,. \tag{4.95}$$

If $p = const$, the eigenvalues reduce to $2, 5, 4 - 1/p_3$. In this case, P_3 is a saddle point for $0 \leq p_3 \leq 1/4$ and unstable otherwise.

- P_4: This point is similar to P_3. It has eigenvalues given by

$$-5\,,\ -3\,,\ 4\left(1 + \frac{1}{p_4}\right)\,. \tag{4.96}$$

It is stable within the interval $-1 < p_4 < 0$ and a saddle otherwise. Neither P_3 nor P_4 can represent the MD or accelerated epochs.

- P_5: This point corresponds to *scaling solutions* where the ratio $\tilde{\Omega}_{\rm m}/\Omega_{\rm DE}$ is constant. A standard MD epoch with $a \propto t^{2/3}$ and $\tilde{\Omega}_{\rm m} = 1$ can be obtained from this point by taking $m_5 \to 0$. The necessary condition for P_5 to exist as an exact standard MD era is

$$p(s = -1) = 0\,. \tag{4.97}$$

The eigenvalues of this point are

$$3\left(1+\frac{dp_5}{ds}\right)\,,\ \frac{-3p_5 \pm \sqrt{p_5(256p_5^3+160p_5^2-31p_5-16)}}{4p_5(p_5+1)}\,. \tag{4.98}$$

In the limit $|m_5| \ll 1$, these eigenvalues reduce to

$$3\left(1+\frac{dp_5}{ds}\right)\,,\ -\frac{3}{4} \pm \sqrt{-\frac{1}{p_5}}\,. \tag{4.99}$$

Generally, models with $m_5 < 0$ are not viable, except for a very narrow range of initial conditions. For $0 < m_5 < 0.327$ and $dp_5/ds > -1$, P_5 can be a saddle point with damped oscillation, allowing the universe to evolve toward P_5 and then transition to a late acceleration. Since $x_3/x_2 = -p(s) - 1$, i.e., $p(s) = -s - 1$, the conditions for a saddle MD epoch with damped oscillation are

$$p(s \leq -1) > 0\,, \quad \frac{dp}{ds}(s \leq -1) > -1\,. \tag{4.100}$$

These conditions supplement Eq. (4.97).

- P_6: This point represents a curvature-dominated point with $w_{\rm eff} = w_{\rm eff}(p)$. Its eigenvalues are

$$-4+\frac{1}{p_6}\,,\ \frac{2-3p_6-8p_6^2}{p_6(1+2p_6)}\,,\ -\frac{2\,(p_6^2-1)\,(1+dp_6/ds)}{p_6(1+2p_6)}\,. \tag{4.101}$$

The stability of P_6 depends on p_6 and dp_6/ds. Notably, P_6 coincides with P_1 for $m_6 = 1$ and transitions to $P_6 \to (-1, 0, 2)$ with $w_{\rm eff} \to -1$ as $p_6 \to \pm\infty$. P_6 is stable and accelerated under four conditions. When $dp_6/ds > -1$, P_6 is stable and accelerated under:

1. For $p_6 < -\frac{1+\sqrt{3}}{2}$, it is accelerated but not phantom ($w_{\rm eff} > -1$);
2. For $-\frac{1}{2} < p_6 < 0$, it is strongly phantom with $w_{\rm eff} < -7.6$; and
3. For $p_6 \geq 1$, it is slightly phantom with $-1.07 < w_{\rm eff} \leq -1$.

Additionally, P_6 is stable and accelerated when $dp_6/ds < -1$ under:

4. For $\frac{\sqrt{3}-1}{2} < p_6 < 1$, it is a non-phantom ($w_{\rm eff} > -1$).

In summary, asymptotic acceleration in $f(R)$ models excludes an EoS within $-7.6 < w_{\rm eff} < 1.07$ [44].

Incorporating radiation modifies the fixed points by introducing two additional points, P_7 and P_8, while retaining the original fixed points P_1 to P_6. Here is a

breakdown of these two new points and their implications:

$$P_7 : (x_1, x_2, x_3, x_4) = (0, 0, 0, 1), \quad \tilde{\Omega}_{\rm m} = 0, \quad w_{\rm eff} = 1/3\,, \tag{4.102}$$

$$P_8 : (x_1, x_2, x_3, x_4) = \left(\frac{4p}{x_p}, -\frac{2p}{x_p^2}, \frac{2p}{x_p}, \frac{h_p}{x_p^2}\right), \quad \tilde{\Omega}_{\rm m} = 0, \quad w_{\rm eff} = w_p\,, \tag{4.103}$$

where $h_p \equiv 1 - 2p - 5p^2$ and $w_p \equiv (1 - 3p)/(3 + 3p)$. Notably, P_7 corresponds to a standard radiation point. When p is constant, it has eigenvalues of $1, 4, 4, -1$, indicating that P_7 is a saddle point in this case. In contrast, P_8 represents a new ψ-RD epoch with non-vanishing DE. Observations from BBN constrain $w_{\rm eff}$ to be close to $1/3$, so P_8 can yield an acceptable RD epoch only for $p_8 \approx 0$. The eigenvalues of P_8 are

$$1\,,\ 4\left(1 + \frac{dp_8}{ds}\right)\,,\ \frac{p_8 - 1 \pm \sqrt{81p_8^2 + 30p_8 - 15}}{2(p_8 + 1)}\,. \tag{4.104}$$

For $p_8 \to 0$, the last two eigenvalues are complex with negative real parts, indicating that P_8 is a saddle point around the radiation point. Consequently, the solutions eventually repel away from the RD era and transition to one of the previously mentioned fixed points. Additionally, it is noticed that P_8 (like P_5) lies on the line $p(s) = -s - 1$. Therefore, if the condition for the existence of the matter point P_5 (i.e., $p \approx 0$ and ≈ -1) is satisfied, a radiation point P_8 exists within the same region.

This fixed-point analysis enables us to trace the evolutionary path of the $f(R)$ models. Within this framework, a viable cosmological trajectory begins near the radiation point P_8 with $p \approx 0$, then transitions to the matter point P_5 with $p \approx 0$, and ultimately approaches one of the accelerated points mentioned above [44].

4.5.4 $f(R)$ classification and viable models

The preceding discussion, based on the research outlined in Ref. [44], indicates that there are several conditions that must be met for an $f(R)$ model to be cosmologically viable. Essentially, the geometrical properties of the $p(s)$ curve in the plane (s, p) and its intersections with the critical line $p = -s - 1$ allow us to classify the $f(R)$ models into four distinct classes.

- Class I: This class encompasses all cases where the curve $p(s)$ does not connect the accelerated attractor with the standard matter point $(s, p) = (-1, 0)$. Instead, the solutions either reach the fixed point ψMDE or bypass it completely, transitioning into the final attractor without experiencing any MD epoch.

- Class II: This class includes models where the curve $p(s)$ connects the upper vicinity of the standard matter point $(s, p) = (-1, 0)$, satisfying $p > 0$ and

$dp_5/ds > -1$, to the point P_1 with $0 < p(s = -2) \leq 1$, or asymptotically approaches P_6 as $s \to \pm\infty$.

- Class III: This class is characterized by a very fast transient MD era that can only occur within a narrow range of initial conditions. These models are known to cross the critical line at $-1/2 < p < 0$ and generally experience a MD epoch followed by a strongly phantom accelerated epoch, where $w_{\text{eff}} \to -\infty$ as $p \to -0$.

- Class IV: In this class, the curve $p(s)$ connects the upper vicinity of the standard matter point $(s, p) = (-1, 0)$, satisfying $p > 0$ and $dp_5/ds > -1$, to the critical line $p = -s - 1$ with $dp_6/ds > -1$.

The models belonging to Classes I and III can be discarded immediately for the following reasons. First, the point P_2 represents a ψMDE with an incorrect evolution of the scale factor, given by $a \propto t^{1/2}$. Second, a stable and sufficiently long MD epoch is necessary for structure formation in the universe. Additionally, a strongly phantom acceleration, such as $w_{\text{eff}} \approx -7.6$ (which implies $\Omega_{\text{DE}} \simeq w_{\text{eff},0}/\Omega_{\text{DE},0}$ is even smaller) are generally discarded by observations. On the other hand, the models from classes II and IV are, in principle, cosmologically viable, as they possess a sufficiently long MD epoch connected to either a late-time de Sitter expansion (class II) or a late-time non-phantom acceleration with $w_{\text{eff}} > -1$ (class IV).

Of course, our discussion thus far has focused solely on the critical points; we cannot exclude the possibility that unique trajectories with some specific initial conditions could reproduce an acceptable cosmology. Consequently, a thorough numerical analysis is required, conducted on a case-by-case basis. Broadly speaking, the $f(R)$ models should satisfy the following conditions:

1. A suitable MD era necessary for structure formation, satisfying

$$p(s) \approx +0\,, \quad \frac{dp(s)}{ds} > -1\,, \tag{4.105}$$

   at $s = -1$; and

2. A subsequent accelerated phase such that

$$0 \leq p(s) \leq 1 \tag{4.106}$$

   at $s = -2$, or

$$p(s) = -s - 1\,, \quad \frac{\sqrt{3} - 1}{2} < p(s) \leq 1\,, \quad \frac{dp(s)}{ds} < -1\,. \tag{4.107}$$

The ΛCDM model corresponds to the straight line $p = 0$, $\forall s$. Since the viable $f(R)$ models are those that approach the ΛCDM at high-curvature (i.e., when $R \gg R_0$), $p(s)$ must be close to zero during the MD epoch, as indicated by the first condition in Eq. (4.105). The second condition is required to connect the MD epoch to the current acceleration age; the constraints in Eq. (4.106) indicate a purely de Sitter vacuum ($w_{\rm eff} = -1$), while Eqs. (4.107) corresponds to a non-phantom attractor ($w_{\rm eff} > -1$). Therefore, regarding Eqs. (4.106) and (4.107), the $f(R)$ models need to satisfy only one of these conditions.

4.5.5 $f(R)$ cosmological perturbations

As with the general relativistic theory of cosmological perturbation, the idea here is to add perturbations to the uniformly smoothed background so that we can describe the evolution of inhomogeneities and the growth of structures in light of the $f(R)$ theories of modified gravity. As in the GR case, we shall only consider here the first-order terms of the perturbations [62, 63, 244, 245]. The non-linear theory of cosmological perturbations can be reviewed from Refs. [246–248].

The first steps, such as establishing metric fluctuations ($\delta g_{\mu\nu}$) and material content fluctuations ($\delta T_{\mu\nu}$), defining invariant quantities ($\Phi_{\rm B}$, $\Psi_{\rm B}$), and choosing the work gauge (Newtonian gauge) are identical to those in the GR case. However, we shall also need to consider small (linear) fluctuations around f, such that

$$f = \bar{f} + \delta f\,, \quad |\delta f| \ll \bar{f}\,. \tag{4.108}$$

Next, the geometry fluctuations must be incorporated into the perturbation of the modified Einstein tensor, $\delta\tilde{G}_{\mu\nu}$, so that the perturbed $f(R)$ field equations, assuming zero anisotropic stress ($\Pi_{ij} = 0$), are given in the Newtonian gauge by [35]

$$\begin{aligned} 3H(H\Phi + \dot{\Psi}) - a^{-2}\,\nabla^2\Psi = \frac{1}{2f_{,R}}\Big[&3H\delta\dot{f}_{,R} - \left(3H^2 + 3\dot{H} + a^{-2}\,\nabla^2\right)\delta f_{,R} \\ &-3\dot{f}_{,R}\left(H\Phi + \dot{\Psi}\right) - 3H\dot{f}_{,R}\Phi - \kappa^2\bar{\rho}\delta\Big]\,, \end{aligned} \tag{4.109}$$

$$H\Phi + \dot{\Psi} = \frac{1}{2f_{,R}}\left(\delta\dot{f}_{,R} - H\delta f_{,R} - \dot{f}_{,R}\Phi - \kappa^2\delta q\right)\,, \tag{4.110}$$

$$\Psi - \Phi = \frac{\delta f_{,R}}{f_{,R}}\,, \tag{4.111}$$

$$\begin{aligned} 3\dot{H}\Phi + a^{-2}\,\nabla^2\Phi = \frac{1}{2f_{,R}}\Big[&3\,\delta\ddot{f}_{,R} + 3H\delta\dot{f}_{,R} - \left(6H^2 + a^{-2}\,\nabla^2\right)\delta f_{,R} - 3\dot{f}_{,R}\dot{\Phi} \\ &-3\dot{f}_{,R}\left(H\Phi + \dot{\Psi}\right) - \left(3H\dot{f}_{,R} - 6\ddot{f}_{,R}\right)\Phi + \kappa^2\left(\bar{\rho}\delta + \delta P\right)\Big]\,, \end{aligned} \tag{4.112}$$

$$\delta\ddot{f}_R + 3H\delta\dot{f}_R - \left(a^{-2}\,\nabla^2 - M_s^2\right)\delta f_R = \dot{f}_R\left(3H\Phi + 3\dot{\Psi} + \dot{\Phi}\right) + \left(2\ddot{f}_R + 3H\dot{f}_R\right)\Phi + \frac{1}{3}\kappa^2\left(\bar{\rho}\delta - 3\delta P\right)\,, \tag{4.113}$$

In order to derive Eq. (4.113), we have used the squared scalaron mass

$$M_{\rm s}^2 \equiv \frac{1}{3}\left(\frac{f_{,R}}{f_{,RR}} - R\right)\,, \tag{4.114}$$

along with the relation $\delta f_{,R} = f_{,RR}\,\delta R$, where

$$\delta R = -2\left[3\left(2\dot{H}\Phi + H\dot{\Phi} + \ddot{\Psi}\right) + 12H\left(H\Phi + \dot{\Psi}\right) + a^{-2}\left(\nabla^2\Phi - 2\nabla^2\Psi\right)\right]. \tag{4.115}$$

The first thing we must realize is that Eqs. (4.109), (4.110), and (4.111) fully recover the perturbed Einstein equations (3.75), (3.76), and (3.77), respectively, in the GR regime $f(R) = R - 2\Lambda$ and $\Pi_{ij} = 0$ (recalling that the Einstein linearized equations have been written in terms of the conformal time $d\eta \equiv dt/a$). Notice that Eq. (4.111) for the $f(R)$ case tell us that $\Psi \neq \Phi$ even in the absence of anisotropic stress. This fact enable us to detect possible deviations from GR by measuring $\Psi/\Phi \neq 1$ with some precision. After some manipulations in order to make the terms $\ddot{\Psi}$ and $\nabla^2\Psi$ appear, Eq. (4.112) recovers Eq. (3.78) in the GR limit. Finally, Eq. (4.113) implies a pure adiabatic fluctuations case, as shown in Eq. (3.87), with $c_{\rm s}^2 = 1/3$ in the same regime. In the most general case of $f(R)$ gravity, one observes a particular mass term $M_{\rm s}^2$ defined in Eq. (4.114). Using the scalar-tensor formulation of $f(R)$ theories, we see that this term is related to the scalaron effective mass $m_{\rm eff}^2$, defined in Eq. (4.53). Indeed, $M_{\rm s} = m_{\rm eff}$.

4.5.6 Modified contrast equation and growth rate

Let us consider the perturbations of non-relativistic matter with negligible pressure ($P_{\rm m} = 0$). In this way, Eqs. (3.73) and (3.74) yield in Fourier space

$$\delta\dot{\rho}_{\rm m} + 3H\delta\rho_{\rm m} = \bar{\rho}\left(3\dot{\Psi} - \frac{k^2}{a^2}v\right)\,, \tag{4.116}$$

$$\dot{v} = \Phi\,, \tag{4.117}$$

respectively, where we have used the matter continuity equation, $\dot{\bar{\rho}}_{\rm m} + 3H\bar{\rho}_{\rm m} = 0$, in the second line. The matter density contrast, $\delta_{\rm m} = \delta\rho_{\rm m}/\bar{\rho}_{\rm m} + 3Hv$, then obeys the following equation, obtained from Eqs. (4.116) and (4.117):

$$\ddot{\delta}_{\rm m} + 2H\dot{\delta}_{\rm m} + \frac{k^2}{a^2}\Phi = 3\ddot{X}_{\rm B} + 6H\dot{X}_{\rm B}\,, \tag{4.118}$$

where $X_{\rm B} \equiv \Psi + Hv$.

To obtain the equation that approximately describes the evolution of pressureless matter perturbations, let us consider the sub-horizon approximation, where $k \gg aH$. Another useful tool when deriving such an equation is the so-called quasi-static approximation, under which the dominant terms in Eqs. (4.109)-(4.113) and (4.118) correspond to those including k^2/a^2, $\delta_{\rm m}$, and $M_{\rm s}^2$. It follows from Eqs. (4.109) and (4.111) that

$$\Psi \simeq \frac{1}{2f_{,R}}\left(\delta f_{,R} - \frac{a^2}{k^2}\kappa^2\bar{\rho}_{\rm m}\delta_{\rm m}\right), \quad \Phi \simeq -\frac{1}{2f_{,R}}\left(\delta f_{,R} + \frac{a^2}{k^2}\kappa^2\bar{\rho}_{\rm m}\delta_{\rm m}\right), \tag{4.119}$$

and from Eq. (4.113) that

$$\left(\frac{k^2}{a^2} + M_{\rm s}^2\right)\delta f_{,R} \simeq \frac{1}{3}\kappa^2\bar{\rho}_{\rm m}\delta_{\rm m}\,. \tag{4.120}$$

Therefore, we have

$$\frac{k^2}{a^2}\Psi \simeq -\frac{\kappa^2\bar{\rho}_{\rm m}\delta_{\rm m}}{2f_{,R}}\frac{2 + 3M_{\rm s}^2a^2/k^2}{3\left(1 + M_{\rm s}^2a^2/k^2\right)}\,, \tag{4.121}$$

and

$$\frac{k^2}{a^2}\Phi \simeq -\frac{\kappa^2\bar{\rho}_{\rm m}\delta_{\rm m}}{2f_{,R}}\frac{4 + 3M_{\rm s}^2a^2/k^2}{3\left(1 + M_{\rm s}^2a^2/k^2\right)}\,. \tag{4.122}$$

We can also define the effective potential $\Phi_{\rm eff} \equiv (\Phi + \Psi)/2$. From Eqs. (4.121) and (4.122), we obtain

$$\Phi_{\rm eff} \simeq -\frac{\kappa^2}{2f_{,R}}\frac{a^2}{k^2}\bar{\rho}_{\rm m}\delta_{\rm m}\,. \tag{4.123}$$

This quantity characterizes the light-ray deviation, which is related to the integrated Sachs-Wolfe (ISW) effect observed through CMB and weak lensing observations.

Neglecting the right-hand side of Eq. (4.118) relative to its left-hand side, and using Eq. (4.122), we finally obtain

$$\ddot{\delta}_{\rm m} + 2H\dot{\delta}_{\rm m} - 4\pi G_{\rm eff}\,\bar{\rho}_{\rm m}\delta_{\rm m} \simeq 0\,, \tag{4.124}$$

where $G_{\rm eff}$ is the *effective gravitational constant*, defined as

$$G_{\rm eff} \equiv \frac{G}{f_{,R}}\frac{1 + 4\,p\left(\frac{k^2}{a^2R}\right)}{1 + 3\,p\left(\frac{k^2}{a^2R}\right)}\,. \tag{4.125}$$

In obtaining this expression for $G_{\rm eff}$, we have used the fact that $M_{\rm s}^2 = \frac{R}{3}\left(\frac{1}{p} + 1\right)$.

We would like to recall that the viable $f(R)$ models are constructed to have a large $M_{\rm s}$ in the region of high density $R \gg R_0$. Throughout the RD and deep MD eras, we should have $p \ll 1$ so that $M_{\rm s}^2 \gg R$. If p reaches the order of 0.1

in the present epoch instead, then we should have $M_{\rm s}^2 \sim H_0^2$. The GR regime is characterized by the condition $M_{\rm s}^2 \gg k^2/a^2$, in which the effective gravitational constant has the asymptotic form $G_{\rm eff} \simeq G/f_{,R}$. Since $f_{,R} \simeq 1$ in this limit, we should have $G_{\rm eff} \simeq G$ and, therefore, Eq. (4.124) recovers Eq. (3.90). In contrast, when $M_{\rm s}^2 \ll k^2/a^2$, resulting in $G_{\rm eff} \simeq 4G/3f_{,R}$, this is known as the scalar-tensor regime, where the evolution of the matter density fluctuations is non-standard. The transition from one regime to the other is characterized by the condition $M_{\rm s}^2 = k^2/a^2$ and can occur during the MD phase for the wavenumbers relevant to the matter power spectrum [35].

Chapter 5

$f(R)$ models: Numerical Solutions & Observational Constraints

Everything we have discussed thus far applies to any $f(R)$ function. In this chapter, we focus on three specific forms of viable $f(R)$ known as the Appleby-Battye [49–51], Hu-Sawicki [46], and Starobinsky [47] models. In summary, we construct systems of coupled differential equations for each of these models and solve them numerically using the *Python* programming language. In doing so, we utilize the *solve_ivp* routine from the *scipy* library and alternate between the numerical methods LSODA[1] and RK48[2]. Next, we present three sets of cosmological observations: the Hubble rate $H(z)$ measurements obtained via the cosmic chronometer technique, the growth rate $[f\sigma_8](z)$ measurements derived from redshift-space distortion, and the apparent magnitudes $m_{\rm B}(z)$ of SNe Ia cataloged by the Pantheon+ and SH0ES collaborations. We then constrain each model's parameters via MCMC simulations. Finally, we compare two of these models using AIC statistics, alongside the concordance flat-ΛCDM model. Our findings on the R^2-AB model are published in Ref. [249].

5.1 Three viable $f(R)$ models

A number of $f(R)$ models available in the literature fulfill all the requirements discussed in the previous chapter and produce a cosmic evolution consistent with observations. Such $f(R)$ cosmological dynamics closely resemble the ΛCDM model and are practically indistinguishable from it at the background level in most cases. In the high-curvature regime or in the very early universe, where $R \gg R_0$, these models fully recover the ΛCDM phenomenology.

[1]LSODA is the acronym for *livermore solver for ordinary differential equations*. This solver differs from the others since it switches automatically between the stiff BDF and the nonstiff Adams methods. So the user does not need to determine whether the problem is stiff or not.

[2]RK48 means the explicit Runge-Kutta method of order 5(4), where the error is controlled by assuming fourth-order method accuracy, but steps are taken using the fifth-order formula.

5.1.1 Appleby-Battye model

One requirement imposed on $f(R)$ theories is that they should appropriately mimic ΛCDM behavior in the high-curvature regime, where gravity is well constrained by both BBN and CMB observations. Essentially, this condition requires that $f_{,R} \to 1$ as $R \to \infty$. Additionally, since we must ensure the positivity of the first derivative of $f(R)$ with respect to R, we conclude that $f_{,R}$ must be an increasing function of R, satisfying

$$0 < f_{,R}(R) < 1. \tag{5.1}$$

Since the hyperbolic tangent function $\tanh(x)$ is restricted to the interval $[-1, 1]$, a simple choice satisfying Eq. (5.1) is to set

$$f_{,R}(R) = \frac{1}{2}\left[1 + \tanh\left(\epsilon_1 R - b\right)\right], \tag{5.2}$$

for any $\epsilon_1 > 0$. Integrating this expression with respect to R, we obtain

$$f(R) = \frac{R}{2} + \frac{\epsilon_{\rm AB}}{2} \ln\left[\cosh\left(\frac{R}{\epsilon_{\rm AB}} - b\right)\right] + \epsilon_2\,, \tag{5.3}$$

where $\epsilon_{\rm AB} \equiv 1/\epsilon_1$ and ϵ_2 is an integration constant. Because we seek $f(R)$ models that exhibit late-time accelerating solutions in the absence of DE, we need to impose that $f(0) = 0$. Thus, we find

$$\epsilon_2 = -\frac{\epsilon_{\rm AB}}{2} \ln\left(\cosh b\right). \tag{5.4}$$

Substituting this into Eq. (5.3), we arrived at the Appleby-Battye (AB) model [49]:

$$f^I_{\rm AB}(R) \equiv \frac{R}{2} + \frac{\epsilon_{\rm AB}}{2} \ln\left[\frac{\cosh\left(\frac{R}{\epsilon_{\rm AB}} - b\right)}{\cosh b}\right], \tag{5.5}$$

where $\epsilon_{\rm AB}$ and b are the model parameters, two more than the flat-ΛCDM model.

For this model, we have $f_{,R}(R_0) \sim 1$ and $f(R_0) \sim R_0 \ll f_{,R}(R_0)$, which means it satisfy the condition in Eq. (4.32) as well as the first condition in Eq. (4.34). However, the second condition, $f_{,RR}(R_0) \ll f_{,R}(R_0)$, required for an appropriate Newtonian limit, is not generally satisfied. From Eq. (5.2), we find the second derivative of $f(R)$ to be

$$f_{,RR}(R) = \frac{1}{2\epsilon_{\rm AB}} \mathrm{sech}^2\left(\frac{R}{\epsilon_{\rm AB}} - b\right). \tag{5.6}$$

Thus, the condition $f_{,RR}(R_0) \ll 1$ is satisfied if $R_0/\epsilon_{\rm AB} - b \gg 1$. This condition can be used in order to fix $\epsilon_{\rm AB}$ in terms of R_0 and b. To do so, we first expand

$f(R)$ around the de Sitter minimum, $R \sim R_0 \equiv R_{\rm vac}$, for large $y_{\rm AB} \equiv R/\epsilon_{\rm AB} - b$, obtaining [49]

$$f(R) \approx R - \frac{\epsilon_{\rm AB}}{2}\ln\left(1+e^{2b}\right) + \frac{\epsilon_{\rm AB}}{2}e^{-2y_{\rm AB}} + \mathscr{O}(e^{-4y_{\rm AB}})\,, \tag{5.7}$$

$$f_{,R}(R) \approx 1 - e^{-2y_{\rm AB}} + \mathscr{O}(e^{-4y_{\rm AB}})\,, \tag{5.8}$$

$$f_{,RR}(R) \approx \frac{2}{\epsilon_{\rm AB}}e^{-2y_{\rm AB}} + \mathscr{O}(e^{-4y_{\rm AB}})\,. \tag{5.9}$$

In this way, the vacuum field equations (4.25) give us

$$\epsilon_{\rm AB} = \frac{R_{\rm vac}}{b + \ln(\,2\cosh b\,)}\,, \tag{5.10}$$

$$R_{\rm vac} \equiv 12H_0^2\,. \tag{5.11}$$

The equations above tell us that the only free parameter of the AB model is b, whose allowed range will be determined below. Furthermore, GR is fully recovered in the limit $b \to \infty$ with $\Lambda \equiv R_{\rm vac}/4$.

The $f(R)$ function defined in Eq. (5.5) and its first derivative with respect to the Ricci scalar, R, are equivalent to writing

$$f^{I}_{\rm AB}(R) = R - \frac{R_{\rm vac}}{2} + \frac{\epsilon_{\rm AB}}{2}\ln\left[1+e^{-2\left(\frac{R}{\epsilon_{\rm AB}}-b\right)}\right] \tag{5.12}$$

and

$$f^{I}_{{\rm AB},R}(R) = 1 - \left[1+e^{2\left(\frac{R}{\epsilon_{\rm AB}}-b\right)}\right]^{-1}\,, \tag{5.13}$$

respectively. Thus, the vacuum field equations – i.e., Eqs. (4.22) – for the AB model correspond to

$$\mathscr{Q}(y) \equiv y + \ln\left[1+e^{-2(y-b)}\right] + \frac{y}{1+e^{2(y-b)}} - b - \ln\left(2\cosh b\right) = 0\,, \tag{5.14}$$

where $y \equiv R/\epsilon_{\rm AB}$. A stable de Sitter vacuum exists if $\frac{d\mathscr{Q}}{dy}(y_0) = 0$ has a solution $y = y_0 > 1$ for which $\frac{d^2\mathscr{Q}}{dy^2}(y_0) > 0$ and $\mathscr{Q}(y_0) \leq 0$ [250]. The authors of Refs. [51, 250] studied a generalized version of this model in which a parameter $g \in \left[0, \frac{1}{2}\right]$ was introduced, so that the last four terms in Eq. (5.14) are multiplied by $2g$. They then derived the following approximate relation between g and b:

$$\frac{1}{4} + \frac{0.28}{(b-0.46)^{0.81}} \leq g\,. \tag{5.15}$$

Since the model under investigation here corresponds to $g = 1/2$, we determine that $b \geq 1.6$ is required to achieve a stable de Sitter solution [51, 250, 251].

5.1.2 Hu-Sawicki model

The second $f(R)$ theory refers to the usual class of power-law models, known as the Hu-Sawicki (HS) models, described by [46]

$$f^I_{\rm HS}(R) = R - m_0^2 \frac{c_1 (R/m_0^2)^n}{c_2 (R/m_0^2)^n + 1}\,, \tag{5.16}$$

with $n > 0$, and c_1 and c_2 dimensionless parameters. This class of theories satisfies the requirements where $f(R \to \infty) = constant$ and $f(R \to 0) = 0$, ensuring the appropriate ΛCDM phenomenology as a limiting case but with no true cosmological constant. The curvature scale m_0 is defined as

$$m_0^2 \equiv \frac{\kappa^2 \rho_0}{3} = H_0^2 \Omega_{\rm m,0}\,. \tag{5.17}$$

In the high-curvature regime, $R \gg m_0^2$, Eq. (5.16) can be expanded as

$$\lim_{m_0^2/R \to 0} f(R) \approx R - \frac{c_1}{c_2} m_0^2 + \frac{c_1}{c_2^2} m_0^2 \left(\frac{m_0^2}{R}\right)^n\,. \tag{5.18}$$

Thus, the GR limiting case, for which $c_1/c_2^2 \to 0$ at fixed c_1/c_2, corresponds to a no true cosmological constant, given by

$$\Lambda \equiv \frac{m_0^2 c_1}{2 c_2}\,. \tag{5.19}$$

We can then use Eq. (5.17) along with $\Lambda = 3H_0^2\,(1 - \Omega_{\rm m,0})$ to derive the relation

$$c_1 = 6 c_2 \frac{1 - \Omega_{\rm m,0}}{\Omega_{\rm m,0}}\,, \tag{5.20}$$

which links the model parameters c_1 to c_2. This implies that the true free parameters of this models are 2: n and c_2 (or n and c_1). This results in one more free parameter than in the AB model and two more than in the flat-ΛCDM model.

The expression in Eq. (5.16) can be rewritten in an alternative form

$$f^I_{\rm HS}(R) = R - 2\Lambda \frac{R^n}{R^n + \mu^{2n}}\,, \tag{5.21}$$

where Λ is defined by Eq. (5.19) and

$$\mu^2 \equiv m_0^2\, c_2^{-1/n}. \tag{5.22}$$

The number of free extra parameters remains 2, namely n and μ^2. In this framework, the ΛCDM model is recovered in the limit $\mu^2 \to 0$.

5.1.3 Starobinsky model

The third and last theory studied in this thesis is also a class of power-law $f(R)$ models, proposed by Starobinsky, defined as [47]

$$f_{\rm S}^{I}(R) = R + \lambda_{\rm S} R_{\rm S} \left[\left(1 + \frac{R^2}{R_{\rm S}^2} \right)^{-n} - 1 \right] , \tag{5.23}$$

where $n, \lambda_{\rm S} > 0$ and $R_{\rm S} \sim R_0$ is the present curvature scale. Similar to the first two models, this class also satisfies $f(0) = 0$, meaning the cosmological constant vanishes in flat spacetime.

In the high-curvature regime, $R \gg R_{\rm S}$, the functional form in Eq. (5.23) can be approximated as

$$\lim_{R/R_{\rm S}\to 0} f_{\rm S}^{\rm I}(R) \approx R - \lambda_{\rm S} R_{\rm S} + \lambda_{\rm S} R_{\rm S} \left(\frac{R}{R_{\rm S}} \right)^{-2n} , \tag{5.24}$$

from which we can identify

$$\Lambda \equiv \frac{\lambda_{\rm S} R_{\rm S}}{2}, \tag{5.25}$$

and thus obtain

$$R_{\rm S} = \frac{6H_0^2(1-\Omega_{m,0})}{\lambda_{\rm S}} . \tag{5.26}$$

In this form, n, $\lambda_{\rm S}$ and $R_{\rm S}$ are free parameters, although this relation shows that the actual free parameters of this class are two: n and $\lambda_{\rm S}$ (or n and $R_{\rm S}$). This matches the number of free parameters in the HS model, giving it one more than the AB model and two more than the flat-ΛCDM model.

On the other hand, the late-time asymptotic de Sitter solution has a curvature given by $R \equiv R_1 \equiv \bar{x}_1 R_{\rm S}$, where $R_1 = constant$ and $\bar{x}_1 > 0$ is the maximal solution of the equation [47, 252]

$$\lambda_{\rm S} = \frac{\bar{x}\,(1+\bar{x}^2)^{n+1}}{2\left[(1+\bar{x}^2)^{n+1} - 1 - (n+1)\bar{x}^2\right]} . \tag{5.27}$$

It satisfies the inequality $\bar{x}_1 < 2\lambda_{\rm S}$, so that $\Lambda(R_1) = R_1/4 < \Lambda(\infty)$. Finally, the stability condition of this future de Sitter solution, $f_{,R}(R_1) > R_1 f_{,RR}(R_1)$, imposes the following constraint on $\bar{x}_1$ [47, 252]:

$$\left(1+\bar{x}_1^2\right)^{2+n} > 1 + (n+2)\bar{x}_1^2 + (n+1)(2n+1)\bar{x}_1^4 . \tag{5.28}$$

For each n, there exists a corresponding $\bar{x}_1$ that marginally satisfies Eq. (5.28), providing the minimum allowed value of $\lambda_{\rm S}$. Table 5.1 summarizes the minimum values for both $\bar{x}_1$ and $\lambda_{\rm S}$ given n, obtained numerically from Eqs. (5.27) and (5.28) [252].

n	$\bar{x}_{1,\min}$	$\lambda_{\rm S,min}$
1	$\sqrt{3}$	$8/(3\sqrt{3})$
2	1.267	0.944
3	1.041	0.726
4	0.903	0.608

Table 5.1: Minimum allowed values of $\bar{x}_1$ and $\lambda_{\rm S}$, given n, as obtained from the stable de Sitter future conditions in Eqs. (5.27) and (5.28), for the Starobinsky model.

5.2 High curvature regime

As discussed in the previous chapter, $f(R)$ models must reproduce GR in the high-curvature limit and in the very early universe, $R \to \infty$. Thus, we expect only small corrections to GR for R much larger than the present curvature R_0. This implies that in the limit $R \gg R_0$, $f(R)$ models can be expanded as

$$f(R) \simeq R - 2\Lambda + \Xi(R)\,, \tag{5.29}$$

where the functions $\Xi(R)$ represent corrections to GR theory. For the AB, HS, and Starobinsky models, it can be shown that [46, 47, 51]

$$\Xi(R) = \begin{cases} (\epsilon_{\rm AB}/2)\exp\left[-\left(R/\epsilon_{\rm AB} - b\right)\right] & \text{(AB)} \\ (c_1 m_0^2/c_2)\left(R/m_0^2\right)^{-n} & \text{(HS)} \\ \lambda_{\rm S} R_{\rm S}\left(R/R_{\rm S}\right)^{-2n} & \text{(Starobinsky)} \end{cases} . \tag{5.30}$$

In addition to differing in their number of free parameters, the AB, HS, and Starobinsky models differ in the type of corrections they introduce to GR: the AB model has exponentially suppressed corrections, while both the HS and Starobinsky models contain power-law-type corrections to GR.

5.3 Weak curvature singularity

A sudden *weak curvature singularity* is known to form generically when $f_{,RR}(R)$ becomes zero for some finite value of R, such that the condition $f_{,RR}(R) > 0$ is marginally violated. This leads to two more elementary problems: an unbounded growth of the scalaron mass, which can be approximated by [35]

$$M_{\rm s}^2 \approx \frac{1}{3 f_{,RR}(R)}\,, \tag{5.31}$$

for $R \gg R_{\rm vac}$, and an undesired overabundance of this particle at high curvatures. In other words, this means that the scalaron decouples with the theory as R grows indefinitely at $R \gg R_{vac}$ [50, 51]. For the models in Eqs. (5.5), (5.16), and (5.23), as well as many others discussed in the literature, this behavior occurs for values of R within the range of cosmological interest, highlighting an incompleteness of these models.

Let us now examine the second derivative with respect to the curvature scalar R for the three $f(R)$ models. It can be shown that

$$f_{,RR}(R) \propto \begin{cases} \exp\left(-2R/\epsilon_{\rm AB}\right) & \text{(AB)} \\ \left(R/m_0^2\right)^{-(n+2)} & \text{(HS)} \\ \left(R/R_{\rm S}\right)^{-2(n+1)} & \text{(Starobinsky)} \end{cases} , \tag{5.32}$$

which indicates that $f_{,RR}(R)$ decrease either exponentially (in the AB model) or via a power-law (in both the HS and Starobinsky model). Since $f_{,RR}(R)$ vanishes much more rapidly in the AB model than in the HS and Starobinsky cases, we expect that the singularity ($M_{\rm s} \to \infty$) forms earlier in the AB model.

However, it has been observed that simply adding a term proportional to R^2 to the $f(R)$ action, with a sufficiently small coefficient to ensure the existence of the primordial inflation, solves this type of singularity [35, 47]. This term is often assumed to be the Starobinsky inflationary term, $R^2/6\mathcal{M}^2$. Thus, the R^2-corrected versions of the AB, HS, and Starobinsky models are given, respectively, by

$$f_{\rm AB}(R) = f^I_{\rm AB}(R) + \frac{R^2}{6\mathcal{M}^2}\,, \tag{5.33}$$

$$f_{\rm HS}(R) = f^I_{\rm HS}(R) + \frac{R^2}{6\mathcal{M}^2}\,, \tag{5.34}$$

$$f_{\rm S}(R) = f^I_{\rm S}(R) + \frac{R^2}{6\mathcal{M}^2}\,, \tag{5.35}$$

The R^2-corrected AB model, or simply R^2-AB model (first line), is equivalent to the improved gR^2-AB model with $g = 1/2$, whose main cosmological constraints are reported in Refs. [51, 250, 251]. Similar versions of the R^2-HS model (second line) and the R^2-Starobinsky model (third line) have also been studied in Refs. [51] and [252], respectively.

Finally, it can be verified that adding the starobinsky-like term to the $f(R)$ action results in an upper limit for the scalaron rest-mass, $M_{\rm s} \leq \mathcal{M}$. In order to fit the observed amplitude of the primordial power spectrum, this mass scale should be chosen as $\mathcal{M} \approx 1.2 \times 10^{-5} M_{\rm Pl}$ [51], where $M_{\rm Pl} = 2.44 \times 10^{18}\,\text{GeV}$ is the Planck mass (conventionally, $M_{\rm Pl} = \kappa^{-1} = 1/\sqrt{8\pi G}$). Thus, the R^2 correction is negligibly small at present curvatures $R \sim R_{\rm vac}$.

5.4 Cosmological evolution

Let us start with the R^2-AB model defined in Eq. (5.33). Assuming the universe is filled with a fluid consisting of non-relativistic matter and radiation, the background dynamical equations are given by

$$3H^2 = \kappa^2 \left(\rho_{\rm m} + \rho_{\rm r} + \rho_{\rm DE}\right) , \tag{5.36}$$

$$2\dot{H} + 3H^2 = -\kappa^2 \left(P_{\rm m} + P_{\rm r} + P_{\rm DE}\right) , \tag{5.37}$$

with [249]

$$\begin{aligned}\kappa^2\rho_{\rm DE} = \frac{R}{4} - \left(\frac{1}{3\mathcal{M}^2} + \frac{\mathrm{sech}^2 y_{\rm AB}}{2\epsilon_{\rm AB}}\right)3H\dot{R} - \frac{\epsilon_{\rm AB}}{4}\ln\left(\frac{\cosh y_{\rm AB}}{\cosh b}\right) - \frac{R^2}{12\mathcal{M}^2} \\ + \left[\frac{R}{\mathcal{M}^2} + \frac{3(\tanh y_{\rm AB} - 1)}{2}\right](\dot{H} + H^2) ,\end{aligned} \tag{5.38}$$

$$\begin{aligned}\kappa P_{\rm DE} = -\frac{R}{4} + \left(\frac{1}{3\mathcal{M}^2} + \frac{\mathrm{sech}^2 y_{\rm AB}}{2\epsilon_{\rm AB}}\right)\xi_R + \frac{\epsilon_{\rm AB}}{4}\ln\left(\frac{\cosh y_{\rm AB}}{\cosh b}\right) + \frac{R^2}{12\mathcal{M}^2} \\ - \frac{\dot{R}^2 \tanh y_{\rm AB}\,\mathrm{sech}^2 y_{\rm AB}}{\epsilon_{\rm AB}^2} - \left[\frac{R}{3\mathcal{M}^2} + \frac{(\tanh y_{\rm AB} - 1)}{2}\right]\xi_H .\end{aligned} \tag{5.39}$$

where we define the auxiliary variables $y_{\rm AB} \equiv R/\epsilon_{\rm AB} - b$, $\xi_R \equiv \ddot{R} + 2H\dot{R}$, and $\xi_H \equiv \dot{H} + 3H^2$. Throughout the RD and deeper MD eras, when $R_{\rm vac} \ll R \ll \mathcal{M}^2$, the expressions in Eqs. (5.38) and (5.39) can be approximated, respectively, by

$$\kappa^2\rho_{\rm DE} \simeq \frac{R_{vac}}{4} + \frac{1}{\mathcal{M}^2}\left(\mathscr{H}_1 - \frac{R^2}{12}\right) - \frac{1}{e^{2y_{\rm AB}}}\left(3\frac{\ddot{a}}{a} + \frac{6H\dot{R}}{\epsilon_{\rm AB}} + \frac{\epsilon_{\rm AB}}{4}\right) \tag{5.40}$$

and

$$\kappa^2 P_{\rm DE} \simeq -\frac{R_{vac}}{4} + \frac{1}{\mathcal{M}^2}\left(\mathscr{H}_2 + \frac{R^2}{12}\right) - \frac{1}{e^{2y_{\rm AB}}}\left(\mathscr{H}_3 - \frac{4\dot{R}^2}{\epsilon_{\rm AB}^2} + \frac{\epsilon_{\rm AB}}{4}\right) . \tag{5.41}$$

where $\mathscr{H}_1 \equiv (\dot{H}+H^2)R - H\dot{R}$, $\mathscr{H}_2 \equiv (\xi_R - \xi_H R)/3$, and $\mathscr{H}_3 \equiv (2\xi_R/\epsilon_{\rm AB}) + \xi_H$. Since R and $\mathcal{M}$ are both very large in these epochs, we expect a strong suppression of the last two terms in Eqs. (5.40) and (5.41), and, consequently, an EoS $w_{\rm DE} \simeq -1$. This implies that the R^2-AB model recovers GR at high z. On the other hand, at later times, when $R \sim R_{\rm vac}$, the scalaron mass becomes small, and significant deviations from $w_{\rm DE} = -1$ are expected.

To derive the equations of motion for both the R^2-HB and Starobinsky models, given by Eqs. (5.34) and (5.35), respectively, we use a different approach, that was

introduced in Ref. [46]. First, we introduce the variables

$$y_H \equiv \frac{H^2}{m_0^2} - a^{-3} - \chi_{\rm r} a^{-4}\,, \tag{5.42}$$

$$y_R \equiv \frac{R}{m_0^2} - 3a^{-3}\,, \tag{5.43}$$

where $\chi_{\rm r} \equiv \Omega_{\rm r,0}/\Omega_{\rm m,0}$. We can then rewrite Eqs. (4.62) and (4.66) as

$$\frac{d^2 y_H}{dN^2} + J_1 \frac{dy_H}{dN} + J_2 y_H + J_3 = 0 \tag{5.44}$$

and

$$R = 3m_0^2 \left(a^{-1} \frac{dy_H}{dN} + 4y_H - a^{-3} \right)\,, \tag{5.45}$$

respectively, where $N \equiv \ln a$ (remember) is the number of e-folds, and

$$J_1 = 4 + \frac{1}{y_H + a^{-3} + \chi_{\rm r} a^{-4}} \frac{1 - f_{,R}}{6m_0^2 f_{,RR}}\,, \tag{5.46}$$

$$J_2 = \frac{1}{y_H + a^{-3} + \chi_{\rm r} a^{-4}} \frac{2 - f_{,R}}{3m_0^2 f_{,RR}}\,, \tag{5.47}$$

$$J_3 = -3a^{-3} + \frac{(1 - f_{,R})\,(a^{-3} + 2\chi_{\rm r} a^{-4}) + (R - f)/3m_0^2}{y_H + a^{-3} + \chi_{\rm r} a^{-4}} \frac{1}{6m_0^2 f_{,RR}}\,. \tag{5.48}$$

After solving these background equations and obtaining $y_H = y_H(a)$, we can invert Eq. (5.42) to obtain the Hubble function $H = H(a)$ for both the HS and Starobinsky models. Additionally, we can reconstruct the EoS $w_{\rm DE} = -1 - (dy_H/dN)/3y_H$.

The choice of using two distinct methods to solve the equations of motion for the $f(R)$ models under discussion arises for the following reasons. For the R^2-AB model, the second method encountered a high number of numerical issues that we were unable to solve. Conversely, we found it challenging to effectively apply the first method to the R^2-HS and Starobinsky models. Generally, in the literature, the second method is more commonly used in studies involving these last latter two $f(R)$ models.

5.5 Initial conditions and numerical results

We now discuss the initial conditions and the appropriate mass scale $\mathcal{M}$ required to numerically solve both the background and perturbed equations for the three models under consideration: the AB, HS and Starobinsky $f(R)$ models. Following this, we present our numerical results and provide a thorough analysis of them.

Fist, we set $a_i = 0.2$ (i.e., $z_i = 4$) as the initial scale factor, as it is reasonable to assume that the ΛCDM model accurately describes the observed universe from

this point onwards (*onwards* here means *back in the time*). Notice that the $f(R)$ Friedmann equations are third-order in the Hubble function $H(a)$. Consequently, three initial conditions are needed:

$$H_i \equiv H_{\rm GR}(t_i)\,, \quad \dot{H}_i \equiv \dot{H}_{\rm GR}(t_i)\,, \quad \ddot{H}_i \equiv \ddot{H}_{\rm GR}(t_i)\,, \tag{5.49}$$

where $t_i \equiv t(a_i)$, specifically for the AB model. For the HS and Starobinsky cases, in which we use a different approach based on the function $y_H(a)$, defined in Eq. (5.42), the initial conditions must satisfy

$$y_H(a_i) = \frac{1-\Omega_{\rm m,0}}{\Omega_{\rm m,0}}\,, \quad \frac{dy_H}{dN}(a_i) = 0\,. \tag{5.50}$$

Unlike the equations for $H(a)$, those for the auxiliary variable $y_H(a)$ are second-order, and thus only two initial conditions are required. Since $\Omega_{\rm r,0} \sim 10^{-5}$, we have disregarded the term involving $\chi_{\rm r}$ compared to the others when deriving the initial conditions above.

For the growing modes at the perturbation level, we assume initial conditions such that

$$\delta_{\rm m}(a_i) = a_i\,, \quad \frac{d\,\delta_{\rm m}}{da}(a_i) = 1\,. \tag{5.51}$$

It turns out that we can take $\delta(a) = a$ and $d\,\delta(a)/da = 1$ when $a \ll 1$ [253]. Similar to $y_H(a)$, the equations for the matter fluctuations are second-order in the matter density contrast $\delta_{\rm m}(a)$. Therefore, only two initial conditions are needed when solving Eqs. (4.124).

It is important to note that the frequency of small oscillations of the Ricci scalar, $\omega_{\rm osc} \equiv M_{\rm s} \leq \mathcal{M}$, depends on R, which itself is a function of time. Therefore, both $\omega_{\rm osc}$ and $M_{\rm s}$ are time-dependent, or equivalently, scale factor-dependent. These quantities are upper-bounded by the mass scale $\mathcal{M}$. Notably, $\mathcal{M}$ is very large during inflation ($\sim 10^{13}\,{\rm GeV}$) and decreases as the universe ages. As suggested in Ref. [51], an appropriate mass scale $\mathcal{M}$ corresponds to $\Delta \equiv \epsilon_{\rm X}/\mathcal{M}^2 = 10^{-7}$, for the redshift range $0 \leq z \leq 4$, where the current curvature scale $\epsilon_{\rm X}$ takes three different values: $\epsilon_{\rm AB}$, m_0^2, and $R_{\rm S}$ for the R^2-AB, HS, and Starobinsky models.

In Figure 5.1(a), we display the Hubble function $H(z)$ for the R^2-AB model, obtained from the numerical solution of Eqs. (5.36) and (5.37). For comparison, we include the fiducial $H(z)$ from the standard flat-ΛCDM cosmology. Notice that there is almost no difference between these models from the Hubble function. Next, in Figure 5.1(b), we show the behavior of the EoS parameter, $w_{\rm DE}(z)$. It is possible to observe that the R^2-AB model reproduces the standard ΛCDM cosmology in the past, as expected, with $w_{\rm DE}$ oscillating around -1 for $z > 2$. However, for $z \lesssim 2$,

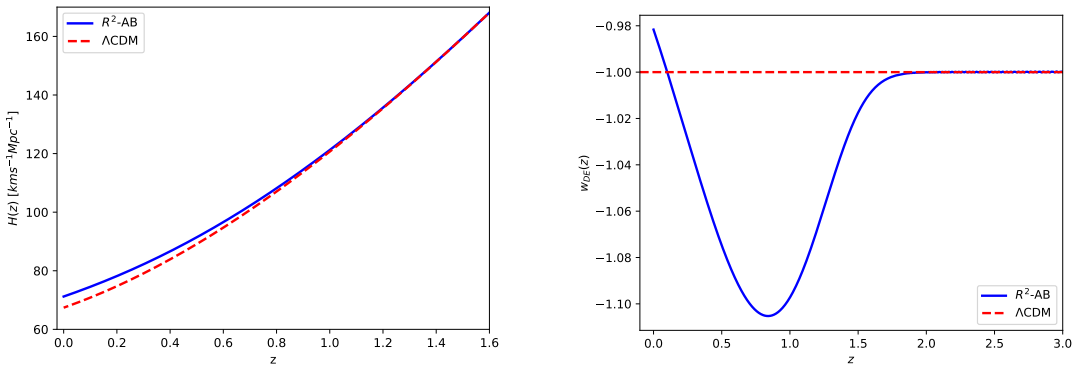

(a) (b)

Figure 5.1: curves of $H(z)$ [**panel** (a)] and $w_{\rm DE}(z)$ [**panel** (b)] for the R^2-AB (blue) and flat-ΛCDM (red) models, assuming $H_0 = 67.4\,\mathrm{km\,s^{-1}\,Mpc^{-1}}$ and $\Omega_{\rm m,0} = 0.315$, as determined by Planck [88], along with $b = 2$ and $\Delta = 10^{-7}$, following Ref. [51].

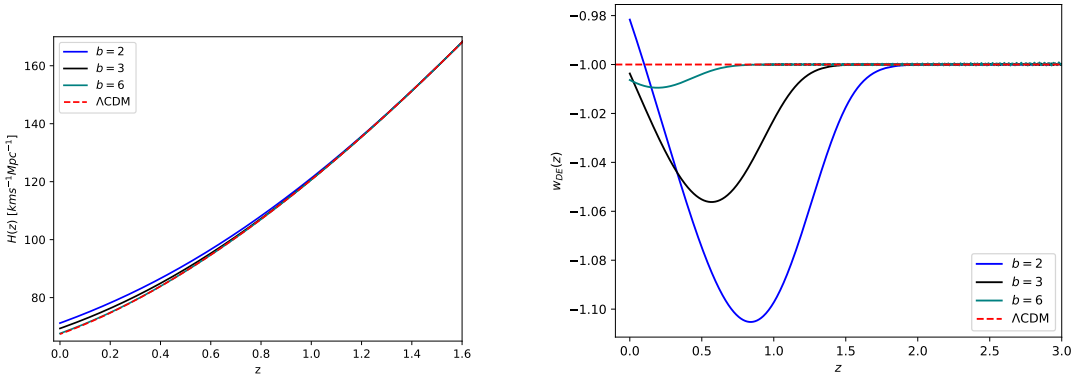

(a) (b)

Figure 5.2: Curves of $H(z)$ [**panel** (a)] and $w_{\rm DE}(z)$ [**panel** (b)] for the R^2-AB model with $b = 2$ (blue), 3 (black), and 6 (teal). Assumptions include $H_0 = 67.4\,\mathrm{km\,s^{-1}\,Mpc^{-1}}$, $\Omega_{\rm m,0} = 0.315$, and $\Delta = 10^{-7}$. For comparison, the flat-ΛCDM model curves (red) were plotted using the same values of H_0 and $\Omega_{\rm m,0}$.

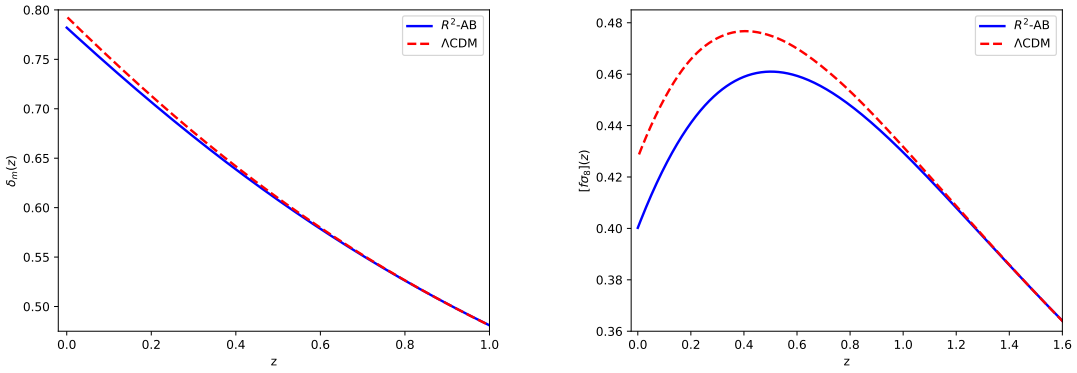

(a) (b)

Figure 5.3: Curves of $\delta_{\rm m}(z)$ [**panel** (a)] and $f\sigma_8(z)$ [**panel** (b)] for the R^2-AB (blue) and flat-ΛCDM (red) models. Assumptions include $H_0 = 67.4\,\mathrm{km\,s^{-1}\,Mpc^{-1}}$, $\Omega_{\rm m,0} = 0.315$, $\sigma_{8,0} = 0.811$, $b = 2$, and $\Delta = 10^{-7}$.

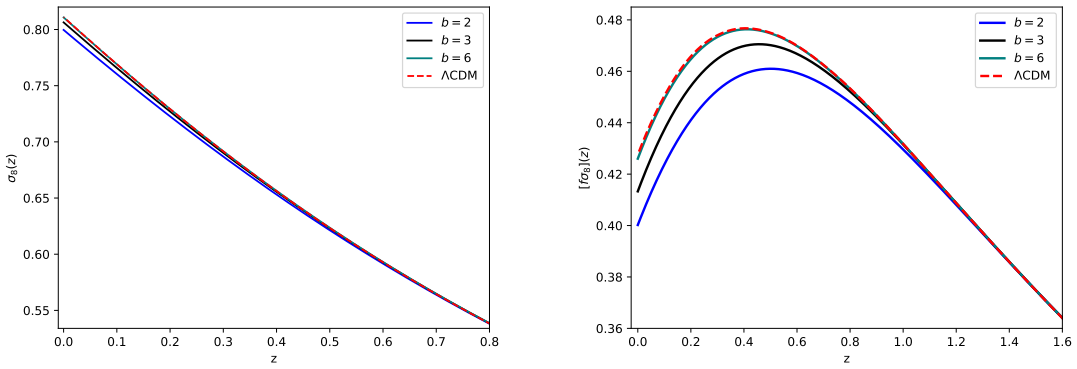

(a) (b)

Figure 5.4: $\sigma_8(z)$ [**panel (*a*)**] and $f\sigma_8(z)$ [**panel (*b*)**] curves according to the R^2-AB model for $b = 2$ (blue), 3 (black), and 6 (teal) assuming $H_0 = 67.4\ \mathrm{km\,s^{-1}\,Mpc^{-1}}$, $\Omega_{\mathrm{m},0} = 0.315$, $\sigma_{8,0} = 0.811$, and $\Delta = 10^{-7}$. For comparison, the flat-ΛCDM curves (red) were plotted for the same values of H_0, $\Omega_{\mathrm{m},0}$, and $\sigma_{8,0} = 0.811$.

it diverges from its GR value, exhibiting a phantom behavior for $0.2 \lesssim z < 2$ and $w_{\mathrm{DE}} > -1$ for $z \lesssim 0.2$. This behavior changes very little as we vary the cosmological parameters involved, H_0 and $\Omega_{\mathrm{m},0}$. We can also observe that as we increase the value of the parameter b, the R^2-AB model approaches the flat-ΛCDM model, as seen in Figures 5.2(a) and 5.2(b).

Due to degeneracy in the cosmological background, it is necessary to move to the perturbative level. We then examine cosmological perturbations via the matter density contrast, $\delta_{\mathrm{m}}(z)$, and the parameterized growth rate, $[f\sigma_8](z)$. It is worth mentioning that in MTGs, such as $f(R)$ or the scalar-tensor theories, structure formation depends on the scale k through the effective gravitational coupling, $G_{\mathrm{eff}}(z,k)$ [see Eq. (4.125)]. Figures 5.3(a) and 5.3(b) show, respectively, the numerical solutions for $\delta_{\mathrm{m}}(z)$ and $[f\sigma_8](z)$ for both the R^2-AB and standard flat-ΛCDM models, assuming $k = 0.125\,\mathrm{Mpc}^{-1}$ and $\sigma_{8,0} = 0.811$ [88]. Similarly to the background level, increasing the parameter b causes the blue curves to overlap with the red ones (see Figures 5.4(a) and 5.4(b)), indicating that this parameter provides a measure of the similarity (or difference) between GR theory and the R^2-AB $f(R)$ model. Thus, the R^2-AB model recovers GR phenomenology whenever $R \gg R_{\mathrm{vac}}$ or $b \gg 1$.

The numerical results above pertain specifically to the R^2-AB model and are published in [249]. We now present results from the numerical analyses of the HS and Starobinsky models and compare them with those of the R^2-AB model. For simplicity, we assume $n = 1$ in both theories. Setting $n = 1$ is also the most studied case, with several works exploring this choice (see, e.g., Refs. [254, 255] for the HS model, Refs. [67, 252] for the Starobinsky model, and Refs. [256, 257] for both).

As seen in Figures 5.2(a) and 5.5, the $H(z)$ solution for the R^2-AB model never crosses $H^{\mathrm{AB}} \leq H^{\Lambda\mathrm{CDM}}$, while those of HS and Starobinsky allow $H^{\mathrm{HS}}, H^{\mathrm{S}} < H^{\Lambda\mathrm{CDM}}$.

However, it is not possible to distinguish between these models through experiments or current data based on background alone. In contrast, the curves for $w_{\rm DE}(z)$ show slight differences from each other and are notably distinct from the ΛCDM model. As shown in Figure 5.6(a), each model exhibits a phantom-like behavior, with $w_{\rm DE} < -1$, at slightly different redshift ranges. Among these models, the R^2-AB model exhibits the most pronounced phantom behavior and is the first to recover the ΛCDM evolution. The Starobinsky model shows the highest values of $w_{\rm DE}$ in the recent period ($z \lesssim 0.5$), while the HS model deviates the least from $w_{\rm DE} = -1$ throughout the background evolution.

At the perturbative level, as seen in Figure 5.6(b), both the HS and Starobinsky models predict more pronounced late-time structure growth compared to the R^2-AB model, which is upper limited by the ΛCDM solution (i.e., $f\sigma_8^{\rm AB} \leq f\sigma_8^{\Lambda{\rm CDM}}$; see again Figure 5.4(b)). Since structure evolution in the framework of $f(R)$ gravity depends on the scale k, this conclusion applies only to the scales studied here – namely, $k = 0.125\,h\,{\rm Mpc}^{-1}$ and $k = 0.1\,h\,{\rm Mpc}^{-1}$.

In general terms, we can say that the cosmological background in $f(R)$ theories is almost entirely degenerate with each other and with the ΛCDM model, with the rare exception of the equation of state. In fact, the DE EoS serves as an excellent model discriminator at the background level, whether they are quintessential, Chaplygin gas, or geometric $f(R)$ models. On the other hand, at the perturbative level, significant differences between these models emerge. In summary, we conclude that the R^2-AB model most closely resembles the standard ΛCDM model, both at the background and perturbative levels.

5.6 Cosmological datasets

In this section, we present the cosmological datasets used to constrain the free parameters of the R^2-AB and HS models: $H(z)$ from cosmic chronometer (CC) observations, $[f\sigma_8](z)$ from redshif-space distortion (RSD) observations, and $m_B(z)$ measurements of SNe Ia from Pantheon+ and SH0ES catalogs.

5.6.1 Cosmic Chronometers

One effective way to measure $H(z)$ without assuming a cosmological model is the cosmic chronometers method. This approach is based on the relationship

$$H\left(z\right) = -\frac{1}{(1+z)}\frac{dz}{dt} \simeq -\frac{1}{(1+z)}\frac{\Delta z}{\Delta t}\,, \tag{5.52}$$

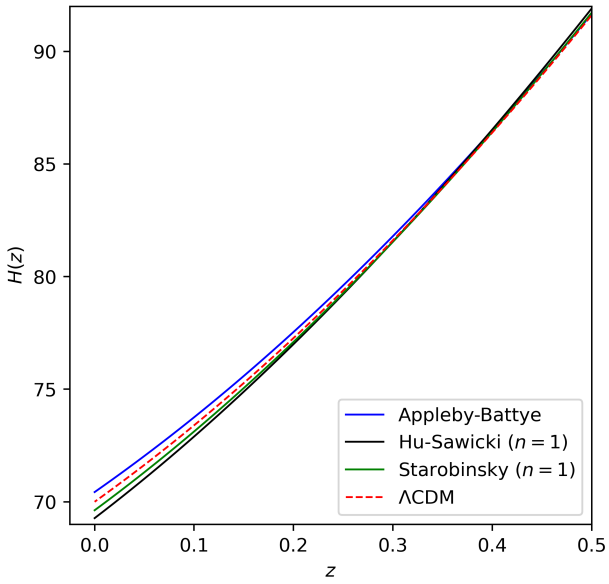

Figure 5.5: Curves of $H(z)$ for the R^2-AB (blue), HS (black), and Starobinsky (green) models, along with the flat-ΛCDM (red dashed) model. The parameters used in this plot are $b = 5$, $n = 1$, $c_2 = 1$, and $\lambda_{\rm S} = 2$, along with $\{H_0, \Omega_{m,0}\} = \{70, 0.3\}$. The $H(z)$ solution for the R^2-AB model is lower-bounded by $H^{\rm AB} \geq H^{\Lambda{\rm CDM}}$, while the HS and Starobinsky models allow for $H^{\rm HS}, H^{\rm S} < H^{\Lambda{\rm CDM}}$.

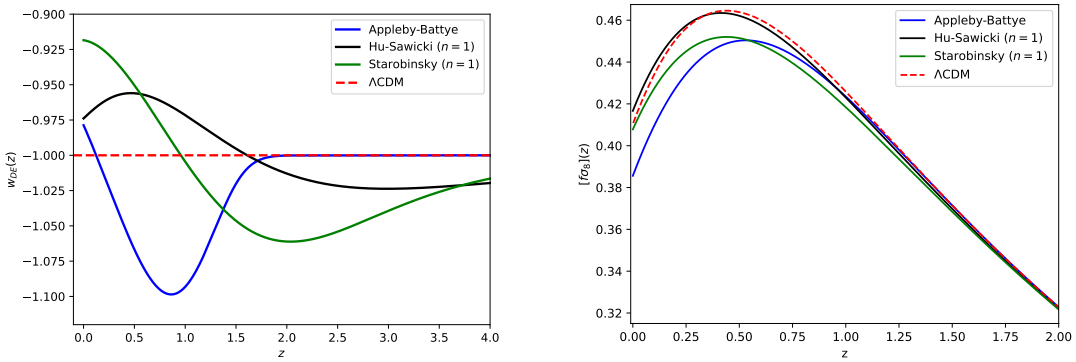

(a) (b)

Figure 5.6: Curves of $w_{\rm DE}(z)$ [**panel** (a)] and $f\sigma_8(z)$ [**panel** (b)] for the R^2-AB (blue), HS (black), and Starobinsky (green) models, as well as the flat-ΛCDM model (red). Both plots assume $b = 2$, $n = 1$, $c_2 = 1$, and $\lambda_{\rm S} = 2$, along with the cosmological parameters $\{H_0, \Omega_{\rm m,0}\} = \{70, 0.3\}$ and a physical scale of $k = 0.1\,h\,{\rm Mpc}^{-1}$.

Table 5.2: The 31 $H(z)$ measurements obtained from the CC approach using the BC03 SPS model.

z	$H(z)$	Ref.	z	$H(z)$	Ref.
0.07	69.0 ± 19.6	[258]	0.4783	80.9 ± 9.0	[259]
0.09	69.0 ± 12.0	[260]	0.48	97.0 ± 62.0	[261]
0.12	68.6 ± 26.2	[258]	0.593	104.0 ± 13.0	[262]
0.17	83.0 ± 8.0	[260]	0.68	92.0 ± 8.0	[262]
0.179	75.0 ± 4.0	[262]	0.781	105.0 ± 12.0	[262]
0.199	75.0 ± 5.0	[262]	0.875	125.0 ± 17.0	[262]
0.2	72.9 ± 29.6	[258]	0.88	90.0 ± 40.0	[261]
0.27	77.0 ± 14.0	[260]	0.9	117.0 ± 23.0	[260]
0.28	88.8 ± 36.6	[258]	1.037	154.0 ± 20.0	[262]
0.352	83.0 ± 14.0	[262]	1.3	168.0 ± 17.0	[260]
0.3802	83.0 ± 13.5	[259]	1.363	160.0 ± 33.6	[263]
0.4	95.0 ± 17.0	[260]	1.43	177.0 ± 18.0	[260]
0.4004	77.0 ± 10.2	[259]	1.53	140.0 ± 14.0	[260]
0.4247	87.1 ± 11.2	[259]	1.75	202.0 ± 40.0	[260]
0.4497	92.8 ± 12.9	[259]	1.965	186.5 ± 50.4	[263]
0.47	89.0 ± 49.6	[264]			

obtained from the definition $H \equiv \dot{a}/a$, where the derivative term,

$$\frac{dz}{dt} \simeq \frac{\Delta z}{\Delta t} \tag{5.53}$$

can be determined from two passively-evolving galaxies, i.e., those with old stellar populations and low star formation rates, whose redshifts are marginally different and whose ages are well-determined. Moreover, the selected galaxies have to differ in age by a significantly lower amount than their passive evolution time. [265]. The age of galaxies are estimated by assuming a stellar population synthesis (SPS) model.

In Table 5.2, we list 31 measurements of $H(z)$ obtained through the CC method, where the age of galaxies was determined by assuming the BC03 SPS model [266]. As a result, these measurements contain systematic uncertainties related only to the SPS model and to possible contamination due to the presence of young stars in quiescent galaxies [267, 268].

5.6.2 Normalized growth rate

The normalized growth rate, given by Eq. (3.94), most commonly used approach for studying the clustering evolution of cosmic structures. One way to obtain it is by first measuring the velocity scale parameter, defined as $v_{\rm sp} = f_g/\delta_{\rm bias}$, where $\delta_{\rm bias}$ is

Table 5.3: The 20 $[f\sigma_8](z)$ measurements obtained from various surveys and cosmological tracers, as compiled by [276].

z	$[f\sigma_8](z)$	Ref.	z	$[f\sigma_8](z)$	Ref.
0.02	0.398 ± 0.065	[269]	0.70	0.473 ± 0.041	[273]
0.025	0.39 ± 0.11	[270]	0.73	0.437 ± 0.072	[277]
0.067	0.423 ± 0.055	[271]	0.74	0.50 ± 0.11	[278]
0.10	0.37 ± 0.13	[272]	0.76	0.440 ± 0.040	[279]
0.15	0.53 ± 0.16	[273]	0.85	0.52 ± 0.10	[278]
0.32	0.384 ± 0.095	[274]	0.978	0.379 ± 0.176	[280]
0.38	0.497 ± 0.045	[273]	1.05	0.280 ± 0.080	[279]
0.44	0.413 ± 0.08	[277]	1.40	0.482 ± 0.116	[281]
0.57	0.453 ± 0.022	[282]	1.48	0.30 ± 0.13	[278]
0.59	0.488 ± 0.060	[283]	1.944	0.364 ± 0.106	[280]

the *bias* factor, and then using it in the relation

$$[f\sigma_8](z) = v_{\rm sp}(z)\, \sigma_8^{\rm tr}(z)\,, \tag{5.54}$$

where $\sigma_8^{\rm tr}(z)$ is the matter fluctuation amplitude of the cosmological tracer, such as HI line extra-galactic sources (EGS), luminous red galaxies (LRG), quasars (QSOs), emission-line galaxies (ELG), and SNe Ia.

The parameterized growth rate data, $[f\sigma_8](z)$, are most often obtained using the RSD effect observed in galaxy surveys [63, 244, 269–275]. In Table 5.3, we present the data compilation from [276], which includes measurements of $[f\sigma_8](z)$. This compilation follows a methodology in which double counting is eliminated and possible biases are reduced, ensuring the reliability of the dataset (see Section 3 of Ref. [276]).

5.6.3 Pantheon+ and SH0ES

When investigating the universe's recent expansion history, SNe Ia have proven to be a crucial probe. They contributed to the first verification of the universe's accelerated expansion [1, 2], in addition to helping map the universe's large-scale structure today. Cosmologists are increasingly relying on SNe Ia data to investigate the dark energy EoS, thanks to the rising abundance of these observations at higher redshifts and advancements in processing techniques.

From an observational point of view, it is assumed that different SNe Ia with identical color, light curve shape, and galactic environment have, on average, the same intrinsic luminosity across all redshifts. This hypothesis is quantified through

the empirical relationship [284]

$$\tilde{\mu}_{\rm obs} = m_{\rm B} - M_{\rm B} + \tilde{\nu}_1 X_1 - \tilde{\nu}_2 X_2 + \delta_{\tilde{\mu}-{\rm bias}}\,, \tag{5.55}$$

where $\tilde{\mu}_{\rm obs}$ is the observed distance modulus, $m_{\rm B}$ correspond to observed magnitude in B-band rest-frame, while $\tilde{\nu}_1$, $\tilde{\nu}_2$, $\delta_{\tilde{\mu}-{\rm bias}}$, and $M_{\rm B}$ are the stretch of the light curve correction X_1, the SNe Ia color at maximum brightness correction X_2, the simulated bias correction, and the absolute magnitude in the B-band rest-frame, respectively [284].

On the other hand, for a bright source at redshift z, the theoretical apparent magnitude $m_{\rm B}$ is given by

$$m_{\rm B}(z) = 5\log\left[\frac{d_{\rm L}(z)}{10\,{\rm pc}}\right] + M_{\rm B}\,, \tag{5.56}$$

where $d_{\rm L}(z)$ is the theoretical luminosity-distance. The theoretical distance modulus reads as $\tilde{\mu}_{\rm theo} = m_{\rm B} - M_{\rm B}$. For a flat cosmology ($K = 0$), the luminosity-distance is given by

$$d_{\rm L}(z) = (1+z)\int_0^z \frac{d\tilde{z}}{H(\tilde{z})}. \tag{5.57}$$

In order to test the $f(R)$ models, we have considered the Pantheon+ (PN$^+$) compilation [192], the successor to the original Pantheon (PN) [285], which analyzed 1701 SNe Ia light curves with redshifts $0.001 \leq z \leq 2.26$. Because of the larger sample size and improved methods for handling systematic uncertainties, the analysis with PN$^+$ presents an improvement factor of 2 in the power of cosmological constraints compared to the original PN [192].

5.7 Analyses and Results

In our analyses, we consider Bayes' theorem [286], which establishes a connection between our prior knowledge of an event and its probability of occurrence. Simply put, it links our knowledge of a specific parameter *posterior* (after acquiring the data) with our *a priori* knowledge (before witnessing the data). An important concept in this regard is the *probability distribution function*, or simply PDF.

Bayes' theorem states that

$$\mathscr{P}(\vartheta|\mathcal{O},\alpha) = \frac{\mathscr{P}(\mathcal{O}|\vartheta,\alpha)\mathscr{P}(\vartheta|\alpha)}{\mathscr{P}(\mathcal{O}|\alpha)}\,, \tag{5.58}$$

where $\mathscr{P}(\vartheta|\mathcal{O},\alpha)$ is the *posterior* PDF, $\mathscr{P}(\mathcal{O}|\vartheta,\alpha)$ matches the *likelihood*, $\mathscr{P}(\vartheta|\alpha)$ corresponds to the *prior*, and $\mathscr{P}(\mathcal{O}|\alpha)$ is the *evidence*. We also have represented in

this formula the following variables: ϑ cover the set of model parameters, $\mathcal{O}$ denotes the observations (data), and α expresses the *prior* information (model). Since the *evidence* $\mathscr{P}(\mathcal{O}|\alpha)$ is independent on model, we can disregard it as a normalizing constant. This approach offers a means to update our understanding of the parameter we aim to infer.

We then considere the Monte Carlo Markov Chain (MCMC) technique, based on the Metropolis-Hastings algorithm, in order to generate random samples from complex, high-dimensional PDFs. This method begins with an initial sample and iteratively proposes new samples based on a proposal distribution. Each proposed sample is accepted or rejected according to an acceptance criterion that ensures the chain converges to the desired distribution. The resulting *posterior* PDF, centered around the most likely values, allows us to obtain the best-fit of model parameters with robust uncertainties.

If the observations $\mathcal{O}_i$ are Gaussian distributed, the likelihood is given by the multivariate Gaussian [287],

$$\mathcal{L}(\vartheta) = \exp\left(-\frac{1}{2}\sum_{ij}\Delta\varepsilon_i^T\, C_{ij}^{-1}\,\Delta\varepsilon_j\right), \tag{5.59}$$

$$\Delta\varepsilon_i \equiv \varepsilon_i(\vartheta|\alpha) - \mathcal{O}_i\,, \tag{5.60}$$

where $\varepsilon_i(\vartheta|\alpha)$ is the i-th expected value (based on a model) and C_{ij} is the covariance matrix encoding statistical and systematic uncertainties related to the dataset $\mathcal{O}_i$. For fully uncorrelated observations, this is simplified as $C_{ij}^{-1} = 1/\sigma_i^2$, where σ_i^2 is the error at datum i.

The sum in Eq. (5.59) is called the *chi-square*, often represented by χ^2. In terms of this quantity, the likelihood is given by

$$\mathcal{L} = \exp\left(-\frac{\chi^2}{2}\right) \tag{5.61}$$

For a joint analysis of our datasets, the total chi-square is expressed as

$$\chi^2 = \chi^2_{\rm SNe} + \chi^2_{\rm CC} + \chi^2_{\rm RSD}\,, \tag{5.62}$$

resulting in the total likelihood $\mathcal{L} = \mathcal{L}_{\rm SNe} \times \mathcal{L}_{\rm CC} \times \mathcal{L}_{\rm RSD}$.

It is common to consider the *prior* sets to have the same probability of occurrence, so that $\mathscr{P}(\vartheta|\alpha)$ has the form of the Dirac delta distribution,

$$\mathscr{P}(\vartheta|\alpha) = \begin{cases} 1 & \text{if} \quad \vartheta^{(0)} < \vartheta < \vartheta^{(1)}, \\ 0 & \text{otherwise,} \end{cases} \tag{5.63}$$

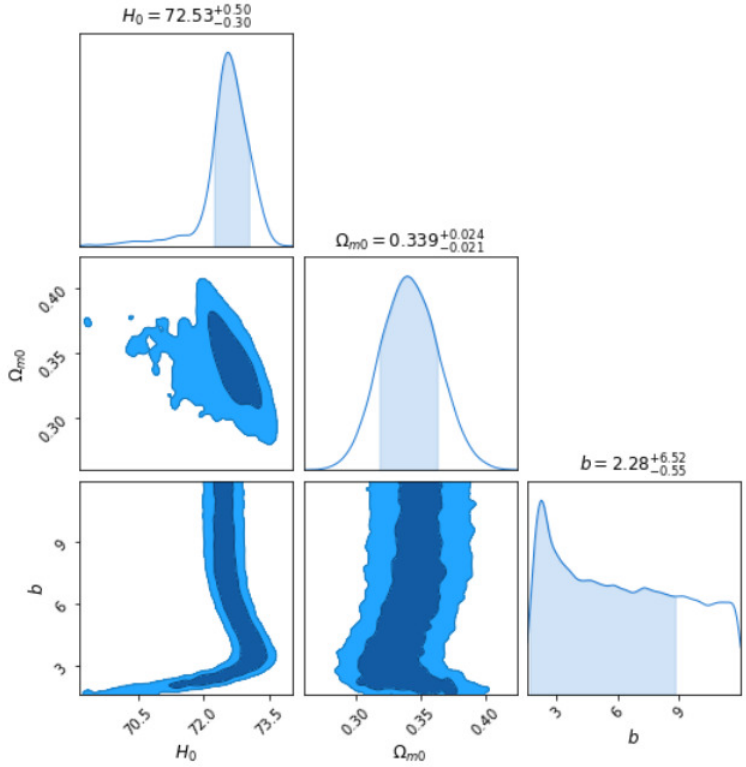

Figure 5.7: MCMC analysis for the R^2-AB model, considering the PN$^+$ SNe Ia data alone. In this analysis, the absolute magnitude was fixed at $M_{\rm B} = -19.253$, as determined by SH0ES [100]. The priors used were $H_0 = [64, 76]$, $\Omega_{\rm m,0} = [0.1, 0.5]$, and $b = [1.6, 12]$.

where $\vartheta^{(0)}$ and $\vartheta^{(1)}$ are the flat *prior* intervals. Consequently, the *posterior* PDF is given by $\mathscr{P}(\vartheta|\mathcal{O}, \alpha) = \mathcal{L}(\vartheta)$, i.e, only by the likelihood.

There are two common methods for estimating the optimum value of the model parameters: (i) the maximum likelihood and (ii) the least chi-square. The latter is more commonly used and can be performed, for example, using the *scipy.optimize* python library. Next, we explore the parametric space of the model parameters, sampling the *posterior distribution* around the best-fit value, following the MCMC method and the Metropolis-Hastings algorithm. The confidence regions are drawn assuming $\mathcal{L} = \mathcal{L}_{max} + \Delta\mathcal{L}_0$, where the constant $\Delta\mathcal{L}_0$ is determined by the cumulative probability density. To implement the MCMC routine, we use Python as well.

In our analyses we set:

- $\vartheta = [H_0, \Omega_{\rm m,0}, \vartheta_{\rm mod}]$, for the Hubble function;
- $\vartheta = [\Omega_{\rm m,0}, \sigma_{8,0}, \vartheta_{\rm mod}]$, for the growth rate; and
- $\vartheta = [H_0, \Omega_{\rm m,0}, M_{\rm B}, \vartheta_{\rm mod}]$, for the apparent magnitude,

where $\vartheta_{\rm mod}$ is the model free parameter: b for the R^2-AB and μ for the R^2-HS. The priors were defined according to the analysis performed.

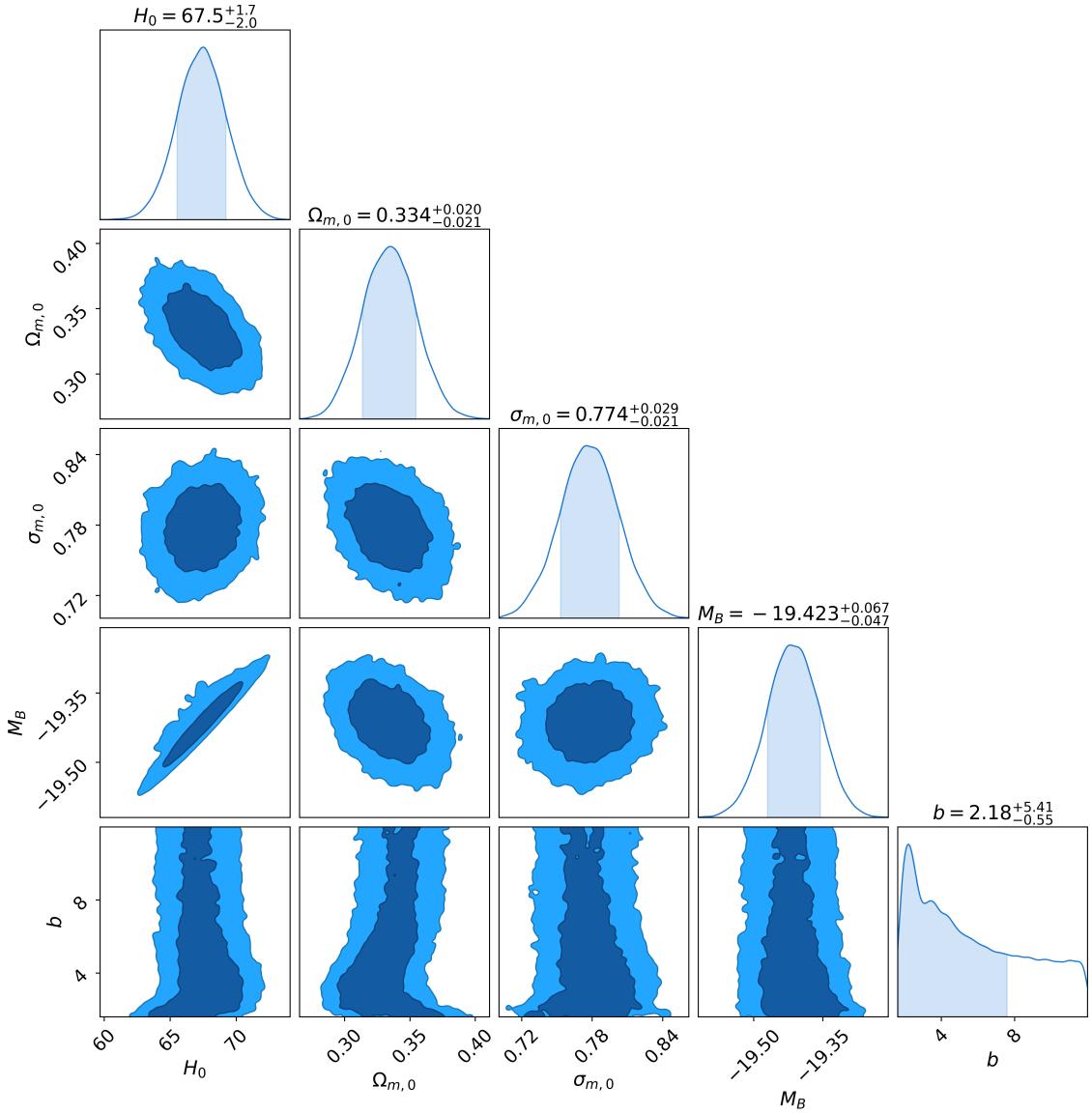

Figure 5.8: MCMC analysis for the R^2-AB model considering the data combination $\mathrm{PN}^+ + \mathrm{CC} + \mathrm{RSD}$. In this analysis, the prior intervals were set as $H_0 = [54, 76]$, $\Omega_{\mathrm{m},0} = [0.1, 0.5]$, $\sigma_{8,0} = [0.7, 0.9]$, $M_{\mathrm{B}} = [-20.2, -19.0]$ and $b = [1.6, 12]$.

Figures 5.7 and 5.8 show our MCMC results for the R^2-AB model, considering only the PN$^+$ SNe Ia dataset and the combination of SNe + CC + RSD, respectively, published in [249]. Figures 5.9 and 5.10, in turn, display our MCMC results for the HS model, considering only the PN$^+$ SNe Ia dataset and the combination of SNe + CC + RSD, respectively. All of these outcomes are summarized in Table 5.4.

Regarding the R^2-AB model, as we can see, the most likely values obtained for the model parameters depend on the analysis. Due to the $H_0 - M_{\rm B}$ degeneracy, for the SNe Ia data alone, we set $M_{\rm B} = -19.253$, which is the value of absolute magnitude measured by SH0ES collaboration [100], compatible with the local universe. This leads to the following results:

1. $H_0 = 72.53^{+0.5}_{-0.3}$ km s^{-1}Mpc^{-1}, which is compatible with SH0ES [100];
2. $\Omega_{\rm m,0} = 0.339^{+0.024}_{-0.021}$, indicating a current matter density slightly larger than that from Planck 2018, but fully consistent when considering the measurement uncertainty [88]; and
3. $b = 2.28^{+6.52}_{-0.55}$.

In the joint analysis, instead, we can see that this degeneracy is broken by adding the CC $H(z)$ dataset, which provides the following results:

4. $H_0 = 67.5^{+1.7}_{-2.0}$ km s^{-1}Mpc^{-1}, fully consistent with Planck 2018 [88];
5. $\Omega_{\rm m,0} = 0.334^{+0.020}_{-0.021}$, with the Planck 2018 value covered by the error bars;
6. $\sigma_{8,0} = 0.774^{+0.029}_{-0.021}$, in weak tension with the Planck 2018 results but fully consistent with LSS observations [288];
7. $M_B = -19.423^{+0.067}_{-0.047}$; and
8. $b = 2.18^{+5.41}_{-0.55}$.

Both results obtained for the model parameter b cover GR within their uncertainties.

Similarly to the R^2-AB model, the most likely values obtained for the HS model parameters depend on the analysis. For the SNe Ia data alone, we obtained the following results:

1. $H_0 = 72.63^{+1.98}_{-0.36}$ km s^{-1}Mpc^{-1}, which is compatible with SH0ES [100];
2. $\Omega_{\rm m,0} = 0.324^{+0.021}_{-0.053}$, indicating a current matter density slightly larger than that from Planck 2018, but fully consistent when considering the measurement uncertainty [88]; and
3. $\mu = 77.0^{+18}_{-56}$.

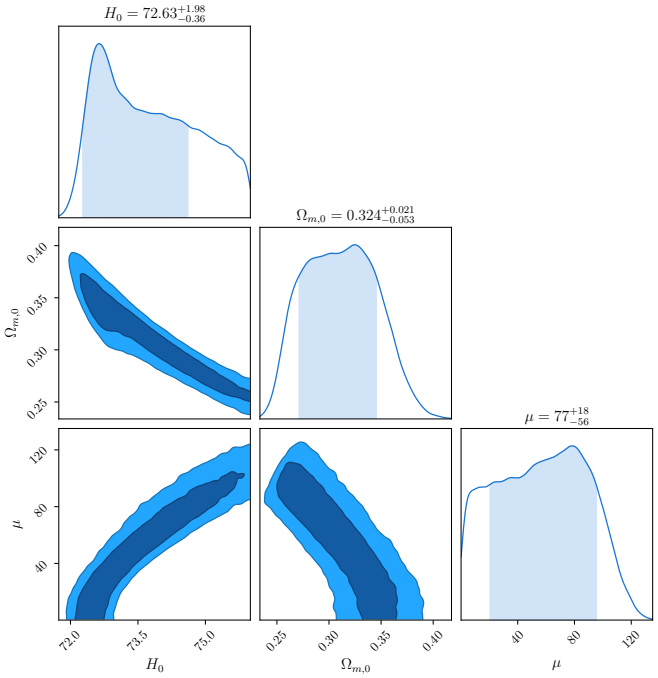

Figure 5.9: MCMC analysis for the HS model considering only PN$^+$ SNe Ia data. Here, we fixed $M_{\rm B} = -19.253$, as determined by SH0ES [100]. The priors used were $H_0 = [54, 76]$, $\Omega_{\rm m,0} = [0.1, 0.5]$, and $\mu = [0, 300]$.

For the joint analysis, we obtained:

4. $H_0 = 69.7^{+4.0}_{-2.6}$ km s^{-1}Mpc^{-1}, fully consistent with Planck 2018 [88];
5. $\Omega_{\rm m,0} = 0.260^{+0.063}_{-0.041}$, with the Planck 2018 value covered by the error bars;
6. $\sigma_{8,0} = 0.725^{+0.037}_{-0.031}$, in tension with the Planck 2018 results but consistent with LSS observations [288];
7. $M_B = -19.391^{+0.053}_{-0.056}$; and
8. $\mu = 93^{+41}_{-55}$.

The values obtained for the parameter μ in both analyses exclude GR at 2σ. Our MCMC results for the R^2-AB and HS models are summarized in Table 5.4.

While the chi-square statistic is very useful for locating the best-fit parameters within a given model, it is not appropriate for establishing comparisons between models with different number of parameters. This is because lower values of χ^2 can be obtained by simply increasing the number of parameters. Accordingly, other criteria for model selection are used in the literature, such as the Akaike Information Criterion (AIC) [289] and $\bar{\chi}^2_{\rm min} \equiv \chi^2_{\rm min}/(\mathscr{N} - \varpi)$, where $\mathscr{N}$ is the number of data points and ϖ is the number of independently adjusted parameters.

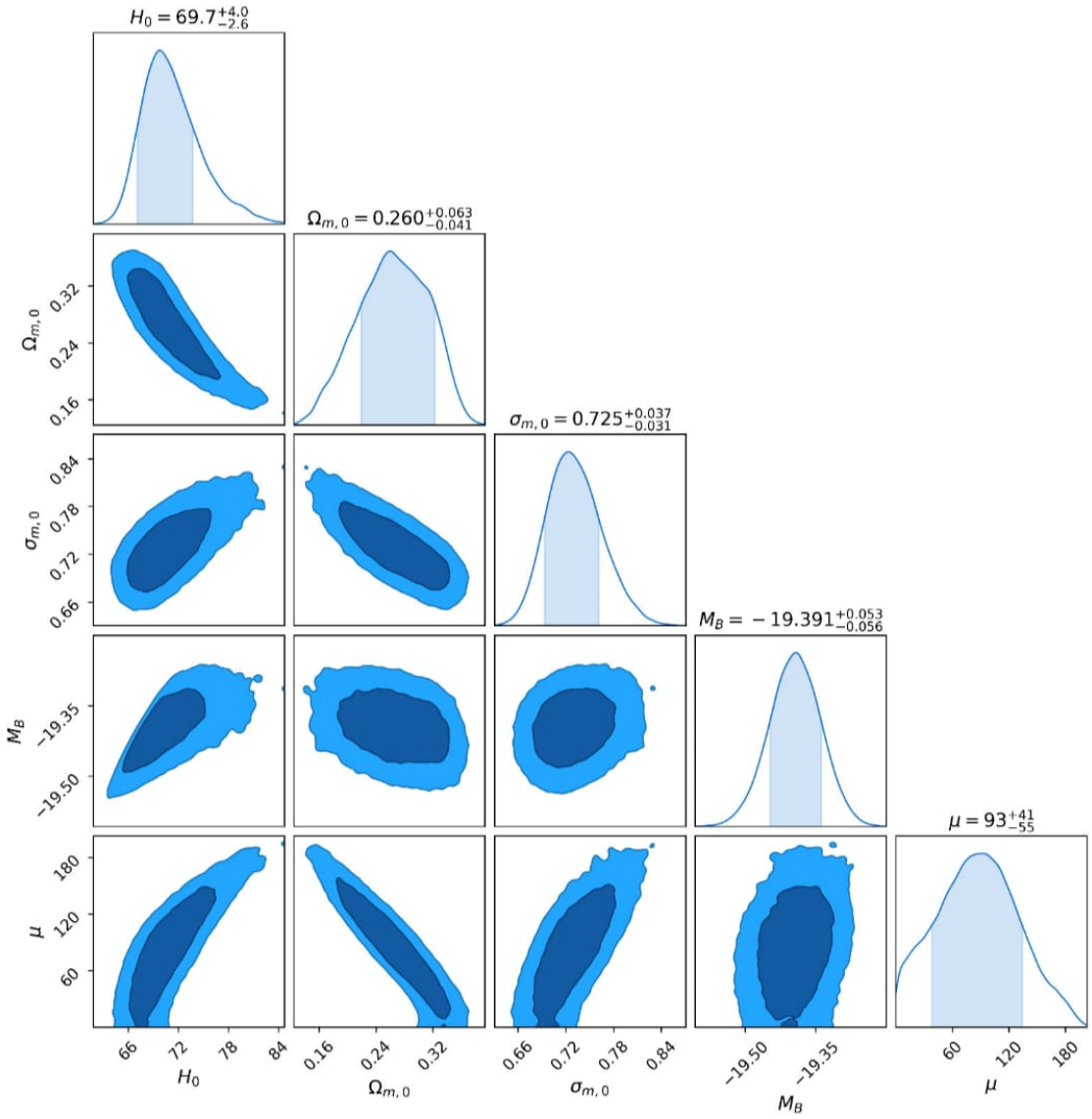

Figure 5.10: MCMC analysis for the HS model considering the data combination $\mathrm{PN}^{+} + \mathrm{CC} + \mathrm{RSD}$. In this analysis, the prior intervals were fixed as $H_0 = [60, 85]$, $\Omega_{\mathrm{m},0} = [0.1, 0.5]$, $\sigma_{8,0} = [0.6, 0.9]$, $M_{\mathrm{B}} = [-20.2, -19.0]$ and $\mu = [0, 300]$.

Model	Parameter	Only SNe	SNe+CC+RSD
R^2-AB	H_0	$72.53^{+0.5}_{-0.3}$	$67.5^{+1.7}_{-2.0}$
	$\Omega_{\mathrm{m},0}$	$0.339^{+0.024}_{-0.021}$	$0.334^{+0.020}_{-0.021}$
	$\sigma_{8,0}$	—	$0.774^{+0.029}_{-0.021}$
	M_{B}	fixed	$-19.423^{+0.067}_{-0.047}$
	b	$2.28^{+6.52}_{-0.55}$	$2.18^{+5.41}_{-0.55}$
R^2-HS	H_0	$72.63^{+1.98}_{-0.36}$	$69.7^{+4.0}_{-2.6}$
	$\Omega_{\mathrm{m},0}$	$0.324^{+0.021}_{-0.053}$	$0.26^{+0.063}_{-0.041}$
	$\sigma_{8,0}$	—	$0.725^{+0.037}_{-0.031}$
	M_{B}	fixed	$-19.391^{+0.053}_{-0.056}$
	μ	$77.0^{+18.0}_{-56.0}$	$93.0^{+41.0}_{-55.0}$

Table 5.4: Best-fit values obtained from our MCMC likelihood analyses.

Table 5.5: χ^2 statistics for model comparison: ΛCDM *versus* R^2-AB *versus* HS model. As observed, the AIC penalizes both the $f(R)$ models, as they have one additional independent parameter.

Estimators	Models		
	ΛCDM	R^2-AB	R^2-HS
$\chi^2_{\rm min}$	2898.865	2897.581	3029.834
$\mathscr{N} - \varpi$	1748	1747	1747
$\bar{\chi}^2_{\rm min}$	1.658	1.659	1.734
ΔAIC	0	0.716	132.969

The AIC for a model with parameters ϑ is defined as

$$AIC(\vartheta) \equiv \chi^2_{\rm min}(\vartheta) + 2\varpi\,, \tag{5.64}$$

where $\chi^2_{\rm min} \equiv -2\ln(\mathcal{L}_{max})$ is the minimum chi-square, and $\mathcal{L}_{max}$ is the maximum likelihood. Thus, the difference between the investigated model and a reference model (typically the flat-ΛCDM model) is given by $\Delta AIC = \Delta\chi^2_{\rm min} + 2\Delta\varpi$.

To make a comparison, we consider the flat-ΛCDM model as the reference model. We analyzed it using the same observational data as for the R^2-AB and HS models. The results are summarized in Table 5.5. It is observed that the AIC penalized both the R^2-AB and HS models, as they each have one additional – b and μ, respectively. Therefore, according to this criterion, the flat-ΛCDM is the model provides the best-fits to the cosmological data analyzed, i.e., the combined datasets of SNe+CC+RSD. However, we highlight that the R^2-AB model exhibits an AIC value very close to that of the flat-ΛCDM model ($\Delta AIC \sim 0.7$), making it a model that can be compared to the standard flat-ΛCDM when describing the accelerated expansion and growth of structures in the universe – without the need for exotic dark energy.

Ultimately, we observe that the R^2-AB model appears to simultaneously alleviate the H_0 and S_8 tensions. In the ΛCDM model, the current Hubble rate corresponds to $H(0) \equiv H_0$. In contrast, in $f(R)$ cosmology, this parameter obeys

$$H(0) \equiv f_1(H_0, \Omega_{\rm m,0}, b) \tag{5.65}$$

where f_1 is a functions of the cosmological and model parameter, evaluated at $t = t_0$. For the best-fit values in Table 5.4 – without accounting for error bars –, we obtain $H(0) = 71.17\,{\rm km\,s^{-1}\,Mpc^{-1}}$. On the other hand, the spectral variance of matter fluctuations follows as in the ΛCDM model, $\sigma_8(0) \equiv \sigma_{8,0}$, giving $S_8 = 0.817$, again without considering error bars.

5.8 Summary

In this chapter, we discuss our methodology for analyzing three viable $f(R)$ models: 1. the Appleby-Battye [49–51], 2. Hu-Sawicki [46], and 3. Starobinsky [47] models. The class of $f(R)$ theories offer alternative scenarios in which the recent cosmic acceleration results from the geometry of spacetime, rather than from an unknown, exotic form of energy [35]. This approach helps address various issues related to the cosmological constant, or any other DE physical interpretation. However, $f(R)$ gravity is known to introduce an extra degree of freedom, called the scalaron [205]. This scalar field couples with the metric and contributes to $g_{\mu\nu}$ in describing the gravitational field.

We began by presenting the models and the physical conditions under which they can be considered viable alternatives to GR and, consequently, to the ΛCDM model. However, $f(R)$ models are known to suffer from a weak singularity problem due to the unbounded growth of the scalaron mass at high curvatures [35, 51]. As a result, $f(R)$ theories cannot be naturally incorporated into any high-energy theory without proper fine-tuning. To address this, we added to the effective action a term proportional to R^2 with a sufficiently small coefficient in order to ensure the primordial inflation, as originally proposed in [35, 47]. Subsequently, we derived the equations of motion for each resulting R^2-corrected model: Eqs. (5.36) and (5.37) for the R^2-corrected AB model, and Eqs. (5.44) and (5.45) for both the HS and Starobinsky models. These equations were then solved, with our numerical results illustrated in Figures (5.5) through (5.5).

Moving to the second part of our analysis, we selected three datasets to constrain the model parameters: 1. $H(z)$ measurements from CC observations, 2. $[f\sigma_8](z)$ from RSD observations [276], and SNe Ia $m_{\rm B}(z)$ measurements from Pantheon+ and SH0ES collaborations [192]. Currently, only two of the three examined $f(R)$ models have been constrained by our analysis: the R^2-AB and HS models. For both models, we constructed the probability density (likelihood) function, defined flat *priors*, and performed MCMC analyses. The results for the R^2-AB model are presented in Figures 5.7 and 5.8, while those for the HS model are shown in Figures 5.9 and 5.10. A summary of these outcomes can be found in Table 5.4.

In the final part of our work, we conducted a model comparison using the AIC, defined by Eq. (5.64), with the flat-ΛCDM cosmology as the reference model, as discussed in Chapter 3. A summary of our results is provided in Table 5.5. Our findings on the R^2-AB model are detailed in Ref. [249].

In general terms, all $f(R)$ models performed well in describing the correct time evolution of the universe along with the observational datasets used. While a certain degree of degeneracy exists between these models and ΛCDM at the background

level, there remains potential for differentiation based on the geometric equation of state, $w_{\rm DE}(z)$. Another approach to breaking this degeneracy is at the perturbative level, given that $f(R)$ theories predict scale-dependent evolution of matter fluctuations. However, parameter determination yielded mixed results: the R^2-AB model's constraints were inconclusive, while the HS model diverged from the ΛCDM model at the 2σ CL. Despite these findings, AIC penalizes both $f(R)$ models due to the extra independent parameter each includes relative to the flat-ΛCDM model. Thus, according to this criterion, the flat-ΛCDM model emerges as the model best-fitting the analyzed cosmological data – namely, the SNe+CC+RSD datasets.

Chapter 6

Conclusions

Nowadays, cosmology possesses a concordance model to call *standard*, known as the flat-ΛCDM model, emerged from efforts to reconcile theoretical predictions with observational data gathered over the past century. This model is based only on GR, the cosmological principle, and the inflationary hypothesis. It belongs to the class of FLRW cosmologies, in which most of the universe's content is *dark*, corresponding to around 26% of DM and approximately 70% of DE. In this scenario, only about 4% is made of baryons (i.e., atoms, planets, dust, gas, and stars) and there is almost no radiation. On the one hand, dark matter is necessary by explaining the rotation curve of objects in gravitationally bound systems, such as galaxies and galaxy clusters, the primordial acoustic oscillations, and the structure formation in the universe. On the other hand, dark energy emerges as the attempt to explain the current acceleration phase of the universe.

The flat-ΛCDM has the advantage of being the simplest cosmological model, advantage a flat spatial three-section, non-relativistic (or cold) dark matter (CDM), and dark energy arising from quantum vacuum energy fluctuation (i.e., the cosmological constant Λ). With only six independent parameters, it provides the best fit to the current range of astronomical observations and is therefore also known as the concordance model.

Despite its success, the flat-ΛCDM model, with its mysterious dark energy component in the form of a cosmological constant, is not considered the final model of cosmology, as it still has unresolved issues. The most significant of these questions is undoubtedly the cosmological constant problem, or vacuum catastrophe, which reveals a staggering staggering of up to 120 orders of magnitude between QFT predictions for vacuum energy and interpretations of cosmological observations in light of the standard model. This discrepancy has led cosmologists and particle physicists to question whether dark energy can indeed be correctly interpreted as a positive cosmological constant or even if GR is the most appropriate theory for describing gravitation on cosmological scales.

These questions have led the community to adopt two main approaches: a more conservative one, which involves allowing dark energy to be dynamic, and another more bolder one, which involves extending GR to enable an accelerated expansion without requiring any dark energy content. The second approach has gained further prominence, as it addresses the long-standing question of GR's renormalization. In this context, we contribute to the efforts aimed at studying alternative cosmological scenarios where GR is modified in order to explain the observed universe – both at the background and perturbative levels – while recovering Einstein's theory as an appropriate limiting case.

The content of this thesis begins in Chapter 2, where we discuss the keynote concepts underlying the current theory of gravity, Einstein's GR, in order to lay the groundwork for understanding modified (or extended) theories of gravity.

In Chapter 3, we address the modern theory of cosmology and the key cosmological observations that support it. Combined with the inflationary hypothesis, these elements yield the standard flat-ΛCDM model, which explains the recent phase of cosmic acceleration as being driven by the cosmological constant, Λ, or equivalently, the quantum vacuum energy density, $\rho_{\rm vac}$. In this framework, structure formation is primarily driven by the dynamics of the non-relativistic dark matter and triggered by the evolution of adiabatic curvature fluctuations established in the very early universe by inflation, which are expected to be approximately Gaussian.

In Chapter 4, we provide an overview of the motivations, methods, and challenges associated with modifying GR, as well as an *X-ray* of the most successful ETGs, namely, the prototype Brans-Dicke gravity, general scalar-tensor theories, the higher-dimensional Kaluza-Klein theories, and the higher-order theories of gravity. Within this last category lies the class of $f(R)$ theories, the primary focus of our investigation and the main subject of the second half of this chapter.

Higher-order $f(R)$ theories are achieved by suitably modifying GR, where the Einstein-Hilbert Lagrangian density, $R - 2\Lambda$ (or simply R by inserting Λ into $T_{\mu\nu}$), is replaced by an arbitrary function of the Ricci scalar, R, in order to reproduce the observed late-time acceleration of the universe without requiring any dark energy content. This new geometric framework for spacetime must satisfy rigorous phenomenological criteria [35, 43, 44, 205, 290, 291]:

- Since GR is a well-established theory for strong gravitational fields and small scales, any modification should recover Einstein's theory as a limiting theory at appropriate scales and in strong gravitational fields;

- In the distant past, $z \gg 1$, $f(R)$ gravity should be consistent with a matter-dominated era;

- At large scales and in the recent past, $z < z_{\rm t}$ (= transition redshift), the

expected behavior of $f(R)$ gravity should explains the universe's accelerated expansion phase, a feature well-established by different cosmological tracers (background level);

- At the perturbative level, $f(R)$ gravity should satisfactorily explain observational data on the growth rate of cosmic structures.

This cosmic phenomenology, required for any contender to the concordance model of cosmology, the flat-ΛCDM model, makes the search for viable $f(R)$ candidates nontrivial. One such candidate is the R^2-AB model [49–51], which has limited references in the literature and is investigated here using cosmological data to constrain its parameters. Additionally, two other widely studied candidates, the HS [46] and Starobinsky [47] models, are investigated here for comparison.

A general criticism of $f(R)$ models is their tendency to exhibit unbounded growth in the scalaron mass at high curvatures, or in the early universe. This type of weak curvature singularity has been observed to develop within the redshift range of cosmological interest, i.e., $|R| < \infty$, for most models, introducing instabilities and indicating an internal incompleteness of these theories [51]. For the AB model in particular, it occurs within the interval $0 \leq z \leq 4$. However, it has been shown that adding an R^2 term can address this issue by effectively constraining the scalaron mass, thereby preventing excessive growth and ensuring the viability of these models [35, 47, 51]. In this context, we investigated the R^2-AB, HS, and Starobinsky models from a theoretical perspective and obtained cosmological constraints for the R^2-AB and HS models using CC [258–264], RSD [276], and SNe [192] data.

In general, an $f(R)$ or other alternative model encounters the problem that a larger number of parameters makes the statistical best-fit process less efficient compared to the flat-ΛCDM model, which has just six independent parameters. For this reason, we focused on models with only one or two additional independent parameters compared to the ΛCDM model, such as the R^2-AB model, with only one additional free parameter: $\{b\}$, and the HS and Starobinsky models both with two additional free parameter: $\{n, \mu\}$ and $\{n, \lambda_{\rm S}\}$, respectively. However, by setting $n = 1$, we reduced both the HS and Starobinsky models to a single free parameter: μ for the HS model and $\lambda_{\rm S}$ for the Starobinsky model.

Thus, we performed MCMC analyses of the R^2-AB and HS models using two approaches: 1) considering only SNe Ia data, and 2) considering the joint analysis of SNe+CC+RSD data. For the fist approach, we obtained H_0 values compatible with SH0ES measurements and $\Omega_{\rm m,0}$ values slightly larger than those from Planck, but in full agreement when considering the erro bars, for both models. For the second approach, we obtained H_0 and $\Omega_{\rm m,0}$ values compatible with Planck, $\sigma_{8,0}$ values in weak tension with Planck, but in full agreement with LSS observations [288], and $M_{\rm B}$ val-

ues compatible with SH0ES, for both models. Additionally, our analyses show that both the R^2-AB and HS model parameters are reasonably well-constrained by the cosmological data applied. First, for the R^2-AB model, SNe Ia data alone returned a best-fit value for the model parameter $b = 2.28^{+6.52}_{-0.55}$, whereas the joint analysis of SNe+CC+RSD returned $b = 2.18^{+5.41}_{-0.55}$; both values are compatible with each other and fall within the interval where the R^2-AB model satisfies all the phenomenological criteria mentioned above [44, 49, 51]. Second, for the HS model, SNe Ia data alone returned $\mu = 77.0^{+18.0}_{-56.0}$, whereas the joint analysis of SNe+CC+RSD returned $\mu = 93.0^{+41.0}_{-55.0}$; both results exclude GR (case with $\mu = 0$) at 2σ CL.

The results of our statistical analyses show that both the R^2-AB and HS models are consistent with the observational data used, encompassing both the background and perturbative aspects. However, the determination of the R^2-AB model parameter b was inconclusive (see Table 5.4), highlighting the need for further investigation into alternative scenarios and additional analyses incorporating different observational datasets. Furthermore, our analyses show that the R^2-AB model exhibits an AIC value very close to that of the flat-ΛCDM model ($\Delta AIC \sim 0.7$), making it a competitive alternative to the standard flat-ΛCDM model when describing the accelerated expansion and growth of structures in the universe – without the need for exotic dark energy. Our findings on the R^2-AB model are published in Ref. [249].

Bibliography

[1] A. G. Riess et al. Observational Evidence from Supernovae for an Accelerating Universe and a Cosmological Constant. *The Astronomical Journal*, 116:1009–1038, 1998.

[2] S. Perlmutter et al. Measurements of Ω and Λ from 42 HighRedshift Supernovae. *The Astrophysical Journal*, 517:565–586, 1999.

[3] S. Perlmutter, M. S. Turner, and M. White. Constraining Dark Energy with Type Ia Supernovae and LargeScale Structure. *Physical Review Letters*, 83:670–673, 1999.

[4] D. Huterer and M. S. Turner. Prospects for probing the Dark Energy via Supernova distance measurements. *Physical Review D*, 60:081301, 1999.

[5] A. Einstein. Kosmologische Betrachtungen zur allgemeinen Relativitätstheorie. *Sitzungsberichte der Königlich Preussischen Akademie der Wissenschaften*, pages 142–152, 1917.

[6] W. de Sitter. On Einstein's Theory of Gravitation and its Astronomical Consequences. Third Paper. *Monthly Notices of the Royal Astronomical Society*, 78:328, 1917.

[7] Ya. B. Zel'Dovich. Cosmological Constant and Elementary Particles. *Soviet Journal of Experimental and Theoretical Physics Letters*, 6:3–16, 1967.

[8] S. Weinberg. The cosmological constant problem. *Rev. Mod. Phys.*, 61:1–23, 1989.

[9] A. Padilla. Lectures on the Cosmological Constant Problem, 2015.

[10] P. J. Steinhardt. *Critical Problems in Physics*. Princeton Series in Physics. Princeton University Press, 1997.

[11] H. E. S. Velten, R. F. vom Marttens, and W. Zimdahl. Aspects of the cosmological "coincidence problem". *Eur. Phys. J. C*, 74(11):3160, 2014.

[12] G. W. Gibbons, S. W. Hawking, and S. T. C. Siklos, editors. *The Very Early Universe: Proceedings of the Nuffield Workshop*. Cambridge University Press, 1983.

[13] L. F. Abbott. A Mechanism for Reducing the Value of the Cosmological Constant. *Physics Letters B*, 150:427–430, 1985.

[14] J. Solà. Scale Gauge Symmetry and the Standard Model. *International Journal of Modern Physics A*, 5:4225–4240, 1990.

[15] J. C. Carvalho, J. A. S. Lima, and I. Waga. Cosmological consequences of a timedependent Λ term. *Physical Review D*, 46:2404–2407, 1992.

[16] C. Moreno-Pulido and J. Solà. Renormalizing the vacuum energy in cosmological spacetime: Implications for the cosmological constant problem. *The European Physical Journal C*, 82(6):551, 2022.

[17] C. Wetterich. Cosmology and the fate of dilatation symmetry. *Nuclear Physics B*, 302:668–696, 1988.

[18] P. G. Ferreira and M. Joyce. Cosmology with a primordial scaling field. *Physical Review D*, 58:023503, 1998.

[19] C. Armendariz-Picon, V. F. Mukhanov, and P. J. Steinhardt. Essentials of k-essence. *Physical Review D*, 63:103510, 2001.

[20] A. Yu. Kamenshchik, U. Moschella, and V. Pasquier. An alternative to quintessence. *Physical Letters B*, 511:265–268, 2001.

[21] A. R. Cooray and D. Huterer. Gravitational lensing as a probe of quintessence. *The Astrophysical Journal*, 513:L95–L98, 1999.

[22] M. Chevallier and D. Polarski. Accelerating universes with scaling dark matter. *International Journal of Modern Physics D*, 10:213–224, 2001.

[23] E. V. Linder. Exploring the expansion history of the universe. *Physical Review Letters*, 90:091301, 2003.

[24] G. Efstathiou. Constraining the Equation of State of the Universe from Distant Type Ia Supernovae and Cosmic Microwave Background Anisotropies. *Monthly Notices of the Royal Astronomical Society*, 310:842–850, 1999.

[25] C. Wetterich. Phenomenological parameterization of quintessence. *Physics Letters B*, 594:17–22, 2004.

[26] S. Hannestad and E. Mörtsell. Cosmological constraints on the dark energy equation of state and its evolution. *Journal of Cosmology and Astroparticle Physics*, 2004:001, 2004.

[27] Y. Gong and Y. Zhang. Probing the curvature and dark energy. *Physical Review D*, 72:043518, 2005.

[28] H. K. Jassal, J. S. Bagla, and T. Padmanabhan. WMAP constraints on low redshift evolution of dark energy. *Monthly Notices of the Royal Astronomical Society: Letters*, 356:L11–L16, 2005.

[29] S. Lee. Constraints on the dark energy equation of state from the separation of CMB peaks and the evolution of α. *Physical Review D*, 71:123528, 2005.

[30] E. M. Barboza, J. S. Alcaniz, Z. H. Zhu, and R. Silva. Generalized equation of state for dark energy. *Physical Review D*, 80(4):043521, 2009.

[31] A. Krasiński. *Inhomogeneous Cosmological Models*. Cambridge University Press, 1997.

[32] D. Vrba. *Inhomogeneous cosmological models*. PhD thesis, Charles University, Prague, 2014.

[33] B. Balazs and G. Bene. Simplified Model of Voids Able to Mimic Accelerating Expansion at High z without Dark Energy. *Gravitation and Cosmology*, 24:331–336, 2018.

[34] T. P. Sotiriou and V. Faraoni. *f(R)* Theories Of Gravity. *Reviews of Modern Physics*, 82:451–497, 2008.

[35] A. De Felice. *f(R)* theories. *Living Reviews in Relativity*, 13:1, 2010.

[36] C. Brans and R. H. Dicke. Mach's Principle and a Relativistic Theory of Gravitation. *Physical Review*, 124:925–935, 1961.

[37] I. Quiros. Selected topics in scalar–tensor theories and beyond. *International Journal of Modern Physics D*, 28:1930012, 2019.

[38] T. Kaluza. Zum Unitätsproblem der Physik. *Sitzungsberichte der Preußischen Akademie der Wissenschaften (Mathematik-Physik)*, pages 966–972, 1921.

[39] O. Klein. Quantentheorie und fünfdimensionale Relativitätstheorie. *Zeitschrift für Physik*, 37:895–906, 1926.

[40] O. Klein. The Atomicity of Electricity as a Quantum Theory Law. *Nature*, 118:516, 1926.

[41] K. S. Stelle. Classical Gravity with Higher Derivatives. *General Relativity and Gravitation*, 9:353–371, 1978.

[42] K. S. Stelle. Renormalization of Higher-Derivative Quantum Gravity. *Physical Review D*, 16:953–969, Aug 1977.

[43] T. Clifton, P. G. Ferreira, A. Padilla, and C. Skordis. Modified Gravity and Cosmology. *Phys. Rep.*, 513:1–189, 2012.

[44] L. Amendola, R. Gannouji, D. Polarski, and S. Tsujikawa. Conditions for the Cosmological Viability of $f(R)$ Dark Energy Models. *Phys. Rev. D*, 75:083504, 2007.

[45] S. Tsujikawa. Observational Signatures of $f(R)$ Dark Energy Models that Satisfy Cosmological and Local Gravity Constraints. *Phys. Rev. D*, 77:023507, 2008.

[46] W. Hu and I. Sawicki. Models of $f(R)$ Cosmic Acceleration that Evade Solar System Tests. *Phys. Rev. D*, 76:064004, 2007.

[47] A. A. Starobinsky. Disappearing Cosmological Constant in $f(R)$ Gravity. *JETP Lett.*, 86:157–163, 2007.

[48] A. A. Starobinsky. A New Type of Isotropic Cosmological Models Without Singularity. *Physics Letters B*, 91:99–102, 1980.

[49] S. A. Appleby and R. A. Battye. Do Consistent $f(R)$ Models Mimic General Relativity Plus Λ? *Phys. Lett. B*, 654:7–12, 2007.

[50] S. A. Appleby and R. A. Battye. Aspects of Cosmological Expansion in $f(R)$ Gravity Models. *JCAP*, 05:019, 2008.

[51] S. A. Appleby, R. A. Battye, and A. A. Starobinsky. Curing Singularities in Cosmological Evolution of $f(R)$ Gravity. *JCAP*, 2010:005, 2010.

[52] B. Li and J. D. Barrow. Cosmology of $f(R)$ Gravity in the Metric Variational Approach. *Phys. Rev. D*, 75:084010, 2007.

[53] L. Amendola and S. Tsujikawa. Phantom Crossing, Equation of State Singularities, and Local Gravity Constraints in $f(R)$ Models. *Phys. Lett. B*, 660:125–132, 2008.

[54] G. Cognola et al. Class of Viable Modified $f(R)$ Gravities Describing Inflation and the Onset of Accelerated Expansion. *Phys. Rev. D*, 77:046009, 2008.

[55] E. V. Linder. Exponential Gravity. *Phys. Rev. D*, 80:123528, 2009.

[56] E. Elizalde et al. Nonsingular Exponential Gravity: A Simple Theory for Early and Late Time Accelerated Expansion. *Phys. Rev. D*, 83, 2011.

[57] B. Chen and Q. Xu. A New Exponential Gravity. *Communications in Theoretical Physics*, 61:141–147, 2014.

[58] A. Nautiyal, S. Panda, and A. Patel. A New $f(R)$ Model in the Light of Local Gravity Test and Late-time Cosmology. *International Journal of Modern Physics D*, 27:1750185, 2018.

[59] D. Gogoi and U. Goswami. A New $f(R)$ Gravity Model and Properties of Gravitational Waves in It. *The European Physical Journal C*, 80:1101, 2020.

[60] V. K. Oikonomou. An Exponential $F(R)$ Dark Energy Model. *General Relativity and Gravitation*, 45:2467–2477, 2013.

[61] V. K. Oikonomou. Unifying Inflation with Early and Late Dark Energy Epochs in Axion $F(R)$ Gravity. *Physical Review D*, 103:044036, 2021.

[62] F. Avila, C. P. Novaes, A. Bernui, E. de Carvalho, and J. P. Nogueira-Cavalcante. The Angular Scale of Homogeneity in the Local Universe with the SDSS Blue Galaxies. *Mon. Not. Roy. Astron. Soc.*, 488(1):1481–1487, 2019.

[63] G. A. Marques and A. Bernui. Tomographic Analyses of the CMB Lensing and Galaxy Clustering to Probe the Linear Structure Growth. *JCAP*, 05:052, 2020.

[64] E. de Carvalho, A. Bernui, F. Avila, C. P. Novaes, and J. P. Nogueira-Cavalcante. BAO Angular Scale at $z_{\rm eff} = 0.11$ with the SDSS Blue Galaxies. *Astron. Astrophys.*, 649:A20, 2021.

[65] C. Franco, F. Avila, and A. Bernui. Probing Cosmic Isotropy in the Local Universe. *Monthly Notices of the Royal Astronomical Society*, 527:7400–7413, 2023.

[66] F. Oliveira, F. Avila, A. Bernui, A. Bonilla, and R. C. Nunes. Reconstructing the growth index γ with Gaussian processes. *Eur. Phys. J. C*, 84(6):636, 2024.

[67] P. Bessa, M. Campista, and A. Bernui. Observational constraints on Starobinsky $f(R)$ cosmology from cosmic expansion and structure growth data. *Eur. Phys. J. C*, 82:506, 2022.

[68] S. Weinberg. *Gravitation and Cosmology: Principles and Applications of the General Theory of Relativity*. John Wiley & Sons, Inc., 1972.

[69] J. Foster and J. D. Nightingale. *A Short Course in General Relativity*. Springer, 2005.

[70] B. Schutz. *A First Course in General Relativity*. Cambridge University Press, 2009.

[71] W. Rindler. *Relativity: Special, General, and Cosmological*. Cambridge University Press, 2006.

[72] S. M. Carroll. *Spacetime and Geometry: An Introduction to General Relativity*. AddisonWesley, 2003.

[73] P. T. Landsberg and N. T. Bishop. Gravitational Redshift and the Equivalence Principle. *Foundations of Physics*, 6(6):727–737, 1976.

[74] H. B. G. Casimir. On the attraction between two perfectly conducting plates. *Indag. Math.*, 10(4):261–263, 1948.

[75] M. J. Sparnaay. Measurements of attractive forces between flat plates. *Physica*, 24:751–764, 1958.

[76] G. Graham. Casimir energies and general relativity energy conditions. *Journal of Physics A: Mathematical and General*, 39:6423, 2006.

[77] G. Sterman. *An Introduction to Quantum Field Theory*. Cambridge University Press, 1993.

[78] R. Rosenfeld. A Cosmologia. *Física na Escola*, 6:31–37, 2005.

[79] D. Baumann. *Cosmology*. Cambridge University Press, 2022.

[80] S. Dodelson and F. Schmidt. *Modern Cosmology*. Elsevier Science, 2020.

[81] V. Mukhanov. *Physical Foundations of Cosmology*. Cambridge University Press, 2005.

[82] T. Padmanabhan. *Structure Formation in the Universe*. Cambridge University Press, 1993.

[83] G. A. Marques, C. P. Novaes, A. Bernui, and I. S. Ferreira. Isotropy analyses of the Planck convergence map. *Monthly Notices of the Royal Astronomical Society*, 473:165–172, 2018.

[84] M. I. Scrimgeour et al. The WiggleZ Dark Energy Survey: the transition to largescale cosmic homogeneity: Cosmic homogeneity in the WiggleZ survey. *Monthly Notices of the Royal Astronomical Society*, 425:1161–134, 2012.

[85] P. Laurent et al. A 14h3Gpc3 study of cosmic homogeneity using BOSS DR12 quasar sample. *Journal of Cosmology and Astroparticle Physics*, 2016:060–060, 2016.

[86] P. Ntelis et al. Exploring cosmic homogeneity with the BOSS DR12 galaxy sample. *JCAP*, 06:19–019, 2017.

[87] F. Avila, C. P. Novaes, A. Bernui, and E. de Carvalho. The scale of homogeneity in the local Universe with the ALFALFA catalogue. *JCAP*, 12:041–041, 2018.

[88] N. Aghanim et al. Planck2018 results: VI. Cosmological parameters. *Astronomy & Astrophysics*, 641:A6–A6, 2020.

[89] N. Khetan et al. A new measurement of the Hubble constant using Type Ia supernovae calibrated with surface brightness fluctuations. *Astronomy & Astrophysics*, 647:A72–A72, 2021.

[90] E. Hubble. A Relation between Distance and Radial Velocity among ExtraGalactic Nebulae. *Proceedings of the National Academy of Science*, 15:168–173, 1929.

[91] E. Di Valentino. A combined analysis of the H0 late time direct measurements and the impact on the Dark Energy sector. *Monthly Notices of the Royal Astronomical Society*, 502:2065–2073, 2021.

[92] W. L. Freedman et al. Final Results from the Hubble Space Telescope Key Project to Measure the Hubble Constant. *The Astrophysical Journal*, 553:47–72, 2001.

[93] W. L. Freedman et al. Carnegie Hubble Program: A MidInfrared Calibration of the Hubble Constant. *The Astrophysical Journal*, 758:24–24, 2012.

[94] L. Macri et al. Cosmological Constraints from Type Ia Supernovae and the Hubble Diagram. *Astrophys. J.*, 705:1324–1336, 2009.

[95] A. G. Riess et al. A 3% Solution: Determination of the Hubble Constant with the Hubble Space Telescope and Wide Field Camera 3. *The Astrophysical Journal*, 730:119–119, 2011.

[96] A. G. Riess et al. A 2.4% Determination of the Local Value of the Hubble Constant. *The Astrophysical Journal*, 826:56–56, 2016.

[97] A. G. Riess et al. New Parallaxes of Galactic Cepheids from Spatially Scanning the Hubble Space Telescope: Implications for the Hubble Constant. *The Astrophysical Journal*, 855:136–136, 2018.

[98] A. G. Riess et al. Large Magellanic Cloud Cepheid Standards Provide a 1% Foundation for the Determination of the Hubble Constant and Stronger Evidence for Physics beyond *Lambda*CDM. *The Astrophysical Journal*, 876:85–85, 2019.

[99] A. G. Riess et al. Cosmic Distances Calibrated to 1% Precision with Gaia EDR3 Parallaxes and Hubble Space Telescope Photometry of 75 Milky Way Cepheids Confirm Tension with ΛCDM. *The Astrophysical Journal Letters*, 908:L6–L6, 2021.

[100] A. G. Riess et al. A Comprehensive Measurement of the Local Value of the Hubble Constant with $1\,\mathrm{km\,s^1\,Mpc^1}$ Uncertainty from the Hubble Space Telescope and the SH0ES Team. *The Astrophysical Journal Letters*, 934:L7–L7, 2022.

[101] D. N. Spergel et al. First-Year Wilkinson Microwave Anisotropy Probe (WMAP) Observations: Determination of Cosmological Parameters. *The Astrophysical Journal Supplement Series*, 148:175–194, 2003.

[102] D. N. Spergel et al. Wilkinson Microwave Anisotropy Probe (WMAP) three year results: implications for cosmology. *The Astrophysical Journal Supplement Series*, 170:377–377, 2007.

[103] G. Hinshaw et al. FiveYear Wilkinson Microwave Anisotropy Probe (WMAP) Observations: Data Processing, Sky Maps, and Basic Results. *The Astrophysical Journal Supplement Series*, 180:225–245, 2009.

[104] E. Komatsu et al. SevenYear Wilkinson Microwave Anisotropy Probe (WMAP) Observations: Cosmological Interpretation. *The Astrophysical Journal Supplement Series*, 192:18–18, 2011.

[105] C. L. Bennett et al. NineYear Wilkinson Microwave Anisotropy Probe (WMAP) Observations: Final Maps and Results. *The Astrophysical Journal Supplement Series*, 20, 2013.

[106] P. A. R. Ade et al. Planck2013 results. XVI. Cosmological parameters. *Astronomy & Astrophysics*, 571:A16–A16, 2014.

[107] P. A. R. Ade et al. Planck2015 results: XIII. Cosmological parameters. *Astronomy & Astrophysics*, 594:A13–A13, 2016.

[108] S. Aiola et al. The Atacama Cosmology Telescope: DR4 maps and cosmological parameters. *Journal of Cosmology and Astroparticle Physics*, 2020:047047, 2020.

[109] B. Wang, M. López Corredoira, and J. Wei. The Hubble tension survey: A statistical analysis of the 2012–2022 measurements. *Monthly Notices of the Royal Astronomical Society*, 527:7692–7700, 2024.

[110] B. Pritychenko. A Nuclear Data Approach for the Hubble Constant Measurements, 2015.

[111] R. B. Tully. The Hubble Constant: A Historical Review, 2023.

[112] E. Di Valentino et al. In the realm of the Hubble tension — a review of solutions. *Classical and Quantum Gravity*, 38:153001, 2021.

[113] E. Abdalla et al. Cosmology intertwined: A review of the particle physics, astrophysics, and cosmology associated with the cosmological tensions and anomalies. *Journal of High Energy Astrophysics*, 34:49–211, 2022.

[114] L. Perivolaropoulos and F. Skara. Challenges for ΛCDM: An update. *New Astronomy Reviews*, 95:101659, 2022.

[115] J. Hu and F. Wang. Hubble Tension: The Evidence of New Physics. *Universe*, 9:94, 2023.

[116] M. Pospelov and J. Pradler. Big Bang Nucleosynthesis as a Probe of New Physics. *Annual Review of Nuclear and Particle Science*, 60:539–568, 2010.

[117] C. Pitrou, E. Parizot, R. Sivanandam, C. Bonvin, and F. Forastieri. Precision Primordial Nucleosynthesis at Next-to-Next-to-Leading-Order. *Journal of Cosmology and Astroparticle Physics*, 2018:027, 2018.

[118] L. Kawano. Let's Go: Early Universe. 2. Primordial Nucleosynthesis: The Computer Way. Technical report, FERMILABPUB92004A, 1992.

[119] O. Pisanti, A. Cirillo, S. Esposito, F. Iocco, G. Mangano, G. Miele, and P. D. Serpico. PArthENoPE: Public Algorithm Evaluating the Nucleosynthesis of Primordial Elements. *Computer Physics Communications*, 178:956–971, 2008.

[120] R. Consiglio, P. F. de Salas, G. Mangano, G. Miele, S. Pastor, and O. Pisanti. PArthENoPE Reloaded. *Computer Physics Communications*, 233:237–242, 2018.

[121] A. Arbey. AlterBBN: A Program for Calculating the BBN Abundances of the Elements in Alternative Cosmologies. *Computer Physics Communications*, 183:1822–1831, 2012.

[122] A. Arbey, J. Auffinger, K. P. Hickerson, and E. S. Jenssen. AlterBBN v2: A Public Code for Calculating BigBang Nucleosynthesis Constraints in Alternative Cosmologies. *Computer Physics Communications*, 248:106982, 2020.

[123] R. J. Cooke, M. Pettini, and C. C. Steidel. One Percent Determination of the Primordial Deuterium Abundance. *The Astrophysical Journal*, 855:102, 2018.

[124] T. M. Bania, C. Charbonnel, R. T. Rood, and D. S. Balser. The Cosmic Helium3 Abundance: Implications for Big Bang Nucleosynthesis, Stellar Evolution, and Galactic Chemical Evolution. In *37th Rencontres de Moriond on the Cosmological Model*, pages 151–158, Hanoi, 2003. The Gioi.

[125] L. Sbordone et al. The Metalpoor End of the Spite Plateau I. Stellar Parameters, Metallicities, and Lithium Abundances. *Astronomy & Astrophysics*, 522:A26, 2010.

[126] M. Deal and C. J. A. P. Martins. Primordial Nucleosynthesis with Varying Fundamental Constants: Solutions to the Lithium Problem and the Deuterium Discrepancy. *Astronomy & Astrophysics*, 653:A48, 2021.

[127] C. Marrder, G. Mathews, L. Boccioli, and I. S. Suh. Stellar Solutions for the Cosmological Lithium Problem. In *APS April Meeting Abstracts*, volume 2021 of *APS Meeting Abstracts*, page Z09.004, 2021.

[128] A. Bernui, B. Mota, M. J. Rebouças, and R. Tavakol. A note on the large-angle anisotropies in the WMAP cut-sky maps. *International Journal of Modern Physics D*, 16(203):411–420, jan 2007.

[129] A. Bernui. Is the cold spot responsible for the CMB North-South asymmetry? *Physical Review D*, 80(12):123010, dec 2009.

[130] A. Bernui and M. J. Rebouças. Searching for non-Gaussianity in the WMAP data. *Physical Review D*, 79(6):063528, mar 2009.

[131] A. Bernui and M. J. Rebouças. NonGaussianity in the foreground-reduced CMB maps. *Physical Review D*, 81:063533, 2010.

[132] A. Bernui and M. J. Rebouças. Mapping the large-angle deviation from Gaussianity in simulated CMB maps. *Physical Review D*, 85(2):023522, jan 2012.

[133] C. P. Novaes, A. Bernui, G. A. Marques, and I. S. Ferreira. Local analyses of Planck maps with Minkowski functionals. *MNRAS*, 461(2):1363–1373, sep 2016.

[134] A. Bernui, C. P. Novaes, T. S. Pereira, and G. D. Starkman. Topology and the suppression of CMB large-angle correlations. *arXiv eprints*, page arXiv:1809.05924, sep 2018.

[135] Dorothea Samtleben, Suzanne Staggs, and Bruce Winstein. The Cosmic Microwave Background for Pedestrians: A Review for Particle and Nuclear Physicists. *Annual Review of Nuclear and Particle Science*, 57:245–283, 2007.

[136] N. W. Boggess et al. The COBE Mission: Its Design and Performance Two Years after Launch. *The Astrophysical Journal*, 397:420–429, 1992.

[137] G. F. Smoot. COBE observations and results. *AIP Conference Proceedings*, 476:1–10, 1999.

[138] George F. Smoot. The CMB spectrum. In *International School of Astrophysics, D. Chalonge: 5th Course: Current Topics in Astrofundamental Physics*, pages 407–440, May 1997.

[139] D. J. Fixsen. The spectrum of the CMB anisotropy from the combined COBE FIRAS and DMR observations. *The Astrophysical Journal*, 486:623, 1997.

[140] P. de Bernardis et al. A flat Universe from high-resolution maps of the cosmic microwave background radiation. *Nature*, 404:955–959, 2000.

[141] R. Stompor et al. Cosmological Implications of the MAXIMA-1 High-Resolution Cosmic Microwave Background Anisotropy Measurement. *The Astrophysical Journal*, 561:L7–L10, 2001.

[142] G. Hinshaw et al. Nine-Year Wilkinson Microwave Anisotropy Probe (WMAP) Observations: Cosmological Parameter Results. *The Astrophysical Journal Supplement Series*, 208:19, 2013.

[143] A. Bernui, C. Tsallis, and T. Villela. Temperature fluctuations of the cosmic microwave background radiation: A case of nonextensivity? *Physics Letters A*, 356(6):426–430, aug 2006.

[144] A. Bernui, C. Tsallis, and T. Villela. Deviation from Gaussianity in the cosmic microwave background temperature fluctuations. *EPL (Europhysics Letters)*, 78(1):19001, apr 2007.

[145] C. P. Novaes, A. Bernui, I. S. Ferreira, and C. A. Wuensche. Searching for primordial non-Gaussianity in Planck CMB maps using a combined estimator. *JCAP*, 2014(1):018, jan 2014.

[146] C. P. Novaes, A. Bernui, I. S. Ferreira, and C. A. Wuensche. A neural-network-based estimator to search for primordial non-Gaussianity in Planck CMB maps. *JCAP*, 2015(9):064, 2015.

[147] S. R. Kulkarni, D. A. Perley, and A. A. Miller. The Redshift Completeness of Local Galaxy Catalogs. *The Astrophysical Journal*, 860(1):22, jun 2018.

[148] A. G. Riess et al. A Redetermination of the Hubble Constant with the Hubble Space Telescope from a Differential Distance Ladder. *The Astrophysical Journal*, 699:539–563, 2009.

[149] B. Kalbouneh, C. Marinoni, and R. Maartens. Cosmography of the Local Universe by Multipole Analysis of the Expansion Rate Fluctuation Field, 2024.

[150] L. Koutoulidis, G. Mountrichas, I. Georgantopoulos, E. Pouliasis, and M. Plionis. Host galaxy properties of X-ray active galactic nuclei in the local Universe. *Astronomy & Astrophysics*, 658:A35, 2022.

[151] P. Nandi, A. Chatterjee, A. Jana, S. K. Chakrabarti, S. Naik, S. Safi-Harb, H.-K. Chang, and J. Heyl. Survey of Bare Active Galactic Nuclei in the local universe (z ¡ 0.2): I. On the origin of Soft Excess, 2023.

[152] M. Tanaka, M. Koike, S. Naito, J. Shibata, K. Usuda-Sato, H. Yamaoka, M. Ando, K. Ito, U. Kobayashi, Y. Kofuji, A. Kuwata, S. Nakano, R. Shimakawa, K. Tadaki, S. Takebayashi, C. Tsuchiya, T. Umemoto, and C. Bottrell. GALAXY CRUISE: Deep Insights into Interacting Galaxies in the Local Universe, 2023.

[153] G. F. R. Ellis, R. Maartens, and M. A. H. MacCallum. *Relativistic Cosmology*. Cambridge University Press, 2012.

[154] T. M. Davis and C. H. Lineweaver. Expanding Confusion: Common Misconceptions of Cosmological Horizons and the Superluminal Expansion of the Universe. *Publications of the Astronomical Society of Australia*, 21:97–109, 2004.

[155] B. L. Dias, F. Avila, and A. Bernui. Probing cosmic homogeneity in the Local Universe. *MNRAS*, 526(3):3219–3229, dec 2023.

[156] A. Bernui, T. Villela, C. A. Wuensche, R. Leonardi, and I. Ferreira. On the cosmic microwave background large-scale angular correlations. *Astronomy & Astrophysics*, 454:409–414, 2006.

[157] F. Avila, J. Oliveira, M. L. S. Dias, and A. Bernui. The bulk flow motion and the Hubble-Lemaître law in the Local Universe with the ALFALFA survey. *Brazilian Journal of Physics*, 53:49, feb 2023.

[158] M. Lopes, A. Bernui, C. Franco, and F. Avila. Bulk flow motion detection in the Local Universe with Pantheon+ Type Ia Supernovae. *APJ*, 967(1):47, may 2024.

[159] I. M. H. Etherington. On the definition of distance in general relativity. *The London, Edinburgh, and Dublin Philosophical Magazine and Journal of Science*, 15:761–773, 1933.

[160] G. Efstathiou and S. Gratton. The evidence for a spatially flat Universe. *Monthly Notices of the Royal Astronomical Society: Letters*, 496:L91–L95, 2020.

[161] E. M. Barboza. *Sobre a Expansão Acelerada do Universo e a Natureza da Energia Escura*. Phd thesis, Observatório Nacional, 2010.

[162] J. A. Frieman, M. S. Turner, and D. Huterer. Dark Energy and the Accelerating Universe. *Annual Review of Astronomy and Astrophysics*, 46:385–432, 2008.

[163] M. Li, X.D. Li, S. Wang, and Y. Wang. Dark Energy: A Brief Review. *Frontiers of Physics (Beijing)*, 8:828–846, 2013.

[164] V. Mukhanov, A. Feldman, and R. Brandenberger. Theory of Cosmological Perturbations. *Physics Reports*, 215:203–333, 1992.

[165] M. Sasaki. Large Scale Quantum Fluctuations in the Inflationary Universe. *Progress of Theoretical Physics*, 76:1036, 1986.

[166] R. Sachs. Gravitational Waves in General Relativity. VI. The Outgoing Radiation Condition. *Proceedings of the Royal Society A: Mathematical, Physical and Engineering Sciences*, 264:309–338, 1961.

[167] J. Stewart and M. Walker. Perturbations of SpaceTimes in General Relativity. *Proceedings of the Royal Society A: Mathematical, Physical and Engineering Sciences*, 341:49–74, 1974.

[168] J. Bardeen. Gauge-Invariant Cosmological Perturbations. *Physical Review D*, 22:1882–1905, 1980.

[169] H. Kodama and M. Sasaki. Cosmological Perturbation Theory. *Progress of Theoretical Physics Supplement*, 78:1–166, 1984.

[170] P. J. E. Peebles. *Principles of Physical Cosmology*. Princeton Series in Physics. Princeton University Press, 1993.

[171] E. V. Linder and R. N. Cahn. Parameterized Beyond Einstein Growth. *Astroparticle Physics*, 28:481–488, 2007.

[172] T. M. C. Abbott. Dark Energy Survey Year 3 Results: Cosmological Constraints from Galaxy Clustering and Weak Lensing. *Physical Review D*, 105:023520, 2022.

[173] Catherine Heymans et al. KiDS1000 Cosmology: Multiprobe Weak Gravitational Lensing and Spectroscopic Galaxy Clustering Constraints. *Astronomy & Astrophysics*, 646:A140, 2021.

[174] L. F. Secco et al. Dark Energy Survey Year 3 Results: Cosmology from Cosmic Shear and Robustness to Modeling Uncertainty. *Physical Review D*, 105:023515, 2022.

[175] A. Loureiro et al. KiDS and Euclid: Cosmological Implications of a Pseudo Angular Power Spectrum Analysis of KiDS1000 Cosmic Shear Tomography. *Astronomy & Astrophysics*, 665:A56, 2022.

[176] B. A. Bassett, S. Tsujikawa, and D. Wands. Inflation Dynamics and Reheating. *Reviews of Modern Physics*, 78:537–589, 2006.

[177] D. Baumann. Inflation. In *Theoretical Advanced Study Institute in Elementary Particle Physics: Physics of the Large and the Small*, pages 523–686, 2011.

[178] A. H. Guth. The Inflationary Universe: A Possible Solution to the Horizon and Flatness Problems. *Physical Review D*, 23:347–356, 1981.

[179] A. D. Linde. A New Inflationary Universe Scenario: A Possible Solution of the Horizon, Flatness, Homogeneity, Isotropy and Primordial Monopole Problems. *Physics Letters B*, 108:389–393, 1982.

[180] T. W. B. Kibble. Topology of Cosmic Domains and Strings. *Journal of Physics A: Mathematical and General*, 9:1387, 1976.

[181] P. W. Higgs. Broken Symmetries and the Masses of Gauge Bosons. *Physical Review Letters*, 13:508–509, 1964.

[182] F. Englert and R. Brout. Broken Symmetry and the Mass of Gauge Vector Mesons. *Physical Review Letters*, 13:321–323, 1964.

[183] G. S. Guralnik, C. R. Hagen, and T. W. B. Kibble. Global Conservation Laws and Massless Particles. *Physical Review Letters*, 13:585–587, 1964.

[184] G. Aad et al. Observation of a New Particle in the Search for the Standard Model Higgs Boson with the ATLAS Detector at the LHC. *Physics Letters B*, 716:1–29, 2012.

[185] Y. Akrami et al. Planck 2018 Results: X. Constraints on Inflation. *Astronomy & Astrophysics*, 641:A10, 2020.

[186] V. F. Mukhanov. Quantum Theory of Gauge Invariant Cosmological Perturbations. *Soviet Physics JETP*, 67:1297–1302, 1988.

[187] M. A. Troxel et al. Dark Energy Survey Year 1 Results: Cosmological Constraints from Cosmic Shear. *Physical Review D*, 98:043528, 2018.

[188] M. A. Troxel et al. Survey Geometry and the Internal Consistency of Recent Cosmic Shear Measurements. *Monthly Notices of the Royal Astronomical Society*, 479(4):4998–5004, 2018.

[189] H. Hildebrandt et al. KiDS450: Cosmological Parameter Constraints from Tomographic Weak Gravitational Lensing. *Monthly Notices of the Royal Astronomical Society*, 465:1454, 2017.

[190] S. Alam et al. Completed SDSSIV Extended Baryon Oscillation Spectroscopic Survey: Cosmological Implications from Two Decades of Spectroscopic Surveys at the Apache Point Observatory. *Physical Review D*, 103:083533, 2021.

[191] O. H. E. Philcox and M. M. Ivanov. BOSS DR12 Fullshape Cosmology: ΛCDM Constraints from the Large-scale Galaxy Power Spectrum and Bispectrum Monopole. *Physical Review D*, 105:043517, 2022.

[192] D. Scolnic et al. The Pantheon+ Analysis: The Full Data Set and Lightcurve Release. *The Astrophysical Journal*, 938:113, 2022.

[193] D. Rubin et al. Union Through UNITY: Cosmology with 2,000 SNe Using a Unified Bayesian Framework, 2023.

[194] T. M. C. Abbott et al. The Dark Energy Survey: Cosmology Results with 1500 New Highredshift Type Ia Supernovae Using the Full 5year Dataset, 2024.

[195] A. G. Adame et al. DESI 2024 VI: Cosmological Constraints from the Measurements of Baryon Acoustic Oscillations, 2024.

[196] A. G. Adame et al. DESI 2024 III: Baryon Acoustic Oscillations from Galaxies and Quasars, 4 2024.

[197] A. G. Adame et al. DESI 2024 VI: Cosmological Constraints from the Measurements of Baryon Acoustic Oscillations, 4 2024.

[198] L. Perivolaropoulos and F. Skara. Challenges for ΛCDM: An Update. *New Astronomy Reviews*, 95:101659, 2022.

[199] S. Capozziello and M. Francaviglia. Extended Theories of Gravity and their Cosmological and Astrophysical Applications. *General Relativity and Gravitation*, 40:357–420, 2008.

[200] E. Kiritsis. *Introduction to Superstring Theory*. Leuven University Press, 1998.

[201] J. Polchinski. *String Theory: Superstring Theory and Beyond*. Cambridge University Press, 1998.

[202] E. Witten. String Theory Dynamics in Various Dimensions. *Nuclear Physics B*, 443:85–126, 1995.

[203] P. M. R. Binetruy. *Supersymmetry: Theory, Experiment, and Cosmology*. Cambridge University Press, 2007.

[204] G. Dall'agata and M. Zagermann. *Supergravity: From First Principles to Modern Applications*. Springer, 2021.

[205] V. Faraoni and S. Capozziello. *Beyond Einstein Gravity: A Survey of Gravitational Theories for Cosmology and Astrophysics*. Springer, Dordrecht, 2011.

[206] H. S. John. Superstring Theory. *Physics Reports*, 89:223–322, 1982.

[207] A. Tomasiello. *Geometry of String Theory Compactifications*. Cambridge University Press, 2022.

[208] T. Jacobson. Thermodynamics of Spacetime: The Einstein Equation of State. *Phys. Rev. Lett.*, 75:1260–1263, 1995.

[209] C. Rovelli. *Covariant Loop Quantum Gravity*. Cambridge University Press, 2020.

[210] W. El-Kholy et al. Cosmological implications of a varying gravitational constant. *Astrophys. J.*, 183:431–436, 1973.

[211] T. Jacobson. Einstein-Aether Gravity: A Status Report. *PoS*, QGPH:020, 2007.

[212] C. Skordis. The Tensor-Vector-Scalar Theory and its Cosmology. *Classical and Quantum Gravity*, 26:143001, 2009.

[213] D. Lovelock. The Einstein Tensor and its Generalizations. *J. Math. Phys.*, 12:498–501, 1971.

[214] N. D. Birrell and P. C. W. Davies. *Quantum Fields in Curved Space*. Cambridge University Press, 1982.

[215] S. Capozziello and F. Bajardi. Nonlocal Gravity Cosmology: An Overview. *Int. J. Mod. Phys. D*, 31(06):2230009, 2022.

[216] M. Hohmann. Teleparallel Gravity. *Lect. Notes Phys.*, 1017:145–198, 2023.

[217] L. Heisenberg. Review on $f(Q)$ Gravity. *Phys. Rept.*, 1066:1–78, 2024.

[218] I. Bars and C. Kounnas. String and Particle with Two Times. *Phys. Rev. D*, 56:3664–3671, 1997.

[219] X. Chen. Three Dimensional Time Theory: to Unify the Principles of Basic Quantum Physics and Relativity, 10 2005.

[220] P. Jordan. *Schwerkraft und Weltall: Grundlagen der theoretischen Kosmologie*. Die Wissenschaft. F. Vieweg, 1955.

[221] C. R. Almeida, O. Galkina, and J. C. Fabris. Quantum and Classical Cosmology in the Brans-Dicke Theory. *Universe*, 7(8):286, 2021.

[222] G. Brando, J. C. Fabris, F. T. Falciano, and O. Galkina. Stiff matter solution in Brans-Dicke theory and the general relativity limit. *Int. J. Mod. Phys. D*, 28(12):1950156, 2019.

[223] G. Nordström. über die Möglichkeit, das elektromagnetische Feld und das Gravitationsfeld zu vereinigen. *Physikalische Zeitschrift*, 15:504–506, 1914.

[224] E. J. Copeland and D. J. Toms. Stability of self-consistent higher-dimensional cosmological solutions. *Phys. Rev. D*, 32:1921–1927, 1985.

[225] A. Flachi, J. Garriga, O. Pujolas, and T. Tanaka. Moduli stabilization in higher-dimensional brane models. *JHEP*, 08:053, 2003.

[226] E. Palti. Aspects of moduli stabilisation in string and M-theory, 7 2006.

[227] L. McAllister and F. Quevedo. Moduli Stabilization in String Theory, 10 2023.

[228] R. Utiyama and B. S. DeWitt. Renormalization of a classical gravitational field interacting with quantized matter fields. *J. Math. Phys.*, 3:608–618, 1962.

[229] A. Einstein. Einheitliche Feldtheorie von Gravitation und Elektrizität. *Sitzungsberichte der Preussischen Akademie der Wissenschaften (Berlin)*, 1925:414–419, 1925.

[230] M. Ferraris, M. Francaviglia, and C. Reina. Variational formulation of general relativity from 1915 to 1925 "Palatini's method" discovered by Einstein in 1925. *Gen. Rel. Grav.*, 14:243–254, 1982.

[231] M. Amarzguioui, O. Elgaroy, D. F. Mota, and T. Multamaki. Cosmological constraints on $f(R)$ gravity theories within the Palatini approach. *Astronomy & Astrophysics*, 454:707–714, 2006.

[232] M. Campista, B. Santos, J. Santos, and J. S. Alcaniz. Cosmological consequences of exponential gravity in Palatini formalism. *Physics Letters B*, 699:320–324, 2010.

[233] B. Santos, M. Campista, J. Santos, and J. S. Alcaniz. Cosmology with Hu-Sawicki gravity in Palatini Formalism. *Astronomy & Astrophysics*, 548:A31, 2012.

[234] D. A. Gomes, R. Briffa, A. Kozak, J. L. Said, M. Saal, and A. Wojnar. Cosmological constraints of Palatini $f(\mathscr{R})$ gravity. *Journal of Cosmology and Astroparticle Physics*, 01:011, 2024.

[235] E. Barausse, T. P. Sotiriou, and J. C. Miller. Curvature singularities, tidal forces and the viability of Palatini $f(R)$ gravity. *Class. Quant. Grav.*, 25:105008, 2008.

[236] É. É. Flanagan. Palatini Form of $1/R$ Gravity. *Phys. Rev. Lett.*, 92(7):071101, Feb 2004.

[237] A. Iglesias, N. Kaloper, A. Padilla, and M. Park. How (not) to use the Palatini formulation of scalar-tensor gravity. *Phys. Rev. D*, 76(10):104001, Nov 2007.

[238] J. R. Lanahan-Tremblay et al. Relativity and Cosmology: Analysis of Cosmological Models with Varying Constants. *Phys. Rev. D*, 75:043512, 2007.

[239] T. Liu, X. Zhang, and W. Zhao. Constraining $f(R)$ gravity in solar system, cosmology and binary pulsar systems. *Phys. Lett. B*, 777:286–293, 2018.

[240] B. Bertotti, L. Iess, and P. Tortora. A test of general relativity using radio links with the Cassini spacecraft. *Nature*, 425:374–376, 2003.

[241] R. Van On et al. Dark Energy Models and Constraints on Cosmological Parameters. *Phys. Lett. B*, 781:132–141, 2018.

[242] S. Capozziello, S. Nojiri, S. D. Odintsov, and A. Troisi. Cosmological viability of $f(R)$ gravity as an ideal fluid and its compatibility with a matter dominated phase. *Phys. Lett. B*, 639:135–143, 2006.

[243] L. Amendola, D. Polarski, and S. Tsujikawa. Power-laws $f(R)$ theories are cosmologically unacceptable. *Int. J. Mod. Phys. D*, 16:1555–1561, 2007.

[244] F. Avila, A. Bernui, R. C. Nunes, E. de Carvalho, and C. P. Novaes. The homogeneity scale and the growth rate of cosmic structures. *Mon. Not. Roy. Astron. Soc.*, 509:2994–3003, 2021.

[245] E. de Carvalho, A. Bernui, H. S. Xavier, and C. P. Novaes. Baryon Acoustic Oscillations Signature in the Three-point Angular Correlation Function from the SDSS DR12 Quasar Survey. *Monthly Notices of the Royal Astronomical Society*, 492:4469–4476, 2020.

[246] D. Langlois and F. Vernizzi. Evolution of nonlinear cosmological perturbations. *Physical Review Letters*, 95:091303, 2005.

[247] K. A. Malik and D. Wands. Cosmological perturbations. *Physics Reports*, 475:1–51, 2009.

[248] L. Amendola and S. Tsujikawa. *Dark Energy: Theory and Observations*. Cambridge University Press, 2010.

[249] B. Ribeiro, A. Bernui, and M. Campista. Cosmological constraints on the R^2-corrected Appleby-Battye model. *Eur. Phys. J. C*, 84(2):114, 2024.

[250] H. Motohashi and A. Nishizawa. Reheating after $f(R)$ inflation. *Phys. Rev. D*, 86:083514, Oct 2012.

[251] A. Nishizawa and H. Motohashi. Constraint on reheating after $f(R)$ inflation from gravitational waves. *Phys. Rev. D*, 89:063541, Mar 2014.

[252] H. Motohashi, A. A. Starobinsky, and J. Yokoyama. Phantom boundary crossing and anomalous growth index of fluctuations in viable $f(R)$ models of cosmic acceleration. *Prog. Theor. Phys.*, 123:887–902, 2010.

[253] S. Nesseris, G. Pantazis, and L. Perivolaropoulos. Tension and constraints on modified gravity parametrizations of $G_{\rm eff}(z)$ from growth rate and Planck data. *Phys. Rev. D*, 96(2):023542, 2017.

[254] B. Hu, M. Raveri, M. Rizzato, and A. Silvestri. Testing Hu-Sawicki $f(R)$ gravity with the effective field theory approach. *Monthly Notices of the Royal Astronomical Society*, 459(4):3880–3889, 2016.

[255] R. Kou, C. Murray, and J. G. Bartlett. Constraining $f(R)$ gravity with cross-correlation of galaxies and cosmic microwave background lensing. *Astronomy & Astrophysics*, 686:A193, 2024.

[256] R. C. Nunes, S. Pan, E. N. Saridakis, and E. M. C. Abreu. New observational constraints on f(R) gravity from cosmic chronometers. *Journal of Cosmology and Astroparticle Physics*, 2017:005–005, 2017.

[257] R. Perez-Romero et al. Supernovae and the Hubble Constant in $f(R)$ Gravity Models. *J. Cosmol. Astropart. Phys.*, 2017:023, 2017.

[258] C. Zhang, H. Zhang, S. Yuan, S. Liu, T. Zhang, and Y. Sun. Four new observational $H(z)$ data from luminous red galaxies in the Sloan Digital Sky Survey data release seven. *Research in Astronomy and Astrophysics*, 14(10):1221, 2014.

[259] M. Moresco et al. A 6% measurement of the Hubble parameter at $z \sim 0.45$: direct evidence of the epoch of cosmic reacceleration. *JCAP*, 05:014, 2016.

[260] J. Simon, L. Verde, and R. Jimenez. Constraints on the redshift dependence of the dark energy potential. *Phys. Rev. D*, 71:123001, 2005.

[261] D. Stern, R. Jimenez, L. Verde, M. Kamionkowski, and S. A. Stanford. Cosmic chronometers: constraining the equation of state of dark energy. I: $H(z)$ measurements. *Journal of Cosmology and Astroparticle Physics*, 2010:008, 2010.

[262] M. Moresco et al. Improved constraints on the expansion rate of the Universe up to $z \sim 1.1$ from the spectroscopic evolution of cosmic chronometers. *Journal of Cosmology and Astroparticle Physics*, 2012:006, 2012.

[263] M. Moresco. Raising the bar: new constraints on the Hubble parameter with cosmic chronometers at $z \sim 2$. *MNRAS*, 450:L16–L20, 2015.

[264] A. L. Ratsimbazafy et al. Agedating luminous red galaxies observed with the Southern African Large Telescope. *Monthly Notices of the Royal Astronomical Society*, 467:3239–3254, 2017.

[265] R. Jimenez and A. Loeb. Constraining Cosmological Parameters Based on Relative Galaxy Ages. *The Astrophysical Journal*, 573:37–40, 2002.

[266] G. Bruzual and S. Charlot. Stellar population synthesis at the resolution of 2003. *Mon. Not. Roy. Astron. Soc.*, 344:1000, 2003.

[267] A. Gomez-Valent et al. Observational Constraints on Modified Gravity Models and the Late-Time Accelerated Expansion. *Phys. Rev. D*, 98:023510, 2018.

[268] Y. Yang and Y. Gong. The evidence of cosmic acceleration and observational constraints. *JCAP*, 06:059, 2020.

[269] S. J. Turnbull, M. J. Hudson, H. A. Feldman, M. Hicken, R. P. Kirshner, and R. Watkins. Cosmic flows in the nearby universe from Type Ia Supernovae. *Monthly Notices of the Royal Astronomical Society*, 420:447–454, 2012.

[270] I. Achitouv, C. Blake, P. Carter, J. Koda, and F. Beutler. Consistency of the growth rate in different environments with the 6degree Field Galaxy Survey: Measurement of the void-galaxy and galaxy-galaxy correlation functions. *Phys. Rev. D*, 95:083502, 2017.

[271] F. Beutler et al. The 6dF Galaxy Survey: $z \approx 0$ measurements of the growth rate and σ_8. *Monthly Notices of the Royal Astronomical Society*, 423:3430–3444, 2012.

[272] M. Feix, A. Nusser, and E. Branchini. Growth Rate of Cosmological Perturbations at $z \sim 0.1$ from a New Observational Test. *Phys. Rev. Lett.*, 115:011301, 2015.

[273] S. Alam et al. The clustering of galaxies in the completed SDSSIII Baryon Oscillation Spectroscopic Survey: cosmological analysis of the DR12 galaxy sample. *Mon. Not. Roy. Astron. Soc.*, 470:2617–2652, 2017.

[274] A. G. Sanchez et al. The clustering of galaxies in the SDSSIII Baryon Oscillation Spectroscopic Survey: cosmological implications of the full shape of the clustering wedges in the data release 10 and 11 galaxy samples. *Mon. Not. Roy. Astron. Soc.*, 440:2692–2713, 2014.

[275] F. Avila, A. Bernui, E. de Carvalho, and C. P. Novaes. The growth rate of cosmic structures in the local Universe with the ALFALFA survey. *Mon. Not. Roy. Astron. Soc.*, 505:3404–3413, 2021.

[276] F. Avila, A. Bernui, A. Bonilla, and R. C. Nunes. Inferring $S_8(z)$ and $\gamma(z)$ with cosmic growth rate measurements using machine learning. *Eur. Phys. J. C*, 82:594, 2022.

[277] C. Blake et al. The WiggleZ Dark Energy Survey: Joint measurements of the expansion and growth history at $z < 1$. *Monthly Notices of the Royal Astronomical Society*, 425:4054–1414, 2012.

[278] M. Aubert et al. The completed SDSSIV extended Baryon Oscillation Spectroscopic Survey: growth rate of structure measurement from cosmic voids. *Monthly Notices of the Royal Astronomical Society*, 513:1862–1863, 2022.

[279] M. J. Wilson. *Geometric and growth rate tests of General Relativity with recovered linear cosmological perturbations*. PhD thesis, Edinburgh U., 2017.

[280] G. B. Zhao et al. The clustering of the SDSSIV extended Baryon Oscillation Spectroscopic Survey DR14 quasar sample: a tomographic measurement of cosmic structure growth and expansion rate based on optimal redshift weights. *Monthly Notices of the Royal Astronomical Society*, 482:3497–3513, 2018.

[281] T. Okumura et al. The Subaru FMOS galaxy redshift survey (FastSound). IV. New constraint on gravity theory from redshift space distortions at $z \sim 1.4$. *Publications of the Astronomical Society of Japan*, 68:38, 2016.

[282] S. Nadathur, P. M. Carter, W. J. Percival, H. A. Winther, and J. Bautista. Beyond BAO: Improving cosmological constraints from BOSS data with measurement of the void-galaxy cross-correlation. *Phys. Rev. D*, 100:023504, 2019.

[283] C. H. Chuang et al. The clustering of galaxies in the SDSSIII Baryon Oscillation Spectroscopic Survey: single-probe measurements from CMASS anisotropic galaxy clustering. *Monthly Notices of the Royal Astronomical Society*, 461:3781–3793, 2016.

[284] B. Popovic, D. Brout, R. Kessler, and D. Scolnic. The Pantheon+ Analysis: Forward Modeling the Dust and Intrinsic Color Distributions of Type Ia Supernovae, and Quantifying Their Impact on Cosmological Inferences. *Astrophys. J.*, 945:84, 2023.

[285] D. M. Scolnic et al. The Complete Lightcurve Sample of Spectroscopically Confirmed SNe Ia from PanSTARRS1 and Cosmological Constraints from the Combined Pantheon Sample. *Astrophys. J.*, 859:101, 2018.

[286] C. Robert and G. Casella. *Monte Carlo Statistical Methods*. Springer Texts in Statistics. Springer New York, 2005.

[287] L. Verde. Statistical methods in cosmology. In *Lectures on Cosmology: Accelerated Expansion of the Universe*, pages 147–177. Springer, 2010.

[288] C. Franco, J. Oliveira, M. Lopes, F. Avila, and A. Bernui. Measuring the matter fluctuations in the Local Universe with the ALFALFA catalog. *arXiv eprints*, 2406:arXiv:2406.16693, jun 2024.

[289] H. Akaike. A new look at the statistical model identification. *IEEE Transactions on Automatic Control*, 19:716–723, 1974.

[290] E. Papantonopoulos. *Modifications of Einstein's Theory of Gravity at Large Distances*. Lecture Notes in Physics. Springer International Publishing, 2014.

[291] T. P. Sotiriou and V. Faraoni. $f(R)$ Theories of Gravity. *Reviews of Modern Physics*, 82:451–497, 2010.

[292] E. J. Baxter et al. Determining the Hubble constant without the sound horizon scale: measurements from CMB lensing. *Monthly Notices of the Royal Astronomical Society*, 501:1823–1835, 2020.

[293] D. Dutcher et al. Measurements of the E-mode polarization and temperature-E-mode correlation of the CMB from SPT3G 2018 data. *Physical Review D*, 104:022003, 2021.

[294] L. Balkenhol et al. Constraints on ΛCDM extensions from the SPT3G 2018 EE and TE power spectra. *Physical Review D*, 104:083509, 2021.

[295] G. D'Amico et al. The cosmological analysis of the SDSS/BOSS data from the Effective Field Theory of Large-Scale Structure. *Journal of Cosmology and Astroparticle Physics*, 2020:005–005, 2020.

[296] M. M. Ivanov, M. Simonović, and M. Zaldarriaga. Cosmological parameters from the BOSS galaxy power spectrum. *Journal of Cosmology and Astroparticle Physics*, 2020:042–042, 2020.

[297] L. Pogosian, G. Zhao, and K. Jedamzik. Recombination-independent determination of the sound horizon and the Hubble constant from BAO. *The Astrophysical Journal Letters*, 904:L17, 2020.

[298] O. H. E. Philcox et al. Determining the Hubble constant without the sound horizon: Measurements from galaxy surveys. *Physical Review D*, 103:023538, 2021.

[299] O. H. E. Philcox et al. Determining the Hubble constant without the sound horizon: A 3.6% constraint on H0 from galaxy surveys, CMB lensing, and supernovae. *Physical Review D*, 106:063530, 2022.

[300] A. Bernui et al. Exploring the H_0 tension and the evidence for dark sector interactions from 2D BAO measurements. *Physical Review D*, 107:103531, 2023.

[301] M. Madhavacheril et al. The Atacama Cosmology Telescope: DR6 Gravitational Lensing Map and Cosmological Parameters. *The Astrophysical Journal*, 962:113, 2024.

[302] J. Schombert, S. McGaugh, and F. Lelli. Using the Baryonic Tully–Fisher Relation to Measure H_0. *The Astronomical Journal*, 160:71, 2020.

[303] D. W. Pesce et al. The Megamaser Cosmology Project. XIII. Combined Hubble Constant Constraints. *The Astrophysical Journal Letters*, 891:L1, 2020.

[304] W. L. Freedman et al. Calibration of the Tip of the Red Giant Branch. *The Astrophysical Journal*, 891:57, 2020.

[305] M. Millon et al. TDCOSMO: I. An exploration of systematic uncertainties in the inference of H_0 from time-delay cosmography. *Astronomy & Astrophysics*, 639:A101, 2020.

[306] T. de Jaeger et al. A measurement of the Hubble constant from Type II supernovae. *Monthly Notices of the Royal Astronomical Society*, 496:3402–3411, 2020.

[307] J. Soltis, S. Casertano, and A. G. Riess. The Parallax of ω Centauri Measured from Gaia EDR3 and a Direct, Geometric Calibration of the Tip of the Red Giant Branch and the Hubble Constant. *The Astrophysical Journal Letters*, 908:L5, 2021.

[308] G. S. Anand et al. Comparing Tip of the Red Giant Branch Distance Scales: An Independent Reduction of the Carnegie-Chicago Hubble Program and the Value of the Hubble Constant. *The Astrophysical Journal*, 932:15, 2022.

[309] R. Abbott et al. Constraints on the Cosmic Expansion History from GWTC–3. *The Astrophysical Journal*, 949:76, 2023.

[310] J. Qi et al. Measurements of the Hubble constant and cosmic curvature with quasars: ultracompact radio structure and strong gravitational lensing. *Monthly Notices of the Royal Astronomical Society*, 503:2179–2186, 2021.

[311] J. P. Blakeslee et al. The Hubble Constant from Infrared Surface Brightness Fluctuation Distances. *The Astrophysical Journal*, 911:65, 2021.

[312] D. Camarena and V. Marra. On the use of the local prior on the absolute magnitude of Type Ia supernovae in cosmological inference. *Monthly Notices of the Royal Astronomical Society*, 504:5164–5171, 2021.

[313] E. Mörtsell, A. Goobar, J. Johansson, and S. Dhawan. Sensitivity of the Hubble Constant Determination to Cepheid Calibration. *The Astrophysical Journal*, 933:212, 2022.

[314] S. Dhawan et al. A Uniform Type Ia Supernova Distance Ladder with the Zwicky Transient Facility: Absolute Calibration Based on the Tip of the Red Giant Branch Method. *The Astrophysical Journal*, 934:185, 2022.

[315] T. de Jaeger et al. A 5% measurement of the Hubble–Lemaître constant from Type II supernovae. *Monthly Notices of the Royal Astronomical Society*, 514:4620–4628, 2022.

[316] S. Hagstotz, R. Reischke, and R. Lilow. A new measurement of the Hubble constant using fast radio bursts. *Monthly Notices of the Royal Astronomical Society*, 511:662–667, 2022.

[317] E. Kourkchi et al. Cosmicflows4: the baryonic Tully–Fisher relation providing $\sim 10,000$ distances. *Monthly Notices of the Royal Astronomical Society*, 511:6160–6178, 2022.

[318] S. Mukherjee et al. Cross-correlating Dark Sirens and Galaxies: Constraints on H_0 from GWTC-3 of LIGO–Virgo–KAGRA. *The Astrophysical Journal*, 975(2):189, 2024.

[319] Y. Liu, H. Yu, and P. Wu. Cosmological-model-independent Determination of Hubble Constant from Fast Radio Bursts and Hubble Parameter Measurements. *The Astrophysical Journal Letters*, 946:L49, 2023.

[320] R. B. Tully et al. Cosmicflows4. *The Astrophysical Journal*, 944:94, 2023.

[321] A. J. Shajib et al. TDCOSMO: XII. Improved Hubble constant measurement from lensing time delays using spatially resolved stellar kinematics of the lens galaxy. *Astronomy & Astrophysics*, 673:A9, 2023.

[322] C. D. Huang et al. The Mira Distance to M101 and a 4% Measurement of H_0. *The Astrophysical Journal*, 963:83, 2024.

Appendix A

Appendix A

In this appendix, we give two tables containing details of relevant H_0 measurements to supplement Chapter 3. The first table, Table A.1, shows the time evolution of H_0 measurements from 2003 to 2022, a period during which the current Hubble tension has been characterized, based on CMB and SNe Ia observations. Figure 3.4 is based on the measurements on this table. The second table, Table A.2, includes 50 of the most recent H_0 measurements, distributed across three groups: (*i*) measurements 1–7 are derived from early cosmological probes and assume a flat-ΛCDM model; (*ii*) measurements 8–23 are late-time measurements that also assume a fiducial flat-ΛCDM cosmology; and (*iii*) measurements 24–50 are model-independent, involving only late-time probes. The measurements in this table serve as the basis for Figure 3.5.

Table A.1: Timeline of H_0 measurements from CMB (early universe) and distance-ladder (late-time universe) observations.

Nº	Year	H_0 $\left[\mathrm{km\,s^{-1}\,Mpc^{-1}}\right]$	Methods	Authors	Ref.
1	2003	72.00 ± 5.00	WMAP1	Spergel et al.	[101]
2	2007	$73.20^{+3.1}_{-3.2}$	WMAP3	Spergel et al.	[102]
3	2009	$71.90^{+2.6}_{-2.7}$	WMAP5	Hinshaw et al.	[103]
4	2011	70.40 ± 2.50	WMAP7	Komatsu et al.	[104]
5	2013	69.32 ± 0.80	WMAP9	Bennett et al.	[105]
6	2014	67.30 ± 1.20	Planck13	Ade et al.	[106]
7	2016	67.80 ± 0.90	Planck15	Ade et al.	[107]
8	2018	67.36 ± 0.54	Planck18	Aghanim et al.	[88]
9	2020	67.60 ± 1.10	ACT20	Aiola et al.	[108]
10	2001	72.00 ± 8.00	HST Key Project	Freedman et al.	[92]
11	2009	74.20 ± 3.60	Cepheids+SNe Ia	Macri et al.	[94]
12	2011	73.08 ± 2.40	Cepheids+SNe Ia	Riess et al.	[95]
13	2012	74.30 ± 2.10	CHP12	Freedman et al.	[93]
14	2016	73.24 ± 1.74	Cepheids+SNe Ia	Riess et al.	[96]
15	2018	73.48 ± 1.66	Cepheids+SNe Ia	Riess et al.	[97]
16	2019	74.03 ± 1.42	Cepheids+SNe Ia	Riess et al.	[98]
17	2021	73.20 ± 1.30	Cepheids+SNe Ia	Riess et al.	[99]
18	2022	73.04 ± 1.04	Cepheids+SNe Ia	Riess et al.	[100]

Table A.2: 50 recent H_0 measurements from early, late, and combined early-late cosmological probes, with or without dependence on the cosmological model.

Nº	Year	H_0 $\left[\mathrm{km\,s^{-1}\,Mpc^{-1}}\right]$	Methods	Authors	Ref.
1	2020	67.27 ± 0.60	Planck18	Aghanim et al.	[88]
2	2020	73.50 ± 5.30	lens	Baxter et al.	[292]
3	2020	67.36 ± 0.54	Planck18+lens	Aghanim et al.	[88]
4	2020	67.90 ± 1.50	ACT20	Aiola et al.	[108]
5	2020	67.60 ± 1.10	ACT20+WMAP9	Aiola et al.	[108]
6	2021	68.80 ± 1.50	SPT18	Dutcher et al.	[293]
7	2021	67.49 ± 0.53	Planck18+SPT18+ACT20	Balkenhol et al.	[294]
8	2020	68.50 ± 2.20	BOSS DDR12+BBN	D'Amico et al.	[295]
9	2020	67.90 ± 1.10	BOSS+BBN	Ivanov et al.	[296]
10	2020	69.60 ± 1.80	eBOSS+Planck18	Pogosian et al.	[297]
11	2021	67.35 ± 0.97	BOSS+eBOSS+BBN	Alam et al.	[190]
12	2021	$65.6^{+3.4}_{-5.5}$	BOSS DR12+BAO	Philcox et al.	[298]
13	2021	$70.6^{+3.7}_{-5.0}$	BOSS DR12+BAO+lens	Philcox et al.	[298]
14	2022	$69.6^{+4.1}_{-5.4}$	BOSS+BBN	Philcox et al.	[299]
15	2022	$65.0^{+3.9}_{-4.3}$	BOSS+BBN+lens	Philcox et al.	[299]
16	2023	67.65 ± 0.44	Planck18+BAO	Bernui et al.	[300]
17	2023	67.60 ± 0.43	Planck18+BAO+lens	Bernui et al.	[300]
18	2024	68.30 ± 1.10	ACT20+BAO+BBN	Madhavacheril et al.	[301]
19	2024	68.10 ± 1.00	ACT20+BAO+BBN+Planck18	Madhavacheril et al.	[301]
20	2024	68.53 ± 0.80	DESI+BBN	Adame et al.	[195]
21	2024	68.52 ± 0.62	DESI+BBN+θ_*	Adame et al.	[195]
22	2024	67.97 ± 0.38	DESI+ACT20+Planck18+lens	Adame et al.	[195]
23	2024	72.60 ± 1.50	SNe Ia (directional analysis)	Lopes et al. (arXiv)	[158]
24	2020	75.10 ± 3.80	Tully-Fisher relation	Schombert et al.	[302]
25	2020	73.90 ± 3.00	Maser	Pesce et al.	[303]
26	2020	69.60 ± 2.50	TRGB+SNe Ia	Freedman et al.	[304]
27	2020	74.20 ± 1.60	Gravitational lens	Millon et al.	[305]
28	2020	$75.8^{+5.2}_{-4.9}$	SNe II	de Jaeger et al.	[306]
29	2021	72.10 ± 2.00	TRGB+SNe Ia	Soltis et al.	[307]
30	2021	71.50 ± 1.80	TRGB+SNe Ia	Anand et al.	[308]
31	2021	$68.0^{+12.0}_{-8.0}$	GWTC-3	Abbott et al.	[309]
32	2021	73.60 ± 1.70	Gravitational lens	Qi et al.	[310]
33	2021	70.50 ± 5.75	SBF+SNe Ia	Khetan et al.	[89]
34	2021	73.30 ± 3.10	SBF+SNe Ia	Blakeslee et al.	[311]
35	2021	74.30 ± 1.45	Cepheids+SNe Ia	Camarena and Marra	[312]
36	2021	73.20 ± 1.30	Cepheids+SNe Ia	Riess et al.	[99]
37	2022	73.04 ± 1.04	Cepheids+SNe Ia	Riess et al.	[100]
38	2022	72.53 ± 0.99	Cepheids+TRGB+SNe Ia	Riess et al.	[100]
39	2022	73.20 ± 1.30	Cepheids+SNe Ia	Mörtsell et al.	[313]
40	2022	76.70 ± 2.00	Cepheids	Mörtsell et al.	[313]
41	2022	76.94 ± 6.40	TRGB+SNe Ia	Dhawan et al.	[314]
42	2022	$75.4^{+3.8}_{-3.7}$	SNe II	de Jaeger et al.	[315]
43	2022	62.30 ± 9.10	FRB	Hagstotz et al.	[316]
44	2022	75.50 ± 2.50	Tully-Fisher relation	Kourkchi et al.	[317]
45	2022	$75.4^{+11.0}_{-6.0}$	GW170817+GWTC–3	Mukherjee et al.	[318]
46	2023	71.00 ± 3.00	FRB	Liu et al.	[319]
47	2023	74.60 ± 0.80	Tully-Fisher relation	Tully et al.	[320]
48	2023	74.20 ± 1.60	Quasar lens	Shajib et al.	[321]
49	2024	72.37 ± 2.97	Miras-SNe Ia	Huang et al.	[322]
50	2024	70.39 ± 1.40	SNe Ia (directional analysis)	Lopes et al.	[158]

Appendix B

Appendix B

In this appendix, we provide our main computer codes along with a brief explanation about them. The codes are written in python programming language and are primarily designed to solve ODEs and to draw samples from probability distributions via MCMC analyses.

First, we provide all the libraries, cosmological parameters, and their derivatives with respect to the scale factor, general constants, quantities associated with $f(R)$ theories, those related to the specific $f(R)$ model, and the fiducial (assumed *a priori*) quantities.

```
# ------------------------------------------------------------------------
# Libraries:
import numpy as np
import pandas as pd
import scipy
from scipy import integrate
from scipy.integrate import solve_ivp
from multiprocessing import Pool
import emcee
import time
from chainconsumer import ChainConsumer
import matplotlib.pyplot as plt
# ------------------------------------------------------------------------
# Cosmological parameters:
#1      t = scale factor
#2      z = cosmological redshift
#3      H = Hubble-Lemaître parameter
#4      E = normalized Hubble-Lemaître parameter
#5      yH = auxiliary parameter
```

#6 R = Ricci curvature scalar
#7 O_m = normalized matter energy density
#8 O_r = normalized radiation energy density
#9 w = equation of state
#10 weff = effective equation of state
#11 D = matter density contrast
#12 sig8 = amplitude of matter perturbations at physical scales of 8Mpc/h
#13 fs8 = normalized growth rate at physical scales of 8Mpc/h
#14 k = wavenumber or scale of the perturbations
#15 dL = luminosity-distance
#16 mB = relative magnitude
#17 MB = absolute magnitude

Derivatives of the cosmological parameters:
#1 dH = 1st. derivative of H with respect to t
#2 ddH = 2nd. derivative of H with respect to t
#3 dddH = 3rd. derivative of H with respect to t
#4 dE = 1st. derivative of E with respect to t
#5 ddE = 2nd. derivative of E with respect to t
#6 dddE = 3rd. derivative of E with respect to t
#7 YH = 1st. derivative of yH with respect to t
#8 dD = 1st. derivative of D with respect to t
#9 ddD = 2nd.derivative of D with respect to t

Constants:
#1 H0 = Hubble constant
#2 R_vac = vacuum Ricci curvature scalar
#3 O_m0 = current normalized matter energy density
#4 O_r0 = current normalized radiation energy density
#5 sig80 = current amplitude of matter perturbations at 8Mpc/h
#6 G = Newtonian gravitational constant
#7 c = speed of light

Regarding the f(R):
#1 fR = 1st. derivative of f(R) with respect to R
#2 fRR = 2nd. derivative of f(R) with respect to R
#3 Delta = scalaron mass scale
#4 M2 = squared scalaron mass
#5 Geff = effective gravitational “constant”

```
# ------------------------------------------------------------------------
# Appleby-Battye (AB) model parameters:
#1      e_AB = dependent AB model parameter
#2      b = independent AB model parameter
# ------------------------------------------------------------------------
# Hu-Sawicki (HS) model parameters:
#1      n = fixed HS model parameter
#2      c1 = dependent HS model parameter
#3      c2 (or mu) = independent HS model parameter
# ------------------------------------------------------------------------
# Starobinsky model parameters:
#1      n = fixed parameter
#2      Rs = dependent model parameter
#3      lbd = independent model parameter
# ------------------------------------------------------------------------
# Fiducial:
ti = 0.2
tf = 1.0
p = 1000
O_r0 = 0
Delta = 10**(-7)
n = 1
t_span = [ti, tf]
t = np.linspace(ti, tf, p)
z = (1/t) - 1
# ------------------------------------------------------------------------
```

We then provide the Hubble-Lemaître parameter H as a function of the scale factor a, according to the GR/ΛCDM theory/model, i.e.,

```
# ------------------------------------------------------------------------
# H(t) according to the GR/LCDM theory/model:
def H_GR(H0, O_m0):
    O_m = O_m0*t**(-3)
    O_r = O_r0*t**(-4)
    O_L = 1 - O_m0 - O_r0
    H_GR = H0*np.sqrt(O_m + O_r + O_L)
return H_GR
# ------------------------------------------------------------------------
```

and according to the three $f(R)$ models, i.e.,

```
# ------------------------------------------------------------------------
# H(t) according to the R2-AB model:
def Hubble_AB(t, y, H0, O_m0, b):
    H = y[0]
    dH = y[1]
    ddH = y[2]
    O_m = O_m0*t**(-3)
    O_r = O_r0*t**(-4)
    R_vac = 12*H0**2
    e_AB = R_vac/np.log(1 + np.exp(2*b))
    M2 = e_AB/Delta
    R = 6*H*(2*H + t*dH)
    alpha = (R/e_AB) - b
    if abs(alpha) < 25:
        s = 1/np.cosh(alpha)
    else:
        s = 0
    A = (H0**2)*(3*O_m + 4*O_r)
    B = (2*t*H*dH*R)/(3*M2)
    C = t*H*dH*(np.tanh(alpha) + 1)
    fAB1 = 6*(t**2)*(H**2)/e_AB
    fAB2 = ddH + ((dH**2)/H) + (5*dH/t)
    if abs(alpha) < 15:
        F = ((fAB1*fAB2*s)**2)*np.tanh(alpha)
    else:
        F = 0
    if abs(alpha) < 15:
        I = 6*(t**3)*(H**3)*((1/(3*M2)) + (0.5*s*s/e_AB))
    else:
        I = 6*(t**3)*(H**3)*(1/(3*M2))
    U = (11*dH*dH/(t*H)) + (dH*dH*dH/(H*H)) + (6*ddH/t) + (4*dH*ddH/H)
    dddH = - ((A + B + C - F)/I) - U
    return [dH, ddH, dddH]

def H_AB(H0, O_m0, b):
    # Initial conditions according to the GR/LCDM theory
```

```
    O_mi = O_m0*ti**(-3)
    O_ri = O_r0*ti**(-4)
    O_L = 1 - O_m0 - O_r0
    Hi = H0*np.sqrt(O_mi + O_ri + O_L)
    dHi = - ((H0*H0)/(2*ti*Hi))*(3*O_mi + 4*O_ri)
    ddHi = 0.5*(H0/(ti*Hi))**2*(Hi + ti*dHi)*(3*O_mi + 4*O_ri) +
                    0.5*(H0/(ti*Hi))**2*Hi*(9*O_mi + 16*O_ri)
    y0 = [Hi, dHi, ddHi]
    # H_AB solution
    sol_AB = solve_ivp(Hubble_AB, t_span, y0, t_eval=t, method='LSODA',
                    rtol = 10**(-6), args=(H0, O_m0, b))
    H_AB = sol_AB.y[0]
    return H_AB
# ------------------------------------------------------------------

# ------------------------------------------------------------------
# H(t) for both HS and Starobinsky models:
def yH_HS(t, y, H0, O_m0, c2):
# def yH_S(t, y, H0, O_m0, lbd):
    yH = y[0]
    YH = y[1]
    O_m = O_m0*t**(-3)
    O_r = O_r0*t**(-4)
    chi = O_r0/O_m0
    ms = (H0**2)*O_m0
    R = 3*ms*(4*yH + t*YH + t**(-3))
    # ---- HS model ----
    # M2 = ms/Delta
    c1 = 6*c2*(1 - O_m0)/O_m0
    xn1 = (R/ms)**n
    xn2 = c1/(ms**n)
    xn3 = (n+1)*(c2/ms)*R**(2*(n-1))
    xn4 = (n-1)*R**(n-2)
    xn5 = ((c2*xn1) + 1)
    f = R - ms*((c1*xn1)/((c2*xn1) + 1)) #+ R**2/(6*M2)
    fR = 1 - n*xn2*ms*((R**(n-1))/(xn5**2)) #+ R/(3*M2)
    fRR = n*xn2*ms*( (xn3 - xn4)/(xn5**3)) #+ 1/(3*M2)
    # ---- Starobinsky model ----
    # Rs = 6*(H0**2)*(1 - O_m0)/lbd
```

```
    # M2 = Rs/Delta
    # star = 1 + (R/Rs)**2
    # f = R + lbd*Rs*( (star**(-n)) - 1 ) #+ R**2/(6*M2)
    # fR = 1 - 2*n*lbd*(R/Rs)*((star)**(-(n+1))) #+ R/(3*M2)
    # fRR = (2*n*lbd/Rs)*(2*(n+1)*((R/Rs)**2)*(star**(-n-2)) - (star**(-n-1)))
              #+ 1/(3*M2)
    # ——— for both models ———
    yaux1 = yH + t**(-3) + chi*t**(-4)
    yaux2 = t**(-3) + 2*chi*t**(-4)
    j1 = 4 + (1/yaux1)*(1-fR)/(6*ms*fRR)
    j2 = (1/yaux1)*(2-fR)/(3*ms*fRR)
    j3 = - 3*t**(-3) - (((1-fR)*yaux2 + (R-f)/(3*ms))/yaux1)*(1/(6*ms*fRR))
    J1 = (1/t)*(1 + j1)
    J2 = (1/t)*(j2/t)
    J3 = (1/t)*(j3/t)
    dYH = - J1*YH - J2*yH - J3
    return [YH, dYH]

def H_HS(H0, O_m0, c2):
# def H_S(H0, O_m0, lbd):
    # Initial conditions according to the GR/LCDM theory
    y0 = [(1-O_m0)/O_m0, 0]
    # yH(t) solutions
    sol_HS = solve_ivp(yH_HS, t_span, y0, t_eval=t, method='LSODA',
                       rtol = 10**(-6), args=(H0, O_m0, c2))
    # sol_S = solve_ivp(yH_S, t_span, y0, t_eval=t, method='LSODA',
                       rtol = 10**(-6), args=(H0, O_m0, lbd))
    yH_HS1 = sol_HS.y[0]
    # yH_S1 = sol_S.y[0]
    # H(t) solutions
    chi = O_r0/O_m0
    ms = (H0**2)*O_m0
    H_HS = np.sqrt(ms*(yH_HS1 + (1/t)**3 + chi*(1/t)**4))
    # H_S = np.sqrt(ms*(yH_S1 + (1/t)**3 + chi*(1/t)**4))
    return H_HS
    # return H_S
# ————————————————————————————————————————————————————
```

The DE equation of state $w_{\rm DE}(a)$ is given through

```
# ------------------------------------------------------------------------
# wDE(t) solution Appleby-Battye model:
def wDE_AB(H0, O_m0, b):
    y0 = [Hi, dHi, ddHi] # recall this above
    sol_AB = solve_ivp(Hubble_AB, t_span, y0, t_eval=t, method='LSODA',
                       rtol = 10**(-6), args=(H0, O_m0, b))
    H_AB = sol_AB.y[0]
    dH_AB = sol_AB.y[1]
    ms = O_m0*H0**2
    chi = O_r0/O_m0
    yH_AB = (H_AB*H_AB/ms) - sol_AB.t**(-3) - chi*sol_AB.t**(-4)
    YH_AB = (2*H_AB*dH_AB/ms) + 3*sol_AB.t**(-4) + 4*chi*_AB.t**(-5)
    wDE_AB = - 1 - sol.t*YH_AB/(3*yH_AB)
    return wDE_AB
# ------------------------------------------------------------------------

# ------------------------------------------------------------------------
# wDE(t) solutions for the Hu-Sawicki and Starobinsky models:
def wDE_HS(H0, O_m0, c2):
# def wDE_S(H0, O_m0, lbd):
    y0 = [(1-O_m0)/O_m0, 0]
    sol_HS = solve_ivp(yH_HS, t_span, y0, t_eval=t, method='LSODA',
                       rtol = 10**(-6), args=(H0, O_m0, c2))
    yH_HS1 = sol_HS.y[0]
    YH_HS1 = sol_HS.y[1]
    wDE_HS = - 1 - sol_HS.t*YH_HS1/(3*yH_HS1)
    # sol_S = solve_ivp(yH_S, t_span, y0, t_eval=t, method='LSODA',
                       rtol = 10**(-6), args=(H0, O_m0, lbd))
    # yH_S1 = sol_S.y[0]
    # YH_S1 = sol_S.y[1]
    # wDE_S = - 1 - sol_S.t*YH_S1/(3*yH_S1)
    return wDE_HS
    # return wDE_S
# ------------------------------------------------------------------------
```

At the perturbative level, we numerically solved the differential equations for the matter density contrast, $\delta_m(a)$, and used the results to compute the normalized growth rate, $[f\sigma_8](a)$, for both the GR/ΛCDM and the three $f(R)$ models. For the GR/ΛCDM model, we have

```
# ------------------------------------------------------------------------
# D(t) from the GR/LCDM model:
def contrast_GR(t, y, H0, O_m0):
    D_GR = y[0]
    dD_GR = y[1]
    O_m = O_m0*t**(-3)
    O_r = O_r0*t**(-4)
    O_L = 1 - O_m0 - O_r0
    H_GR = H0*np.sqrt(O_m + O_r + O_L)
    dH_GR = - (H_GR/t) - 0.5*(H0/t)*(H0/H_GR)*(O_m + 2*O_r - 2*O_L)
    fGR1 = 3*H0**2
    fGR2 = 2*(t**2)*(H_GR**2)
    ddD_GR = - ((3/t) + (dH_GR/H_GR))*dD_GR + (fGR1/fGR2)*O_m*D_GR
    return [dD_GR, ddD_GR]

def D_GR(H0, O_m0):
    y0 = [0.2, 1]
    sol_GR = solve_ivp(contrast_GR, t_span, y0, t_eval=t, method='LSODA',
                       args=(H0, O_m0))
    D_GR = sol_GR.y[0]
    return D_GR

def fs8_GR(H0, O_m0, sig80):
    y0 = [0.2, 1]
    sol_GR = solve_ivp(contrast_GR, t_span, y0, t_eval=t, method='LSODA',
                       args=(H0, O_m0))
    dD_GR = sol_GR.y[1]
    fs8_GR = sig80*sol_GR.t*(dD_GR/D_GR(H0, O_m0)[999])
    return fs8_GR
# ------------------------------------------------------------------------
```

In case of the R^2-AB model, we have

```
# ------------------------------------------------------------------------
# D(t) according to the R2-AB model:
def contrast_AB(t, y, H0, O_m0, b):
    H_AB = y[0]
    dH_AB = y[1]
    ddH_AB = y[2]
```

```
D_AB = y[3]
dD_AB = y[4]
O_m = O_m0*t**(-3)
O_r = O_r0*t**(-4)
R_vac = 12*H0**2
e_AB = R_vac/np.log(1 + np.exp(2*b))
M2 = e_AB/Delta
R_AB = 6*H_AB*(2*H_AB + t*dH_AB)
alpha = (R_AB/e_AB) - b
if abs(alpha) < 25:
    s = 1/np.cosh(alpha)
else:
    s = 0
A = (H0**2)*(3*O_m + 4*O_r)
B = (2*t*H_AB*dH_AB*R_AB)/(3*M2)
C = t*H_AB*dH_AB*(np.tanh(alpha) + 1)
fAB1 = 6*(t**2)*(H_AB**2)/e_AB
fAB2 = ddH_AB + ((dH_AB**2)/H_AB) + (5*dH_AB/t)
if abs(alpha) < 15:
    F = ((fAB1*fAB2*s)**2)*np.tanh(alpha)
else:
    F = 0
if abs(alpha) < 15:
    I = 6*(t**3)*(H_AB**3)*((1/(3*M2)) + (0.5*s*s/e_AB))
else:
    I = 6*(t**3)*(H_AB**3)*(1/(3*M2))
U = (11*dH_AB**2/(t*H_AB)) + (dH_AB**3/(H_AB**2)) + (6*ddH_AB/t) +
                    (4*dH_AB*ddH_AB/H_AB)
dddH_AB = - ((A + B + C - F)/I) - U
fR = 0.5*(1 + np.tanh(alpha)) + R_AB/(3*M2)
fRR= (0.5/e_AB)*s**2 + 1/(3*M2)
k = 0.125*H0/100
gaux3 = (fRR/fR)*(k/t)**2
Geffn = (1/fR)*(1 + 4*gaux3)/(1 + 3*gaux3)
fABaux1 = 3*Geffn*H0**2
fABaux2 = 2*t*t*H_AB*H_AB
ddD_AB = - ((3/t) + (dH_AB/H_AB))*dD_AB +
                    (fABaux1/fABaux2)*O_m*D_AB
return [dH_AB, ddH_AB, dddH_AB, dD_AB, ddD_AB]
```

```
def D_AB(H0, O_m0, b):
    y0 = [Hi, dHi, ddHi, 0.2, 1] # recall this above
    sol_AB = solve_ivp(contrast_AB, t_span, y0, t_eval=t, method='LSODA',
                       rtol = 10**(-6), args=(H0, O_m0, b))
    D_AB = sol_AB.y[3]
    return D_AB

def fs8_AB(H0, O_m0, sig80, b):
    y0 = [Hi, dHi, ddHi, 0.2, 1] # recall this above
    sol_AB = solve_ivp(contrast_AB, t_span, y0, t_eval=t, method='LSODA',
                       rtol = 10**(-6), args=(H0, O_m0, b))
    D_AB = sol_AB.y[3]
    dD_AB = sol_AB.y[4]
    fs8_AB = sig80*sol_AB.t*(dD_AB/D_GR(H0, O_m0)[999]
    return fs8_AB
# ------------------------------------------------------------------
```

For the HS and Starobinsky models, we have

```
# ------------------------------------------------------------------
# D(t) according to the HS and Starobinsky models:
def contrast_HS(t, y, H0, O_m0, c2):
# def contrast_S(t, y, H0, O_m0, lbd):
    yH = y[0]
    YH = y[1]
    D_HS = y[2]
    dD_HS = y[3]
    # D_S = y[2]
    # dD_S = y[3]
    O_m = O_m0*t**(-3)
    O_r = O_r0*t**(-4)
    chi = O_r0/O_m0
    ms = (H0**2)*O_m0
    R = 3*ms*(4*yH + t*YH + t**(-3))
    # ---- HS model ----
    # M2 = ms/Delta
    c1 = 6*c2*(1 - O_m0)/O_m0
    xn1 = (R/ms)**n
```

```
    xn2 = c1/(ms**n)
    xn3 = (n+1)*(c2/ms)*R**(2*(n-1))
    xn4 = (n-1)*R**(n-2)
    xn5 = ((c2*xn1) + 1)
    f = R - ms*((c1*xn1)/((c2*xn1) + 1)) #+ R**2/(6*M2)
    fR = 1 - n*xn2*ms*((R**(n-1))/(xn5**2)) #+ R/(3*M2)
    fRR = n*xn2*ms*( (xn3 - xn4)/(xn5**3)) #+ 1/(3*M2)
    # ——— Starobinsky model ———
    # Rs = 6*(H0**2)*(1 - O_m0)/lbd
    # M2 = Rs/Delta
    # star = 1 + (R/Rs)**2
    # f = R + lbd*Rs*((star**(-n)) - 1) #+ R**2/(6*M2)
    # fR = 1 - 2*n*lbd*(R/Rs)*((star)**(-(n+1))) #+ R/(3*M2)
    # fRR = (2*n*lbd/Rs)*(2*(n+1)*((R/Rs)**2)*(star**(-n-2)) - (star**(-n-1)))
            #+ 1/(3*M2)
    # ——— for both models ———
    yaux1 = yH + t**(-3) + chi*t**(-4)
    yaux2 = t**(-3) + 2*chi*t**(-4)
    j1 = 4 + (1/yaux1)*(1-fR)/(6*ms*fRR)
    j2 = (1/yaux1)*(2-fR)/(3*ms*fRR)
    j3 = - 3*t**(-3) - (((1-fR)*yaux2 + (R-f)/(3*ms))/yaux1)*(1/(6*ms*fRR))
    J1 = (1/t)*(1 + j1)
    J2 = (1/t)*(j2/t)
    J3 = (1/t)*(j3/t)
    dYH = - J1*YH - J2*yH - J3
    H = np.sqrt(ms*(yH + (1/t)**3 + chi*(1/t)**4))
    dH = (R/(6*t*H)) - (2*H/t)
    k = 0.125*H0/100
    gaux3 = (fRR/fR)*(k/t)**2
    Geffn = (1/(fR))*(1 + 4*gaux3)/(1 + 3*gaux3)
    faux1 = 3*Geffn*H0**2
    faux2 = 2*t*t*H*H
    ddD_HS = - ((3/t) + (dH/H))*dD_HS + (faux1/faux2)*O_m*D_HS
    # ddD_S = - ((3/t) + (dH/H))*dD_S + (faux1/faux2)*O_m*D_S
    return [YH, dYH, dD_HS, ddD_HS]
    # return [YH, dYH, dD_S, ddD_S]

def D_HS(H0, O_m0, c2):
# def D_S(H0, O_m0, lbd):
```

```
    y0 = [(1-O_m0)/O_m0, 0, 0.2, 1]
    sol_HS = solve_ivp(contrast_HS, t_span, y0, t_eval=t, method='LSODA',
                       rtol = 10**(-6), args=(H0, O_m0, c2))
    D_HS = sol_HS.y[2]
    # sol_S = solve_ivp(contrast_S, t_span, y0, t_eval=t, method='LSODA',
                       rtol = 10**(-6), args=(H0, O_m0, lbd))
    # D_S = sol_S.y[2]
    return D_HS
    # return D_S

def fs8_HS(H0, O_m0, sig80, c2):
# def fs8_S(H0, O_m0, sig80, lbd):
    y0 = [(1-O_m0)/O_m0, 0, 0.2, 1]
    sol_HS = solve_ivp(contrast_HS, t_span, y0, t_eval=t, method='LSODA',
                       rtol = 10**(-6), args=(H0, O_m0, c2))
    D_HS = sol_HS.y[2]
    dD_HS = sol_HS.y[3]
    fs8_HS = sig80*sol_HS.t*(dD_HS/D_GR(H0, O_m0)[999])
    # sol_S = solve_ivp(contrast_S, t_span, y0, t_eval=t, method='LSODA',
                       rtol = 10**(-6), args=(H0, O_m0, lbd))
    # D_S = sol_S.y[2]
    # dD_S = sol_S.y[3]
    # fs8_S = sig80*sol_S.t*(dD_S/D_GR(H0, O_m0)[999])
    return fs8_HS
    # return fs8_S
# ------------------------------------------------------------------
```

As a final numerical test, we plotted the $\sigma_8(a)$ function for both the ΛCDM and R^2-AB models, i.e.,

```
# ------------------------------------------------------------------
# sig8(t) according to the LCDM model:
def sig8_GR(H0, O_m0, sig80):
    y0 = [0.2, 1]
    sol_GR = solve_ivp(contrast_GR, t_span, y0, t_eval=t, method='LSODA',
                       rtol = 10**(-6), args=(H0, O_m0))
    D_GR = sol_GR.y[0]
    sig8_GR = sig80*D_GR/D_GR[999]
    return sig8_GR
```

```
# ------------------------------------------------------------------------
```

and

```
# ------------------------------------------------------------------------
# sig8(t) according to the R2-AB model:
def sig8_AB(H0, O_m0, sig80, b):
    y0 = [Hi, dHi, ddHi, 0.2, 1]
    sol_AB = solve_ivp(contrast_AB, t_span, y0, t_eval=t, method='LSODA',
                       rtol = 10**(-6), args=(H0, O_m0, b))
    D_AB = sol_AB.y[3]
    sig8_AB = sig80*D_AB/D_GR(H0, O_m0)[999]
    return sig8_AB
# ------------------------------------------------------------------------
```

respectively. Having done this, we covered all the numerical solutions presented in this thesis, as shown in Figures 5.1(b) to 5.6(b).

The final steps involved adding the observational datasets for SNe, CC, and RSD, constructing the SNe and joint likelihoods, $\mathcal{L}_{\rm SNe}$ and $\mathcal{L} = \mathcal{L}_{\rm SNe} \times \mathcal{L}_{\rm CC} \times \mathcal{L}_{\rm RSD}$, respectively, and performing MCMC analyses for each model. To achieve this, we developed the following Python code for the R^2-AB model.

```
# ------------------------------------------------------------------------
# Fiducial:
O_r0 = 7.88*10**(-5)
c = 299792.458
w = - 1
k = 0.125
# ------------------------------------------------------------------------
# CC H(a) data:
aCC = [0.337, 0.364, 0.395, 0.412, 0.423, 0.435, 0.491, 0.526, 0.532, 0.533, 0.561,
       0.595, 0.628, 0.676, 0.676, 0.680, 0.690, 0.702, 0.714, 0.714, 0.725, 0.740,
       0.781, 0.787, 0.833, 0.834, 0.848, 0.855, 0.893, 0.917, 0.935]
HCC = [186.5, 202.0, 140.0, 177.0, 160.0, 168.0, 154.0, 117.0, 90.0, 125.0,
       105.0, 92.0, 104.0, 97.0, 80.9, 89.0, 92.8, 87.1, 77.0, 95.0, 83.0, 83.0, 88.8,
       77.0, 72.9, 75.0, 75.0, 83.0, 68.6, 69.0, 69.0]
sigmaCC = [50.4, 40.0, 14.0, 18.0, 33.6, 17.0, 20.0, 23.0, 40.0, 17.0, 12.0,
           8.0, 13.0, 62.0, 9.0, 49.6, 12.9, 11.2, 10.2, 17.0, 13.5, 14.0,
           36.6, 14.0, 29.6, 5.0, 4.0, 8.0, 26.2, 12.0, 19.6]
```

```
CC = pd.DataFrame({"aCC":aCC, "HCC":HCC, "sigmaCC":sigmaCC})
# ------------------------------------------------------------------------
# RSD fs8(a) data:
aRSD = [0.340, 0.403, 0.417, 0.488, 0.506, 0.541, 0.568, 0.575, 0.578, 0.588, 0.629,
        0.637, 0.694, 0.725, 0.758, 0.870, 0.909, 0.937, 0.976, 0.980]
fRSD = [0.364, 0.30, 0.482, 0.280, 0.379, 0.52, 0.440, 0.50, 0.437, 0.473, 0.488,
        0.453, 0.413, 0.497, 0.384, 0.53, 0.37, 0.423, 0.39, 0.398]
sigmaRSD = [0.106, 0.13, 0.116, 0.080, 0.176, 0.10, 0.040, 0.11, 0.072, 0.041, 0.060,
            0.022, 0.080, 0.045, 0.095, 0.16, 0.13, 0.055, 0.11, 0.065]
RSD = pd.DataFrame({"aRSD":aRSD, "fRSD":fRSD, "sigmaRSD":sigmaRSD})
# ------------------------------------------------------------------------
# Pantheon+ data and covariant matrix:
df= pd.read_csv('/home/usuario/Downloads/DataRelease-main/Pantheon+_Data/
      4_DISTANCES_AND_COVAR/Pantheon+SH0ES.dat', sep=' ')
df=df.sort_values("zCMB", ascending=False)
df['acmb'] = 1/(1+df["zCMB"])
a_sn = df['acmb']
mcov = np.loadtxt('/home/usuario/Downloads/DataRelease-main/
        Pantheon+_Data/4_DISTANCES_AND_COVAR/
        Pantheon+SH0ES_STAT+SYS.cov', skiprows=1)
cov = np.reshape(mcov, (1701, 1701))
Icov=np.linalg.inv(cov)
# ------------------------------------------------------------------------
# H_AB(aCC) solution:
acc = CC['aCC']
def HCC_AB(acc, H0, O_m0, b):
    y0 = [Hi, dHi, ddHi]
    sol_HCC_AB = solve_ivp(Hubble_AB, t_span, y0, t_eval=acc, method='LSODA',
                           rtol = 10**(-6), args=(H0, O_m0, b))
    H_AB = sol_HCC_AB.y[0]
    return H_AB
# ------------------------------------------------------------------------
# fs8_AB(aRSD) solution:
arsd = RSD['aRSD']
def norm_contrast_AB(t, y, O_m0, b):
    E_AB = y[0]
    dE_AB = y[1]
    ddE_AB = y[2]
    D_AB = y[3]
```

```
dD_AB = y[4]
O_m = O_m0*t**(-3)
O_r = O_r0*t**(-4)
e_AB = 12/np.log(1 + np.exp(2*b))
M2 = e_AB/Delta
R_AB = 6*E_AB*(2*E_AB + t*dE_AB)
alpha = (R_AB/e_AB) - b
if abs(alpha) < 25:
    s = 1/np.cosh(alpha)
else:
    s = 0
A = (3*O_m + 4*O_r)
B = (2*t*E_AB*dE_AB*R_AB)/(3*M2)
C = t*E_AB*dE_AB*(np.tanh(alpha) + 1)
fAB1 = 6*(t**2)*(E_AB**2)/e_AB
fAB2 = ddE_AB + ((dE_AB**2)/E_AB) + (5*dE_AB/t)
if abs(alpha) < 15:
    F = ((fAB1*fAB2*s)**2)*np.tanh(alpha)
else:
    F = 0
if abs(alpha) < 15:
    I = 6*(t**3)*(E_AB**3)*((1/(3*M2)) + (0.5*s*s/e_AB))
else:
    I = 6*(t**3)*(E_AB**3)*(1/(3*M2))
U = (11*dE_AB**2/(t*E_AB)) + (dE_AB**3/(E_AB**2)) + (6*ddE_AB/t) +
                (4*dE_AB*ddE_AB/E_AB)
dddE_AB = - ((A + B + C - F)/I) - U
fR = 0.5*(1 + np.tanh(alpha)) + R_AB/(3*M2)
fRR= (0.5/e_AB)*s**2 + 1/(3*M2)
gaux3 = (fRR/fR)*(0.01*k/t)**2
Geffn = (1/fR)*(1 + 4*gaux3)/(1 + 3*gaux3)
fABaux1 = 3*Geffn
fABaux2 = 2*t*t*E_AB*E_AB
ddD_AB = - ((3/t) + (dE_AB/E_AB))*dD_AB +
                (fABaux1/fABaux2)*O_m*D_AB
return [dE_AB, ddE_AB, dddE_AB, dD_AB, ddD_AB]
```

```
def norm_contrast_GR(t, y, O_m0):
    D_GR = y[0]
    dD_GR = y[1]
    O_m = O_m0*t**(-3)
    O_r = O_r0*t**(-4)
    O_L = 1 - O_m0 - O_r0
    E_GR = np.sqrt(O_m + O_r + O_L)
    dE_GR = - (E_GR/t) - ((O_m + 2*O_r - 2*O_L)/(2*t*E_GR))
    fGR1 = 3
    fGR2 = 2*(t**2)*(E_GR**2)
    ddD_GR = - ((3/t) + (dE_GR/E_GR))*dD_GR + (fGR1/fGR2)*O_m*D_GR
    return [dD_GR, ddD_GR]

def D_norm_GR(O_m0):
    y0 = [0.2, 1]
    sol_AB = solve_ivp(norm_contrast_GR, t_span, y0, t_eval=t, method='LSODA',
                       rtol = 10**(-6), args=(O_m0,))
    D_RSD_AB = sol_AB.y[0]
    return D_RSD_AB

def fs8RSD_AB(arsd, O_m0, sig80, b):
    O_mi = O_m0*ti**(-3)
    O_ri = O_r0*ti**(-4)
    O_L = 1 - O_m0 - O_r0
    Ei = np.sqrt(O_mi + O_ri + O_L)
    dEi = - (Ei/ti) - ((O_mi + 2*O_ri - 2*O_L)/(2*ti*Ei))
    au1 = Ei/(ti**2)
    au2 = 0.5*(Ei + ti*dEi)/(ti*Ei)
    au3 = (O_mi + 2*O_ri - 2*O_L)/(ti*Ei)
    au4 = (3*O_mi + 8*O_ri)/Ei
    ddEi = au1 + au2*au3 + 0.5*(ti**(-2))*au4 - (dEi/ti)
    y0 = [Ei, dEi, ddEi, 0.2, 1]
    sol_AB = solve_ivp(norm_contrast_AB, t_span, y0, t_eval=arsd,
                       method='LSODA', rtol = 10**(-6), args=(O_m0, b))
    D_RSD_AB = sol_AB.y[3]
    dD_RSD_AB = sol_AB.y[4]
    fs8_AB = sig80*sol_AB.t*(dD_RSD_AB/D_norm_GR(O_m0)[999])
    return fs8_AB
# ------------------------------------------------------------------------
```

```
# mB_AB(a_sn) solution:
# —— Initial conditions according to the GR/LCDM model ——
def int_GR(H0, O_m0):
    ms = H0*np.sqrt(O_m0)
    O_m = O_m0*t**(-3)
    O_L = 1 - O_m0 - O_r0
    hyper = scipy.special.hyp2f1
    H_GR = H0*np.sqrt(O_m + O_L)
    x1 = - 1/(6*w)
    x2 = 1 + x1
    x3 = 1 - (1/O_m0)
    x4 = 1 - ((1/O_m)*(H_GR/H0)**2)
    intGR = (2/ms)*(hyper(1/2,x1,x2,x3) - np.sqrt(t)*hyper(1/2,x1,x2,x4))
    return intGR
# —— Integral into dL ——
def integral_AB(H0, O_m0, b):
    y = 1/((t**2)*H_AB(H0, O_m0, b))
    intAB = int_GR(H0, O_m0)[0] + integrate.cumulative_trapezoid(y, t, initial=0)
    return intAB
# —— Primitive ——
def primitive_AB(H0, O_m0, b):
    prim_AB = integral_AB(H0, O_m0, b)[999] - integral_AB(H0, O_m0, b)
    return prim_AB
# —— Interpolating with data points ——
def IntAB_interp(H0, O_m0, b):
    x_interp = df['acmb']
    y_interp = np.interp(x_interp, t, primitive_AB(H0, O_m0, b))
    return y_interp
# —— Luminosity-distance ——
def Lumi_AB(H0, O_m0, b):
    dL_AB = (c/df['acmb'])*(IntAB_interp(H0, O_m0, b))
    return dL_AB
# —— Relative magnitude ——
def mag_AB(a_sn, H0, O_m0, Mb, b):
    mb_AB = 5*np.log10(Lumi_AB(H0, O_m0, b)) + 25 + Mb
    return mb_AB
# ————————————————————————————————————————————————————————
# CC chi-square:
y_cc = CC['HCC']
```

```
yerr_cc = CC['sigmaCC']
def chiCC(acc, H0, O_m0, b, y_cc, yerr_cc):
    ycc_model = HCC_AB(acc, H0, O_m0, b)
    return np.sum(((y_cc - ycc_model)/yerr_cc)**2)
def chi2cc(theta_cc, acc, y_cc, yerr_cc):
    H0, O_m0, b = theta_cc
    return chiCC(acc, H0, O_m0, b, y_cc, yerr_cc)
# ------------------------------------------------------------------
# RSD chi-square:
y_rsd = RSD['fRSD']
yerr_rsd = RSD['sigmaRSD']
def chiRSD(arsd, O_m0, sig80, b, y_rsd, yerr_rsd):
    yrsd_model = fs8RSD_AB(arsd, O_m0, sig80, b)
    return np.sum(((y_rsd - yrsd_model)/yerr_rsd)**2)
def chi2rsd(theta_rsd, arsd, y_rsd, yerr_rsd):
    O_m0, sig80, b = theta_rsd
    return chiRSD(arsd, O_m0, sig80, b, y_rsd, yerr_rsd)
# ------------------------------------------------------------------
# SNe chi-square:
y_sn = df["m_b_corr"]
def deltaSNe(a_sn, H0, O_m0, Mb, b, y_sn):
    mb_model = mag_AB(a_sn, H0, O_m0, Mb, b)
    deltaSNe = y_sn - mb_model
    return deltaSNe
def chi2_SN(a_sn, H0, O_m0, Mb, b, y_sn, Icov):
    chisq = np.sum(np.dot(np.dot(deltaSNe(a_sn, H0, O_m0, Mb, b, y_sn), Icov),
                deltaSNe(a_sn, H0, O_m0, Mb, b, y_sn)))
    return chisq
def chisq_SN(theta_sn, a_sn, y_sn, Icov):
    H0, O_m0, Mb, b = theta_sn
    return chi2_SN(a_sn, H0, O_m0, Mb, b, y_sn, Icov)
# ------------------------------------------------------------------
# Total chi-square:
def chi_tot(acc, arsd, a_sn, H0, O_m0, sig80, Mb, b, y_cc,
        y_rsd, y_sn, yerr_cc, yerr_rsd, Icov):
    chicc = chiCC(acc, H0, O_m0, b, y_cc, yerr_cc)
    chirsd = chiRSD(arsd, O_m0, sig80, b, y_rsd, yerr_rsd)
    chisn = chi2_SN(a_sn, H0, O_m0, Mb, b, y_sn, Icov)
    return chicc + chirsd + chisn
```

```
def chi2_tot(theta, acc, arsd, a_sn, y_cc, y_rsd, y_sn, yerr_cc, yerr_rsd, Icov):
    H0, O_m0, sig80, Mb, b = theta
    return chi_tot(acc, arsd, a_sn, H0, O_m0, sig80, Mb, b, y_cc, y_rsd, y_sn,
                   yerr_cc, yerr_rsd, Icov)
# ------------------------------------------------------------------------
# likelihood:
def lnlike(theta, acc, arsd, a_sn, y_cc, y_rsd, y_sn, yerr_cc, yerr_rsd, Icov):
    H0, O_m0, sig80, Mb, b = theta
    return -0.5*chi2_tot(theta, acc, arsd, a_sn, y_cc, y_rsd, y_sn, yerr_cc,
                yerr_rsd, Icov)
# ------------------------------------------------------------------------
# prior:
def lnprior(theta):
    H0, O_m0, sig80, Mb, b = theta
    if 54 < H0 < 76 and 0.1 < O_m0 < 0.5 and 0.7 < sig80 < 0.9 and
            -20.2 < Mb < -19 and 1.6 < b < 12:
        return 0.0
    return -np.inf
# ------------------------------------------------------------------------
# Posterior:
def lnprob(theta, acc, arsd, a_sn, y_cc, y_rsd, y_sn, yerr_cc, yerr_rsd, Icov):
    lp = lnprior(theta)
    if not np.isfinite(lp):
        return -np.inf
    return lp + lnlike(theta, acc, arsd, a_sn, y_cc, y_rsd, y_sn, yerr_cc, yerr_rsd, Icov)
# ------------------------------------------------------------------------
# Config:
data = (acc, arsd, a_sn, y_cc, y_rsd, y_sn, yerr_cc, yerr_rsd, Icov)
nwalkers = 25
niter = 8000
initial = np.array([70, 0.3, 0.8, -19.253, 2])
ndim = len(initial)
p0 = [np.array(initial) + 1e-4*np.random.randn(ndim) for i in range(nwalkers)]
# ------------------------------------------------------------------------
# Run MCMC:
with Pool() as pool:
    def main(p0,nwalkers,niter,ndim,lnprob,data):
        sampler = emcee.EnsembleSampler(nwalkers, ndim, lnprob, args=data,
                        pool=pool)
```

```
        print("Running burn-in...")
        p0, _, _ = sampler.run_mcmc(p0, 1500, progress=True)
        sampler.reset()
        print("Running production...")
        pos, prob, state = sampler.run_mcmc(p0, niter, progress=True)
        return sampler, pos, prob, state
    sampler, pos, prob, state = main(p0,nwalkers,niter,ndim,lnprob,data)
# ------------------------------------------------------------------
burnin = 1500
like_model = sampler.get_log_prob(discard=burnin, flat=False)
chi2_model = -2*like_model
np.savetxt('log_pro_SNe+CC+RSD.txt', like_model, fmt="%s")
print(chi2_model.min())
# ------------------------------------------------------------------
samples1 = sampler.flatchain
samples1[np.argmax(sampler.flatlnprobability)]
np.savetxt("Results_SNe+CC+RSD.txt", samples1, fmt="%s")
# ------------------------------------------------------------------
# Triangle plot:
c=ChainConsumer().add_chain(samples1, parameters=[r"$H_0$", r"$\Omega_{m,0}$", r"$\sigma_{8,0}$",
            r"$M_B$", r"$b$"])
c.configure(shade_alpha=1, summary=True, colors=["blue"],
            max_ticks=4,legend_artists=True)
fig = c.plotter.plot()
fig.set_size_inches(3 + fig.get_size_inches())
plt.savefig('SN+CC+RSD.pdf', dpi=520, format='pdf', bbox_inches='tight')
# ------------------------------------------------------------------
```

The HS model, in turn, proceeded from the following similar code.

```
# ------------------------------------------------------------------
# H_HS(aCC) solution:
def yH_HS2(t, y, H0, O_m0, mu):
    yH = y[0]
    YH = y[1]
    O_m = O_m0*t**(-3)
    O_r = O_r0*t**(-4)
    Lbd = 3*(H0**2)*(1 - O_m0)
    chi = O_r0/O_m0
```

```
    ms = (H0**2)*O_m0
    R = 3*ms*(4*yH + t*YH + t**(-3))
    A = (R**n) + (mu**(2*n))
    B = (R**n)
    C = (n+1)*(R**(2*n - 2)) - (n- 1)*(mu**(2*n))*(R**(n-2))
    D = A**3
    f = R - 2*Lbd*(B/A)
    fR = 1 - 2*n*Lbd*(mu**(2*n))*(B/A)*(1/(R*A))
    fRR = 2*n*Lbd*(mu**(2*n))*(C/D)
    yaux1 = yH + t**(-3) + chi*t**(-4)
    yaux2 = t**(-3) + 2*chi*t**(-4)
    j1 = 4 + (1/yaux1)*(1-fR)/(6*ms*fRR)
    j2 = (1/yaux1)*(2-fR)/(3*ms*fRR)
    j3 = - 3*t**(-3) - (((1-fR)*yaux2 + (R-f)/(3*ms))/yaux1)*(1/(6*ms*fRR))
    J1 = (1/t)*(1 + j1)
    J2 = (1/t)*(j2/t)
    J3 = (1/t)*(j3/t)
    dYH = - J1*YH - J2*yH - J3
    return [YH, dYH]

def HCC_HS(acc, H0, O_m0, mu):
    y0 = [(1-O_m0)/O_m0, 0]
    sol_yHCC_HS = solve_ivp(yH_HS2, t_span, y0, t_eval=acc, method='LSODA',
                            rtol = 10**(-6), args=(H0, O_m0, mu))
    yHCC_HS = sol_yHCC_HS.y[0]
    chi = O_r0/O_m0
    ms = (H0**2)*O_m0
    HCC_HS = np.sqrt(ms*(yHCC_HS + (1/acc)**3 + chi*(1/acc)**4))
    return HCC_HS
# ------------------------------------------------------------------
# fs8_HS(aRSD) solution:
def contrast_HS2(t, y, H0, O_m0, mu):
    yH = y[0]
    YH = y[1]
    D_HS = y[2]
    dD_HS = y[3]
    O_m = O_m0*t**(-3)
    O_r = O_r0*t**(-4)
    Lbd = 3*(H0**2)*(1 - O_m0)
```

```
    chi = O_r0/O_m0
    ms = (H0**2)*O_m0
    R = 3*ms*(4*yH + t*YH + t**(-3))
    A = (R**n) + (mu**(2*n))
    B = (R**n)
    C = (n+1)*(R**(2*n - 2)) - (n- 1)*(mu**(2*n))*(R**(n-2))
    D = A**3
    f = R - 2*Lbd*(B/A)
    fR = 1 - 2*n*Lbd*(mu**(2*n))*(B/A)*(1/(R*A))
    fRR = 2*n*Lbd*(mu**(2*n))*(C/D)
    yaux1 = yH + t**(-3) + chi*t**(-4)
    yaux2 = t**(-3) + 2*chi*t**(-4)
    j1 = 4 + (1/yaux1)*(1-fR)/(6*ms*fRR)
    j2 = (1/yaux1)*(2-fR)/(3*ms*fRR)
    j3 = - 3*t**(-3) - (((1-fR)*yaux2 + (R-f)/(3*ms))/yaux1)*(1/(6*ms*fRR))
    J1 = (1/t)*(1 + j1)
    J2 = (1/t)*(j2/t)
    J3 = (1/t)*(j3/t)
    dYH = - J1*YH - J2*yH - J3
    H_HS = np.sqrt(ms*(yH + (1/t)**3 + chi*(1/t)**4))
    dH_HS = (R/(6*t*H_HS)) - (2*H_HS/t)
    gaux3 = (fRR/fR)*(0.01*k/t)**2
    Geffn = (1/fR)*(1 + 4*gaux3)/(1 + 3*gaux3)
    fAB1 = 3*Geffn*H0**2
    fAB2 = 2*t*t*H_HS*H_HS
    ddD_HS = - ((3/t) + (dH_HS/H_HS))*dD_HS + (fAB1/fAB2)*O_m*D_HS
    return [YH, dYH, dD_HS, ddD_HS]

def fs8_HS2(arsd, H0, O_m0, sig80, mu):
    y0 = [(1-O_m0)/O_m0, 0, 0.2, 1]
    sol_HS = solve_ivp(contrast_HS2, t_span, y0, t_eval=t, method='LSODA',
                       rtol = 10**(-6), args=(H0, O_m0, mu))
    D_HS = sol_HS.y[2]
    dD_HS = sol_HS.y[3]
    fs8_HS = sig80*sol_HS.t*(dD_HS/D_GR(H0, O_m0)[999])
    return fs8_HS
# ---------------------------------------------------------------------
# mB_HS(a_sn) solution:
def H_HS2(H0, O_m0, mu):
```

```
    y0 = [(1-O_m0)/O_m0, 0]
    sol_yHCC_HS = solve_ivp(yH_HS2, t_span, y0, t_eval=t, method='LSODA',
                            rtol = 10**(-6), args=(H0, O_m0, mu))
    yHCC_HS = sol_yHCC_HS.y[0]
    chi = O_r0/O_m0
    ms = (H0**2)*O_m0
    H_HS = np.sqrt(ms*(yHCC_HS + (1/sol_yHCC_HS.t)**3 +
                  chi*(1/sol_yHCC_HS.t)**4))
    return H_HS

def integral_HS2(H0, O_m0, mu):
    y = 1/((t**2)*H_HS2(H0, O m0, mu))
    intHS = int_GR(H0, O_m0)[0] + integrate.cumulative_trapezoid(y, t, initial=0)
    return intHS

def primitive_HS2(H0, O_m0, mu):
    prim_HS = integral_HS2(H0, O_m0, mu)[999] - integral_HS2(H0, O_m0, mu)
    return prim_HS

def IntHS_interp2(H0, O_m0, mu):
    x_interp = df[‘acmb’]
    y_interp = np.interp(x_interp, t, primitive_HS(H0, O m0, mu))
    return y_interp

def Lumi_HS2(H0, O_m0, mu):
    dL_HS = (c/df[‘acmb’])*(IntHS_interp2(H0, O m0, mu))
    return dL_HS

def mag_HS(a_sn, H0, O_m0, Mb, mu):
    mb_HS = 5*np.log10(Lumi_HS2(H0, O m0, c2)) + 25 + Mb
    return mb_HS
# ——————————————————————————————————————
```

The next steps for the HS model, which include building the total chi-square, likelihood, prior, posterior, running MCMC, and generating the triangle plot, are identical to those for the AB model, with the following substitutions: $b \rightarrow \mu$, HCC_AB(acc, $H_0, \Omega_{\mathrm{m},0}, b$) $\rightarrow$ HCC_HS(acc, H_0, Ω_{m0}, μ), fs8RSD_AB(arsd, $\Omega_{\mathrm{m},0}, \sigma_{80}, b$) $\rightarrow$ fs8RSD_HS(arsd, $H_0, \Omega_{\mathrm{m},0}, \sigma_{8,0}, \mu$), and finally mag_AB(a_sn, $H_0, \Omega_{\mathrm{m},0}, M_b, b$) $\rightarrow$ mag_HS(a_sn, $H_0, \Omega_{\mathrm{m},0}, M_b, \mu$).